

CO₂-microemulsions with additives:
Phase behaviour, microstructure
and pressure-induced kinetics

Inaugural-Dissertation

zur

Erlangung des Doktorgrades

der Mathematisch-Naturwissenschaftlichen Fakultät

der Universität zu Köln

vorgelegt von

Yvonne Pütz

aus Bad Soden

Köln, Februar 2015

Berichtersteller: Prof. Dr. Reinhard Strey
Prof. Dr. Annette M. Schmidt

Tag der mündlichen Prüfung: 10. April 2015

Meiner wunderbaren Familie



„There are times in life when people must know when not to let go.

Balloons are designed to teach small children this.“

- Terry Pratchett

ABSTRACT

Improved building insulation is an important part of today's efforts on energy saving. Here, nano-insulation materials promise especially low thermal conductivity. Therefore, an easy and cost-efficient production of these materials is an aim of present material research. One approach towards these materials is the expansion and fixation of polymerisable microemulsions of supercritical blowing agents. However, the nano-sized bubbles are found to undergo undesired coarsening processes. In order to reduce the increasing interfacial tension emerging during expansion and therewith the coarsening it was suggested to add low-molecular hydrophobic substances to the supercritical microemulsion. And indeed, the addition of cyclohexane to a microemulsion of the type brine – CO₂ – fluorinated surfactants was found to reduce the fluorinated surfactant content – a measure for the interfacial tension - considerably. In this work a systematic small-angle neutron scattering (SANS) contrast variation was performed and the data were analysed by model-independent Fourier analysis. It was found that a concentration gradient of cyclohexane inside the CO₂/cyclohexane microemulsion droplets forms. Interestingly, the analysis reveals a depletion zone close to the amphiphilic film which presumably develops due to the known repulsive interactions of cyclohexane and the fluorinated surfactant tails. Using a specially designed high pressure SANS cell to perform stroboscopic pressure jumps, the influence of cyclohexane on pressure-induced elongation of microemulsion droplets as well as the early state of foaming after expansion was studied. Here, the pressure-dependent thermodynamic stability of such microemulsions allows for a fast repeatability of the pressure cycles. It turned out that cyclohexane systematically slows down the structural changes in all processes. Parallel pressure jump experiments with poly-(*N*-isopropylacrylamide) (PNIPAM) particles revealed that hydration and dehydration kinetics can be studied with the same experimental setup. The first kinetic experiments which combine a CO₂-microemulsion mixed with PNIPAM particles indicate that PNIPAM acts as a stabiliser for the microemulsion and further reduces the thermodynamic driving force of the demixing process.

KURZZUSAMMENFASSUNG

Die Gebäudeisolation stellt einen wichtigen Teil der Bemühungen zur Energieeinsparung dar, wobei nano-Isolationsmaterialien besonders niedrige Wärmeleitfähigkeiten versprechen. Eine einfache und kosteneffiziente Produktion solcher Materialien steht daher im Fokus aktueller Forschung. Eine Möglichkeit zur Herstellung solcher Materialien besteht aus Expansion und Fixierung einer polymerisierbaren Mikroemulsion mit überkritischem Treibmittel, wobei bei der Expansion allerdings durch Zunahme der Grenzflächenspannung Vergrößerungsprozesse der nano-skaligen Tröpfchen auftreten können. Ein Ansatz, diese Alterung zu verringern, besteht aus dem Zusatz niedermolekularer hydrophober Substanzen zu der überkritischen Mikroemulsion. Durch Zugabe von Cyclohexan zu einer Mikroemulsion des Types Salzlösung – CO₂ – fluorierte Tenside konnte eine deutliche Reduzierung des Tensidgehaltes – ein Maß für die Grenzflächenspannung – erzielt werden. In dieser Arbeit wurde eine systematische Kontrastvariation mit Kleinwinkelneutronenstreuung (SANS) durchgeführt, wobei die Daten mit einer modelunabhängigen Fourier-Analyse ausgewertet wurden. Es stellte sich heraus, dass ein Konzentrationsgradient an Cyclohexan innerhalb der mit CO₂ und Cyclohexan gefüllten Mizellen gebildet wird. Dies macht deutlich, dass es zu einer Verarmung an Cyclohexan in der Nähe des amphiphilen Films kommt, welche auf die bekannten repulsiven Wechselwirkungen zwischen Cyclohexan und den fluorierten Tensidschwänzen zurückzuführen ist. Unter Verwendung einer speziell entwickelten Hochdruck-SANS-Zelle wurde bei stroboskopischen Drucksprüngen beobachtet, dass Cyclohexan die Kinetik von druckinduzierten Elongationen und die frühen Stadien des Schäumprozesses deutlich verlangsamt. Parallel dazu durchgeführte Drucksprungexperimente mit poly-(*N*-isopropylacrylamid) (PNIPAM) Partikeln zeigten, dass die Hydratations- und Dehydratationskinetiken ebenfalls mit diesem experimentellem Aufbau untersucht werden konnten. Erste kinetische Experimente, welche CO₂-Mikroemulsionen mit PNIPAM Partikeln kombinieren, deuten an, dass PNIPAM als Stabilisator für die Mikroemulsion fungiert und die thermodynamische Triebkraft zur Entmischung weiter reduziert.

DANKSAGUNG

Die vorliegende Arbeit wurde im Zeitraum Juni 2012 bis Februar 2015 am Institut für Physikalische Chemie der Universität zu Köln unter der wissenschaftlichen Anleitung von Herrn Prof. Dr. *Reinhard Strey* angefertigt. Ihnen, Herr Strey, möchte ich für die Möglichkeit danken, diese Arbeit in Ihrer Arbeitsgruppe anzufertigen, dass Sie mich immer unterstützt haben und mit Ihrer steten Diskussionsbereitschaft viele wertvolle Anstöße für diese Arbeit geliefert haben. Einen besonderen Dank möchte ich dafür aussprechen, dass Sie mir stets großes Vertrauen entgegen gebracht haben und ich auch eine Vielzahl von eigenen Ideen verfolgen durfte, die nicht von Anfang an geplant waren. Darüber hinaus bin ich Ihnen sehr dankbar, dass Sie mir immer wieder die Gelegenheit gegeben haben, internationale Erfahrungen zu sammeln – sei es durch Messreisen nach Grenoble, durch den Besuch internationaler, wissenschaftlicher Tagungen oder durch den Forschungsaufenthalt in London.

Frau Prof. Dr. *Annette M. Schmidt* möchte ich für die Übernahme des Korreferats dieser Arbeit danken. Auch für Ihre Unterstützung für mögliche zukünftige Projekte bin ich Ihnen sehr dankbar. Ihre Vorlesung und die Diskussionen im Rahmen einer Bachelorarbeit haben einige wichtige Denkanstöße besonders für den PNIPAM Teil geliefert!

Ein ganz besonderer Dank geht an Herrn PD Dr. *Thomas Sottmann*. Du hast mich von Beginn an unterstützt und in die Neutronenstrommessungen einbezogen, wofür ich Dir sehr dankbar bin. Deine stete Bereitschaft, meine zahlreichen Fragen zu beantworten, die vielen wissenschaftlichen Diskussionen über meine Daten und die viele Zeit, die Du in Proposals, Paper, verschiedene Anträge und nicht zuletzt in die Durchsicht meiner Arbeit gesteckt hast, haben entscheidend dazu beigetragen, dass diese Arbeit so möglich war. Die vielen Schichten, die wir zusammen in Grenoble verbracht haben, werden mir mit Sicherheit in Zukunft fehlen!

Für stets exzellente und erfolgreiche Zusammenarbeit möchte ich mich bei allen Mitarbeitern der Feinmechanischen Werkstatt, besonders aber bei Herrn *Herbert Metzner* bedanken. Ohne Ihre vielen Ideen und Ihren Glaube an das Projekt wäre die Weiterentwicklung der SANS-Zelle nicht möglich gewesen. Darüber hinaus möchte ich mich bei Herrn *Viktor Clippert* bedanken, für das Engagement und die vielen interessanten technischen Diskussionen. Außerdem gilt mein Dank Herrn *Thomas Michaelis*, für die vielen Stunden, die Sie an der Zelle herumgeschraubt haben. Und vielen Dank dafür, dass Sie immer so große Geduld aufgebracht haben, mir die technischen Zeichnungen und das Innenleben einiger Geräte und Bauteile zu erklären. Darüber hinaus möchte ich mich bei Frau *Leyla Balici* für die Anfertigung der technischen Zeichnungen bedanken.

Für die stets gute Zusammenarbeit während der Neutronenstrommessungen möchte ich mich bei den Local Contacts des D22, Herrn Dr. *Albrecht Wiedenmann* und Herrn Dr. *Lionel Porcar*, bedanken.

Danke, dass ihr beide auch außerhalb der Messzeiten stets zeitnah auf Fragen geantwortet und für Diskussionen zur Verfügung gestanden habt! Auch den Local Contacts vom D11, Herrn Dr. *Ralf Schweins* und Herrn Dr. *Peter Lindner*, möchte ich herzlich für die Zusammenarbeit danken. Besonders Dir, Ralf, außerdem ein herzlicher Dank für die Unterstützung des geplanten Projekts. Dabei möchte ich auch Herrn *Kenneth Honniball* (D22) und Herrn *David Bowyer* (D11), Techniker am ILL, nicht vergessen. Vielen Dank für die Besorgung der Vielzahl an Gasflaschen und die Spezialanfertigungen während der Messzeit!

Ebenfalls im Zusammenhang mit Neutronenstreuemessungen möchte ich mich bei den Mitgliedern der SANS Teams bedanken. Besonders die TISANE Messzeiten mit Herrn Dr. *Nils Becker*, Frau *Lena Grassberger*, Herrn Dr. *Alexander Müller*, Herrn Dr. *Roland Oberhoffer* und Herrn PD Dr. *Thomas Sottmann* waren immer ein ganz besonderes Erlebnis! Mit exzellenter Teamarbeit haben wir alle zusammen so manch scheinbar unlösbares Problem gelöst! Von den vielen Dichtungen, die wir zusammen gewechselt haben, Thomas, werde ich bestimmt eine als Erinnerung aufheben. Vielen Dank für die tatkräftige Unterstützung, die hervorragende Zusammenarbeit und die zwar anstrengenden, aber auch oft sehr lustigen Nachtschichten, in denen besonders Du, Lena, mich mit einem geklatschtem „Hopp, hopp!“ öfter wieder auf Trab gebracht hast! Ganz besonders bedanken möchte ich mich an dieser Stelle bei Dir, Alex, dafür, dass Du mir Neutronenstreuung und TISANE mit großer Geduld erklärt hast. Auch die Messzeiten mit Frau *Carola Harbauer*, Herrn Dr. *Helge Klemmer*, Herrn *Stefan Lülsdorf*, Frau *Ji-Yoon Yang* und Frau *Diana Zauser* waren sehr lehrreich für mich und auch an euch vielen Dank für die gute Zusammenarbeit und die vielen interessanten Diskussionen! Für die Unterstützung im Zusammenhang mit dem GIFT Verfahren möchte ich mich darüber hinaus herzlich bei Herrn Prof. Dr. *Otto Glatter* und bei Herrn Dr. *Michael Klostermann* bedanken.

Einen kurzen aber besonderen Teil meiner Doktorarbeit habe ich in der „Polymer and Microfluidics group“ von Dr *João T. Cabral* am Imperial College in London verbracht. João, ich möchte Dir noch einmal ganz herzlich danken, dass ich, wenn auch nur für ein paar Wochen, Mitglied Deiner Gruppe werden durfte, und auch für die vielen interessanten Diskussionen über die gesammelten Daten. In dieser Zeit habe ich nicht nur viel gelernt, sondern auch viele neue Freunde gewonnen! Den Mitgliedern dieser Gruppe, ganz besonders aber Herrn *Carlos Garcia-Lopez* und Herrn Dr. *Andreas Stavros Poulos*, möchte ich einen herzlichen Dank aussprechen für die Unterstützung bei den SLS Messungen und des Microfluidic-Projektes! An dieser Stelle ist ein Dankeschön an den Fonds der Chemischen Industrie passend für die finanzielle Unterstützung, die diesen Forschungsaufenthalt ermöglicht hat.

Für die sorgfältige Durchsicht dieser Arbeit möchte ich mich zudem bei Frau *Lena Grassberger*, Frau *Carola Harbauer*, Herrn Dr. *Helge Klemmer* (besonders bei Dir), Herrn Dr. *Alexander Müller*, Herrn

Dr. *Thomas Sottmann* und Herrn Dr. *Andreas Stavros Poulos* ganz herzlich bedanken! Bei Herrn Dr. *Lhoussaine Belkoura* bedanke ich mich für die Unterstützung beim Aufbau der HPDLS Anlage. Ohne Sie, Herr Belkoura, wäre dieses Projekt so nicht möglich gewesen!

Natürlich gebührt auch den Mitgliedern des Arbeitskreises ein großer Dank für die stets angenehme, konstruktive Arbeitsatmosphäre und die ständige Diskussionsbereitschaft. Dabei besonders hervorheben möchte ich meine Laborkollegen Frau *Lena Grassberger*, Frau *Melissa Hermes*, Herrn Dr. *Alexander Müller*, Herrn Dr. *Roland Oberhoffer* und Frau *Kavita Singh-Ghotra*. Besonders, wenn es um SANS Ergebnisse ging, warst auch Du, Helge, immer für Diskussionen zu haben. Für die vielen Phasendiagramme und DLS-Messungen möchte ich mich außerdem sehr herzlich bei Frau *Melissa Hermes* bedanken. Gerade in Zeiten vor Grenoble weiß ich nicht, wie ich die Vorbereitung ohne Dich geschafft hätte! Auch bei Frau *Vanessa Rauch* möchte ich mich bedanken, für Dein Engagement während Deiner Bachelorarbeit, deren Ergebnisse auch in meine Doktorarbeit beeinflusst haben. Den Herren Dr. *Jan-Hubert Wittmann* und *Tim Schreiner* bin ich für sehr kompetente Hilfe bei allen IT-Problemen sehr dankbar!

Zusätzlich zu all jenen namentlich nicht genannten Freunden und Bekannten in der Chemie der Uni Köln möchte ich mich natürlich auch bei meinen Freunden außerhalb der Universität bedanken, die stets für ein gutes Gleichgewicht zwischen Arbeit und Freizeit gesorgt haben. Nicht nur meine Freunde, sondern natürlich auch meine großartige Familie ist mir immer eine verlässliche Stütze. Dabei besonders bedanken möchte ich mich vor allem bei meinen vier Großeltern, die mich bereits mein ganzes Leben lang unterstützt haben und ausnahmslos und immer für mich da waren und sind. Ich bin sehr stolz, solche Großeltern wie Euch zu haben! Auch meinen Eltern, Frau *Susanne Pütz-Hebel* und Herrn *Peter Pütz* möchte ich danken. Wann immer ich Dich besucht habe, Mama, habe ich bestimmt ein Kilo zugenommen und noch genug Essen für eine Woche mit nach Köln zurück genommen! Bei Dir, Papa, möchte ich mich neben der allgegenwärtigen Unterstützung vor allem für die Radtouren im Kölner Umland bedanken, die meine Ortskenntnisse erheblich verbessert haben!

Ein ganz besonderer Dank geht an Herrn *Stefan Reimann*. Du weißt selbst am besten, wie wichtig Deine Unterstützung nicht nur in den stressigen Zeiten vor Grenoble und vor der Abgabe für mich war. Ich bin sehr froh, Dich an meiner Seite zu haben!

TABLE OF CONTENTS

1	Introduction	1
2	Fundamentals	7
2.1	Microemulsions	7
2.1.1	Phase behaviour of binary mixtures	7
2.1.2	The phase prism – ternary mixtures	8
2.1.3	Curvature of the amphiphilic film and microstructure	12
2.2	Microemulsions with supercritical carbon dioxide	16
2.2.1	Flourinated surfactants and their impact on CO ₂ -microemulsions	16
2.2.2	CO ₂ -microemulsions as templates for nanoporous foams	17
2.2.3	Aging phenomena and the concept of anti-ageing agents	19
2.3	Thermoresponsive polymers	23
2.3.1	Emulsion polymerisation.....	23
2.3.2	Swelling of poly-(<i>N</i> -isopropyl)acrylamide.....	27
2.3.3	Microgel applications	29
2.4	Neutron scattering	31
2.4.1	Small angle neutron scattering	32
2.4.2	Neutron contrast variation	34
2.4.3	Raw data treatment and data recording for static measurements	36
2.4.4	Data analysis: Description of scattering curves.....	38
2.4.5	The stroboscopic high pressure SANS cell	51
2.4.6	Data recording for kinetic measurements	55
2.4.7	Time Involved Small Angle Neutron Scattering Experiments (TISANE)	58
2.5	Light scattering.....	64
2.5.1	Dynamic light scattering.....	65
2.5.2	Dynamic light scattering under high pressure	68
2.5.3	Static Light Scattering	69
3	Cyclohexane as hydrophobic additive to supercritical fluorinated microemulsions	70
3.1	Microstructure of CO ₂ /cyclohexane-microemulsions with flourinated surfactants	70
3.1.1	Phase behaviour.....	70
3.1.2	Systematic SANS contrast variation	72
3.1.3	Data evaluation I: Model-dependent analytical fitting functions	76
3.1.4	Data evaluation II: Model-independent Fourier transformation.....	78
3.1.5	Measurements at elevated temperature and w_B	85
3.1.6	Conclusion.....	87
3.2	Kinetics of structural changes of CO ₂ -microemulsions.....	89
3.2.1	Phase behaviour and microstructure.....	89
3.2.2	Pressure jumps within the thermodynamically stable state	98
3.2.3	Influence of cyclohexane on changes of microstructure	107
3.2.4	Pressure jumps to thermodynamically unstable states.....	109
3.2.5	Influence of cyclohexane on kinetics of demixing processes.....	113
3.3	The TISANE option	117
3.3.1	TISANE experiments: State of the art.....	117
3.3.2	Improvements of the SHP-SANS cell	117
3.3.3	Applying the TISANE option to microemulsions	120

3.4	Conclusion.....	124
4	Influence of hydrostatic pressure on PNIPAM particles.....	127
4.1	PNIPAM particles at elevated hydrostatic pressure	127
4.1.1	Dynamic light scattering.....	128
4.1.2	Small Angle Neutron Scattering.....	132
4.1.3	Static light scattering	138
4.2	Swelling and deswelling kinetics induced by sudden pressure jumps	142
4.3	Microfluidics	149
4.3.1	Newly developed microfluidic setup for temperature jumps	149
4.3.2	Results of temperature jump experiments	150
4.3.3	Discussion	153
4.4	Conclusion.....	154
5	Microemulsions and PNIPAM under mutual confinement.....	155
5.1	Phase behaviour.....	155
5.2	Light and neutron scattering.....	157
5.3	First kinetic experiment with microemulsions and PNIPAM	161
5.4	Conclusion.....	161
6	Summary.....	163
7	Appendix.....	167
7.1	Abbreviations and Symbols.....	167
7.2	Experimental methods	172
7.2.1	Determination of the Phase Boundaries of Microemulsions	172
7.2.2	Neutron Scattering.....	174
7.2.3	Light Scattering	176
7.2.4	Emulsion polymerisation.....	177
7.2.5	Microfluidics	178
7.3	Chemicals and Substances.....	179
7.4	Tables	179
8	Bibliography	183

1 Introduction

Polymer foams are an aspect of modern life. Disposable packaging of fast food, building insulation, cushioning of furniture, running shoes and bicycle helmets are a few examples [1]. The properties of the foams differ considerably with the polymer and its processing. While polystyrene (PS) is a common example for insulation applications, polymethylmethacrylate (PMMA) is often used in automotive industry and civil engineering because of its exceptional resistance to weathering [2].

In recent years the prospect of foams with a pore size in the submicron range has achieved increasing attention. These materials exhibit a high application and market potential due to a high-performance thermal insulation capacity which can be improved by a factor of at least 3 if the pores are smaller than 100 nm [3]. A high sound absorption, optical transparency and a uniquely high stability against applied forces are further benefits [4, 5]. The reasons for these improved features are based on the nanostructure. Optical transparency is achieved because light scattering is negligible if the pore size is much smaller than the wavelength of visible light. The Knudsen effect predicts that heat transfer over the cell gas collapses if the pore size of the foam pore which encloses the gas is smaller than the mean free path length of the gas [6-8], explaining the improvement of heat insulation. This is valid for foams with pore sizes smaller than 100 nm [9].

Motivated by these promising characteristics different approaches to nanoporous materials were developed. To date, the only nano-porous bulk materials realised are aerogels [4]. They can consist of organic, inorganic or organic-inorganic hybrid networks which form a highly porous solid material [4, 10-13]. Preparation of aerogels according to the sol-gel-process invented by Kistler [14, 15] starts from a precursor substance dissolved in an adequate solvent. The addition of a catalyst induces formation of sol particles with a size of a few nanometres. These particles aggregate to a network structure which builds the foundation of the future aerogel. The solvent removal, i.e. drying, further shrinks the characteristic size of the solid aerogel by about two orders of magnitude. In order to keep the network structure intact the use of supercritical fluids is necessary. These enable a continuous and steady process without many capillary forces if the pressure and thus the density of the supercritical fluid is reduced carefully. This process is gentle but slow which makes aerogels expensive and limits their use to special applications like space engineering [16, 17].

A promising two-step process to nano-porous foams was presented in 1987 by Colton and Suh [18-22]. The first step consists of the saturation of a glassy thermoplastic polymer with an inert blowing agent like CO₂ which diffuses into the polymer. In a second step the temperature is raised above the glass transition temperature T_G . Releasing the pressure leads to a foaming due to the blowing agent inside the polymer. Thereby, the morphology of the resulting material depends on saturation pressure, foaming time and temperature. This concept was successfully applied by Krause *et al.* to, for example, polyetherimides, resulting in foams with an open cell porosity down to 100 nm [23-27]. Since,

however, already thin films of a few millimetres require saturation times of several hours this technique is not appropriate for bulk materials.

Another approach to nanoporous materials was developed by Strey and Müller in 2011 [28, 29]. The “Nano-Foams by Continuity Inversion of Dispersion” (NF-CID) principle utilises the voids in a close-packed colloidal polymer nano-lattice. They are filled with super- or near-critical fluid at appropriate pressure and at a temperature below T_G . Since the filling is not diffusion-limited it is finished within seconds. The lower interfacial tension of polymer and fluid compared to the higher polymer-air interfacial tension further promotes this process. Traversing T_G , which is lowered by the presence of supercritical fluids like CO_2 [30], induces a “continuity inversion”. Now, the former discrete polymer particles melt into one continuous material in which the former voids develop nano-sized spherical inclusions. Diameter and number density of the inclusions are directly proportional to the size of the polymer particles. Releasing the pressure leads to a foaming of the material and a simultaneous fixation of the foam due to an increase of T_G . Compared to the procedure by Krause *et al.* the important advantage of the NF-CID principle is that no saturation times are necessary, resulting in considerably lower preparation times. Applying this procedure PS as well as PMMA foams with pore diameters in the submicron range were realised [29].

The “Principle of Supercritical Microemulsion Expansion” (POSME) [31, 32] was presented by Schwan, Sottmann and Strey in 2003. Here, thermodynamically stable, nanostructured microemulsions are used as a template. In microemulsions an amphiphilic surfactant film mediates the mixture of two otherwise immiscible components by separating them on the nanoscale. The driving force behind that process is the dramatically decreased interfacial tension. The POSME procedure suggests the use of compressed near- or supercritical fluids which function as hydrophobic component and simultaneously as blowing agent. Thereby, a detailed knowledge of phase behaviour and microstructure of supercritical microemulsions [33-40] is crucial. Fixation, i.e. polymerisation [41-44], and expansion, i.e. an increase of volume, are known to induce demixing process. These are accompanied by coarsening like Ostwald ripening [45] and coagulation with subsequent coalescence [46]. POSME foams display pore sizes in the range of 100 μm [29, 47, 48].

In order to prevent or slow down ageing processes the concept of “Anti-Ageing Agents (AAA) for Nanoporous foams” was developed by Strey *et al.* [47, 49]. This concept is based on the addition of a low-molecular hydrophobic additive to supercritical microemulsions. It is supposed to accumulate at the thermodynamically unfavourable contact sites of CO_2 and the polar component, lowering the interfacial tension. These contact sites emerge due to an increase of volume upon expansion. The influence of the cyclohexane mass fraction in the hydrophobic phase $\beta_{\text{cyclohexane}}$ on balanced microemulsions of the type brine – CO_2 – fluorinated surfactants has been systematically studied previously as shown in Figure 1.1 left. Note that the efficiency of the system without cyclohexane, i.e. at $\beta_{\text{cyclohexane}} = 0.0$, strongly depends on pressure. The weight mass fraction $\tilde{\gamma}$ needed to formulate a

one-phase microemulsion can be considerably reduced by increasing the pressure from 150 to 300 bar. This is due to an increase of density of CO_2 which leads to a reduced interfacial tension with water [50, 51] and an improved surface-to-volume ratio.

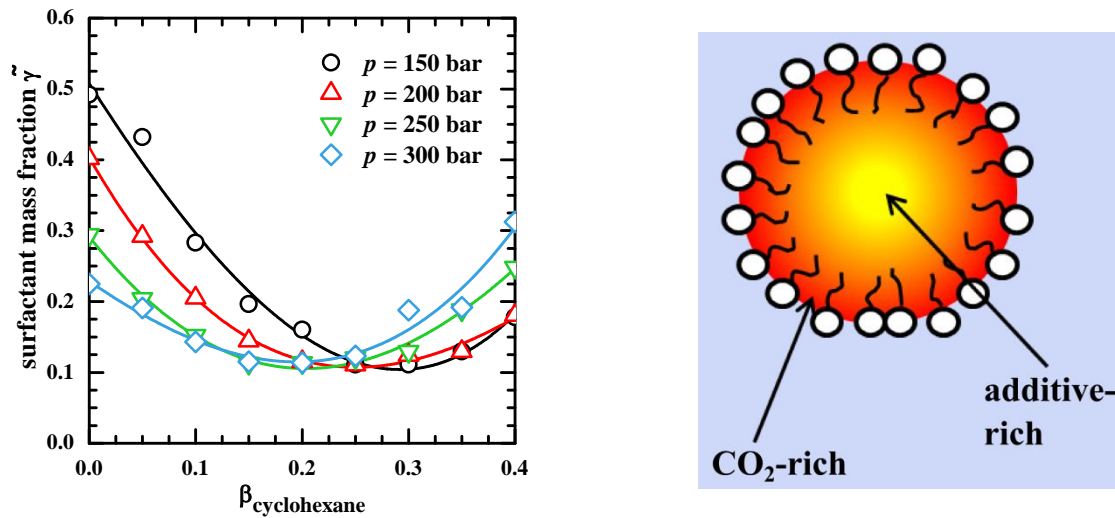


Figure 1.1: *Left:* Plot of the surfactant mass fraction $\tilde{\gamma}$ at the point of maximum efficiency against the mass fraction $\beta_{\text{cyclohexane}}$ of cyclohexane in the hydrophobic phase, for the balanced microemulsion system $\text{H}_2\text{O}/\text{NaCl} - \text{CO}_2/\text{cyclohexane} - \text{Zonyl FSO 100}/\text{Zonyl FSN 100}$ ($\alpha = 0.4$, $\delta_{\text{FSN}} = 0.75$, $\varepsilon = 0.01$). The efficiency increases to a pressure-specific cyclohexane mass fraction but decreases if this concentration is exceeded [52, 53]. *Right:* Graphic illustration of the hypothesis of a concentration gradient of cyclohexane in a micelle with fluorinated surfactants. Taken from [52].

Surprisingly, it was found that the partial replacement of CO_2 by cyclohexane enables a reduction of fluorinated surfactant by a factor 2 at $p = 300$ bar and even 5 at $p = 150$ bar. Here, the higher efficiency at $\beta_{\text{cyclohexane}} = 0.0$ and 300 bar offers less potential improvement than at 150 bar. The repulsive interactions between fluorinated surfactants and protonated substances such as cyclohexane [54, 55] likely reduce the monomeric solubility of fluorinated surfactants in the $\text{CO}_2/\text{cyclohexane}$ mixture, which is rather high (11 wt%) in case of pure CO_2 [34]. However, the decreased monomeric solubility and hence increased interfacial area is not sufficient to explain the enormous and unexpected efficiency increase. Thus, a hypothesis to explain this effect was postulated [52] which is shown graphically in Figure 1.1 right. Based on the repulsive cyclohexane/ fluorinated surfactant tails interactions the formation of a depletion zone of cyclohexane close to the surfactants and a cyclohexane-enriched zone at the centre of the domains was postulated. This would result in a concentration gradient of cyclohexane within the respective microemulsion domains. The observed trend of $\tilde{\gamma}$ with β (Figure 1.1 left) might be discussed as follows: Increasing the mass fraction $\beta_{\text{cyclohexane}}$ of cyclohexane in the CO_2 -swollen domains leads to the formation of a depletion zone, which becomes more and more pronounced and causes a considerable decrease of $\tilde{\gamma}$, i.e. an increase of efficiency. This may be caused by improved CO_2 / surfactant interactions triggered through repulsive interactions of cyclohexane and the fluorinated surfactant chains. Above a certain (pressure

dependent) concentration of cyclohexane, a spatially avoidance of repulsive interactions is no longer possible, causing a decrease of efficiency. At the outset of this work, however, this was only a postulation.

In the context of supercritical microemulsions the investigation of the kinetics of structural changes is a challenge which has so far only been met by Müller *et al.* [29, 56]. A high-pressure cell for small-angle neutron scattering (SANS) which provides stroboscopic pressure jumps with adjustable amplitude was developed by the mechanical workshop of the University of Cologne within the frame of the BMBF project TISANE [57, 58]. A schematic drawing of this cell is shown in Figure 1.2. Therein, the key component is a metal bellow (green) which is inserted into the sample volume (orange). By pumping hydraulic oil (yellow) in or out of the bellow it can extend or shrink, respectively, and thus transfer different pressures. Pressure jumps can be performed with a maximum frequency of 5 Hz (status as of March 2013) whereby the maximum pressure is 300 bar. Since the bellow provides nearly unlimited repeatability of pressure jumps this stroboscopic high-pressure SANS cell (SHP-SANS cell) is a unique setup.

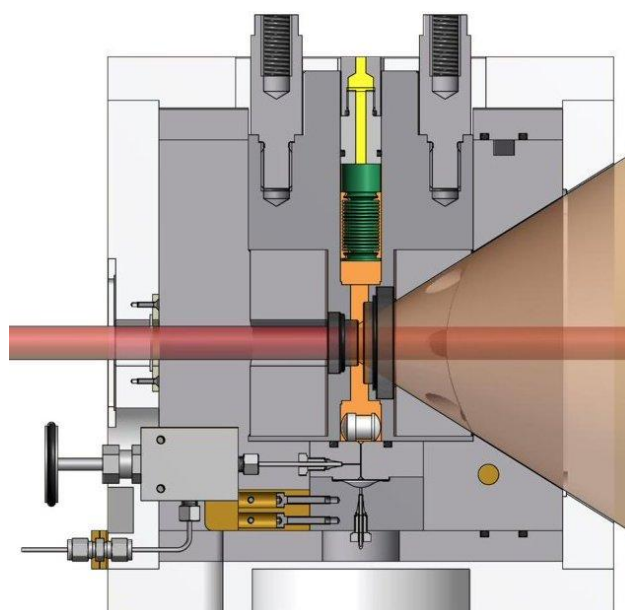


Figure 1.2: Cross section of the SHP-SANS cell, prepared by the internal mechanical workshop. The sample volume, which is sealed by two sapphire windows, is marked in orange, where the neutron beam (red) is partly scattered. The pressure jump is performed by means of a metal bellow (green) which can shrink or extend in order to transfer the desired pressure.

Using the SHP-SANS cell the demixing kinetics of a CO₂-microemulsion were investigated, showing that they strongly depend on the depth of the pressure jump [29]. In the frame of the anti-ageing project Müller also formulated a diluted microemulsion with 20 wt% cyclohexane in the mixture of cyclohexane and CO₂ and found an increase of microemulsion efficiency similar to the one described for balanced microemulsions (see Figure 1.1 left). The reason for this effect, however, was not yet explained. It turned out that the substitution of CO₂ by cyclohexane decelerates the demixing process

by one order of magnitude. The TISANE option itself, an instrumental setup to investigate kinetic processes with a time resolution < 5 ms, was not yet applied successfully in combination with the SHP-SANS cell. This is due to the fact that the achieved pressure jump frequency (5 Hz) was too slow for the TISANE requirements [29].

Kinetic processes, however, are also important in the area of biomedical applications. Here, understanding drug-release kinetics is of fundamental interest. In this field especially Poly-(*N*-isopropylacrylamide) (PNIPAM) microgel particles have attracted much attention in recent years. Their lower critical solution temperature is located around 32°C and therefore very close to the temperature of the human body [59-61]. At this temperature PNIPAM particles undergo a change from swollen microgel to dehydrated spheres due to a change of miscibility with the solvent [62-64]. Co-nonsolvency, which means that PNIPAM particles are soluble in two different solvents (such as water and methanol) but not necessarily in mixtures of both, has also been thoroughly investigated [65, 66]. Besides that other stimuli like pH, salt concentration, solvent composition and also the effect of hydrostatic pressure on the swelling behaviour of microgels were tested [67-69].

However, there are hardly any publications on the kinetics of the volume transition so far, which are crucial for biomedical applications. Admittedly, kinetics according to a change of temperature are difficult to determine. While a rapid heating of the particles can be performed applying for example a Joule-heating temperature jump [70], fast and precise cooling is a challenge. To date, such measurements were only possible by modifying the particles [71, 72]. Utilising small iron oxide particles at the PNIPAM surface rapid magnetic heating can be induced [73]. However, these techniques do not feature a fast repetition as the rebuilding of the initial structure, e.g. by external cooling, is slow. Using co-nonsolvency to induce the structural changes, for example in stopped-flow devices, allows a fast repetition of the experiment [74]. However, since the structural changes are induced by a change of composition the correlation to temperature-induced kinetics is vague.

Recently, it turned out that the transition temperature of thermoresponsive materials can be shifted to higher temperatures by hydrostatic pressure [29, 75]. Consequently, both swelling and deswelling kinetics can be investigated using the SHP-SANS cell. The benefit of hydrostatic pressure is that it can be changed rapidly and reversibly and occurs homogeneously throughout the sample without any gradients like in temperature-changing setups. Such measurements will provide completely new insights into the kinetics of structural changes of thermoresponsive polymers.

The intersection of these two soft-matter systems are consequently microemulsions with polymer particles in the hydrophilic phase. Comparable systems are known as orthogonal self-assembled systems, describing independently coexisting structures [76]. While the most obvious example for such systems are the complex mixtures of structures present in living cells, a variety of systematic studies on less complex systems exists [77-79]. Recently Laupheimer *et al.* identified a gelled bicontinuous microemulsion as an orthogonal self-assembled system and investigated its phase

behaviour and microstructure [80, 81]. Unifying articles on both microemulsions and polymer particles commonly deal with particle synthesis using either the high interfacial area or the nanostructure of microemulsions [82-86]. The only study concentrating on the coexistence of microemulsions and PNIPAM particles (Zhou and Wu, 1995) is on the influence of PNIPAM particles on water – hexane – SDS/AOT microemulsions, finding that PNIPAM acts as a stabiliser [87].

Here, the SHP-SANS cell enables not only a detailed investigation of such coexisting structures by means of SANS. It also permits studying the influence of polymer particles on the kinetics of pressure-induced structural changes on microemulsions. Applying appropriate contrast conditions this can also be studied vice versa.

OBJECTIVES

Cyclohexane was found to considerably increase the efficiency of balanced microemulsions of the type brine – CO₂ – fluorinated surfactants [29, 52] which is unexpected due to repulsive interactions of hydrophobic protonated and fluorinated substances. The hypothesis of a concentration gradient of cyclohexane with a depletion zone close to the amphiphilic film was postulated but not yet proven [52]. Thus, performing a systematic SANS contrast variation with subsequent detailed analysis of the scattering data was the first goal of this work. The *Generalised Indirect Fourier Transformation* was to be applied to elucidate the distribution of cyclohexane in such micelles.

Furthermore, a systematic study on the influence of cyclohexane on phase behaviour and microstructure of diluted microemulsions of the same type was planned. It was intended to systematically investigate pressure-induced elongation processes within the thermodynamically stable state at different cyclohexane concentrations. Furthermore, the demixing properties of microemulsions with different cyclohexane contents upon a pressure jump to 70 bar, at which a CO₂-in-water microemulsion coexists with a CO₂-excess phase, was to be examined.

Besides microemulsions the influence of hydrostatic pressure on different PNIPAM particles was to be studied. Using the SHP-SANS cell should also reveal kinetic aspects of pressure-induced structural changes at temperatures close to the volume phase transition temperature.

Since the focus was on both microemulsions and PNIPAM particles it reasonably follows to also investigate both systems under mutual confinement, i.e. study phase behaviour and microstructure. Again provided by means of the SHP-SANS cell first SANS experiments regarding kinetic processes under confinement of the respective structure were planned.

Since the SHP-SANS cell is the main tool of this work the improvement of this unique sample holder was an important aspect throughout this work. Especially regarding the possible application of the cell for TISANE measurements it was important to perform faster pressure jumps in order to meet the TISANE principle requirements.

2 Fundamentals

2.1 Microemulsions

The first time that a mixture of water – soap – oil was described in dependence of temperature and composition was by Schulman and Hoar in 1943 [88], although the term “microemulsion” was not used until 1959 [89]. Using ionic surfactants, Winsor performed a systematic study of the three-phase region with ionic surfactants [90] and classified four different phase equilibria [91]. The temperature sensitivity of the one-phase microemulsion with non-ionic surfactant was described 1967 by Shinoda [92-95]. Starting from there, the most significant work regarding phase behaviour and microstructure of microemulsions with non-ionic surfactant was performed by Kahlweit and co-workers [96, 97].

Microemulsions are by definition thermodynamically stable, macroscopically homogeneous and isotropic but nano-structured mixtures of at least three components [97-99]. Two of these three components are mutually immiscible, for example a polar one (water, A) and a hydrophobic one (alkane, B). The third, amphiphilic component (C), a surfactant, mediates the mixing by adsorbing at the interface between the immiscible components due to its amphiphilic nature and thus reducing the interfacial tension σ by several orders of magnitude. For the system water – octane σ is reduced from 50 mN m^{-1} [100] to $4.9 \cdot 10^{-3} \text{ mN m}^{-1}$ upon addition of the surfactant C_{10}E_5 [101]. The amphiphilic nature of the surfactant is due to its ambivalent structure. It is composed of the hydrophilic head group which is soluble in polar substances and the hydrophobic tail which is soluble in non-polar oils. Surfactants can be non-ionic, cationic, anionic, zwitterionic or amphoteric depending on the nature of the polar head group. In this work, only non-ionic surfactants were used. Common commercially available non-ionic surfactants are *n*-alkyl-polyglycol ether which consist of a tail with *i* CH_2 units and have *j* glycol units in the polar head group. Thus, they are commonly abbreviated with C_iE_j .

Although macroscopically a microemulsion is isotropic and homogeneous, on a microscopic scale the two immiscible components are still separated from each other by an extended film of a monolayer of surfactant. Depending on parameters like composition, temperature and, in the case of compressible components, hydrostatic pressure one finds a number of different equilibrium states, and among these occur numerous different structures like spherical droplets or bicontinuous phases. In order to investigate kinetics of structural changes in microemulsions, it is crucial to understand the phase behaviour of microemulsions first.

2.1.1 Phase behaviour of binary mixtures

The binary systems water (A) – oil (B), water (A) – non-ionic surfactant (C) and oil (B) – non-ionic surfactant (C) display characteristic miscibility gaps depending on temperature and composition. A schematic drawing of these systems is shown in Figure 2.1. For the two immiscible components (A) and (B) the miscibility gap can be found over the whole temperature range with the critical point far

above the boiling point of the single components. In the mixture of the hydrophobic component and the non-ionic surfactant only a lower miscibility gap occurs, with an upper critical point cp_α with its corresponding temperature T_α which is usually below the freezing point of the mixture [102]. cp_α and T_α , however, depend strongly on the nature of the surfactant.

The mixture (A) – (C) also has a lower miscibility gap which is usually well below the melting point of the mixture, and is therefore difficult to measure. More important for microemulsions is the upper miscibility gap which is closed for thermodynamic reasons. Consequently, there is an upper and a lower critical point. The upper critical point usually lies above the boiling point and is therefore not of interest for the phase behaviour of microemulsions. The lower critical point cp_β , however, is normally in a temperature range which is relevant to microemulsions. The location of this miscibility gap depends on the amphiphilic features of the surfactant and the composition of the polar phase. Between the upper and the lower miscibility gap the surfactant is monomerically dissolved in the polar phase at very low surfactant concentrations. Increasing the surfactant concentration leads to surfactant micelles above the critical micelle concentration (*cmc*) [103]. If the surfactant concentration is increased further, lyotropic mesophases (‘liquid crystals’) occur with almost all types of amphiphiles [104].

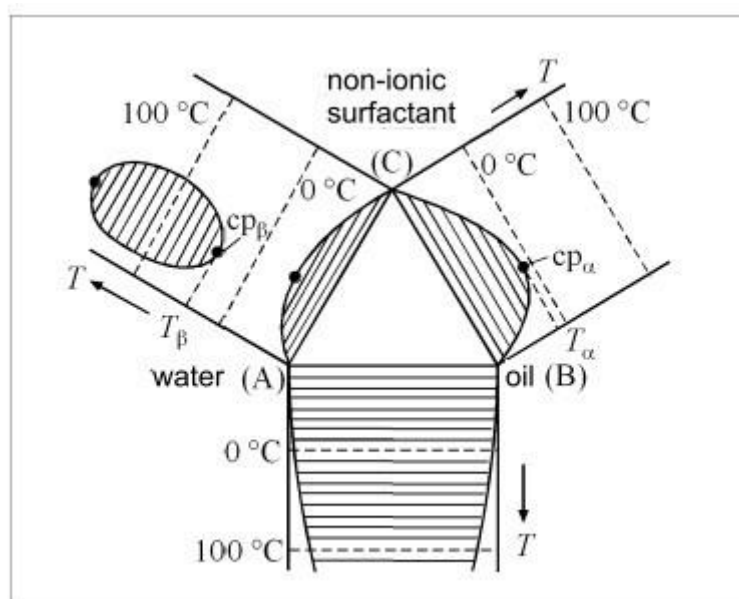


Figure 2.1: Schematic drawing of the three binary systems (A)-(B), (A)-(C) and (B)-(C). While (A) and (B) are immiscible over almost the whole temperature range, B and C only have a lower miscibility gap which is often below 0°C. (A) and (C) show a lower miscibility gap, which is lower than the miscibility gap of the system (B)-(C), and an upper miscibility gap which is relevant to microemulsions. Redrawn from [97].

2.1.2 The phase prism – ternary mixtures

Starting from the triangle shown in Figure 2.2 with the three components at the edges and using the temperature as the ordinate perpendicular to this base triangle, i.e. flipping up the side systems, the Gibbs phase prism is generated. At ternary mixtures, i.e. at compositions between the binary systems

at the sides of the prism, many different phases can be observed. The phase behaviour is quite complex and mainly depends on the interplay of the upper miscibility gap of water and non-ionic surfactant and the lower miscibility gap of oil and non-ionic surfactant. Furthermore, the change of solubility of the surfactant from soluble in water at low temperature to soluble in oil at high temperature is a determining factor. This change of solubility can be explained by the partial dehydration of the surfactant head group at high temperature [105].

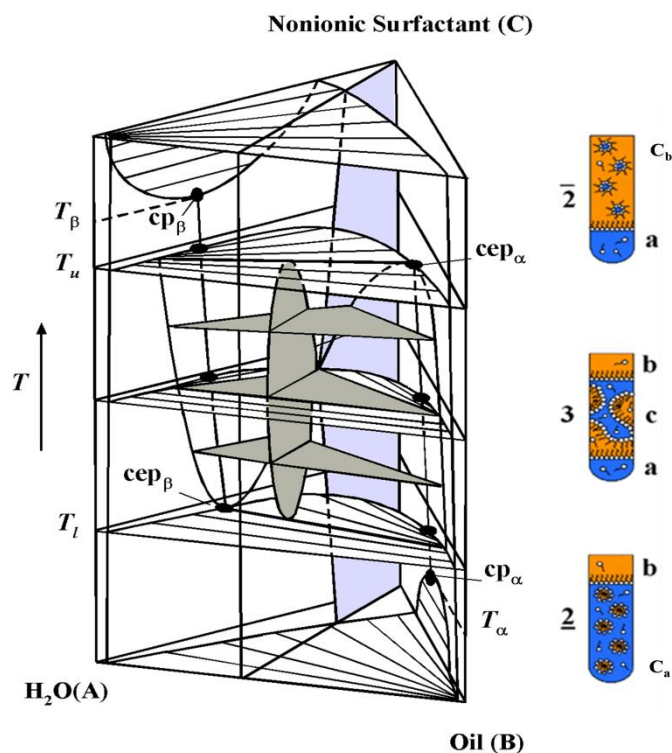


Figure 2.2: Schematic phase prism of a ternary mixture containing water (A), oil (B) and non-ionic surfactant (C). Highlighted in grey is the three-phase region, in light blue the one-phase region. The test tubes on the right illustrate the different states of $\underline{2}$, 3 and $\bar{2}$. Redrawn from [106].

The test tubes shown in Figure 2.2 next to the phase prism indicate different possible equilibrium states of the mixture at three different temperatures. Starting at low temperatures, a surfactant-rich oil-in-water (o/w)-microemulsion (c_a) coexists with an oil excess phase (b) (lowest test tube). Surfactant molecules are monomerically dissolved in both phases. Since the interactions between water and surfactant are much stronger than the ones between surfactant and oil, the amphiphilic film is curved around the oil. The surfactant-rich microemulsion phase is usually of higher density, so that it is below the oil excess phase. This state is termed $\underline{2}$ to indicate that the lower phase is the surfactant-rich microemulsion.

By increasing the temperature (middle test tube) the interactions of surfactant and polar phase are weakened, which leads to a partial dehydration of the polar head groups of the surfactant. This lowers the solubility of surfactant in the polar phase, until at the temperature T_l the oil-in-water microemulsion splits up to a surfactant-rich microemulsion (c_a) and a water excess phase (a) because

the surfactant interacts about equally well with water and oil. The volume of the oil excess phase (b) decreases because more oil can be dissolved in the microemulsion phase (c), which in turn grows in volume. Therefore, three phases coexist at ambient temperatures. Because the surfactant interacts well both with water and oil at ambient temperature the curvature of the microemulsion phase (c) is zero. By increasing the temperature further (upper test tube) the hydrophobic interactions of surfactant and oil become stronger, and thus the microemulsion phase dissolves more oil until at a certain temperature T_u the microemulsion phase (c) merges with the oil excess phase (b) to a surfactant-rich water-in-oil (w/o)-microemulsion (c_b) and a water excess phase (a). As the density of the microemulsion is now usually lower than the one of the water excess phase, the surfactant-rich microemulsion is the upper phase, which is indicated by $\bar{2}$.

The determination of all phase boundaries in a three-dimensional Gibbs phase prism is complicated and a lot of work. Therefore, it is convenient to use different sections through the phase prism by keeping one ratio constant [99]. Examples are the $T(\gamma)$ section and the $T(w_B)$ -section which are both shown schematically in Figure 2.3.

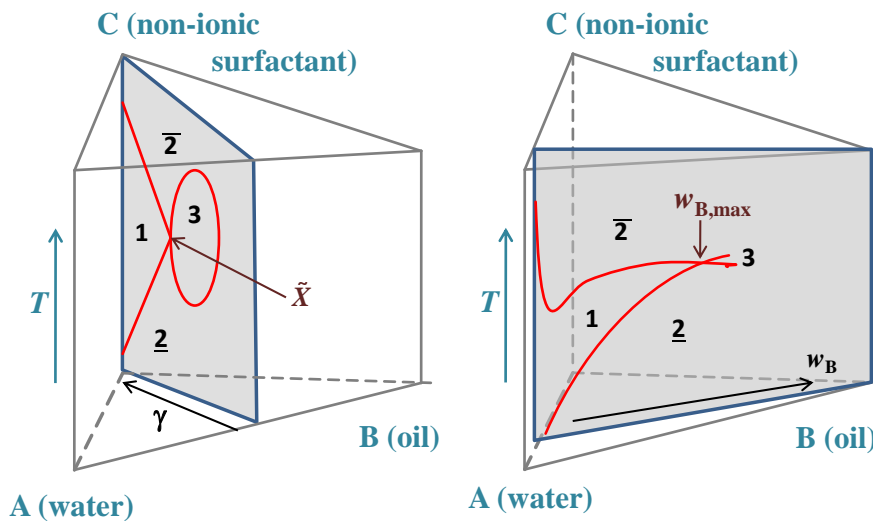


Figure 2.3: $T(\gamma)$ -section (left) and $T(w_B)$ -section (right) through the upright phase prism. The $T(\gamma)$ -section shows a variation of temperature and surfactant mass fraction γ at a constant water-to-oil ratio, whereas the water-surfactant ratio is kept constant in a $T(w_B)$ -section. Here, the oil mass fraction w_B is varied.

Figure 2.3 left shows a schematic drawing of a $T(\gamma)$ -section [97, 107]. Here, ratio alpha

$$\alpha = \frac{m_B}{m_A + m_B} \quad \text{Eq. 2-1}$$

of oil in the mixture of water and oil is kept constant and the surfactant concentration γ is varied, with γ being the mass fraction of surfactant in the overall mixture

$$\gamma = \frac{m_{\text{surfactant}}}{m_{\text{water}} + m_{\text{oil}} + m_{\text{surfactant}}}. \quad \text{Eq. 2-2.}$$

Note that it is also common to use volume fractions in order to describe the composition of the sample.

An extended three phase region can be found at low γ -values and intermediate temperatures. At temperatures below and above the three phase region the two different two phase regions $\underline{2}$ and $\bar{2}$ occur. The three-phase region meets the one-phase region at the so-called optimum point \tilde{X} at which the microemulsion is at the optimum state [99] or balanced (from an HLB point of view) [108, 109]. This point is correlated to the optimum temperature \tilde{T} , at which the surfactant has the highest solubilisation properties, and the lowest surfactant mass fraction $\tilde{\gamma}$ with which it is possible to formulate a one-phase microemulsion. As $\tilde{\gamma}$ is used to characterise the efficiency of the surfactants in the system under investigation, \tilde{X} is also called the efficiency point.

As microemulsion changes from oil-in-water to water-in-oil at the temperature \tilde{T} , this temperature is also called *phase inversion temperature* (PIT) [110, 111]. The phase inversion is founded in the change of solubility of the surfactant. Increasing temperature leads to weaker hydrogen bonds due to more molecular erratic movement [105].

The optimum state is a unique feature for every individual microemulsion composition. The location of the \tilde{X} -point is influenced by the hydrophobicity of the oil as well as by the amphiphilic properties of the surfactant. As can be seen in Figure 2.4 left, increasing the hydrophobic chain length from $i = 6$ to 12, the solubilisation efficiency of the surfactant increases. Furthermore, the higher hydrophobicity leads to a decrease of T_m so that lower temperatures are needed to change the solubility of the surfactant from water-soluble to hydrophobic. On the other hand, an increase of the hydrophilic chain length by varying the number of ethoxy units j between 2 and 7, leads to an increase of T_m which is accompanied by a slight decrease of γ_m .

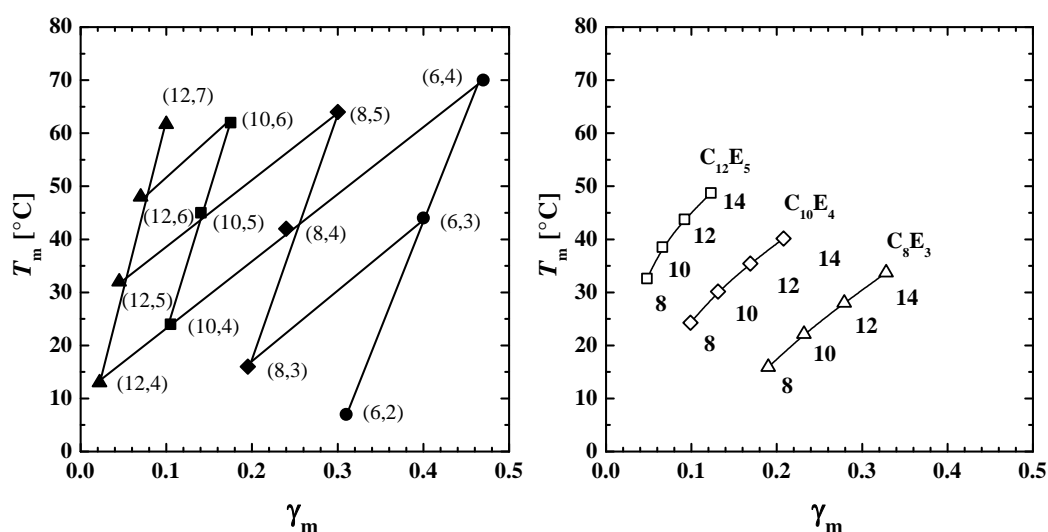


Figure 2.4: Left: X_m points of various $H_2O - n\text{-octane} - C_iE_j$ microemulsions with equal volumes of water and octane as a function of the mean temperature T_m and the surfactant mass fraction γ_m [106]. The numbers in brackets indicate the chain length of the hydrophobic part i and the number of ethoxy units j in the hydrophilic chain in the form of (i, j) . Right: Influence of alkanes (C_nH_{2n+2}) with different chain lengths on the X_m point in various microemulsions $H_2O - \text{alkane} - C_iE_j$ [106]. For all three surfactants, an increase of the chain length of the alkane leads to a shift of the X_m point to higher temperatures T_m and surfactant mass fractions γ_m .

Figure 2.4 right illustrates the influence of the chain length of the hydrophobic component. Increasing the length of the alkane (which is indicated by the numbers below the points) leads to a shift of the X_m point to higher temperatures as well as to higher surfactant mass fractions γ_m . This is mainly due to the fact that longer oils are harder to solubilise. Since the lower miscibility gap within the binary system B-C shifts to higher temperatures with increasing alkane chain length higher temperatures are necessary to drive the surfactant from the water to the oil phase. A similar effect can also be seen for the binary mixture of alkane and surfactant [112].

In contrast to the $T(\gamma)$ -section, the ratio γ_a

$$\gamma_a = \frac{m_C}{m_A + m_C} \quad \text{Eq. 2-3}$$

of surfactant in the water-surfactant mixture is kept at a constant value in a $T(w_B)$ -section (Figure 2.3 right). Here, the mass fraction of oil is varied. Accordingly, the composition of the sample is given by the mass fraction

$$w_B = \frac{m_B}{m_A + m_B + m_C} \quad \text{Eq. 2-4}$$

of oil (m_B) in the overall mixture. At low w_B the whole amount of oil can be solubilised by the water-surfactant mixture and the one-phase region stretches over a wide range of temperature. At higher oil mass fractions, the two different two-phase regions also occur, whereby the phase sequence is similar to the one already mentioned for $T(\gamma)$ sections. The point of maximum efficiency here is $w_{B,\max}$ at T_1 and characterises the maximum amount of oil which can be solubilised by the given water-surfactant mixture. The lower phase boundary which separates the one-phase microemulsion from the $\underline{2}$ state is called oil emulsification failure boundary (*oefb*) [113, 114]. The upper phase boundary very often runs through a minimum at low w_B which is caused by the miscibility gap of the binary mixture water-surfactant for surfactants with high amphiphilic strength [98, 115]. Because of its proximity to the critical point of the binary mixture the upper phase boundary is also called the near critical boundary (*ncb*). In this case, a closed loop miscibility gap causes an unstable microemulsion which separates. The reasons for this closed loop are discussed in the following chapter.

2.1.3 Curvature of the amphiphilic film and microstructure

The most crucial point to predict the phase behaviour is the nature of the surfactant. Depending on the strength of its interactions with the hydrophilic and the hydrophobic phase a local curvature of the amphiphilic film develops [98]. Starting from the two principle radii R_1 and R_2 the curvatures c_i can be described by

$$c_1 = \frac{1}{R_1} \quad \text{and} \quad c_2 = \frac{1}{R_2} \quad \text{Eq. 2-5}$$

Figure 2.5 shows three examples of different structures and the according radii.

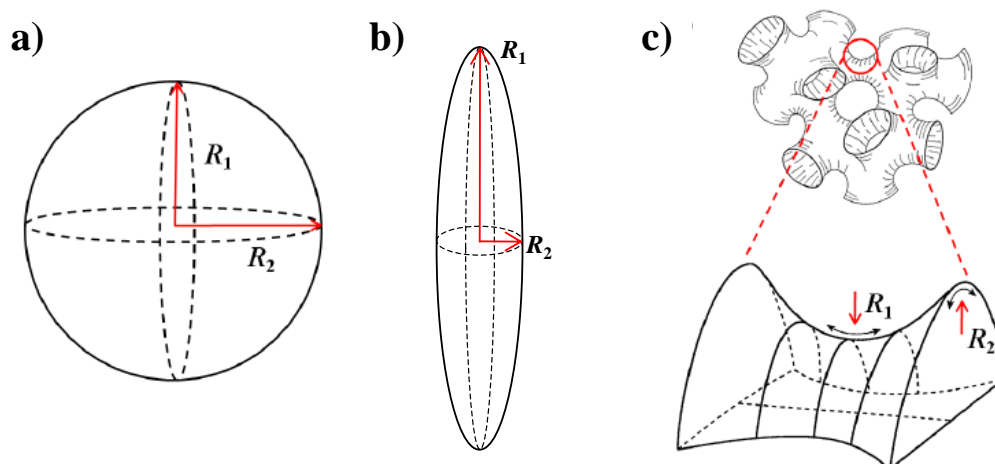


Figure 2.5: Principal curvature of a spherical (a) and a cylindrical (b) membrane and the membrane in a sponge structure, together with the curvature radii R_1 . Redrawn and extended from [116].

For a spherical structure (Figure 2.5 a), the radii R_1 and R_2 are the same. Thus, it follows that $c_1 = c_2 = 1/R$. For a cylindrical structure as indicated by Figure 2.5 b) one radius is much larger than the other one. Figure 2.5 c) depicts a sponge-like structure with two different curvature radii, where R_1 describes the radius of the channel and R_2 represents the curvature of the channel itself.

Based on the parameters c_i it is also possible to define the mean curvature H

$$H = \frac{1}{2}(c_1 + c_2). \quad \text{Eq. 2-6}$$

The structures shown in Figure 2.5 and many more occur in microemulsions depending on composition and temperature. The mean curvature in microemulsions with non-ionic surfactants is mainly a function of temperature as a tuning parameter [98, 99] which is shown graphically in Figure 2.6 left by means of the so-called wedge model [117]. Here, a surfactant is represented by a wedge consisting of two parts and the strength of the interaction is represented by the volume (or area in a 2D plot) of the according part of the surfactant wedge. Thus, at low temperature the interactions between the surfactant head group and water outweigh the ones of surfactant and oil, which is why the hydrophilic part of the wedge requires a bigger volume than the hydrophobic part, leading to a curvature of the amphiphilic film around the oil ($H > 0$). At intermediate temperature the surfactant interacts both with water and oil, the parts of the wedge have the same value and the mean curvature is zero. Increasing the temperature further the interactions of oil and the hydrophobic part of the surfactant overbalance the ones of water and the hydrophilic part of the surfactant, thus leading to an amphiphilic film which is curved around water. This state is indicated by a negative value of H . The relation between morphology of the microstructure and the temperature-dependent mean curvature has experimentally been studied by means of conductivity and NMR-self diffusion measurements [98,

118-123], electron microscope imaging [124-126] as well as light, X-ray and neutron scattering [123, 127-141].

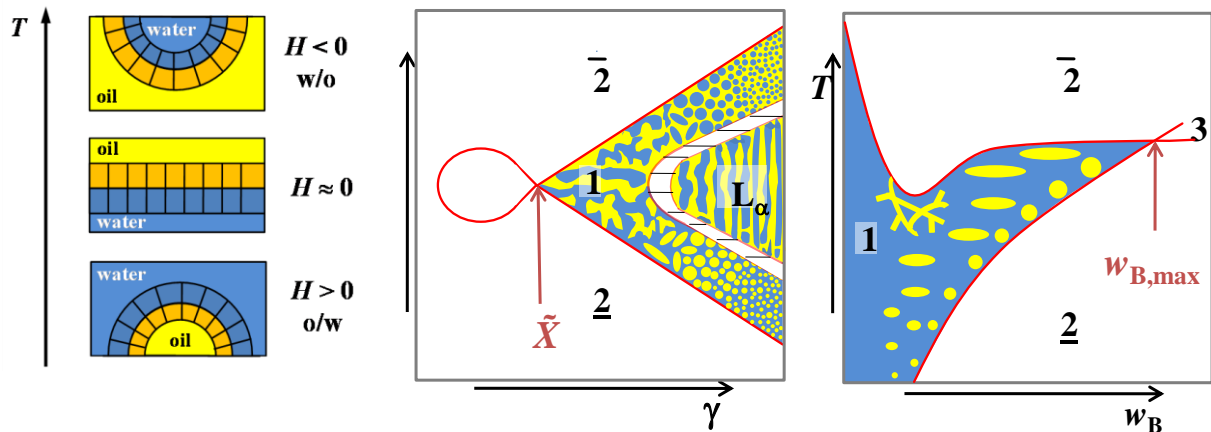


Figure 2.6: Schematic drawing of the mean curvature of the amphiphilic film as a function of temperature (left). Redrawn from [99]. This trend of the curvature can also be found in the different sections through the phase prism, the $T(\gamma)$ -section (middle, redrawn according to [98]) and the $T(w_B)$ -section (right), although the structures in the one-phase microemulsion differ considerably among these sections.

While the mean curvature of the amphiphilic film is mainly a function of temperature, the global structure also highly depends on the composition of the sample. For a microemulsion with a balanced ratio of oil and water, depicted in a $T(\gamma)$ -section in Figure 2.6, the structure of the microemulsion close to the efficiency point is of bicontinuous nature [98]. By increasing the concentration of surfactant γ more interfacial area can be covered and thus the characteristic size decreases, leading to elongated structures and finally to spherical micelles at high surfactant concentration. At temperatures lower than \tilde{T} oil-in-water structures can be found and at higher temperatures water-in-oil structures are present, following the trend of the curvature of the amphiphilic film in Figure 2.6 left.

In diluted microemulsion systems, as shown in Figure 2.6 right, spherical micelles can be found along the oil emulsification failure boundary [121]. Keeping the composition constant and increasing the temperature an elongation of the spherical micelles can be observed. The amphiphilic film at low temperature is, as shown in Figure 2.6 left, curved around the oil. By increasing the temperature the curvature of the film slowly approaches zero, leading to a flat amphiphilic film. In terms of microstructure, this effect becomes visible by the development of cylindrical structures where the curvature in the direction of the length is zero. Only the half-sphere shaped cylinder end caps have a high energy at this state. To avoid these high-energy parts the cylindrical micelles eventually form networks with Y-like junctions where the mean curvature of the amphiphilic film further approximates zero. If the minimum of the upper phase boundary is reached, given the according composition of the microemulsion, the microemulsion separates into two different phases, one concentrated and one diluted network structure. This can be explained by the number density of the network junctions which increases upon the connection of formerly independent cylinders. These junctions enable a certain

attraction of different oil domains which lead to the separation into two network phases with different concentrations of network structures. A mean curvature of $H = 0$ can be found in form of lamellar phases (L_α) at even higher temperatures.

By increasing the amount of oil in the microemulsion, i.e. increasing w_B , an oil-in-water microemulsion coexists with an oil excess phase at low temperature. Since the amount of oil in the microemulsion is low compared to the amount of water, the volume of the oil excess phase is very small. Upon increasing the temperature above the close proximity to the *oefb* the elongation to cylindrical micelles can also be observed at high w_B . Before the connection to networks happens, however, the microemulsion separates into a water-in-oil microemulsion and a water excess phase since the upper phase boundary is commonly at temperatures below the phase inversion temperature. Considering the volume ratios it becomes obvious that the microemulsion phase must be much smaller in volume than the water excess phase. Note that the three-phase region in a diluted microemulsion occurs at higher temperatures than the one of the point of maximum efficiency.

2.2 Microemulsions with supercritical carbon dioxide

Supercritical CO₂ (scCO₂) has attracted much attention in previous years because of its potential as a replacement for organic solvents, as it is cheap, nontoxic, non-flammable and environmentally responsible. It was shown first in 1978 by Hubert and Vitzthum that supercritical gases and especially scCO₂ is highly appropriate for the extraction of natural products [142]. As its critical point is easily accessible (31°C and 73 bar), the solvent power can be influenced via density and thus via pressure and temperature. Tunable solvents [143, 144] can be applied in various fields, for example enzymatic catalysis [145] or the synthesis of nanoparticles [146, 147]. In many industrial processes CO₂ is already used routinely [148], the perhaps best-known process being the de-caffeination of coffee [149, 150]. However, CO₂ is a very poor solvent for polar substances and such of high molecular weight, which is why emulsions and microemulsions are of interest for applications in which both polar and non-polar substances need to be dissolved. By combining CO₂ and microemulsions via formulation of CO₂-microemulsions it is possible to change the properties of the microemulsion without changing the composition, which makes supercritical microemulsions also interesting to fundamental research.

2.2.1 Fluorinated surfactants and their impact on CO₂-microemulsions

It was shown already in 1990 by Consani and Smith that most commercially available hydrocarbon surfactants are not compatible with CO₂ [151]. This was verified later, for example that with the use of technical grade Lutensol® surfactants the efficiency of a microemulsion system was very poor. At least 40 wt% of surfactant were necessary to formulate a one-phase microemulsion with equal amounts of water and CO₂ [32]. It turned out that the use of fluorinated or partly fluorinated surfactants changed the necessary amount of surfactant for the better, meaning that considerably less surfactant is needed. This aspect was initiated by Beckman *et al.*, who for the first time postulated the resemblance of fluorocarbons and CO₂, indicating that a fluorinated version of AOT should improve the solubility of CO₂ and water [152].

The enhanced solubility of fluorocarbons in CO₂ compared to hydrocarbons lead to the idea of specific solute-solvent interactions between CO₂ and fluorocarbons which was proposed by Dardin *et al.* [153], but was also disputed by various other groups [154-157]. In order to understand these interactions on a molecular level Raveendran and Wallen performed a series of *ab initio* calculations on the interaction of CO₂ with fluoromethanes using a stepwise increase in the number of fluorine atoms [158]. These calculations revealed that fluorocarbons prefer the interaction with CO₂ over the interactions with an identical molecule. They reason that fluorine atoms in a molecule compete for electrons of the other fluorine atoms, which makes the molecule itself a very weak electron donor. However, they also found out that more polar fluoromethanes interact more favourably with CO₂ as compared to the less polar

ones, irrespective of the fluorine number. Thus, they also devoted a publication to the polar attributes of CO₂, explaining for example the H-O interaction of hydrogen from water and O from CO₂ [159].

Another approach to understand the unique interaction features of fluorocarbons was performed by Dalvi and Rosicky [55]. They performed contact-angle molecular simulations of water on self-assembled monolayers of hydrocarbon and fluorocarbon, revealing that fluorocarbons pack in a less dense way on a water surface than hydrocarbons, thus leading to lower van der Waals` interactions and to a higher hydrophobicity. Furthermore, they also examined the effectiveness of fluorocarbon ligands in CO₂, revealing that the high polarity of the C-F bond (compared to the low one of a C-H bond) interacts better with the quadrupole moment of CO₂, which is one of the main reasons why such a chain is more CO₂-philic [54, 160]. It also turned out that the fluorocarbon ligands adopt a unique geometry in which the slightly negative dipole moments at the outside of the chain lead to a slightly angled alignment which is favourable over the straight alignment. The negative dipole at the outside surface of the fluorocarbon chain can also lead to slightly repulsive interactions.

Due to the unique and exceptional interactions of fluorinated surfactants with CO₂ they are used for the formulation of microemulsions with near- or supercritical CO₂. In the last decade different types of fluorinated supercritical microemulsions and their microstructure have been investigated, most studies dealing with the formulation of water-in-CO₂ (w/c) microemulsions [161]. The first ones to reveal the microstructure of w/c microemulsions were Eastoe *et al.* by performing high pressure SANS experiments [36]. Since then research in this range has spread and numerous publications deal with the microstructure of microemulsions [35, 162, 163], the influence of cosurfactants [164], formation kinetics [165] or with the design and synthesis of new fluorinated surfactants [166, 167].

In this work, only commercially available fluorinated surfactants were used. The principal structure of these surfactants is shown in Figure 2.7. These surfactants can be described by means of the acronym F(CF₂)_iE_j, which resembles the notation of C_iE_j for hydrocarbon surfactants.

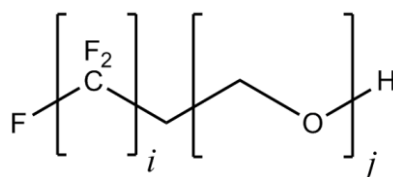


Figure 2.7: General chemical structure of perfluoroalkyl-polyglycoether surfactants. *i* gives the number of CF₂ units and *j* the number of ethylene units.

2.2.2 CO₂-microemulsions as templates for nanoporous foams

Because the structure of microemulsions is usually in the range of 5-20 nm microemulsions promise to be a highly appropriate template for foams if one aims for foam pores with a diameter below 100 nm. On top of that, the high number density of microemulsion droplets should lead to a very low density of the foam. In order to take advantage of these features of microemulsions the Principle of Supercritical

Microemulsion Expansion (POSME) was developed [32, 168]. This procedure consists of three steps which are illustrated in Figure 2.8.

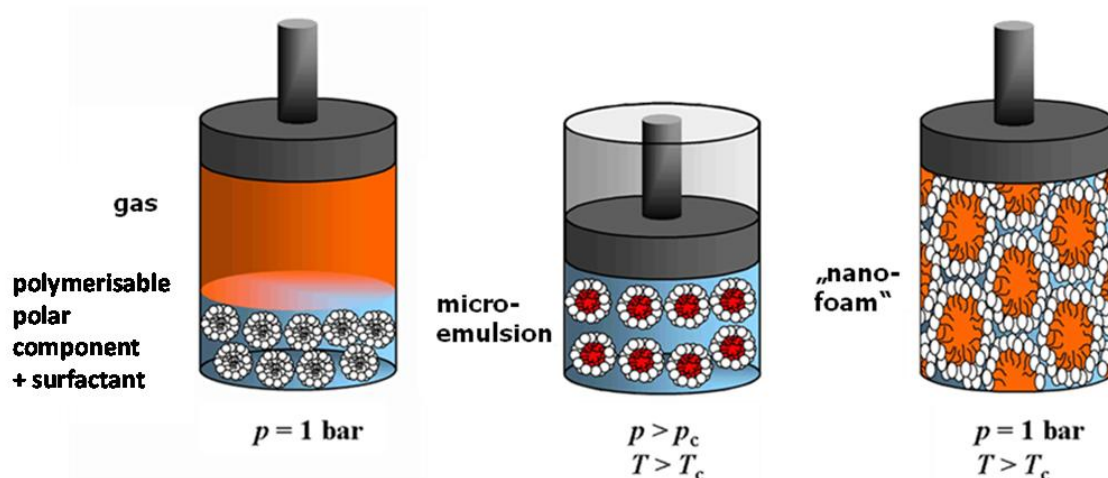


Figure 2.8: Schematic illustration of the Principle of Supercritical Microemulsion Expansion (POSME). The first step is to provide a micellar surfactant solution in a fixable polar solvent in coexistence with a gas. Upon increasing pressure and temperature above the critical values the gas changes to a supercritical fluid which can be solubilised by the surfactant in the polar phase, resulting in a microemulsion (middle). Lowering the pressure and thus the density of the blowing agent initiates the foaming of the microemulsion (right). Redrawn from [169].

The first step of the POSME procedure provides a suitable mixture of surfactant and fixable polar solvent (for example a monomer or a highly concentrated sugar solution) in which the surfactant forms spherical micelles. This mixture is then covered with a known amount of gas (*e.g.* CO₂ or N₂). The second step increases the pressure and temperature above the critical parameters of the gas (T_c , p_c), thus inducing a change of state of aggregation from gas to supercritical fluid. The supercritical fluid can subsequently be solubilised in the polar solvent if an appropriate surfactant was chosen, leading to a microemulsion with droplets swollen with supercritical fluid. These droplets have a size of a few nanometres serve and function as a template for the nanometre-scaled bubbles in the foam. The last step consists of expanding the microemulsion to normal pressure while keeping the temperature above T_c . Thus, the pressure-induced lowering of density leads to foaming the microemulsion. The polar component can be fixed simultaneously or slightly previous to the expansion if the polymer is soft enough to allow the foaming process. As the temperature is still kept above T_c , the fluid remains in a supercritical state and will change from liquid-like density to vapour-like density without nucleation. In theory, every micelle in the microemulsion becomes a bubble in the foam. The size of each bubble can be calculated from the density change of the blowing agent.

However, the last step in this method, the fixation of the polar component during the expansion, has proved to be a challenge. Because the density of the supercritical fluid decreases dramatically upon expansion the micelles grow in size and thus the surface area of each micelle increases which gives

rise to contact sites of polar solvent and supercritical fluid. This process is shown graphically for the example of a CO₂ swollen micelle in aqueous solution in Figure 2.9.

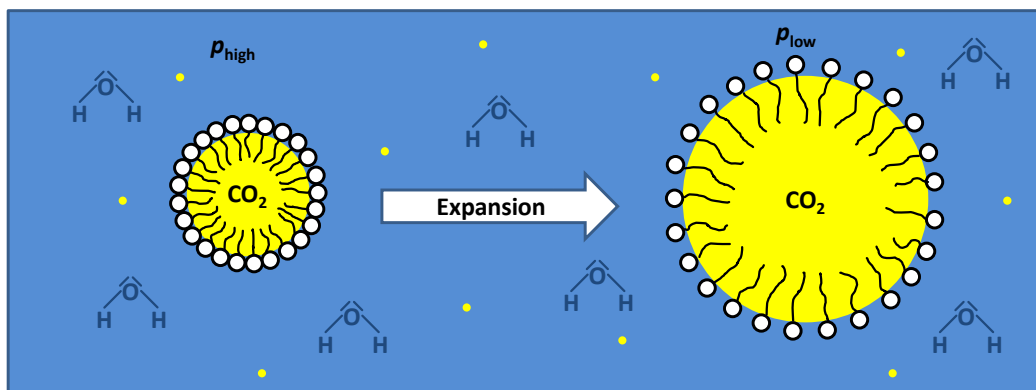


Figure 2.9: Schematic drawing of a CO₂ swollen micelle in aqueous solution under high pressure (left) and after expansion (right). Whereas the surfactant layer is dense enough to cover the whole surface area of the micelle in the compressed state, contact sites of water and CO₂ arise when the surfactant layer stretches after expansion. The yellow circles indicate CO₂ which is monomerically dissolved in water.

2.2.3 Aging phenomena and the concept of anti-ageing agents

The interface tension of polar solvent and supercritical fluid is rather high (about 35 mN m⁻¹ [50, 170]). Since the energy of contact sites is thus very high and thermodynamically unfavourable, the system attempts to reduce the interfacial area in order to avoid the high-energy contact sites. This can be achieved by the formation of bigger droplets out of many small ones. As such a reorganisation reduces the interface area while the amount of surfactant remains constant, the surfactants can cover a higher percentage of the interface. The size of big droplets, however, makes them thermodynamically unstable and so that coagulation occurs until phase separation is reached. The driving force for the formation of big droplets is the Laplace pressure Δp which can be calculated using the Young-Laplace equation:

$$\Delta p_{\text{Laplace}} = |p_{\text{inside}} - p_{\text{outside}}| = \frac{2\sigma}{R_{\text{bubble}}} = 2\sigma H. \quad \text{Eq. 2-7}$$

As can be seen in Eq. 2-7, the Laplace pressure is also connected to the mean curvature H which is described in Eq. 2-6. The parameter σ represents the interfacial tension between liquid and CO₂ and is the main parameter which is to be reduced via ageing processes. Considering Eq. 2-7 with the radius of the droplet R_{bubble} there are two ways to reduce the Laplace pressure which are both applicable for ageing processes. On one hand, reduction of the interfacial tension σ occurs because the interface area decreases. On the other hand, an increase of the droplet radius leads to a decrease of the Laplace pressure since R_{bubble} and $\Delta p_{\text{Laplace}}$ are inversely proportionate.

However, not only the thermodynamic driving force for ageing processes is of interest but also the mechanism these processes follow. In the context of microemulsions Ostwald ripening [171-178] (see

A in Figure 2.10) and coagulation with subsequent coalescence [46, 179] (B in Figure 2.10) occur the most. These two routes are shown exemplarily for CO₂ in aqueous solution in Figure 2.10.

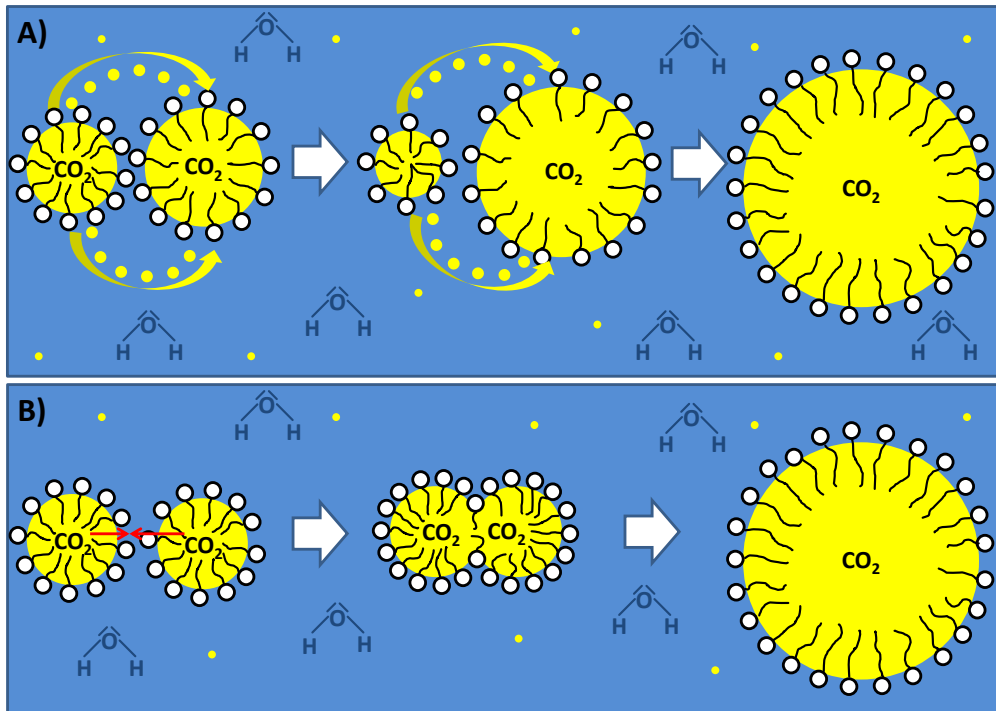


Figure 2.10: Overview of two different ageing processes for the example of an expanded CO₂ swollen micelle in water. A) *Ostwald ripening*: Because of comparably high monomeric solubility this process is based on diffusion of CO₂ molecules from small to larger micelles until the small droplet vanishes completely. The higher the monomeric solubility of the fluid the faster is this process. B) *Coagulation with subsequent coalescence*: The diffusion movement of the micelle itself leads to two micelles collide (coagulation). The subsequent reordering process of forming one spherical micelle is called coalescence. The faster the micelles diffuse the more likely is this process to happen.

Ostwald ripening occurs due to the difference of solubility of small and large droplets. This was described mathematically by Lord Kelvin [180] by

$$c(r) = c(\infty) \exp\left(\frac{2\sigma V_m}{rRT}\right) \quad \text{Eq. 2-8}$$

where $c(r)$ is the solubility of a particle or droplet with radius r , $c(\infty)$ is the bulk phase solubility, σ is the interfacial tension and V_m is the molar volume of the dispersed phase.

The key factor for Ostwald ripening is the diffusion of, in this example, CO₂ in water. This process is advantaged if the micelles have a broad size distribution. For two droplets with radii r_1 and r_2 Eq. 2-8 can be rewritten as

$$\left(\frac{RT}{V_m}\right) \ln\left(\frac{c(r_1)}{c(r_2)}\right) = 2\sigma\left(\frac{1}{r_1} - \frac{1}{r_2}\right) \quad \text{Eq. 2-9}$$

which clearly shows that the larger the difference between the two radii is the higher is the rate of Ostwald ripening.

Coagulation, in contrast, depends on the diffusion of the micelle itself since a fast-moving micelle is more likely to collide with a second micelle. Once the micelles contact each other, i.e. coagulate, a reordering process (coalescence) can follow, in which the interface reorganises to spherical shape. Here, the diffusion coefficient of the micelles is the key factor, so that this process can be influenced by parameters as solvent viscosity, temperature and the hydrodynamic radius of the micelle (Eq. 2-84). Ripening processes lead to a coarsening of the pore sizes in the production of foams. If one aims for pores in the range of or even below 100 nm these processes are highly unfavourable. Thus, the concept of *Anti-Aging-Agents* (AAA) was developed by Strey, Khazova *et al.* in 2009 [181]. It suggests adding a hydrophobic low-molecular substance to the microemulsion which is supposed to reduce the increasing interfacial tension emerging during expansion and thus slow down ageing process. Thus, following the anti-ageing concept leads to micelles which are swollen with both the fluid and the additive. Upon expansion the micelles grow and the interfacial area increases (Figure 2.9). Since the interfacial tension of the additive and water is slightly lower than the one of the fluid and water, the additive is supposed to accumulate at the interface, thus lowering the interface tension in comparison to the micelle without additive. This is shown graphically in Figure 2.11.

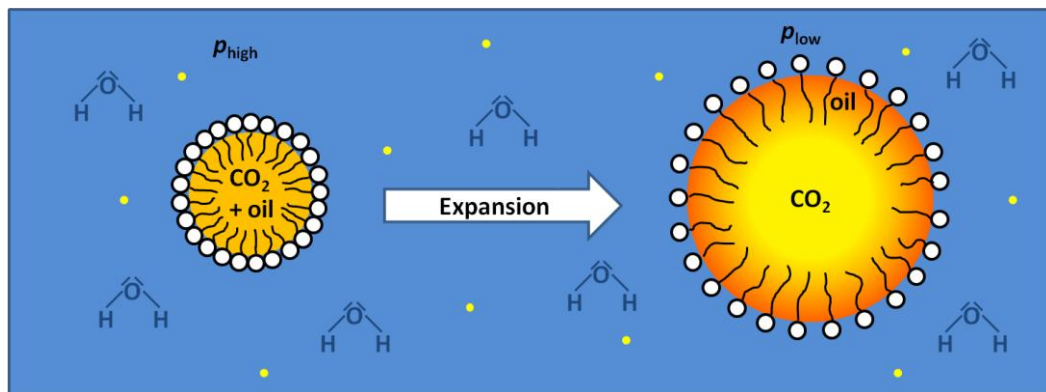


Figure 2.11: Schematic drawing of the assumed behaviour of a mixture of CO₂ and additive at high and low pressure. CO₂ and the hydrophobic additive form a homogeneous mixture inside the micelle at high pressure because the two components are completely miscible. Upon lowering the pressure, the additive accumulates at the interface because of the favourable interface tension situation.

Since the additive is supposed to decelerate the ageing process it is called anti-ageing agent (AAA).

The composition of oil, i.e. the fluid, and AAA is described by the parameter β :

$$\beta = \frac{m_{AAA}}{m_{fluid} + m_{AAA}} \quad \text{Eq. 2-10}$$

While planning the composition of the microemulsion it is important to consider that the mixture of gas and oil has the critical composition, as this leads to spinodal decomposition upon lowering the pressure. This was first described by Cahn *et al.* in 1965 [182] and occurs for example in binary systems. In this context, the two components are considered to be supercritical fluid (scCO₂) and low-molecular oil. The pressure-dependent miscibility is shown in Figure 2.12.

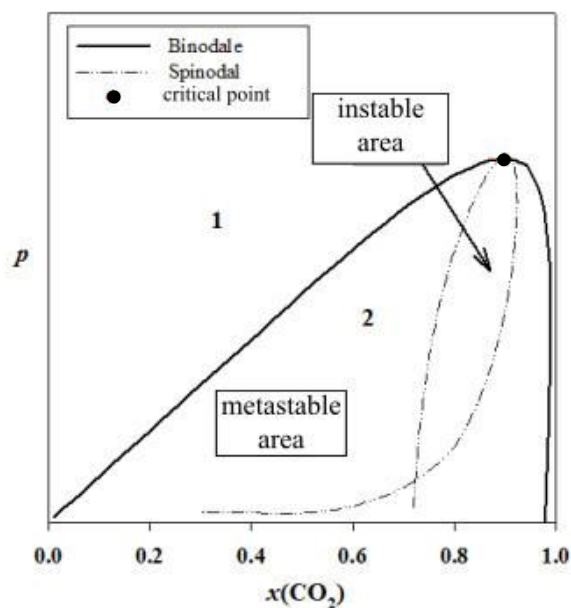


Figure 2.12: Schematic plot of the phase behaviour of a mixture of CO₂ and a low-molecular additive as a function of pressure and molar fraction $x(\text{CO}_2)$ and at constant temperature. The separation of the two components is spinodal and thus fast if the pressure is lowered at the critical $x(\text{CO}_2)$. At all other molar fractions, the separation after lowering the pressure to the metastable area is binodal and comparably slow. Redrawn from [183].

In order to mix CO₂ and the additive high pressure is necessary, especially at high CO₂ molar fractions. However, if the pressure is lowered, the two components separate which can happen in two different ways. At most compositions a decrease of pressure brings the mixture to a metastable state (straight line in Figure 2.12, *binodal*). There, the decomposition happens on a comparably long time scale as nucleation processes occur. Thus, first only small aggregates form which grow in size until the two phases are separated. On the opposite, spinodal decomposition happens spontaneously and is in no need of nucleation steps, which means that there is no energy barrier as for nucleation. Therefore it is much faster. The dotted line Figure 2.12 (*spinodal*) shows the region of composition in which spinodal decomposition occurs. This region is rather small compared to the binodal decomposition. This means that applying the critical composition of CO₂ and additive in a microemulsion allows for the mixture to separate very fast and thus the AAA can adsorb at the interface very fast.

2.3 Thermoresponsive polymers

2.3.1 Emulsion polymerisation

Since all Poly-(*N*-isopropyl)acrylamide (PNIPAM) particles presented and characterised in this work were synthesised via emulsion polymerisation this chapter explains the theoretical background of this technique. On top, nearly a quarter of the overall polymer production, around $5 \cdot 10^7$ metric tons per year [184], is performed via this method.

Most commonly emulsion polymerisations are carried out in water because water provides excellent heat transfer possibilities and can also be easily evaporated if dried polymer particles are needed. Since the (*N*-isopropyl)acrylamide monomer (NIPAM) is water soluble it is possible to synthesise PNIPAM particles with as well as without surfactant. In general, the synthesis in presence of surfactants is preferred as the formation of monomer droplets, and thus also the resulting particles, is less polydispers with surfactant. Polymerisation takes place inside the micelles which form if the critical micelle concentration (*cmc*) is exceeded. Using surfactants at a low concentration influences the viscosity and thus the homogenisation of the reaction solution only in a negligible manner.

Emulsion polymerisation takes place in three different stages: the initiation, in which the radicals are formed, the propagation, during which the polymer chains grow, and the completion stage, in which the radical reaction terminates. Before polymerisation starts, however, there is an induction period in which free radicals are consumed by residual oxygen. This interval is, however, commonly ignored because it does not provide information on particles growth.

In conventional polymerisations an initiator is needed to start the radical reaction. Since peroxydisulfate is water soluble and thermally decomposes at comparably moderate temperatures around 60°C it is very commonly used as initiator, especially in its salt form with potassium. Thereby, one peroxydisulfate molecule splits homolytically into two sulphate radicals ($S_2O_8^{2-} \rightarrow 2 SO_4^{\cdot -}$). In a second step the primary radicals react with a monomer. After these initial reactions the polymerisation and thus the growth of the particles can be divided into three different stages of polymerisation rates which are illustrated in Figure 2.13.

Interval I is called period of nucleation. At this stage each newly formed radical leads to a higher reaction rate since in each micelle a new polymer particle starts to grow, increasing the number of particles. This period is rapid and transitory.

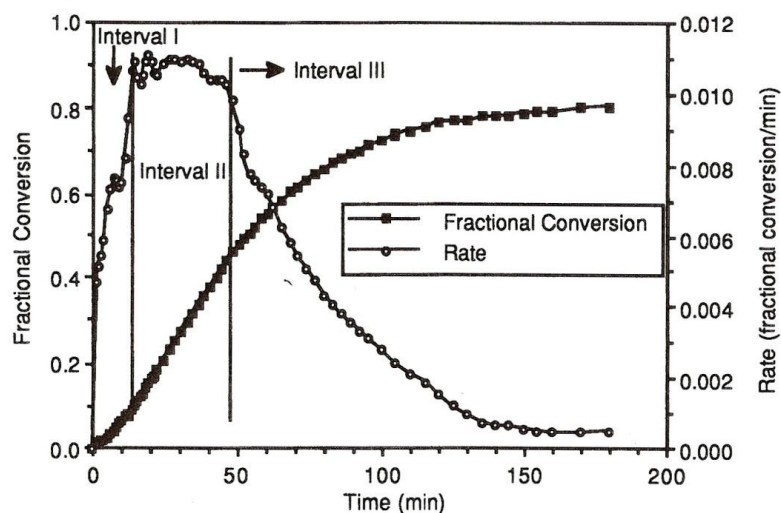


Figure 2.13: Fractional conversion of monomer into polymer and rate of polymerisation, both as a function of time, for a styrene *ab initio* emulsion polymerisation system. The three different intervals of polymerisation are marked. Taken from [185].

Interval II, the particle growth stage, is connected to a relatively constant rate of reaction, i.e. polymerisation proceeds homogeneously. At the beginning of this stage about 50% of the micelles are occupied with a radical and polymerisation is going on in these micelles. In order to both maintain the reaction and to swell the newly formed polymer monomer molecules from emulsion droplets without a radical diffuse through the aqueous solvent to these emulsion droplets in which polymerisation takes place. Thus, the monomer concentration in the particles remains constant during this interval, as well as the reaction rate. The probability of a polymerisation to start in such a feeding emulsion droplet at this time of the polymerisation is very low, especially since the number density of these emulsion droplets is about seven orders of magnitude smaller than the one of droplets in which polymerisation takes place. This stage ends when monomer droplets disappear, i.e. when about 50-80% of monomers are converted.

Interval III, the completion stage, is the final stage of reaction. It starts as soon as the monomer stash in emulsion droplets is consumed, so that the rate of reaction decreases monotonically because only the remaining monomer which swells the polymer can be spent for reaction.

The mechanism of monomers feeding polymerising micelles can be described by the model of Smith and Ewart [186] who showed experimentally in 1948 that particle formation stops if the surfactant concentration drops below the *cmc*. A schematic drawing of this process is shown in Figure 2.14. During this stage also termination reactions such as recombination occur.

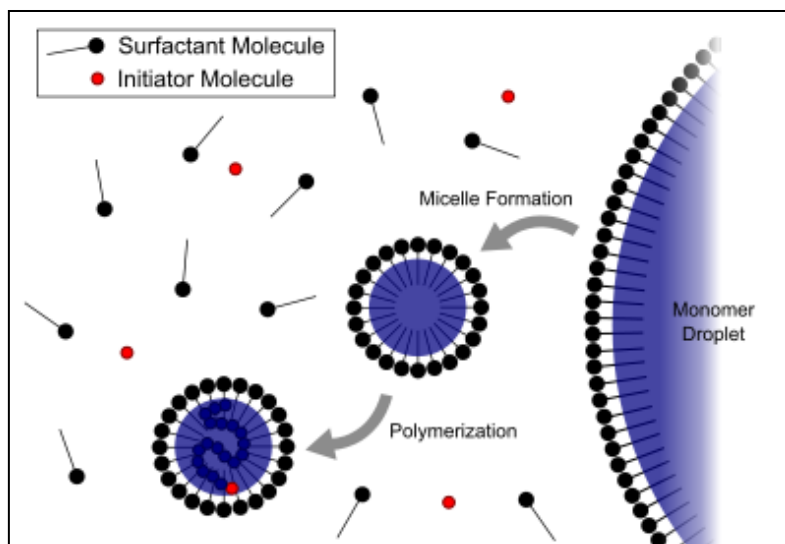


Figure 2.14: Schematic drawing of a typical emulsion polymerisation with surfactant. Starting from big monomer droplets small monomer micelles are formed in which polymerisation takes place after the initiator enters a micelle. Thus, the polymer is formed inside the micelle. Thereby, monomer molecules diffuse from monomer droplets into the micelles. Taken from [187].

The experiments by Smith and Ewart and their results are, however, predominantly valid if the monomer is hydrophobic, as for example styrene. In the case of more hydrophilic monomers as NIPAM, the synthesis can also be performed if no surfactant is present. Thus, the theory was extended by Fitch and Tsai in 1970 [188] and by Hansen and Ugelstad [189] in 1982 to polymerisations in non-micellar systems. This theory of “homogeneous nucleation” includes the formation of particle nuclei in the continuous aqueous phase, started by initiator molecules. In such a case, the feeding mechanism shown in Figure 2.14 is still valid as monomers are usually better soluble in their respective polymer. Emulsifier may be needed to ensure colloidal stability of the product as it is formed and subsequently on the outer shell of the polymer.

A different particle nucleation was proposed by Feeney, Napper and Gilbert [190]. They showed that the particle size distribution during particle formation (Interval I) was positively skewed, i.e. that particles occurred larger than predicted. This, according to their “coagulation nucleation” mechanism is due to coagulation processes which are induced by instabilities in the absence of emulsifier. Finally, it was postulated by Gilbert and Hansen in 1992 [191] that the mechanisms described above, homogeneous and coagulation nucleation, are always competing and depend strongly on the nature and hydrophilicity of the monomer.

In order to understand the kinetic properties of an emulsion polymerisation it is reasonable to start with the rate of the first reaction, i.e. the generation of a pair of free radicals $R\cdot$ from one initiator molecule I according to



where k_d is the rate constant for the dissociation of the initiator. Thus, the rate of dissociation R_d is given by

$$R_d = 2fk_d[I] \quad \text{Eq. 2-12}$$

where $[I]$ is the concentration of initiator and f is the initiator efficiency. This value describes the fraction of free radicals which successfully initiate polymerisation. Due to wastage reactions f is usually in the range of 0.3-0.8. The factor 2 enters due to the formation of two primary free radicals from each initiator molecule.

The next step is initiation in which a free radical $R \cdot$ reacts with a monomer M to the first part of the chain $RM \cdot$ with a radical located at the monomer according to



Since the rate of initiation R_i is equal to the rate of dissociation of an initiator it can be described as follows

$$R_i = 2fk_d[I] \quad \text{Eq. 2-14.}$$

Starting from the radical $RM \cdot$ the polymerisation propagates by reaction of $RM \cdot$ with other monomers M



The rate of propagation R_p is also known as the rate of monomer consumption. Thereby, monomer is consumed both by propagation reaction and by the initiation reaction. The rate of propagation R_p is then:

$$R_p = -\frac{d[M]}{dt} = k_i[R \cdot][M] + k_p[M \cdot][M] \quad \text{Eq. 2-16.}$$

Here, $M \cdot$ is the total concentration of every size of chain radicals. Since the amount of monomer consumed in the initiation step is small compared to the amount consumed in the propagation step the according term in Eq. 2-16 can be neglected.

Termination reactions must also be considered. The two main mechanisms are recombination, in which two polymer radicals react to one large polymer molecule, and disproportionation, in which one growing chain abstracts a hydrogen atom from another, leaving it with an unsaturated endgroup. To describe the rate of termination R_t with the according rate constant k_t it needs to be considered that *steady state conditions* must be obtained in polymerisation kinetics [185]. This means that the rate of free radical generation is equal to their disappearing rate, meaning initiation and termination rate are the same. Thus, the concentration of free radicals in the form of $M \cdot$ remains constant. Under consideration of Eq. 2-16, the equation for the steady state condition is

$$R_i = R_t = -\frac{d[R \cdot]}{dt} = 2k_t[M \cdot]^2 \quad \text{Eq. 2-17.}$$

Rearranging this equation leads to

$$[M \cdot] = \left(\frac{R_i}{2k_t}\right)^{\frac{1}{2}} \quad \text{Eq. 2-18}$$

which can be combined with the simplified Eq. 2-16 to

$$R_p = k_p[M] \left(\frac{R_i}{2k_t}\right)^{\frac{1}{2}} \quad \text{Eq. 2-19.}$$

Eq. 2-19 clearly shows that the rate of polymerisation depends on the square root of the rate of initiation and thus, considering Eq. 2-14, on the square root of the initiator concentration $[I]$.

Furthermore, the properties of the resulting polymer are also influenced by a variety of other parameters such as temperature, the concentration of surfactant and the water-to-monomer ratio. Increasing the temperature leads to a higher initiation rate and thus to a higher number of particles with a smaller size and size distribution. Increasing the monomer to water ratio leads to larger particles with a smaller size distribution.

2.3.2 Swelling of poly-(*N*-isopropyl)acrylamide

The most interesting feature of PNIPAM particles and gels is their volume phase transition temperature (VPTT) which is located around 32°C in aqueous solution and therefore very close to the temperature of the human body [62, 69, 192-194]. This transition is completely reversible. Possible applications are discussed in section 2.3.3. Figure 2.15 shows the chemical formula of the monomer (*N*-isopropyl)acrylamid (NIPAM), the polymer PNIPAM and the crosslinker *N,N'*-methylenbisacrylamid (BIS) which was used in this work.

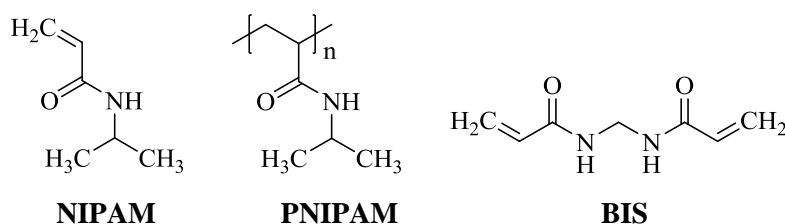


Figure 2.15: Chemical formulas of (*N*-isoproyl)acrylamide (NIPAM), the respective polymer poly-(*N*-isopropyl)acrylamide (PNIPAM) and the crosslinker *N,N'*-methylenbisacrylamide (BIS).

The difference of microgel and macrogel is not clearly defined [63]. In most cases microgel particles have an average diameter in the range between 40 nm and 5 μm [63] while macrogels represent continuous gel pieces which can be handled manually. Regarding the swelling behaviour the properties of both are very similar, just that microgels react much faster than common gels [195, 196] simply because the rate of diffusion is the rate-determining step.

Gels, either micro or macro, are temperature-sensitive if most of the polymer displays temperature-sensitive phase behaviour in the solvent. Starting at temperatures below the phase transition temperature the polymer is swollen with solvent and has a gel-like character. Upon heating the interactions between polymer and solvent change so that the solvent is expelled from the polymer which leads to considerable shrinking. This process is shown schematically in Figure 2.16. In the case of spherical microgel particles this shrinking is displayed by a decrease of the particle radius. Since it is the volume of the gel which changes the temperature at which this phenomenon occurs is called the volume phase transition temperature (VPTT). In literature one often finds publications speaking of the lower critical solution temperature (LCST). Basically, the transition is also a volume phase transition but at the critical concentration of polymer in solvent, which was determined by Heskins and Guillet in 1968 for linear PNIPAM to be around 0.15 wt% [197]. For crosslinked PNIPAM the LCST is located around 32°C [198]. Since, however, the concentration dependence of the transition temperature is not determined in most cases it is reasonable to speak of the volume phase transition temperature instead of the lower critical solution temperature, especially if, as happens in this work, the term lower critical solution temperature is also used in the context of mixtures of oil and surfactant as the phase separation temperature of such a mixture (see section 2.1.2). In contrast to this kind of phase separation the process which happens especially with microgel particles can be seen as microphase separation.

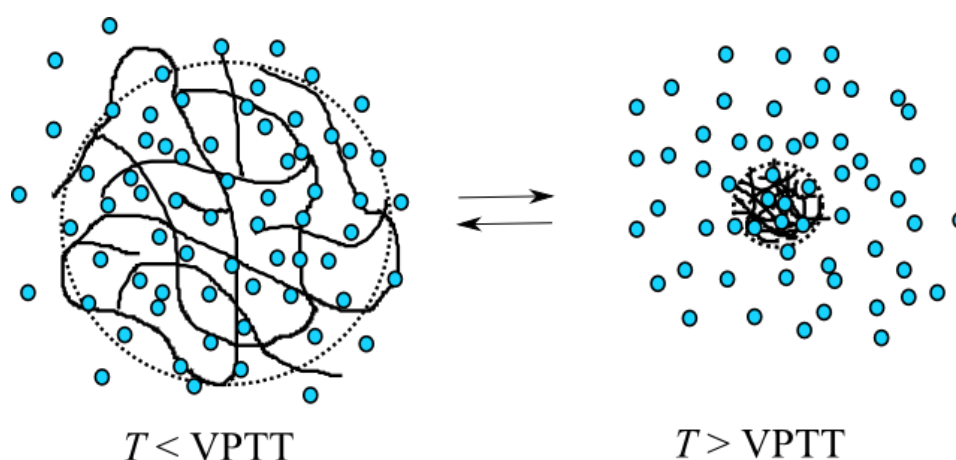


Figure 2.16: Schematic drawing of the structural changes in a PNIPAM microgel particle. The blue dots represent solvent molecules. At temperatures well below the volume phase transition temperature (VPTT) the particle is swollen with solvent and has a large radius with a rather low polymer density within the particle. At temperatures above the VPTT, however, most of the solvent molecules leave the particle which also shrinks considerable in size to a smaller particle with a high polymer density.

The volume phase transition is basically a mixing phenomenon which includes both enthalpic and entropic contributions which should be the same for a 500 nm microgel and a 5 cm macrogel but dynamic processes also depend on the size of the gel. Different theories have been applied in order to predict the processes such as statistical thermodynamic theory [199], lattice-fluid hydrogen bond theory [200] and Flory-Huggins-Staverman theory [201].

Considering the Gibbs-Helmholtz equation for mixing

$$\Delta G_M = \Delta H_M - T\Delta S_M \quad \text{Eq. 2-20}$$

where ΔG_M is the free mixing energy, ΔH_M is the mixing enthalpy, T is the temperature and ΔS_M is the mixing entropy, four different cases are possible which are shown in Table 2-1.

Table 2-1: Overview of different possible cases of energies in the Gibbs-Helmholtz equation. Note that the third case applies for PNIPAM.

ΔH_M	ΔS_M	ΔG_M	interpretation
< 0	> 0	< 0	solution irrespective of T
> 0	< 0	> 0	no solution
< 0	< 0	--	high $T \rightarrow -T\Delta S_M > \Delta H_M \rightarrow \Delta G_M > 0 \Rightarrow$ LCST; special for polymers
> 0	> 0	--	poor interactions but mixing occurs for high T

The third case in Table 2-1 represents the one which applies for PNIPAM gels and particles. In this case the particles are swollen with solvent for sufficiently low temperatures but upon rising the temperature the contribution of $T\Delta S_M$ outweighs the mixing enthalpy ΔH_M so that ΔG_M becomes positive and thus demixing occurs in the form of a volume phase transition.

A very interesting phase behaviour feature of PNIPAM linear polymers, micro- and macrogels is their behaviour in water-alcohol mixtures which is called co-nonsolvency and describes that PNIPAM is soluble in both water and alcohol but not in mixtures of both. Thus, the addition of 55 vol% methanol lowers the VPPT of PNIPAM to below 0°C, while higher concentrations of methanol lead to a dramatic increase of the VPTT, even to temperatures much higher than in water [66, 202-204].

2.3.3 Microgel applications

The possible future applications of PNIPAM for biomedical purposes are too numerous to list. This chapter only gives a brief overview of historic and present experiments which might be relevant to medicine.

The first ones describing the interaction of PNIPAM with biological molecules were Kawaguchi *et al.* who studied the temperature-dependent sorption and desorption of human γ -globulin [205]. They showed that the sorption of the protein to the polymer preferably occurred at 40°C (compared to 25°C) which clearly indicates that hydrophobic interactions are dominating since 40°C is above the VPTT of PNIPAM. Thus, by lowering the temperature to 25°C desorption was induced. The speed of desorption depended strongly on the sorption time, i.e. the longer the mixture was left at 40°C the longer the desorption process took. Very likely this means that the protein enters the polymer. The same group also compared the sorption and desorption properties of PNIPAM and polystyrene to four different proteins [206], finding that

PNIPAM has a much lower tendency to denature enzymes than polystyrene, which is a very promising aspect for PNIPAM particles regarding medical applications.

One of the most thoroughly investigated topics around the application of PNIPAM is the temperature-controlled uptake and release of chemical substances [207-209]. Thereby, it seems that hydrophobic interactions with the polymer backbone are the driving force for binding of organic substances, which are released as a response to the shrinkage of the particles [210].

Besides proteins and the controlled release of substances also the interaction of PNIPAM with enzymes is of interest in order to yield temperature-controlled enzyme activity. This was realised by Shiroya *et al.* who grafted trypsin and peroxidase to PNIPAM, finding that the enzymatic activity decreased if the temperature was raised above the VPTT [211]. Furthermore, also catalytic activity can be temperature-controlled if hybrids build of gel networks and for example gold [212] or platinum [213] nanoparticles are synthesised. On top of that, hybrid particles can also be interesting to tune optical properties like light extinction in the visible range of the electromagnetic spectrum [214]. Contreras-Carcera *et al.* for example used gold nanoparticles as a core material and coated these particles with PNIPAM, obtaining a systematic temperature-sensitivity of the Plasmon bands which shift towards higher wavelengths with increasing temperature due to the increase of the local refractive index during the collapse of the polymer shell [215]. Furthermore, PNIPAM has already been applied for cell culturing [216], control of bimolecular motors [217, 218], protein purification [219] and photolithography [220]. Thus, the application spectrum of PNIPAM is very wide.

2.4 Neutron scattering

The determination of shape and size is of the utmost importance if one works in the field of colloidal systems and studies the relation between physical properties and molecular structure. Thereby, scattering techniques are the most powerful tools to investigate structure and dynamics of materials, since they are based on interactions between incident radiation (e.g. light, neutrons, X-ray) and the particles of interest. Microemulsion micelles display sizes in the order of 5-1000 Å which is why neutrons or X-rays are well suited to examine their structure. Scattering techniques, in contrast to direct imaging techniques like scanning or transmission electron microscopy, also allow for the sample to change structural properties. Furthermore, the scattering of a sample is averaged over a wide range in comparison to the size of the structure, which allows ignoring local defects. The time and length scales of samples which are available for studying with neutrons and the most appropriate neutron scattering techniques are given in Figure 2.17.

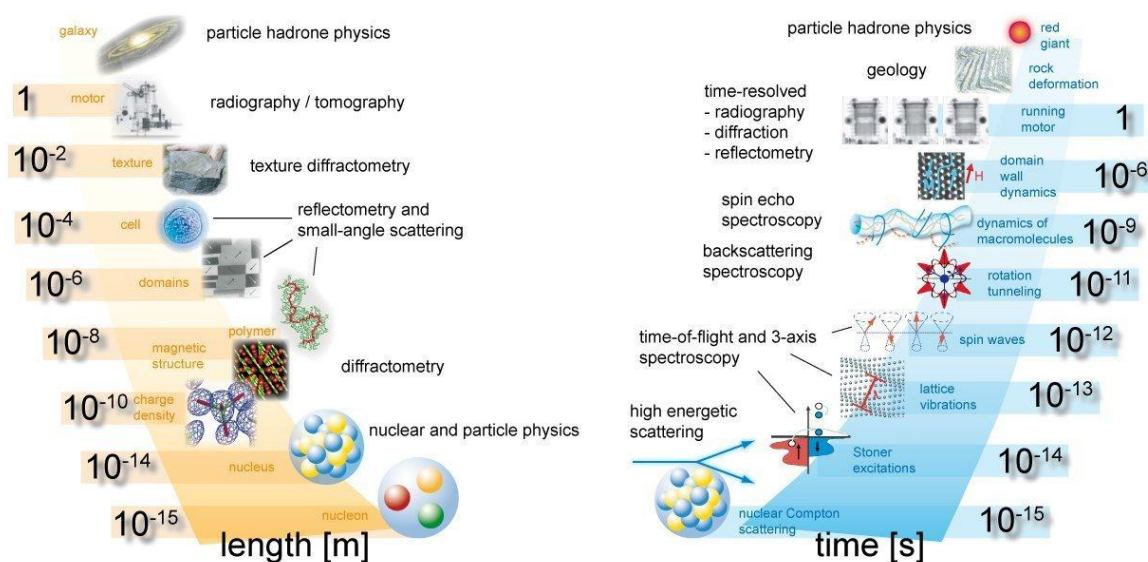


Figure 2.17: Overview of different scales (length and time) of soft matter samples, together with a suggestion of an appropriate neutron scattering technique. Taken from [221].

Neutrons are uncharged subatomic particles with mass $m = 1.675 \cdot 10^{-27}$ kg, a spin of 0.5 and a magnetic moment of -1.913 nuclear magnetons. The lifetime of a free neutron is about 1000 s, although they are stable when bound in an atomic nucleus. The main characteristic of neutrons which is used for classification is the wavelength. If the wavelength of the neutron is about 10 Å the neutrons are called “cold” neutrons, whereas they are “thermal” for wavelengths in the order of 0.1 Å.

In many cases, the size of the sample is the prime reason for choosing neutron or X-ray scattering over light scattering. Since the wavelength of visible light is in the range of 300-700 nm, it is not possible to investigate structures with sizes smaller than about 5 nm [222, 223].

Since neutrons are uncharged particles they can highly penetrate materials because they interact on a short range only with the nuclei of the material under investigation. However, a high penetration can also mean a low amount of interaction and thus little scattering, which requires long measurement times. The high penetration is also the main reason why neutrons are non-destructive, even to sensitive biological samples. Due to their magnetic moment it is also possible to conduct field-dependent measurements or experiments in which the interaction of neutrons with magnetic samples is followed by monitoring the neutron spin (up or down). In contrast to X-rays, the scattering power of an atom does not depend on its atomic number, because neutrons interact with the nucleus. Thus, it is possible to distinguish light atoms such as hydrogen in the presence of heavier ones. Most important, though, is the sensitivity of neutrons to isotopes. This will be explained in more detail in section 2.4.2.

The main drawback of neutron scattering is that it is very difficult and thus also expensive to produce neutrons. Furthermore, one needs to be constantly aware that neutron scattering experiments mean dealing with radiation which always includes health risks.

2.4.1 Small angle neutron scattering

In all scattering experiments waves or particles are directed onto the sample. While a large part of the incident beam passes the sample undisturbed, a fraction of the radiation is adsorbed and another fraction interacts with the sample so that it is diffracted or scattered at a certain angle θ . A schematic drawing of the scattering process is given in Figure 2.18.

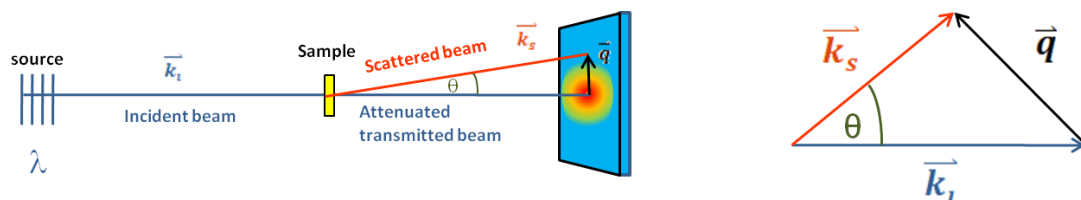


Figure 2.18: *Left:* Schematic drawing of the scattering process. The incident neutron beam \vec{k}_i (blue) coming from the neutron source interacts with the sample. While most of the beam passes the sample unaffected a fraction of the radiation is scattered at the angle θ which is orange and marked as \vec{k}_s . *Right:* The scattering vector \vec{q} (black) is defined by the difference of the incident beam and the scattered beam.

The Fraunhofer approximation states that all wave vectors can be considered planar if the distances between radiation source and sample and between sample and detector are large compared to the wavelength of the radiation. This is the reason why all waves in Figure 2.18 are drawn parallel to each other, i.e. planar.

Figure 2.18 right shows that the scattering vector \vec{q} is calculated from the incident wave vector k_i , the wave vector of the scattered radiation k_s and the scattering angle θ using

$$q = |\vec{q}| = \sqrt{k_i^2 + k_s^2 - 2k_i k_s \cos \theta} \quad \text{Eq. 2-21}$$

Assuming that the scattering experiment is of elastic nature, i.e. that no energy is transferred from the neutrons to the sample, the vectors $|\vec{k}_i|$ and $|\vec{k}_s|$ differ in direction but have the same absolute value. Thus, the equation for q can be simplified to

$$q = \frac{4\pi}{\lambda} \sin \frac{\theta}{2} \quad \text{Eq. 2-22.}$$

with λ being the wavelength of the incident radiation and θ being the scattering angle as indicated in Figure 2.18. Since the scattering occurs as emission of spherical symmetric waves from all scattering centres within the sample volume it is obvious that interferences of the scattered waves will occur, depending on the relative positions of the scattering particles. Thus, the scattering pattern depends on the internal structure of the sample such as the spacing between planes of the lattice d_{Bragg} . Using Bragg's law

$$n \cdot \lambda = 2 \cdot d_{\text{Bragg}} \cdot \sin \frac{\theta}{2} \quad \text{Eq. 2-23}$$

in combination with Eq. 2-22 the length scale of the sample can be connected to the scattering pattern, i.e. the appearance of constructive or destructive interferences at angles θ by

$$d_{\text{Bragg}} = \frac{2\pi}{q} \quad \text{Eq. 2-24.}$$

As mentioned above microemulsion structures occur in the range of 5-1000 Å which means that a q -range from 0.001 to 1 Å⁻¹ is necessary to cover the whole range sufficiently. With neutron scattering a q -range from about 0.001 to 0.1 Å⁻¹ is available, depending on the setup of the SANS instrument. This range is usually well sufficient to obtain all structural information of interest. If more information is needed the q -range can be extended by using very small angle neutron scattering (USANS), X-ray scattering or static light scattering.

The basic setup of a spectrometer for small angle neutron scattering is shown in Figure 2.19. Coming from the neutron source, the neutrons with the appropriate wavelength pass the velocity selector. After that, the neutrons reach the collimation which can be changed in length. Generally speaking, the longer the collimation is the more focussed is the beam, but a long collimation also reduces the intensity of the incident beam. After passing an aperture the beam hits the sample. While most of the beam passes the sample unaffected a fraction of the beam is scattered at the angle θ and is counted at the detector. The distance between sample and detector can be varied by moving the detector inside the detector tube. Thus, different q -ranges can be accessed by different sample-to-detector distances. Specific parameter on the collimation lengths and the detector distances are given in section 7.2.2.

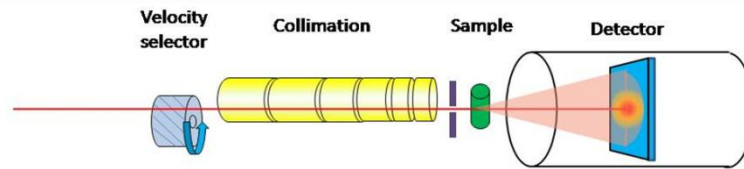


Figure 2.19: Schematic setup of a spectrometer for small angle neutron scattering. The neutron beam (red line) first passes through a velocity selector (light blue) to reduce the wavelength distribution of the neutrons. The length of the collimation (yellow) determines the degree of convergence of the beam. After an aperture (lilac) the beam strikes the sample (green) and a fraction of the neutrons is scattered. The detector (bright blue) counts the position dependent intensity of the scattered neutrons.

In Small Angle Neutron Scattering (SANS) experiments one obtains information on the scattering intensity $I(q)$ in reciprocal space as a function of the scattering vector q in reciprocal Fourier space. Thereby, the thermal motion of each scattering centre is assumed to be irrelevant, so that the nanostructure can be considered constant for the detection time. By analysing the scattering data it is possible to extract information on the structure of the sample, but also, in the case of microemulsions, information on properties such as monomeric solubilities and local concentration of substances can be gained. A detailed explanation of how to analyse scattering data is given in section 2.4.4.

2.4.2 Neutron contrast variation

The unique advantage of neutrons over X-rays or light is that they interact with the nucleus rather than with the electron shell. Thus, neutrons are sensitive to isotopes, which means that for neutron scattering experiments there is a huge difference whether H_2O is used as a solvent or D_2O .

The scattering contrast for neutrons is the difference of the scattering length densities of the sample particle and the bulk material, for example the solvent. The scattering length density is a unique property for every substance and can be calculated using

$$\rho_k = N_A \frac{\rho_k^0}{M_k} \sum_i b_i \quad \text{Eq. 2-25}$$

with N_A being Avogadro's constant, ρ_k^0 the macroscopic density of the substance and M_k the molar mass of the component. Here, b_i represent the scattering length of every atom i in the molecule k . The values for b_i can be drawn for example from the National Institute of Standards and Technology [224]. However, for scattering experiments one often finds that a domain consists of more than one component. In this case, the scattering length density of this phase of mixed components can be calculated according to

$$\rho_{domain} = \sum_k \rho_k \Phi_k \quad \text{Eq. 2-26}$$

where Φ_k is the volume fraction of the component k and ρ_k is the scattering length density according to Eq. 2-25.

The scattering contrast can be calculated by the difference between the scattering length densities of the two domains. A schematic example of different contrast conditions is shown in Figure 2.20.

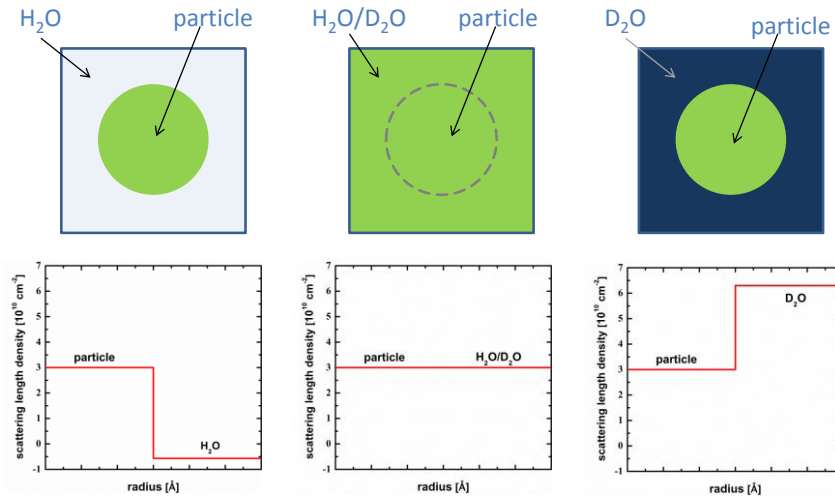


Figure 2.20: Schematic drawing of a particle with a fictitious scattering length density of $\rho_{\text{particle}} = 3 \cdot 10^{10} \text{ cm}^{-2}$. In the first case (left), H_2O with a scattering length density of $\rho_{\text{H}_2\text{O}} = -0.5 \cdot 10^{10} \text{ cm}^{-2}$ is used as a solvent, whereas the graph at the right shows pure D_2O as a solvent with a scattering length density of $\rho_{\text{D}_2\text{O}} = 6.3 \cdot 10^{10} \text{ cm}^{-2}$. The drawing in the middle represents a zero-contrast condition, where a volume ratio of H_2O and D_2O is used that matches exactly the scattering length density of the particle. No scattering intensity is expected in this case.

The example shown in Figure 2.20 describes a particle with a scattering length density of $\rho_{\text{particle}} = 3 \cdot 10^{10} \text{ cm}^{-2}$. Since the absolute difference of the scattering length densities of the particle and H_2O is $\Delta\rho_{\text{particle H}_2\text{O}} = |-0.5 - 3| \cdot 10^{10} \text{ cm}^{-2} = 3.5 \cdot 10^{10} \text{ cm}^{-2}$ and thus almost equal to the contrast condition with pure D_2O as shown on the right ($\Delta\rho_{\text{particle D}_2\text{O}} = |6.3 - 3| \cdot 10^{10} \text{ cm}^{-2} = 3.3 \cdot 10^{10} \text{ cm}^{-2}$) the scattering curve from both contrast conditions is expected to be very similar. The contrast condition shown in the middle should not result in a scattering at all since there is no contrast for the neutrons and thus no scattering.

Regarding microemulsion droplets also the amphiphilic film with its scattering length density needs to be considered. Thus, there are three different domains with different scattering length densities, and one needs to distinguish between the following two scattering contributions:

$$\Delta\rho_{\text{core}} = \rho_{\text{solvent}} - \rho_{\text{core}} \quad \text{Eq. 2-27}$$

and

$$\Delta\rho_{\text{film}} = \rho_{\text{solvent}} - \rho_{\text{film}} \quad \text{Eq. 2-28.}$$

Here, ρ_{core} represents the scattering length density of the substance which is inside the micelle, and ρ_{film} stands for the scattering length density of the surfactant film. In the case of microemulsions both scattering contributions need to be taken into account during data analysis.

If one aims to investigate the structure of a multiple component system in a very detailed way it is possible to perform a systematic contrast variation study. This means that the composition and thus the

structure of the sample is not changed while different neutron contrast conditions are applied. For example the solvent composition can be changed stepwise by applying different volume ratios of H₂O and D₂O. In the case of core-shell particles it is also possible to change the contrast conditions by deuterating different parts of the particle. Furthermore, matching the scattering length density of the solvent to the shell means that only the particle core is visible for neutrons. Matching the scattering length densities of solvent and core leads to the so-called film contrast condition. This method has been successfully applied to investigate the surfactant layers around mineral particles [225] and to characterise complex systems [226].

2.4.3 Raw data treatment and data recording for static measurements

To analyse scattering data qualitatively as well as quantitatively calibration to the absolute scale is necessary, since the raw data contain only information on the number of neutron counts together with the detector pixel position. Thereby, the number of counts depends on instrumental parameters like the incoming neutron flux, the collimation length, the size of the aperture, the sample thickness and the transmission of the sample. Furthermore, properties as the scattering of the empty sample container I_{EC} , its transmission T_{EC} and the efficiency of the detector need to be taken into account. Thus, the scattering data need to be normalised for different instrumental settings and for each setup. For this correction procedure different calibration measurements need to be performed (I_{EC} , T_{EC} , the natural background radiation scattering I_{BG} by blocking the incident beam with Cadmium or boron carbide).

The procedure of raw data treatment starts with the determination of the beam centre by measuring the intensity of the attenuated empty beam. After the sample measurement the data are masked to exclude the intensity at and immediately around the beam stop. Following that, the transmissions of empty cell and sample are calculated and finally the intensity can be averaged radially. The last step is to calibrate the data to the absolute scale, although it is also possible to calibrate first and then perform the averaging.

In order to calibrate the scattering data obtained at the D22 instrument the data normalisation was performed with respect to the empty beam measurement [227] with the incident intensity I_0 according to

$$\frac{d\Sigma}{d\Omega}(\theta) = \frac{1}{V} \frac{I(\theta)}{\varepsilon \Delta \Omega T J_0} = \frac{1}{\varepsilon_p I_0} \frac{I(\theta)}{d_{\text{sample}} T \Delta \Omega} \quad \text{Eq. 2-29.}$$

Here, $d\Sigma/d\Omega(\theta)$ describes the angle-dependant macroscopic cross section, V is the volume of the scatterer, d_{sample} is its thickness, ε_p is the efficiency of the pixel, J_0 is the incident neutron flux, $I(\theta)$ is the intensity measured at that pixel, and T is the transmission of the sample.

At the D11 instrument the data normalisation is performed in comparison to a standard sample, such as H₂O. After measuring the scattering intensity $I_{\text{H}_2\text{O}}$ and its transmission $T_{\text{H}_2\text{O}}$ at a given instrumental setup the scattering intensity of the sample can be calibrated as follows [228]

$$\left(\frac{d\Sigma}{d\Omega}\right)_{\text{sample}}(\theta) = \frac{d_{\text{H}_2\text{O}}}{d_{\text{sample}}} \left(\frac{d\Sigma}{d\Omega}\right)_{\text{H}_2\text{O}} \frac{\left[\frac{I_{\text{sample}} - I_{\text{BG}}}{T_{\text{sample}}} - \frac{I_{\text{sample-EC}} - I_{\text{BG}}}{T_{\text{sample-EC}}}\right]}{\left[\frac{I_{\text{H}_2\text{O}} - I_{\text{BG}}}{T_{\text{H}_2\text{O}}} - \frac{I_{\text{H}_2\text{O-EC}} - I_{\text{BG}}}{T_{\text{H}_2\text{O-EC}}}\right]} \quad \text{Eq. 2-30.}$$

Thereby, the subscript EC refers to the Empty Cell measurements, T is the transmission with respect to the empty beam, and I is the number of neutrons per second for the respective water, background and sample measurements.

The ILL provides two different data treatment software packages for the calibration of the scattering data. In this work both LAMP [229] and GRASP [230] were used, whereby LAMP was preferably used for D11 data treatment and GRASP for D22 data treatment.

After data reduction and radial averaging the result is the scattering intensity $I(q)$ as a function of the scattering vector q . This curve still includes the incoherent scattering background of the sample itself, which can be determined by the constant scattering intensity at high q values. A subtraction of the incoherent scattering background can be helpful for data analysis because often slight oscillations caused by the sample structure are covered by incoherent scattering. After subtraction of I_{incoh} such an oscillation may appear as shown in Figure 2.21.

For the sake of the description of the data recording procedure of kinetic measurements it should be mentioned here that the data recording order is a simple Count-command which counts the number of neutrons for the time the user signs into the instrument control software. This time can be estimated from the count rate which is also displayed in the software. If for example the count rate of a given sample and given instrument parameter is 50000 counts per second it is advisable to measure this sample for at least 40 seconds to achieve a total count number of at least 2 million counts.

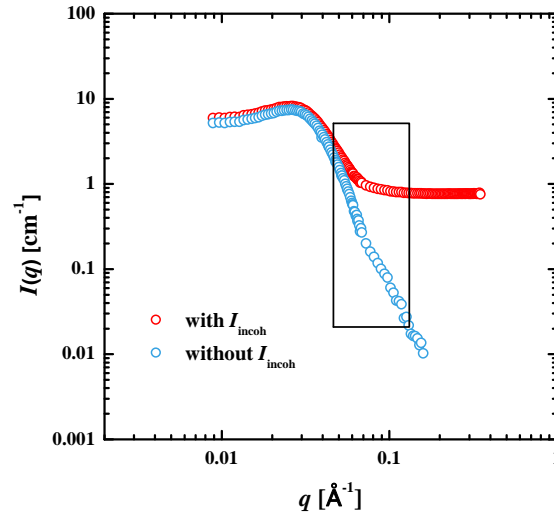


Figure 2.21: Example of a scattering curve of a microemulsion with incoherent scattering background (red) and after subtraction of I_{incoh} (blue). The incoherent scattering background covers the slight oscillation which only becomes perceptible with the subtracted curve (highlighted by the black rectangle).

2.4.4 Data analysis: Description of scattering curves

There are basically two different approaches to obtain structural information out of scattering data which both should lead to the same results. The first one is to compare the scattering curves to a calculated curve for a given structural model, which directly leads to numerical parameters such as particle size and size distribution. However, this approach avoids models with too many or unknown parameters and the knowledge of the structure prior to data analysis is presumed.

The second approach is to Fourier transform the scattering data to real space, which results in the Pair distance distribution function (PDDF) $p(r)$. By evaluation of the shape of the PDDF information on the particle size and shape can be gained, meaning that this method can also be used if the structure is unknown. Here, the number of parameters is very restricted, but this route is also theoretically more demanding.

The primary results of SANS experiments is a distribution of scattering intensity $I(q)$ in reciprocal space as a function of momentum transfer q . In order to gain information on the real-space structure the scattering intensity of N particles in a homogeneous volume V can be factorized into inter- and intraparticle scattering contributions (decoupling approximation) [136]

$$I(\vec{q}) = n \cdot P(\vec{q}) \cdot S(\vec{q}) \quad \text{Eq. 2-31}$$

with n being the particle number density N/V

$$n = \phi_{c,i} \frac{a_c}{4\pi v_c (R_0^2 + \sigma^2)} \quad \text{Eq. 2-32.}$$

The form factor $P(\vec{q})$ describes the intraparticle scattering and is related to the shape of the particles. The structure factor $S(\vec{q})$ accounts for scattering contributions arising from the interference of neutrons

scattered from different particles. The following sections give an overview of the models for form and structure factors used in this work.

SPHERICAL DROPLET FORM FACTOR

The particle form factor is defined as the product of the squared scattering length density difference $\Delta\rho$, the squared particle volume V_{part} and the complex square of the normalised scattering amplitude $A(\vec{q})$:

$$P(\vec{q}) = \Delta\rho^2 \cdot V_{\text{part}}^2 \cdot A(\vec{q}) \cdot A^*(\vec{q}) \quad \text{Eq. 2-33}$$

Thereby, the scattering amplitude $A(\vec{q})$ is the Fourier transform of the scattering length density profile $\Delta\rho(\vec{r})$ which describes the scattering length density and thus also the particle composition in real space as a function of r in all dimensions. By calculating the Fourier integral of $\Delta\rho(\vec{r})$ over the whole volume of the particle V_{part} the scattering amplitude $A(\vec{q})$ can be described as

$$A(\vec{q}) = \int_{V_{\text{part}}} \Delta\rho(\vec{r}) \cdot \exp(i \cdot \vec{q} \cdot \vec{r}) \, d\vec{r} \quad \text{Eq. 2-34.}$$

Here, $\Delta\rho(\vec{r})$ can be described by $\Delta\rho(\vec{r}) = \Delta\rho f(r,R)$ with $\Delta\rho$ being the scattering contrast and $f(r,R)$ the radial density distribution function which describes the radial scattering length density profile of the scattering particle.

In the case of spherical scattering particles or droplets orientation effects can be neglected because the scattering properties of the scattering particle are the same in all three dimensions and the particle is thus radially symmetric. Hence, Eq. 2-34 can be replaced by its one-dimensional, radial symmetric form

$$A(q) = 4\pi \cdot \Delta\rho \int_0^\infty f(r,R) \cdot r^2 \frac{\sin(qr)}{qr} \, dr \quad \text{Eq. 2-35.}$$

Note that after the simplification from three-dimensions to one-dimension the use of vectors is no longer necessary since the direction of the parameter is defined by the dimension. On top of that, $A(q)$ is not complex anymore and thus $A(q) = A^*(q)$ so that Eq. 2-33 can be rewritten as

$$P(q) = \Delta\rho^2 \cdot V_{\text{part}}^2 \cdot (A(q))^2 \quad \text{Eq. 2-36.}$$

Assuming that the radial density distribution function $f(r,R)$ describes a step-like course with a sharp profile of the scattering length density, $f(r,R)$ can be described by $f_{\text{core}}(r,R)$ which defines this situation by

$$f_{\text{core}}(r,R) = \begin{cases} 1 & \text{for } 0 \leq r \leq R \\ 0 & \text{elsewhere} \end{cases} \quad \text{Eq. 2-37.}$$

In the case of $f_{\text{core}}(r,R) = 1$, which is assumed for the step-like profile of the scattering length density, Eq. 2-35 simplifies again so that only the integral needs to be solved

$$\int_0^R r^2 \cdot \frac{\sin(qr)}{qr} dr = q^{-3}(\sin(qR) - qR \cdot \cos(qR)) \quad \text{Eq. 2-38.}$$

Combining Eq. 2-35, Eq. 2-36 and Eq. 2-38 it follows

$$P(q) = \Delta\rho^2 \cdot V_{part}^2 \cdot \left[\frac{3}{(qR)^3} (\sin(qR) - qR \cdot \cos(qR)) \right]^2 \quad \text{Eq. 2-39}$$

which can be solved numerically. Thereby, the scattering amplitude needs to be normalised to the particle volume since the integration in Eq. 2-38 is performed in a one-dimensional way only to an upper boundary of R and not to infinity in three dimensions. An example for a spherical droplet form factor according to Eq. 2-39 together with exemplary experimental data is shown in Figure 2.22.

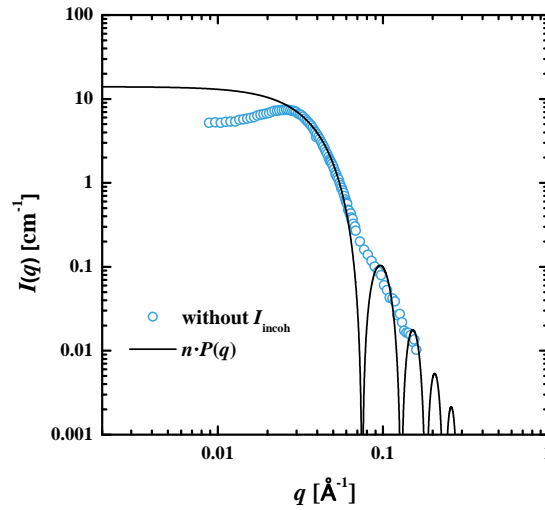


Figure 2.22: Experimental scattering data (blue circles) of a microemulsion plotted together with the sphere form factor according to Eq. 2-39. In order to plot both the data and the form factor on the same absolute scale $P(q)$ was multiplied with the particle number density n . However, the fit considerably overestimates the oscillations.

Note that the form factor $P(q)$ was multiplied with the particle number density so that the form factor at low q does not converge to 1 as it would be the case without the parameter n , $\Delta\rho$ and V_{part} .

In the case of microemulsions the particle number density can be calculated considering the molecular parameter of the surfactant. Thus, the number of surfactants can be calculated from the volume fraction of surfactants at the interface $\phi_{C,i}$ by dividing $\phi_{C,i}$ by the volume of one surfactant molecule v_C . If this value is multiplied with the area of one surfactant head group a_C then the result is the total interfacial area. Dividing this area by the surface area of one spherical micelle with radius R the particle number density can be calculated as follows

$$n = \frac{\phi_{C,i} a_C}{v_C 4\pi R^2} \quad \text{Eq. 2-40.}$$

As can be seen in Figure 2.22 the fitting function of the sphere form factor considerably overestimates the oscillations in comparison to the real experimental data. These oscillations arise from interference patterns of the scattering centres and are smeared out if the size of the scattering particles is

polydisperse rather than monodisperse. On top of that the neutron wavelength distribution and the limited spatial resolution of the detector would also smear out the oscillations even if the sample consisted of perfectly monodisperse spheres. Polydispersity effects can be taken into account by convoluting the form factor $P(q,R)$ for a monodisperse sphere with a radius R with a distribution function $W(R,R_0,\sigma)$ of the radius R around its mean value R_0 with a size distribution width σ_R resulting in

$$\overline{P(q)} = \int_0^{\infty} P(q,R) \cdot W(R,R_0,\sigma_R) dR \quad \text{Eq. 2-41.}$$

It is known that if the width of the distribution is sufficiently small compared to the radius, the shape of the chosen distribution function is of no importance regarding the effect on the size polydispersity of the fitting function [231]. Microemulsions, however, are known to have polydispersity indices $p_R = \sigma_R/R_0 \approx 0.25$ and thus the determination of the exact shape of the distribution function can be determined with high precision. Thus, it has proven feasible to apply a *Gaussian* distribution function to describe the size distribution of microemulsion droplets [139, 232-236] and the respective polydispersity by the standard deviation according to

$$W(R,R_0) = \frac{1}{\sqrt{2\pi\sigma_R^2}} \exp\left\{-\frac{(R-R_0)^2}{2\sigma_R^2}\right\} \quad \text{Eq. 2-42.}$$

Solving the integral in Eq. 2-41 leads to an expression for the polydisperse sphere form factor $\overline{P(q)}$ [141]

$$\overline{P(q)} = n \int_0^{\infty} dR P(q)W(R,R_0,\sigma) = \frac{6\pi^2 n \Delta\rho^2}{q^6} e^{-2q^2\sigma^2} (g_1 + g_2 + g_3) \quad \text{Eq. 2-43.}$$

with

$$\begin{aligned} g_1 &= [1 + q^2(\sigma^2 + R_0^2)] e^{2q^2\sigma^2} \\ g_2 &= [-1 - 4q^4\sigma^4 + q^2(-3\sigma^2 + R_0^2)] \cos(2qR_0) \\ g_3 &= [-2qR_0(1 + 2q^2\sigma^2)] \sin(2qR_0). \end{aligned} \quad \text{Eq. 2-44.}$$

A fitting function for the polydisperse sphere form factor is shown in Figure 2.23. The fitting function was calculated assuming a polydispersity index p_R of 0.25 which is a typical value for microemulsion droplets.

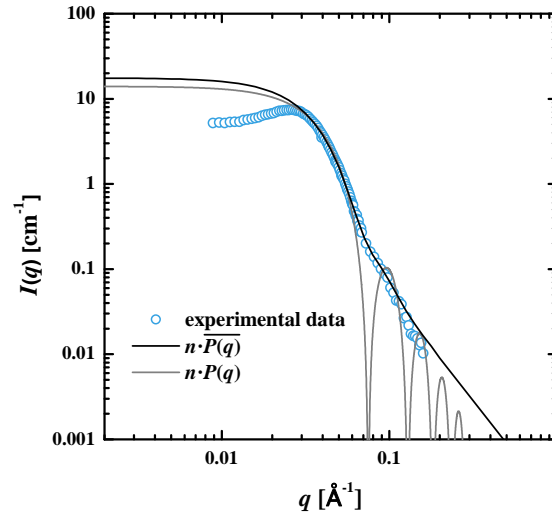


Figure 2.23: Plot of experimental data (blue circles) obtained from a microemulsion consisting of spherical droplets together with the monodisperse sphere form factor (grey line) $P(q)$ and the polydisperse sphere form factor (black line) $\overline{P}(q)$. Although $\overline{P}(q)$ describes the data satisfactorily in a medium q -range, the scattering intensity is not describe at low q and at very high q .

Although microemulsions were mentioned several times so far the sphere form factor as described in Eq. 2-41 does not sufficiently describe scattering curves obtained from microemulsion systems as shown in Figure 2.23. This is due to two things: a sharp step-like interface was assumed as well as only two different regions of scattering length densities. However, in microemulsion systems the surfactant film around a micelle contributes also to the scattering intensity by the contrast factor $\Delta\rho_{\text{film}} = \rho_{\text{bulk}} - \rho_{\text{film}}$ (see Eq. 2-28). Here, ρ_{bulk} is the scattering length density of the bulk phase or the solvent, and ρ_{film} is the scattering length density of the surfactant film. Furthermore, the assumed step-like change of scattering length density from inside to outside the particle is not correct for microemulsion droplets since the scattering length density changes slightly gradually because of hydration of the surfactant head groups, penetration of solvent molecules into the amphiphilic film and thermal fluctuations.

One model that accounts for both film and core scattering contributions of a microemulsion droplet was developed by Foster *et al.* [140]. The radial density distribution function for the microemulsion droplet $f_{\text{droplet}}(r, R)$ is defined as

$$f_{\text{droplet}}(r, R) = \frac{1}{\exp\left(\frac{r - R - \frac{d}{2}}{\chi}\right) + 1} - \frac{1 - \Delta\rho_{\text{core}}/\Delta\rho_{\text{film}}}{\exp\left(\frac{r - R + \frac{d}{2}}{\chi}\right) + 1} \quad \text{Eq. 2-45}$$

where R is the mean radius of the droplet, d is the shell thickness and χ describes the sharpness of the amphiphilic film. The scattering length density differences have been defined earlier (Eq. 2-27 and Eq. 2-28).

In contrast to the application of a Gaussian function to account for both core and shell scattering contributions as well as for the diffuse nature of the amphiphilic film this model does not separate the film and the core scattering contributions and is therefore also appropriate for contrast conditions at which the scattering length density of the film is of the order of magnitude of the one of the core, *i.e.* $\rho_{\text{core}} \approx \rho_{\text{film}} \neq \rho_{\text{bulk}}$.

Using this distribution function the scattering length density profile of the droplet is given by $\Delta\rho_{\text{droplet}}(r) = \Delta\rho_{\text{film}}f_{\text{droplet}}(r,R)$. $P_{\text{droplet}}(q)$ is obtained by Fourier transformation of $\Delta\rho_{\text{droplet}}(r)$ and is subsequently convoluted with a Gaussian size distribution function. A fitting function according to this model is shown in Figure 2.24.

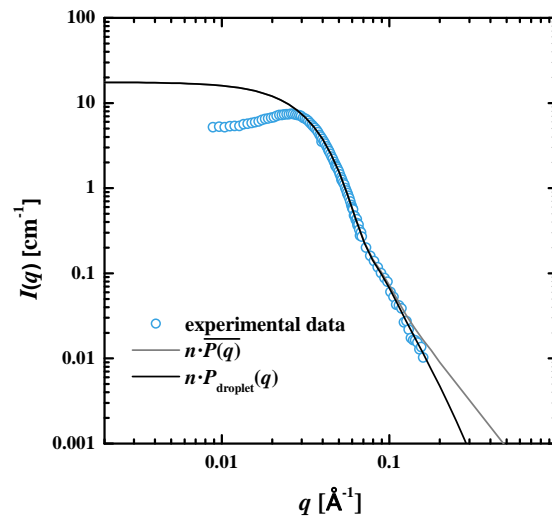


Figure 2.24: Plot of experimental data (blue circles) obtained from a microemulsion consisting of spherical droplets together with the polydisperse sphere form factor (grey line) $\overline{P}(q)$ and the polydisperse sphere form factor with diffusive interface and film scattering contribution $P_{\text{droplet}}(q)$ (black line). The scattering curve is now described satisfactorily in the medium and in the high q -range and deviates only in the low q -region from the experimental scattering intensity.

As can be seen in Figure 2.24 the scattering curve of polydisperse spherical microemulsion droplets with diffusive interface and a film scattering contribution can be described in the high and medium q -range. The fact that the fitting function still deviates considerably from the experimental data in the low q -region is due to interparticle interactions which are explained later in this section.

The free fitting parameters to describe a scattering curve according to this model are the micelle radius R_0 and its polydispersity σ_R , and the thickness d and the sharpness χ of the amphiphilic film.

This calculation cannot be performed analytically and was thus calculated numerically using MATHEMATICA 7.0™.

CYLINDRICAL DROPLET FORM FACTOR

Since the structure of microemulsion droplets is a function of composition and temperature, the structure can easily be influenced so that spherical micelles elongate for example with increasing temperature (Figure 2.6 right). In such a case, a sphere form factor is not appropriate to describe the scattering intensity and a form factor for cylindrical droplets $P_{\text{cylinder}}(q)$ has to be introduced.

Therefore, the contribution of the two different axial contributions of the round cross section $P_{\text{cross}}(q)$ and the rod scattering $P_{\text{rod}}(q)$ need to be taken into account. Furthermore, polydispersity effects naturally also occur with cylindrical droplets which is why the cylinder form factor is convoluted with a Gaussian size distribution both for the radius and the length of the droplets. The factorisation of the intensity into these two single contributions is valid if $qR \ll 1$ [140, 237]. The cylinder form factor is thus as follows

$$P_{\text{cylinder}}(q) = L_0^2 \int_0^{\infty} dL P_{\text{rod}}(q) W_L(L, L_0, \sigma_L) \int_0^{\infty} dR P_{\text{cross}}(q) W_R(R, R_0, \sigma_R) \quad \text{Eq. 2-46}$$

with L_0 being the length of the cylinder, W_R is again given by Eq. 2-42 and W_L is the polydispersity of the length of the cylindrical droplet

$$W(L, L_0, \sigma_L) = \frac{1}{\sqrt{2\pi} \sigma_L} \exp\left[-\frac{(L - L_0)^2}{2\sigma_L^2}\right] \quad \text{Eq. 2-47.}$$

The axial contribution of the rod is given by the form factor

$$P_{\text{rod}}(q) = \frac{2 \text{Si}(qL)}{qL} - \frac{4 \sin(0.5qL)}{q^2 L^2} \quad \text{Eq. 2-48}$$

under the assumption of an infinitely thin rod and by averaging over all possible orientations in space. Here, $\text{Si}(qL)$ is the sine integral function of qL .

In order to account again for both film and core scattering contributions the radial density distribution function $f_{\text{droplet}}(r, R)$ as described by Eq. 2-43 is applied to describe the scattering of the cross section $P_{\text{cross}}(q)$ of the cylinder by

$$P_{\text{cross}}(q) = \left[2\pi \Delta\rho_{\text{film}} \int_0^{\infty} dr r f_{\text{droplet}}(r, R) J_0(qr) \right]^2 \quad \text{Eq. 2-49.}$$

Here, $J_0(qr)$ is the zeroth order Bessel function of first kind. Naturally, the geometry also needs to be considered when calculating the particle number density so that Eq. 2-40 has to be rewritten to

$$n = \frac{\phi_{c,i} a_c}{v_c 4\pi R_0 (R_0 + L_0)} \quad \text{Eq. 2-50.}$$

The free fitting parameter in this case are the radius R_0 of the cross section the length L_0 of the cylinder, the respective polydispersities σ_R and σ_L , and again the thickness d and the sharpness χ of the amphiphilic film. These calculations were also performed numerically in MATHEMATICA 7.0™:

PERCUS-YEVICK STRUCTUR FACTOR

Interactions of particles with other particles which are close-by cause correlations which influence the overall scattering intensity. Thus, neutrons which are scattered by different particles can interfere so that the pure form factor description of the scattering is no longer valid, since these interactions influence the scattering intensity in the low q -range (see Figure 2.24). However, these interparticle interactions can be completely decoupled from the scattering properties of the particle itself (Eq. 2-31). Hence, the structure factor $S_{\text{HS}}(q)$ for hard spheres can be related to the Fourier transform of the direct correlation function $c(q)$ of the particles:

$$S_{\text{HS}}(q) = \frac{1}{1 - nc(q)} \quad \text{Eq. 2-51.}$$

The interparticle interactions of microemulsion droplets formulated with non-ionic surfactants can be described by a repulsive hard-sphere potential and thus the application of the Percus-Yevick structure factor is reasonable. Assuming monodisperse scattering properties the Percus-Yevick approximation [238-240] can be used to calculate $c(q)$ which leads to the following expression:

$$nc(q) = \frac{36}{x^3} \frac{(1 + 2\phi_{\text{disp}})^2}{(1 - \phi_{\text{disp}})^4} \phi_{\text{disp}}^2 [h_1 + h_2 + h_3] \quad \text{Eq. 2-52}$$

with

$$\begin{aligned} h_1 &= -2 \left[\frac{\sin(x) - x\cos(x)}{3\phi_{\text{disp}}} - \frac{4}{x^3} \right] \\ h_2 &= \frac{1}{3} \left[\left(1 - \frac{6}{x^2}\right) 4\sin(x) - \left(1 - \frac{12}{x^2} + \frac{24}{x^4}\right) x\cos(x) \right] \\ h_3 &= 2 \left[\left(\frac{2}{x^2} - 1\right) \frac{x\cos(x)}{2} + \sin(x) - \frac{1}{x} \right] \end{aligned} \quad \text{Eq. 2-53.}$$

The abbreviation $x = 2R_{\text{HS}}q$ is applied where R_{HS} is the hard-sphere radius of the particles.

However, this expression leads to strong oscillations due to the assumption of monodisperse conditions [130, 233] which cannot be found in experimental data from polydisperse systems. Hence, since interparticle interactions are also effected by polydispersity phenomena a Gaussian size

distribution $W(R_{\text{HS}}, R_{\text{HS},0}, \sigma_{\text{HS}})$ of the hard-sphere radius R_{HS} around its mean value $R_{\text{HS},0}$ is convoluted with the Percus-Yevick structure factor:

$$\overline{S_{\text{PY}}(q)} = \int_0^{\infty} dR_{\text{HS}} S_{\text{PY}}(q) W(R_{\text{HS}}, R_{\text{HS},0}, \sigma_{\text{HS}}) \quad \text{Eq. 2-54.}$$

Glatter *et al.* were able to show that the use of the averaged Percus-Yevick structure factor leads to satisfactory results for semi-diluted microemulsions [130, 241]. Convoluting the sphere form factor $P_{\text{droplet}}(q)$ with the particle number density n and the polydisperse Percus-Yevick structure factor $\overline{S_{\text{PY}}(q)}$ also the scattering intensity in the low q -region can be described satisfactorily. Thus the scattering curve is described completely (Figure 2.25).

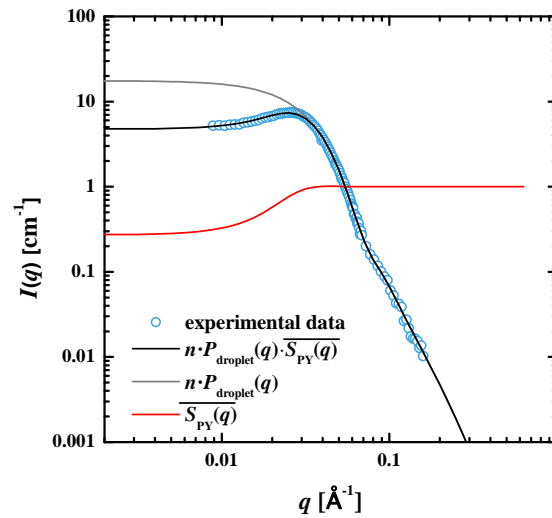


Figure 2.25: Plot of experimental data (blue circles) obtained from a microemulsion consisting of spherical droplets together with the polydisperse sphere form factor $P_{\text{droplet}}(q)$ (grey line), the polydisperse Percus-Yevick structure factor $\overline{S_{\text{PY}}(q)}$ for hard spheres (red line) and a convolution of both (black line), which finally leads to a good description of the scattering intensity over the whole q -range.

This averaged structure factor, in the following simply denoted as $S_{\text{PY}}(q)$, represents a weighted addition of the monodisperse structure factors. The free fitting parameters are the hard-sphere interaction radius R_{HS} , the polydispersity σ_{HS} and the hard-sphere volume fraction ϕ_{disp} . Its calculation was also implemented into MATHEMATICA 7.0TM.

ORNSTEIN-ZERNICKE STRUCTURE FACTOR

The Ornstein-Zernicke function is an equation which accounts for interparticle interactions such as correlation [231, 242, 243]. In terms of microemulsions the interactions described by this function are caused by critical correlations if the system is at a condition close to a critical point. It is, however, also possible to describe the correlation interactions in polymer networks. The Ornstein-Zernicke structure factor is given by

$$S_{OZ}(q) = 1 + \frac{S_{OZ}(0)}{1 + q^2\xi^2} \quad \text{Eq. 2-55.}$$

Here, especially the parameter ξ is interesting since it describes the correlation length of the scattering contribution of interest, e.g. the correlation length of critical scattering or between interacting polymer chains.

To account for scattering contributions from critical scattering in microemulsions at low q -values, the Ornstein-Zernike structure factor $S_{OZ}(q)$ can be multiplied with the Percus-Yevick structure factor $S_{PY}(q)$ and the form factor $P(q)$ if critical scattering contributions were observed. This procedure assumes once again that the factorization of the scattering intensity to its single contributions is possible. In contrast to the Percus-Yevick structure factor the Ornstein-Zernicke structure factor can directly be implemented into ORIGIN 8.5.

SPHERICAL MICROGEL PARTICLES

In order to describe the scattering data of spherical particles with and additional scattering contribution of a gel it is common to use a combination of a term which describes the contribution from the sphere and one which accounts for the scattering of the gel network. The scattering of a swollen gel can be described by a Lorentzian [62, 243]

$$I_L(q) = \frac{I_L(0)}{1 + q^2\xi_L^2} \quad \text{Eq. 2-56}$$

which is very similar to the Ornstein-Zernicke structure factor (Eq. 2-55). In order to account for the scattering contribution of the sphere the sphere form factor as described in Eq. 2-39 was convoluted with a Gaussian size distribution as described in Eq. 2-42. Using these terms together the scattering intensity of a microgel sphere can be described by

$$I(q) = I_L(q) + I_{sphere}(q) = \frac{I_L(0)}{1 + q^2\xi_L^2} + P(q) \cdot W(q) \cdot e^{-q^2t^2} \quad \text{Eq. 2-57.}$$

The term $\exp(-q^2t^2)$ enters to enable the description of the diffusivity of the scattering particle which is not included in the sphere form factor [244]. A similar approach was described by Stieger *et al.* [245]. If the particles are completely hydrated, however, it is not possible to describe the according scattering curves by means of Eq. 2-57 but a Gaussian spatial distribution $I_{Gauss}(q)$ has to be applied [246, 247] to account for inhomogeneities of within the polymer. The Lorentzian contribution $I_L(q)$ of fluctuating polymer chains has to be added to describe the scattering data in the high q -range so that it follows

$$\begin{aligned}
I(q) &= I_{sphere}(q) + I_{Gauss}(q) + I_L(q) \\
&= I_{sphere}(q) + I_{Gauss}(0) \exp\left(\frac{-\Lambda^2 q^2}{3}\right) + I_L(q)
\end{aligned}
\tag{Eq. 2-58}$$

Thereby, a combination of $I_{Gauss}(q)$, $I_L(q)$ and $I_{sphere}(q)$ leads to satisfactory descriptions of scattering data at temperatures close to a slightly below the volume phase transition temperature.

GENERALISED INDIRECT FOURIER TRANSFORMATION (GIFT)

In the limit of low particle number densities a direct relation exists between the particle and its scattering intensity by means of a Fourier transformation. The particle is mathematically represented by its pair distance distribution function which is derived in the following.

Utilising the decoupling approximation the scattering intensity can be simplified to

$$I(\vec{q}) = n \cdot P(\vec{q}) \tag{Eq. 2-59}$$

in the case of a very diluted solution. As the form factor is the complex square of the scattering amplitude it follows

$$I(\vec{q}) = n \cdot \langle A(\vec{q}) \cdot A^*(\vec{q}) \rangle \tag{Eq. 2-60}$$

where the squared brackets indicate the average over all particle orientations and particle sizes. Since the scattering amplitude is defined as the Fourier integral of the scattering length density distribution function $\Delta\rho(\vec{r})$ in Eq. 2-34 the complex square can be written as

$$A(\vec{q}) \cdot A^*(\vec{q}) = \iint_V \Delta\rho(\vec{r}_1) \Delta\rho(\vec{r}_2) \cdot \exp[i \cdot \vec{q} \cdot (\vec{r}_1 - \vec{r}_2)] d\vec{r}_1 d\vec{r}_2 \tag{Eq. 2-61}$$

Replacing $\vec{r}_2 = \vec{r}_1 - \vec{r}$ leads to

$$A(\vec{q}) \cdot A^*(\vec{q}) = \iint_V \Delta\rho(\vec{r}_1) \Delta\rho(\vec{r}_1 - \vec{r}) \cdot \exp[i \cdot \vec{q} \cdot \vec{r}] d\vec{r}_1 d\vec{r} \tag{Eq. 2-62}$$

In this equation, it is sensible to define the spatial autocorrelation function $G(\vec{r})$ which describes the correlation of the scattering centers within a single particle as

$$G(\vec{r}) = \int_V \Delta\rho(\vec{r}_1) \Delta\rho(\vec{r}_1 - \vec{r}) d\vec{r}_1 \tag{Eq. 2-63}$$

Inserting Eq. 2-63 in Eq. 2-62 leads to

$$\langle A(\vec{q}) \cdot A^*(\vec{q}) \rangle = \int_V G(\vec{r}) \cdot \exp[i \cdot \vec{q} \cdot \vec{r}] d\vec{r} \tag{Eq. 2-64}$$

Here, the autocorrelation function $G(\vec{r})$ only depends on the magnitude of $|\vec{r}|$ rather than on its direction which means that the spatial average over all orientations can be performed in one dimension and can thus be written as

$$\gamma(r) = \langle G(\vec{r}) \rangle = \left\langle \int_V \Delta\rho(\vec{r}_1) \Delta\rho(\vec{r}_1 - \vec{r}) d\vec{r}_1 \right\rangle \quad \text{Eq. 2-65.}$$

In order to calculate the scattering intensity the Fourier transformation needs to be performed on Eq. 2-64. Thereby, it is possible to perform only the one-dimensional radial-symmetric transformation since only the magnitude of $|\vec{r}|$ needs to be taken into account. Basically, this was already done to obtain Eq. 2-35 so that it follows

$$I(q) = 4\pi \cdot \Delta\rho \int_0^\infty \gamma(r) \cdot r^2 \frac{\sin(qr)}{qr} dr \quad \text{Eq. 2-66.}$$

Introducing the *pair distance distribution function* $p(r)$ by

$$p(r) = \gamma(r) \cdot r^2 \quad \text{Eq. 2-67.}$$

Eq. 2-67 can be rewritten as

$$I(q) = 4\pi \cdot \Delta\rho \int_0^\infty p(r) \frac{\sin(qr)}{qr} dr \quad \text{Eq. 2-68.}$$

where the scattering intensity $I(q)$ is defined as the one-dimensional Fourier transformation of the pair distance distribution function $p(r)$ (PDDF).

On the other hand, the PDDF can be defined as the inverse Fourier transformation of the scattering intensity $I(q)$ [248]:

$$p(r) = \frac{4\pi}{n} \int_0^\infty I(q)(qr) \sin(qr) dq \quad \text{Eq. 2-69}$$

Note that all information on size and shape of the scattering particle is now included in the PDDF. Thus, the determination of the PDDF via inverse Fourier transformation allows to directly gain information on size and basic geometry of the sample [249, 250]. It is very important to note that this way of analysing scattering intensity does *not* require to adopt a model prior to data analysis.

Structural information on the scatterer can now be obtained from the shape of the PDDF. A schematic drawing of a PDDF typical for homogeneous spheres is shown in Figure 2.26. As can be seen the PDDF of a homogeneous sphere shows a symmetric peak. The radius of the sphere can be gained from the position of the peak maximum and the maximum extension indicates the diameter of the sphere. In case of such a homogeneous sphere, the spatial resolution function $\gamma(r)$ can be interpreted as a probability function of finding the radius r within the homogeneous sphere. Thus, the probability functions starts at 0 and ends if $r > D_0$ with the maximum extension.

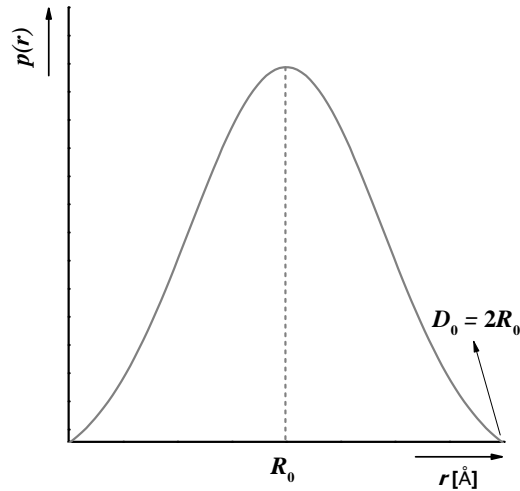


Figure 2.26: Schematic drawing of a pair distance distribution function $p(r)$ (PDDF) for a monodisperse homogeneous sphere, i.e. a sphere with only one constant scattering length density. The PDDF is a symmetric peak with its maximum at the radius R_0 of the sphere and its maximal extension at the diameter $D_0 = 2R_0$ of the sphere. The PDDF passes through the origin at $r = 0 \text{ \AA}$ and drops to zero at $r = D_0$.

The number of different distances r can be calculated by multiplying the spatial resolution function $\gamma(r)$ with the volume of a spherical shell with the radius r and the thickness dr . Thus, the number of distances can be written as

$$\gamma(r) \cdot 4\pi \cdot r^2 \cdot dr = p(r) \cdot 4\pi \cdot dr \quad \text{Eq. 2-70}$$

and therefore the pair distance distribution function $p(r)$ is directly proportional to the number of distances and can thus be seen as a distance histogram.

In the case of polydisperse particles the shape of the PDDF remains similar to the one shown in Figure 2.26. Since also distances with $r > D_0$, i.e. distances with a larger extension than the mean diameter, can be found the maximum and the maximum extension of the PDDF are shifted to higher r values.

However, if the one aims to apply the inverse Fourier transformation to the scattering intensity according to Eq. 2-69 that would require scattering data of the full q -range, i.e. $0 \leq q \leq \infty$ which is not practical for scattering experiments. Due to the limitation of the q -range strong oscillations would arise in such a direct Fourier transformation (termination effects). These can be minimised using the indirect Fourier transformation (IFT) where a limitation of the PDDF is assumed and the PDDF is smoothed, desmeared and Fourier transformed in a simultaneous process [250-252]. Thereby, the basic principle is the assumption that the scattering intensity can be approximated by a finite number of base functions. However, this method is restricted to solutions which are highly diluted so that no interparticle interactions occur, as then the scattering intensity $I(q)$ at low q -values deviates from the ideal particle form factor $P(q)$. Based on the general idea that the PDDF and hence its Fourier transform can be described by a finite number of base functions, Glatter *et al.* developed a way to analyse also scattering data with

interparticle interactions. This method is called the *Generalised Indirect Fourier Transformation* (GIFT) [253, 254]. Using the GIFT method, it is possible to determine the particle form factor $P(q)$ with a minimum of a priori information as it is also a model-free approximation. The structure factor is calculated by separating its scattering contribution from the form factor scattering by means of factorisation (decoupling approximation, see Eq. 2-31 [136]) and hence is not model-free. In this work the polydispers Percus-Yevick structure factor was applied for all calculations using the GIFT procedure [130, 241]. The form and structure factors are approximated in an iterative procedure by means of a nonlinear least-square procedure based on a Boltzmann-Simplex-Simulated-Annealing (BSSA) algorithm [254]. The a priori information which is needed for the form factor is only an upper limit of the particle size for the form factor, an estimated range for the values for the volume of the scattering particle ϕ_{disp} , the radius of the hard-sphere particle R_{HS} and its polydispersity σ_{HS} .

The assumption that the PDDF can be described by a finite number of base functions can also be applied to a subsequent numerical deconvolution of the PDDF to obtain the radial scattering length density profile of the particle. This procedure is implemented into the DECON-tool of the GIFT program package developed by Glatter and Mittelbach [255, 256]. This program only needs information on the size distribution function assumed for the particles. Both the GIFT procedure as well as the DECON tool have already been applied to microemulsions under normal pressure [130] as well as under high pressure [34].

2.4.5 The stroboscopic high pressure SANS cell

STATE OF THE ART: SCATTERING EXPERIMENTS AND PRESSURE JUMPS

Scattering experiments at elevated pressure have been performed with soft condensed matter systems for several years, both with X-rays and neutrons [36, 257-262]. Thereby, also setups for simultaneous measurements of X-ray and light have been developed [263]. For X-ray scattering experiments two articles on different pressure-jump devices were published in 1999 and 2000 by Steinhart *et al.* [264] and Woenckhaus *et al.* [265], with two different sample holders. Steinhart *et al.* prepared special drawings and had the sample cell manufactured by Nova Swiss, whereas Woenckhaus *et al.* seem to have had support from their departmental workshop. While Steinhart *et al.* use Beryllium windows which are commonly used for high-pressure X-ray experiments Woenckhaus *et al.* use diamond windows which allow application of higher pressure (10000 bar compared to 3500 bar). The sample volumes can be reduced to 0.1 mL in the cell designed by Woenckhaus and even to 30 μL in the Steinhart cell. The high-pressure network of these cells is very similar. In both systems, water is used as a pressurising medium, and the sample is separated from this by a Teflon piston. The pressure is transmitted from a pressure reservoir to the sample by opening the relevant valves. The high pressure

is generated by a hydraulic hand-pump (Woenckhaus) or by a pressure generator (Steinhart). While Woenckhaus *et al.* can apparently perform only one pressure jump at a time, Steinhart *et al.* are able to repeat the pressure jump experiment up to 10 times without entering the experimental hutch. After that, however, the water reservoir needs to be refilled. One other setup for a pressure jump with a dead time smaller than 5 ms was presented by Winter *et al.* who, however, only perform one pressure jump and do not have the option for fast repetitions [266].

The situation with neutron scattering, however, is very different, since there is no report of a pressure jump apparatus for SANS apart from the cell [56] which is described in the next section.

STROBOSCOPIC HIGH-PRESSURE SANS CELL

The stroboscopic high-pressure SANS cell was developed to enable pressure jumps with adjustable amplitude, a high frequency and a high number of possible repetitions. The basic idea of this cell is to implement a metal bellow (see Figure 2.27) into the sample volume which can be elongated and shrunk by controlling it from outside. This change of size results in a change of pressure since the volume of the sample is changed.

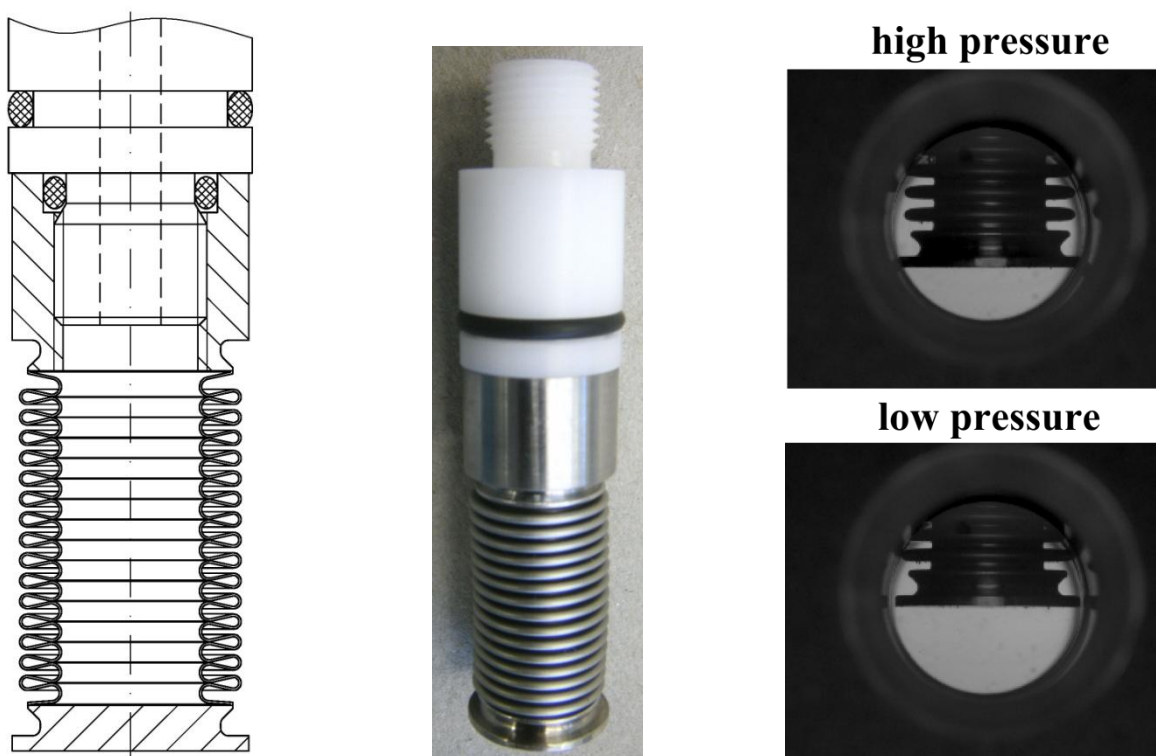


Figure 2.27: *Left:* Technical drawing of the metal bellow with the crinkles around it. The short dashed lines from the top indicate the internal tube of hydraulic oil which is connected to the hydraulic pump. *Middle:* Photography of the metal bellow together with the plastic connection. The black ring is a sealing. At the very top the winding is visible which provides the connection to the tubing filled with hydraulic oil. *Right:* Photographs of the bellow in an extended state (top), applying high pressure to the sample volume, and in a shrunk state (bottom), transferring a lower pressure.

The inside of the bellow is connected to the hydraulic pump, as indicated in Figure 2.27 left by the short dashed line. The pump can provide two different pressures up to 500 bar. Pump and bellow are separated by pneumatic valves which allow to separately apply different pressures. Thus, by opening the first valve a higher pressure can be applied to the sample because the pump transfers hydraulic oil into the bellow, causing it to elongate and thus increasing the pressure inside the sample holder. After closing the first valve the second valve can be opened which connects to the second lower pressure of the pump. Thus, the higher pressure of the sample shrinks the bellow, leading to a flow of hydraulic oil back into the pump. After closing valve two the cycle can be repeated as often as desired. The pressure cycle can be adjusted by means of a software program implemented into *LabView*. The valves are switched via a pneumatic setup, i.e. using a fast impulse of pressurised air. Thus, pneumatic and hydraulic circuit are inextricably intertwined but have to be treated separately. Both circuits and their crossover points are shown in Figure 2.28.

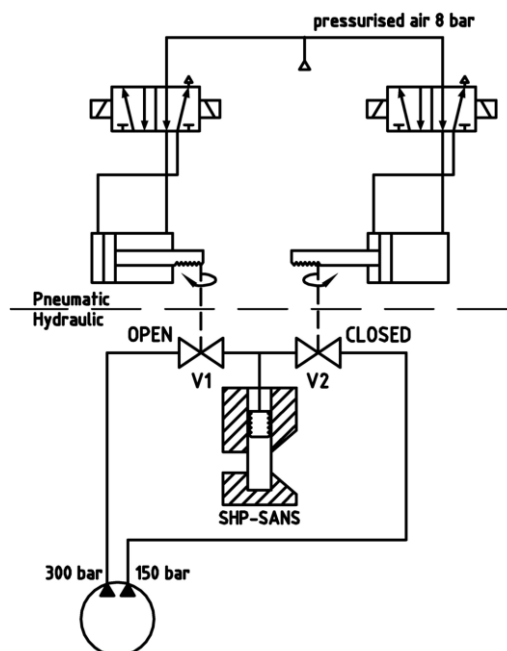


Figure 2.28: Technical sketch of the pneumatic (top half) and the hydraulic circuits (bottom half) of the SHP-SANS cell. The pressures are provided by the hydraulic pump (circle at the bottom). The pneumatic valves are operated with pressurised air at 8 bar. The SHP-SANS cell and the bellow are shown schematically below the valves V1 and V2. Prepared by the internal mechanical workshop.

Since pump and sample holder cell are heavy and bulky a specially modified rolling table is used to handle the whole setup, which is shown in Figure 2.29. This table is used to move the cell and handle it at all times at which the cell is not in the neutron beam. A specially designed holding, mounted on top of the table, on which the cell is fixed with four screws enables to turn the cell overhead. This is used during the filling procedure as well as for homogenisation of the sample. The table also provides the necessary proximity of cell and pump. As the pump heats up very fast a water bath which is used for cooling is placed next to the pump. For the same purpose a set of two fans is attached to the pump.

The house-in build membrane reservoir which is used for transferring CO₂ at controlled pressure to the cell can also be placed on top of the table.

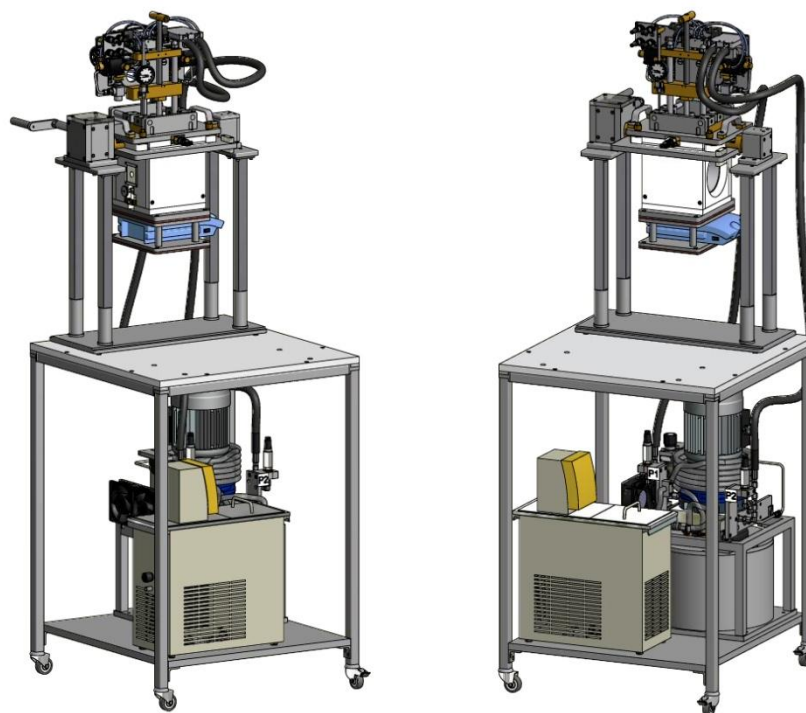


Figure 2.29: Schematic drawing of the SHP-SANS cell together with the immediate equipment. Thus, the SHP-SANS cell is placed at the holding which allows to turn the sample head over. The blue device mounted below the cell is a stirring plate. The piston and the valves are at the top of the cell. The black, flexible tubes connect to the hydraulic pump which is fixed at the lower level of the table. To prevent heat damage of the pump a thermostat is used for cooling. Prepared by the internal mechanical workshop.

Beside the surrounding equipment of the stroboscopic high pressure SANS cell the sample holder is of course always in the focus of attention. A cross section of the SHP-SANS cell is shown in Figure 2.30. Here, also the neutron beam (red) is brought to attention, because it is important that the cell has a conical shape at the side of the cell at which the neutrons exits the sample volume to allow the scattered neutrons to travel to the detector without being scattered at the sample holder. The metal block surrounding the sample volume is furrowed by canals which allow to connect the metal block to an external water bath and thus to precisely control the temperature of the sample. The pressure inside the sample volume is connected by a diaphragm to a pressure sensor. The sample volume has two entrance sites: one via the valve at the bottom of the cell (left hand side, lower part in Figure 2.30) which is used for filling liquid CO₂ into the cell, and the cylindrical opening at the top of the cell which is sealed by the tunable piston in Figure 2.30. This piston also enables to adjust the pressure of the sample independent of the bellow.

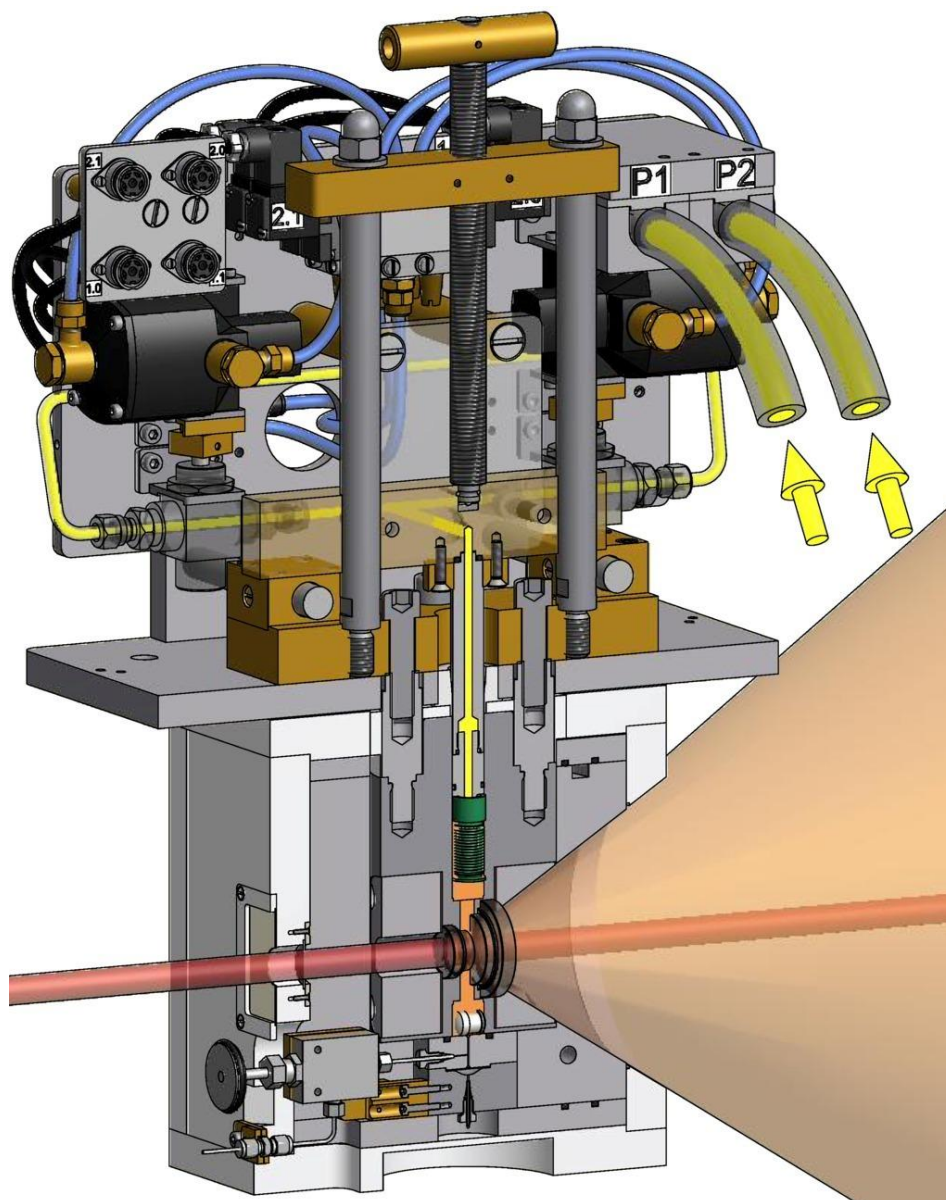


Figure 2.30: Cross section through the SHP-SANS cell (designed by the internal mechanical workshop). The sample volume is marked in orange. Implemented into the sample volume is the bellow (green) which is the key component for pressure jumps. The neutron beam (red) enters the cell on the left hand side and is partially scattered at the sample volume. Due to the conical shape of the cell at the right hand side scattered neutrons can travel to the detector undisturbed by the cell. The sapphire windows which seal the sample volume provide high neutron transmission. The upper part of the setup displays the valves (black boxes) and the tunable piston. The connection from bellow to valves is highlighted in yellow. The yellow arrows at the right indicated the transition to the hydraulic pump.

2.4.6 Data recording for kinetic measurements

Since a variety of different counting methods were used in this work this chapter gives an overview of the different counting methods. Kinetic data collected at the D11 instrument were acquired using the Kinetic Mode, while D22 data usually are ListMode data. The results are, however, the same.

A schematic drawing of the general course of data acquisition is shown in Figure 2.31. The ILL generally uses digital pulse processing systems. This drawing, however, shows only the way the data travel through the system, and does not show the complexity of applications with high timing accuracy and the difficulties which arise if an accurate synchronisation of several devices is necessary.

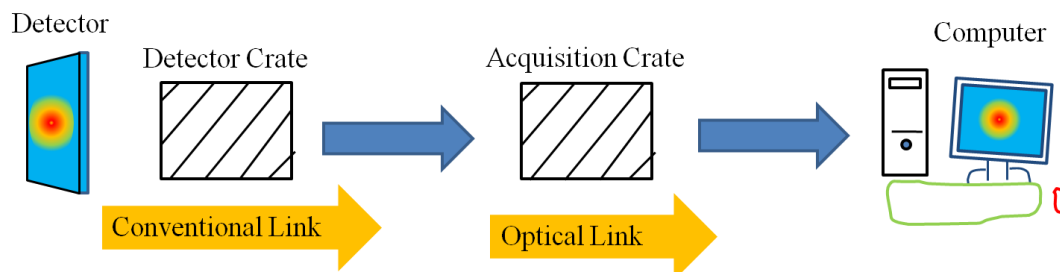


Figure 2.31: Schematic drawing of data acquisition at ILL. The neutrons are counted at the detector and the according data are processed by the detector crate. In order to obtain both a numerical and a graphical representation of the events at the detector a second processing at the acquisition crate is necessary.

COUNT AND REPEAT

Probably the simplest way to collect data with a time resolution is to enter a count command in the instrument control software with a measurement time of for example 1 s and repeat the command 60 times. Thus, the kinetic measurement runs for 60 s with a time resolution of 1 s. This procedure, however, can only be applied for strong scattering samples with a minimum time resolution of 1 s.

KINETIC COUNT

This mode is used if it is possible to change the condition of the sample reversibly and periodically and is therefore also suitable for weak scattering samples. It needs to be distinguished between the electronic control of the sample and the one of the instrument. Besides pressure jump experiments also stopped-flow experiments or setups with oscillating magnetic fields can be measured with this mode.

In order to control the pressure cycle and thus the sample condition six parameters have to be defined prior to the experiment. The first two are of course the two pressures p_{high} (at V1) and p_{low} (at V2) for the pressure cycles. They can be adjusted manually and are read out by the *LabView* software. The opening time of the valves can also be controlled via *LabView* (see chapter 2.4.5). The system automatically runs through the following commands: open V1, close V1, open V2, close V2. Thereby, the duration of each of the steps needs to be defined in the *LabView* software. The software will repeat this cycle until the user disconnects the software from the sample cell. Together with the signal “open V1” the electronic system releases a trigger signal for the instrument to start counting.

Regarding the instrument control, the user first has to generate a setup file that determines the number of slices n_s and the time of each slice t_s (i.e. the time resolution), as well as the number of repaints. Thus, the duration of the counting time t_{count} is calculated by the software by $t_{\text{count}} = n_s \cdot t_s$. Multiplying

t_{count} with the number of repaints gives the time of the whole experiment. The cycle is repeated with every trigger signal. A schematic drawing of a time line of such an experiment is shown in Figure 2.32. Note that it is also possible to choose logarithmic distances between the segments n_s .

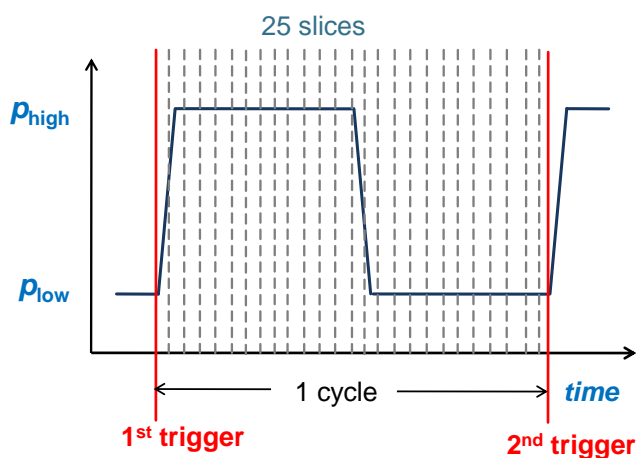


Figure 2.32: Schematic drawing of the course of a kinetic SANS experiment in which the kinetic mode is used. A trigger signal starts both the sample cycle (here exemplary for a pressure jump cycle) and the counting cycle of the detector. The time width and the number of slices are defined before the start of the experiment. Once the counting cycle is finished the detector waits for the next trigger to start the second counting cycle.

Figure 2.33 shows a photograph of the box which contains all electronic control cards which are necessary for a experiment using KineticMode. The four pin inlets at the right which are marked 1.1, 1.0, 2.1 and 2.0 must be connected to the according site at the cell because here the signals to open valve 1 (1.1) and close valve one (1.0) are released. The two inlets P1 and P2 are connected to the pressure control system at the hydraulic pump so that the pressures there can be read out via laptop. `START` and `STOP` mark the positions of the switch in which the experiment is either running or stopped. The `TRIGGER OUT` connection is a BNC-outlet which can be connected to the trigger cable of the instrument while the pressure cycle is controlled by the opening and closing of the respective valves.

To process data collected in KineticMode either GRASP [267] or LAMP [268] can be used.



Figure 2.33: Photograph of the control box for KineticMode measurements. The four pin connections at the left release the signals `open` and `close` for the valves. The inlets P1 and P2 connect to the hydraulic pump to read out the pump pressures via laptop. The inlet marked TRIGGER OUT releases the trigger signal to the SANS instrument. The four black cables at the bottom are power supplies, the two beige ones connect to the laptop to transfer the valve opening times and to read out the pump pressures. The switch starts or stops the experiments.

LIST MODE COUNT

The great advantage of ListMode over KineticMode is that it is not necessary to define the time resolution of the experiment in advance, but the time resolution can be chosen any time after the experiment. During a ListMode count each neutron arriving at the detector is saved with information on its position on the detector and with its time of arrival relative to the last trigger signal. Thus, the data can be regrouped after the experiment with any desired time resolution.

The electronic procedure is very similar as the one describe for KineticMode. The trigger can either be given by the sample control software together with the command for the first valve to open or by the instrument. ListMode counts, however, generate an enormous amount of data.

Data analysis can to date only performed with BerSANS [269] which was programmed by U. Keiderling, Berlin [270].

2.4.7 Time Involved Small Angle Neutron Scattering Experiments (TISANE)

THE INSTRUMENTAL SETUP

Additionally to the setup shown in Figure 2.19 the setup for TISANE measurements requires the presence of a double chopper to pulse the neutron beam. A chopper was installed at the D22 instrument at the Institute Laue-Langevin, Grenoble, France (see Figure 2.34).

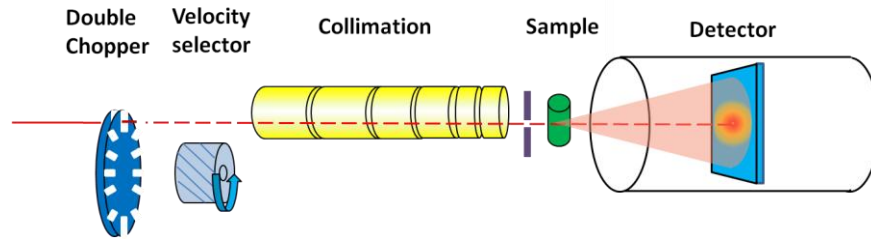


Figure 2.34: Schematic setup of the D22 spectrometer for small angle neutron scattering. In contrast to the setup shown in Figure 2.19 the continuous beam of neutrons passes is the double chopper (left, dark blue). This, however, only happens if the positions of the windows of the rotating chopper disks allow for the neutrons to pass. A lot of neutrons get caught by one of the chopper discs, and the intensity of the remaining beam is pulsed after the chopper. Since a broad wavelength distribution is an integral part of the TISANE principle the velocity selector (light blue) is no longer used. The collimation (yellow) and the detector (bright blue) remain unchanged compared to the standard setup.

Neutron choppers are rotating mechanical devices which have the purpose of blocking the neutron beam for specific time intervals. The chopper system which is installed at D22 was designed and manufactured by Astrium [271]. It consists of a double chopper system in a vacuum tight housing which is equipped with neutron windows made of aluminium foil on each side of the housing. The drive units which are used to rotate the chopper disks are equipped with motors and spindles with active magnetic bearings in all axes. An image of the housing is shown in Figure 2.35.

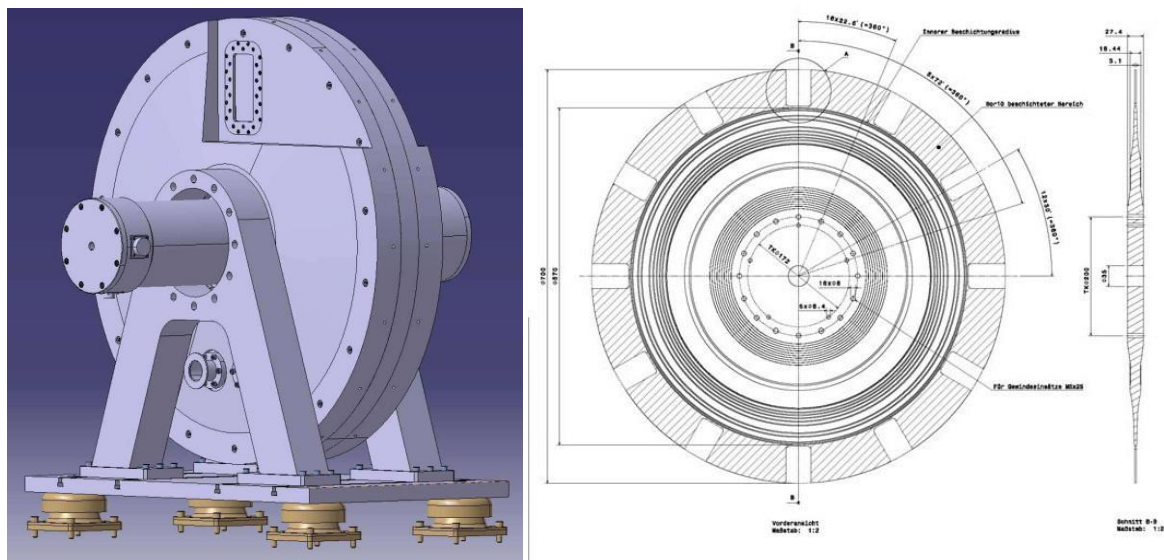


Figure 2.35: *Left:* Rendered picture of the vacuum tight chopper housing with neutron windows (top) and the axes which induce rotation (standing out at front and back). *Right:* Mechanical drawing of one chopper disk with 12 marginal openings (windows). Taken from [271].

Figure 2.35 right shows a mechanical drawing of a chopper disk which have an outer diameter of 700 mm and 12 windows the size of 42 x 57 mm. The disks can be rotated clockwise as well as counter clockwise with a maximum speed of 20000 rpm with a phase resolution of 0.01°.

THE TISANE PRINCIPLE AND FREQUENCY CONDITION

The TISANE principle was first presented time by Gähler and Golub [272], but the first to find an appropriate application for this method were Wiedenmann *et al.* [273] who monitored the magnetic moments of nanoparticles in an oscillating magnetic field with this technique.

The enormous potential of TISANE lies in its time resolution in the range from ms to μ s which is an improvement of two orders of magnitude while simultaneously not losing more than one order of magnitude of intensity compared to common neutron scattering setups. This is facilitated because TISANE makes use of the frame overlap of neutrons caused by wavelength distribution instead of accepting frame overlap as the limiting factor for time resolution. The wavelength distribution in typical time resolved SANS measurements is $\Delta\lambda/\lambda = 0.1$, which means that the time resolution at a detector distance of 20 m is limited to about 5 ms [274].

Following the TISANE principle, the key aspect is the broad wavelength distribution of a pulsed white neutron beam. In addition, TISANE requires a device which modulates the scattering properties of the sample periodically. Given these experimental condition the TISANE principle can be concluded from Figure 2.36. The distance between chopper and sample is thereby abbreviated with L_{CS} and the one between sample and detector with L_{SD} .

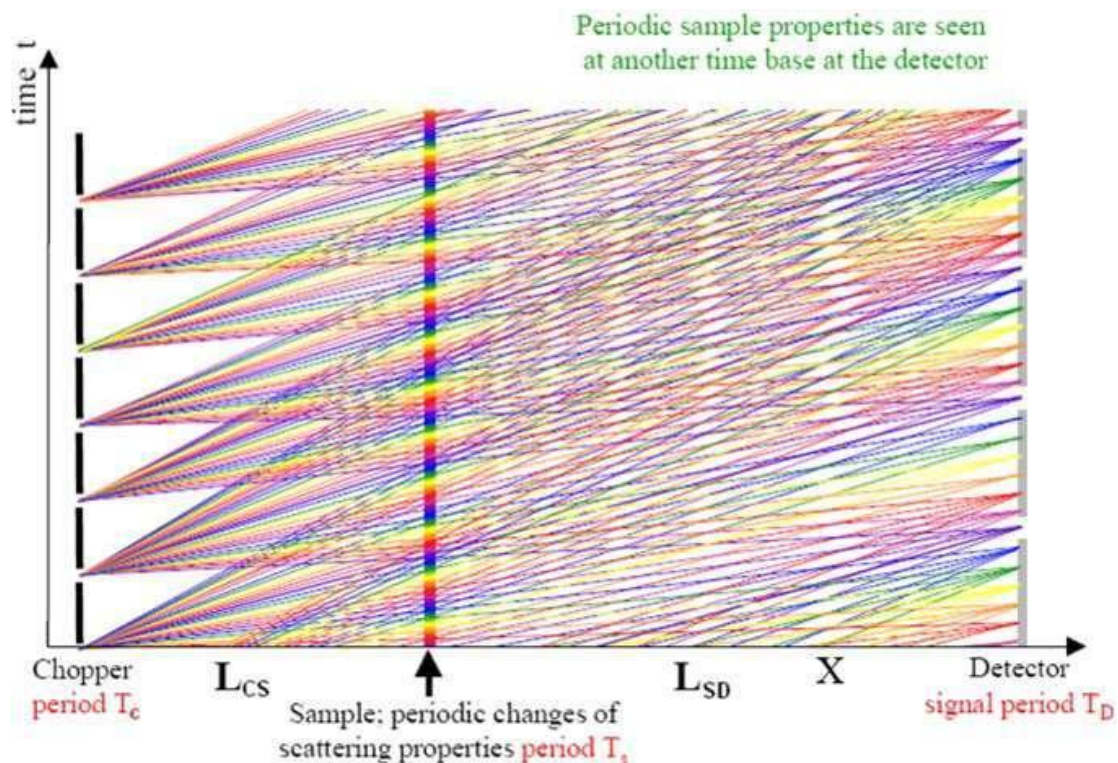


Figure 2.36: Plot of time versus distance for a TISANE experiment at a SANS instrument. The chopper (left) pulses the neutron beam with a time period T_c . The neutron beam has broad wavelength distribution. At the distance L_{CS} from the chopper the scattering properties of the sample are periodically modulated, as indicated by the periodic change of colours which represent certain scattering properties. After a certain distance L_{SD} at which the detector is placed the colours and thus the neutrons rearrange in such a way that all neutrons of one detector interval have seen the same state (colour) of the sample. Taken from [57].

Starting at the very left in Figure 2.36 the chopper pulses the neutron beam with a period time T_C . Although the pulse itself is very narrow in time, the neutron beam diverges on its way to the sample considerably because of the wavelength distribution of the neutrons. Thus, fast neutrons arrive at the sample earlier than slow neutrons, so that the beam is continuous again when passing the sample. The scattering properties of the sample change periodically at a time T_S . After passing through the sample the neutrons rearrange again according to their velocity. This time, however, if the frequencies and distances of the experiment are matched exactly, the neutrons rearrange according to the sample condition they have seen. Observing the detector counts at the required times T_D means that within one time frame of the detector only neutrons arrive which have all passed the same sample condition.

Thinking this through for an exemplary neutron this means that a slow neutron from a pulse x passes the sample at the sample pulse y and is detected in the detector cycles z . Another neutron which is also detected during this detector cycle z but is much faster than the first one saw the same sample state but in the sample cycle $y+1$, i.e. one sample cycle later. Although this sample cycle occurred later on the time scale than the first one the different velocity of the neutrons makes it possible for both to arrive at the detector at the same time. Consequently, the fast neutron probably passed the chopper in during the cycle $x+2$ which has an even wider time gap to the neutron pulse in which the first neutron passed the chopper. This principle is called frame overlap and is also explained graphically in Figure 2.37.

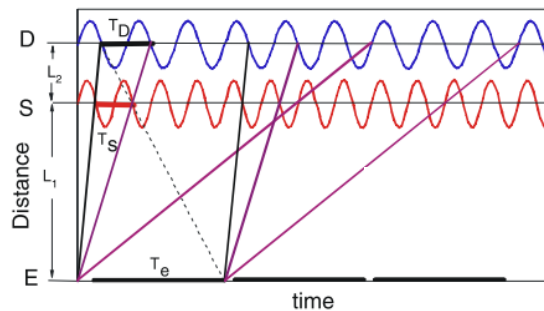


Figure 2.37: Plot of the distances in a TISANE experiment versus time. The waves indicate the different frequencies of sample and detector, while the openings in the bold black line at the x-axis represent the chopper pulses. As can be seen, neutrons from different chopper pulses which probe the same state of the sample arrive at the same respective time channel at the detector if all frequency and distance conditions are obeyed.

In order to evaluate the distances and frequencies for the TISANE experiment the detector distance at which the colours in Figure 2.36 reorder can be calculated according to

$$\frac{T_S}{T_C} = \frac{L_{SD}}{L_{CD}} \quad \text{Eq. 2-71.}$$

and

$$\frac{T_D}{T_S} = \frac{L_{CD}}{L_{CS}} \quad \text{Eq. 2-72.}$$

Here, the letter L_i represents the distance between the sample (S), the detector (D) and the chopper (C), whereby L_{CS} is a constant instrument parameter. As already described in Figure 2.36 the letter T indicates the cycle times of the respective part of the experiment. From these equations the TISANE frequency condition can be deduced:

$$f_D = f_S - f_C \quad \text{Eq. 2-73}$$

with

$$f = \frac{2\pi}{T} \quad \text{Eq. 2-74.}$$

The letter f indicates the frequency of the devices. Considering this and applying the intercept theorem it follows

$$f_C L_{SD} = (f_S - f_C) L_{SD} \quad \text{Eq. 2-75.}$$

Regarding a real experiment it is the sample-to-detector distance and thus the q -range which is determined first. The chopper frequency is then adjusted to L_{SD} and the intended sample frequency.

The higher time resolution and the fact that the loss of intensity compared to static measurements is only one order of magnitude are the major advantages of TISANE over other time resolved techniques. Although the chopper prevents a big fraction of the neutron beam from passing, the loss of intensity can mostly be compensated by moving the velocity selector out of the beam.

TISANE COUNT

The implementation into the electronic system is very different from the one described for the Kinetic Mode. The most important device in a TISANE setup is the chopper. At the start two marked windows are positioned in such a way that the neutron beam can pass. If the chopper disks rotate this position is reached again with a frequency f_C which releases the trigger signal for the other parts of the experiment. Thus, the chopper is the `master` of the experiment. The trigger signal is released to two frequency generators which connect to the sample environment and to the detector. While the detector frequency can be implemented into the instrument control software the sample environment needs to be controlled separately. As it is of high importance that all frequencies are kept exactly throughout the experiment all frequencies are continuously compared to a 10 MHz signal. Experimental results of this mode are discussed in chapter 3.3.

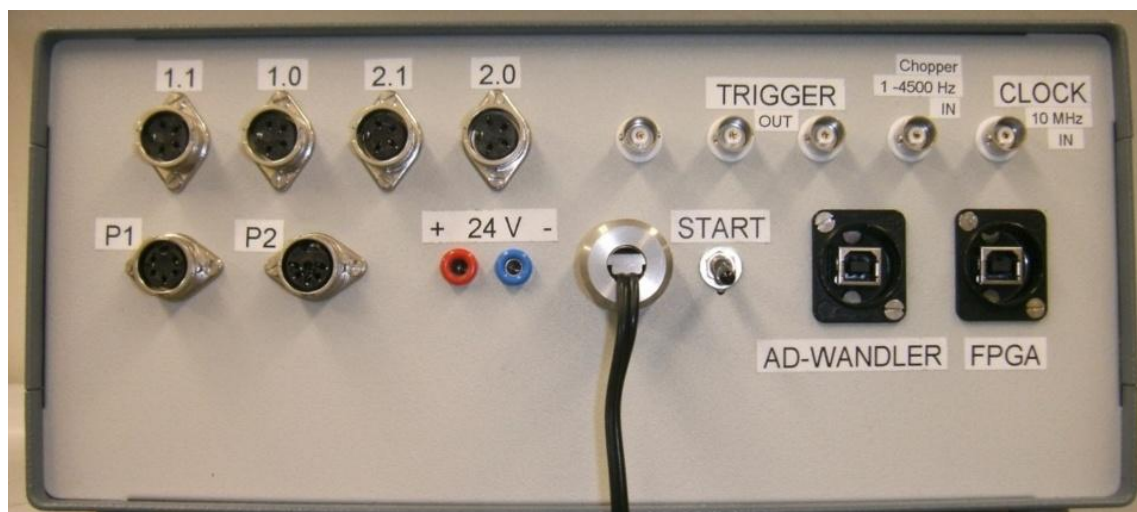


Figure 2.38: Photograph of the electronic control box which is used for TISANE experiments. Here, the BNC inlet marked `CLOCK` is connected to a frequency generator which gives out a frequency of 10 MHz for synchronisation. Left of the CLOCK socket is the connection site for the BNC cable which transfers the trigger signal to the pressure cell. In order to be able to record the ingoing trigger signal the `TRIGGER OUT` connections were established. Although the experiment is started by the chopper trigger signal the pressure cell can be disconnected from this system by the start switch. At the left hand side are the connections to the valves and the hydraulic pump as described in the previous section.

The electronic control box for a TISANE experiment as shown in Figure 2.38 is very similar to the one shown in Figure 2.33 as there are the four connections to the valves which control the commands `open` and `close` of the valves V1 and V2 as well as the two connections to the pressure control of the hydraulic pump. Starting at the right hand side, however, a connection for a BNC-cable exists which is to be connected to a frequency generator which generates a continuous signal of 10 MHz. Since all other signals are synchronised according to this signal the frequency generator is called external clock. The BNC-connection left to the clock connects to the chopper system which releases the trigger signal to trigger the pressure cycles. In order to be able to record the trigger signal together with the pressure there are two positions at which a connection to an oscilloscope can be established. For safety reasons the switch allows to disconnect the pressure cell from the chopper and instrument system.

Since TISANE experiments are conducted with ListMode data analysis can to date only be performed with BerSANS [269].

2.5 Light scattering

A general setup for a light scattering experiment is shown in Figure 2.39. The laser provides coherent and monochromatic light. The sample solution is inside a cylindrical cuvette which is placed inside a toluene bath. Toluene has the same refractive index as glass and is therefore used as an index matching bath. The incident beam is scattered and reflected when it meets the index bath and not when it meets the sample cuvette which prevents disturbing signals.

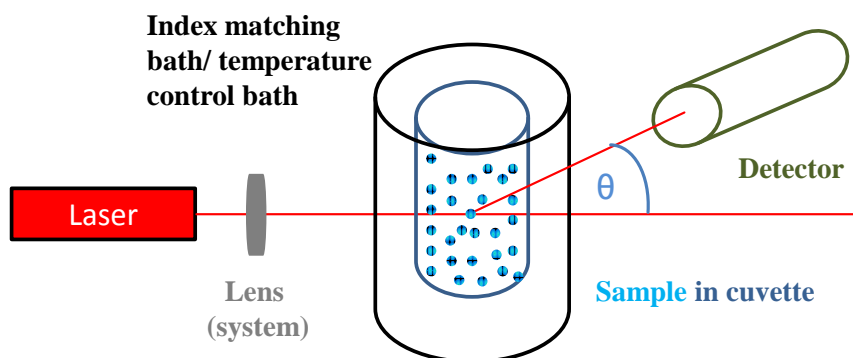


Figure 2.39: Schematic setup of a light scattering device. The sample particles in solution are inside a special light scattering cuvette which is placed in an index matching bath. It also provides temperature control. While most of the light is transmitted a fraction of the light is scattered and can be detected. A lens is used to focus the light beam onto the sample.

The lens (or the lens system) has to be focussed on the exact middle of the sample cuvette. The detector also needs to be focussed onto this spot. Furthermore, the detector and the incoming light have to be exactly on the same level.

The quality of focussing can be controlled by a plot of the absolute scattering intensity versus angle. To obtain a straight line the scattering volume needs to be considered. Considering that the laser is not a line but a beam with a distinctive volume it follows that also the detection does not “see” only one point of the sample solution but a certain volume. This is shown schematically in Figure 2.40.

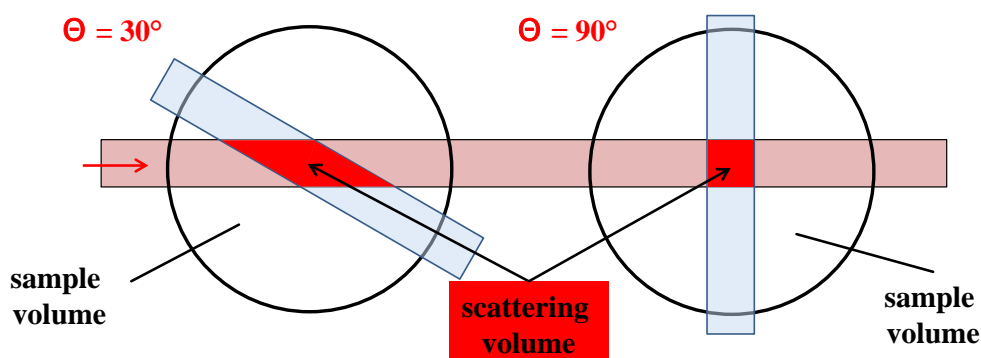


Figure 2.40: Schematic drawing of the scattering volume for the case of $\theta = 30^\circ$ (left) and $\theta = 90^\circ$ (right). As can clearly be seen the scattering volume is higher in the case of $\theta = 30$ and thus needs to be corrected.

Considering the scattering volumes different angles as shown in Figure 2.40 the intensity needs to be corrected by multiplying it with $\sin(\theta)$ with θ in radian measure. Since the scattering volume at $\theta = 90^\circ$ is the smallest all other scattering intensities are compared to this one. The correction term here is $\sin(90^\circ) = \sin(1.57079633) = 1$. For 30° and 150° the scattering volume is twice as big as the one at 90° , thus it follows that $\sin(30^\circ) = \sin(150^\circ) = \sin(2.61799388) = 0.5$. After correction of the scattering volume the scattering intensity should be the same for all angles. If this is the case the instrument is properly focussed.

2.5.1 Dynamic light scattering

Dynamic Light Scattering (DLS) measures the fluctuations of the scattering intensity as a function of time and relates this to the size of the particles. These fluctuations occur because of Brownian motions which have their origin in random density fluctuations of the solvent. These fluctuations lead to collisions of solvent molecules and particles. The movements can be described by a three-dimensional random walk model. Thereby, the mean square distance which is covered by a particle because of Brownian motion has a linear dependence to the time of movement t [275].

The Brownian motions cause fluctuations in intensity for various reasons. First, particles diffuse in and out of the scattering volume, so that the absolute number of scattering particles and thus also the scattering intensity varies. Second, the particles change their relative positions towards the other particles which leads to a change of the interference pattern (Doppler effect). This is shown graphically in Figure 2.41 left.

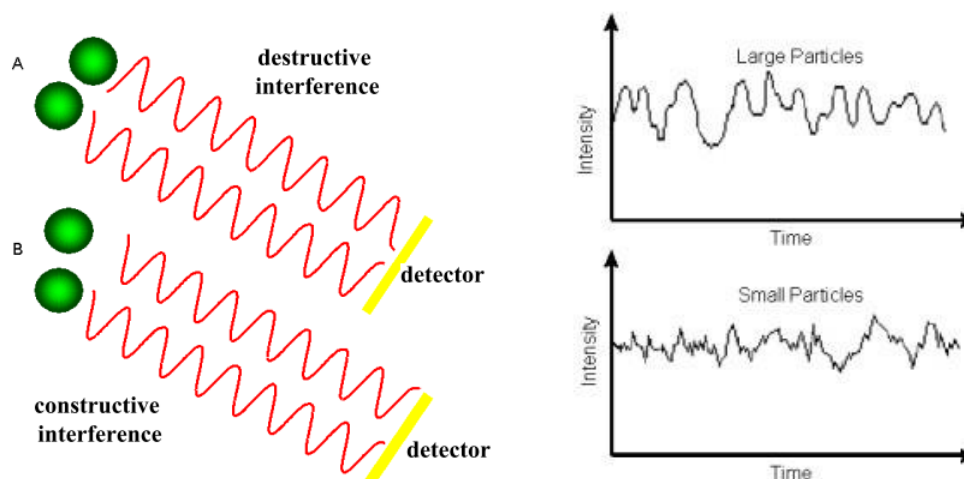


Figure 2.41: *Left:* Different possibilities of interferences which occur due to Brownian motion. *Right:* The recorded scattering intensity fluctuates with time because of Brownian motions. Thereby, fluctuations have a higher frequency for small particles because they move faster than large particles. Taken from [276].

In order to analyse the intensity fluctuations the intensity is correlated. Therefore, the intensity is recorded in time intervals Δt which are in the range from nano- to microseconds and thus small compared to the time scale of the fluctuations. Dividing the measurement time t_M into N intervals Δt it follows

$$t_M = n_s \cdot \Delta t \quad \text{Eq. 2-76.}$$

The correlation is basically a comparison of the scattering intensity at the time t $I(t)$ and the intensity at the time $(t + \tau)$ $I(t + \tau)$ where τ is the delay time and is usually chosen in logarithmic intervals according to

$$\tau = n\Delta t \text{ with } 0 \leq n \leq n_s \quad \text{Eq. 2-77.}$$

The intensity-time-autocorrelation function can be calculated applying

$$\langle I(t) \cdot I(t + \tau) \rangle \cong \frac{1}{t_M} \sum_{t=0}^{t_M} I(t) \cdot I(t + \tau) \Delta t \quad \text{Eq. 2-78.}$$

Eq. 2-78 sums up the intensities for all intervals Δt and normalises these to the measurement time by dividing the sum by t_M . Naturally, the correlation has a higher impact for short delay times whereas the correlation of different scattering particles for greater delay times loses in significance. Considering Figure 2.41 it can be seen that the difference of $I(t)$ and $I(t + \tau)$ is very small for short delay times τ so that the approximation $I(t) = I(t + \tau)$ is valid for $\tau \rightarrow 0$ s. The autocorrelation function is thus given by the mean squared intensity $\langle I(t)^2 \rangle$. For high τ values, however, intensities are similar so that the autocorrelation function is given by the square of the mean intensity $\langle I(t) \rangle^2$. Following this, the autocorrelation function decreases monotonically from $\langle I(t)^2 \rangle$ to $\langle I(t) \rangle^2$ with increasing delay time τ . This is shown graphically in Figure 2.42.

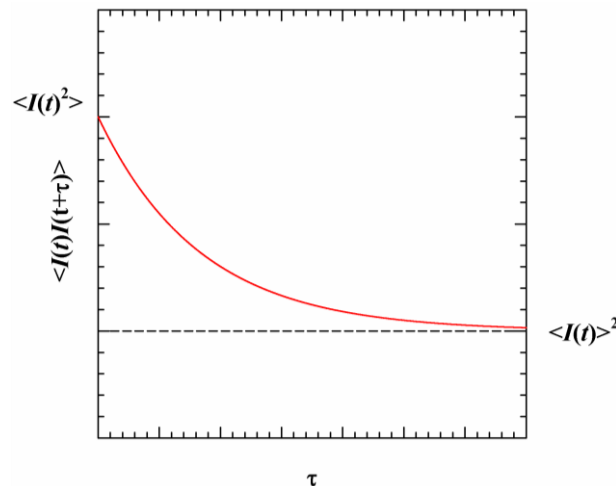


Figure 2.42: Shape of the intensity-time-autocorrelation function $\langle I(t) I(t + \tau) \rangle$ as a function of the delay time τ . For $\tau \rightarrow 0$ s the autocorrelation function can be compared to the mean squared intensity. With increasing delay time the autocorrelation function approaches the squared mean intensity as correlations become weaker. Taken from [277].

If the number of intervals t_M is high enough the sum in Eq. 2-78 can be approximated by an integral. Dividing such a function by the squared mean intensity $\langle I(t) \rangle^2$ leads to the normalised intensity-time-autocorrelation function $g_2(\tau)$

$$g_2(\tau) = \frac{\langle I(t) \cdot I(t + \tau) \rangle}{\langle I(t) \rangle^2} = \frac{\frac{1}{t_M} \int_{t=0}^{t_M} I(t) \cdot I(t + \tau) \Delta t}{\langle I(t) \rangle^2} \quad \text{Eq. 2-79.}$$

Since light is a wave which causes an electrical field the normalised field-time-autocorrelation function $g_1(\tau)$ is used in light scattering experiments

$$g_1(\tau) = \frac{\langle E(t) \cdot E(t + \tau) \rangle}{\langle E(t) \cdot E(t) \rangle^2} \quad \text{Eq. 2-80}$$

because the intensity is proportional to the amplitude of the electric field $E(t)$. The two autocorrelation functions are connected by the Siegert relation which is described as

$$g_2(\tau) = B_1 + \beta_G g_1(\tau)^2 \quad \text{Eq. 2-81.}$$

The parameter β_G is a geometry factor and is equal to 1 if the electric field amplitude $E(t)$ has a Gaussian distribution. The parameter B_1 can be described as the value of the autocorrelation function at infinite delay times τ and is also equal to 1 for an optimal experimental geometry.

In order to extract information on the particle size and shape the $g_1(\tau)$ function can be used which is also connected to the inverse relaxation time Γ by

$$g_1(\tau) = e^{-\Gamma\tau} \quad \text{Eq. 2-82.}$$

Γ is connected to the translational diffusion coefficient D by the Landau-Placzek relation

$$\Gamma = Dq^2 \quad \text{Eq. 2-83}$$

where q is the scattering vector according to Eq. 2-22, multiplied with the refractive index of the solvent. In the case of spherical particles the diffusion coefficient is inversely proportionate to the hydrodynamic radius R_h according to the Stokes-Einstein relation

$$D = \frac{k_B T}{6\pi\eta_s R_h} \quad \text{Eq. 2-84}$$

where k_B is the Boltzmann constant, T is the temperature and η_s is the viscosity of the solvent. Describing the autocorrelation function $g_1(\tau)$ by a single exponential function according to Eq. 2-82 is, however, not possible in reality since scattering particles are never perfectly monodisperse. Thus, the $g_1(\tau)$ function is described by a number n of exponential functions which are weighted by the factor γ_i according to the quality of the description of the exponential function. This can be described mathematically by

$$g_1(\tau) = \sum_{i=0}^n \gamma_i e^{-\Gamma_i \tau} \quad \text{Eq. 2-85.}$$

Each weighting factor γ_i corresponds to one inverse relaxation time Γ_i and thus also to one hydrodynamic radius $R_{h,i}$ of the distribution of different radii.

One way to analyse such set of weighted autocorrelation functions is the cumulant method which can be seen as an expansion of the autocorrelation function

$$\ln(g_1(\tau)) = -\kappa_1\tau + \frac{1}{2!} \kappa_2\tau^2 - \frac{1}{3!} \kappa_3\tau^3 + \dots \quad \text{Eq. 2-86.}$$

The first cumulant parameter κ_1 gives the mean diffusion coefficient $\langle D \rangle = \kappa_1/q^2$ which can be used to calculate the hydrodynamic radius according to Eq. 2-84. The second cumulant parameter $\kappa_2 = (\langle D \rangle^2 - \langle D^2 \rangle)q^4$ gives quantitative information on the polydispersity. This analysis, however, can only be used for systems with polydispersities smaller than 20%. A more general application is provided by the CONTIN analysis in the course of which the $g_1(\tau)$ function is Laplace transformed and thus also gives information on the mean diffusion coefficient and the polydispersity of the particles.

2.5.2 Dynamic light scattering under high pressure

Performing DLS under high pressure (HPDLS) is in most cases only possible for a limited number of angles, for example one [278, 279], three [280] or five [281] angles. In all of these cases each angle requires a single sapphire window which is the main reason why the number of angles is restricted. The five angle device constructed by Kermis *et al.* [281] can only host this comparably high number of angles because the windows are attached at both sides of the laser beam, where it is very common to use only one hand side to detect the scattered light.

In this work, a HPDLS device is presented which is capable of measuring an arbitrary number of angles between 30° and 150° . For this setup an optically cut sapphire disk with an outer diameter of 2.5 cm and an inner diameter of 1 cm is implemented into a Brookhaven light scattering device.

The basic setup is very similar to the one shown in Figure 2.40 just that a toluene bath cannot be realised and the laser meets the sapphire disc directly. This does not provide a problem since the laser passes through the disc for 1.25 cm before hitting the sample. All reflections and refractions are thus unlikely to be detected. A photograph and a technical drawing of this setup are shown in Figure 2.43.

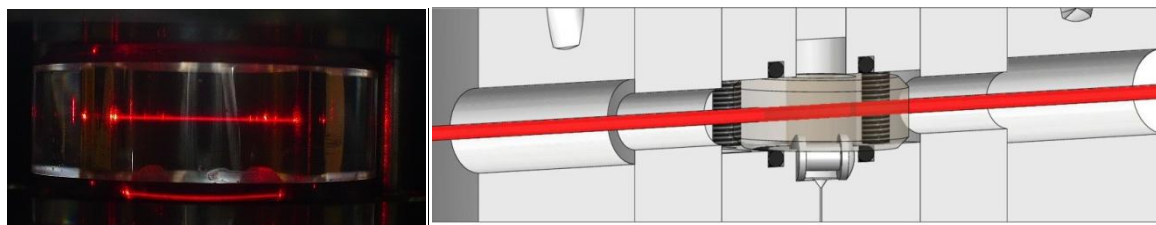


Figure 2.43: *Left:* Photograph of the laser beam passing through a sample of polymer particles for 1 cm. The sample container is a sapphire disk. A magnetic stirrer can be seen at the bottom. *Right:* Technical drawing of a cross-section through the device, prepared by the internal mechanical workshop. The sapphire disk is shown in light grey.

2.5.3 Static Light Scattering

Static light scattering (SLS) analyses the absolute intensity in form of the average over the measurement time. In contrast to the DLS setup shown in Figure 2.39 SLS setups do not contain a correlator. Sample holders have an average diameter of 3 cm and the sample concentration is usually lower than for DLS. Since the absolute intensity is of interest here it is even more important that the device is focussed correctly.

In order to extract information on the structural size of the particles the q -dependence of the excess Rayleigh Ratio $R(q)$ of dilute solutions is found which is defined as

$$R(q) = \frac{S_{\text{sample}}(q) - S_{\text{solvent}}(q)}{S_{\text{standard}}(q)} R_{\text{standard}} \quad \text{Eq. 2-87}$$

where $S_i(q)$ are the scattering intensities of sample, solvent and standard and R_{standard} is the known Rayleigh Ratio of a standard, usually toluene with $R_{\text{toluene}, \lambda = 633 \text{ nm}} = 1.35 \cdot 10^{-3} \text{ m}^{-1}$. Using $R(q)$ for Zimm plots information on the radius of gyration R_G can be found because $R(q)$ is related to the weight average molar mass M_W , the second virial coefficient A_2 and the root-mean-square radius of gyration $\langle R_G^2 \rangle^{1/2}$ or simply $\langle R_G \rangle$ according to [282]

$$\frac{Kc}{R(q)} \cong \frac{1}{M_W} \left(1 + \frac{1}{3} \langle R_G^2 \rangle q^2 \right) + 2A_2C \quad \text{Eq. 2-88}$$

where K is the contrast factor which is defined as

$$K = \frac{4\pi^2 n^2}{N_A \lambda^4} \left(\frac{dn}{dc} \right)^2 \quad \text{Eq. 2-89.}$$

Here, N_A is Avogadro's number, λ is the laser wavelength and n is the refractive index of the solvent. The parameter dn/dc describes the refractive index increment of the sample. If one is only interest in R_G this value can be determined by a linear fit to a plot of $1/R(q)$ versus q^2 according to

$$\frac{1}{R(q)} \cong \frac{1}{R_{q=0}} \left(1 + \frac{q^2 R_G^2}{3} \right) \quad \text{Eq. 2-90}$$

which is valid and independent of the particle shape at $qR_G \leq 1$. If, however, a large angular dependence is observed Zimm's approximation is no longer valid as the slopes and intercepts close to zero cause large uncertainties in finding R_G . In such a case the Guinier approximation can be used [283]

$$\ln R(q) = \ln R_{q=0} - \left(\frac{q^2 R_G^2}{3} \right) \quad \text{Eq. 2-91}$$

as an alternative to Eq. 2-90 to extract R_G from strongly angular dependent scattering data.

3 Cyclohexane as hydrophobic additive to supercritical fluorinated microemulsions

3.1 Microstructure of CO₂/cyclohexane-microemulsions with fluorinated surfactants

Since fluorinated surfactants are expensive and non-biodegradable, the direction of research has changed as to finding ways to lower the degree of fluorination or replace fluorinated surfactants completely. Examples of surfactants which have been extensively investigated regarding their effectiveness to form CO₂-microemulsions are fluorinated sulfosuccinate surfactants [170, 284, 285], phosphate surfactants [166, 286] and numerous self-designed surfactants [287, 288]. A very interesting study was presented by Sagisaka *et al.* who performed a systematic study on the influence of the tail length of various double-tail anionic surfactants, finding that the highest amount of water can be solubilised with a tail length of 12-14 Å [289]. Different molecular structures with low fluorine content have been investigated by Mohamed *et al.*, indicating that a double-branched sodium sulfate surfactant is very appropriate for the formulation of microemulsions with supercritical CO₂ [290]. In this chapter, another approach to reduce the necessary amount of fluorinated surfactant will be introduced.

3.1.1 Phase behaviour

In previous experiments it was found that the partial replacement of CO₂ by cyclohexane considerably reduces the amount of surfactant in balanced fluorinated CO₂ microemulsions [29, 52]. This was briefly discussed in the introduction chapter (chapter 1, Figure 1.1 left). To explain this unexpected effect a concentration gradient of cyclohexane in a CO₂/cyclohexane swollen micelle was postulated, which is shown graphically in Figure 1.1 right. Thereby, the repulsive interactions between cyclohexane and fluorinated surfactant tails are postulated to lead to a depletion zone of cyclohexane close to the amphiphilic film. These interactions likely reduce the monomeric solubility of surfactant in CO₂, which is about 11% and therefore rather high [34]. Although more surfactant is available at the interface in this case this effect is too low to explain the enormous increase of efficiency.

In order to determine whether a depletion zone of cyclohexane within the micelle develops a systematic contrast variation study using Small Angle Neutron Scattering (SANS) was performed. Using the *Generalised Indirect Fourier Transformation* (GIFT) procedure it is possible to extract the scattering length density distribution which revealed the substructure within a CO₂/cyclohexane swollen micelle.

However, the structures in a $T(\gamma)$ -section close to the efficiency point are known to be of bicontinuous

nature [35, 291] and are not appropriate to investigate sphere-like micelles. Hence, the phase behaviour was investigated in a $T(w_B)$ section through the phase prism (see Figure 2.3 right). The phase behaviour is shown in Figure 3.1 for the system brine – CO₂/cyclohexane – Zonyl FSO 100/ Zonyl FSN 100 at a constant water-to-surfactant ratio $\gamma_a = 0.08$ with $\gamma_a = m_{\text{surfactant}} / (m_{\text{surfactant}} + m_{\text{water}})$. Note that in the following the parameter β_i

$$\beta_i = \frac{m_{\text{cyclohexane}}}{m_{\text{CO}_{2,i}} + m_{\text{cyclohexane}}} \quad \text{Eq. 3-1}$$

will be used instead of β (Eq. 2-10). Here, $m_{\text{CO}_{2,i}}$ is the mass of CO₂ which is inside the micelle, i.e. the total mass of CO₂ minus the mass which is dissolved monomerically in the hydrophilic phase. Thus, the system without cyclohexane is shown in Figure 3.1 left and the system in which 20 wt% CO₂ were replaced by cyclohexane is shown at the right hand sight.

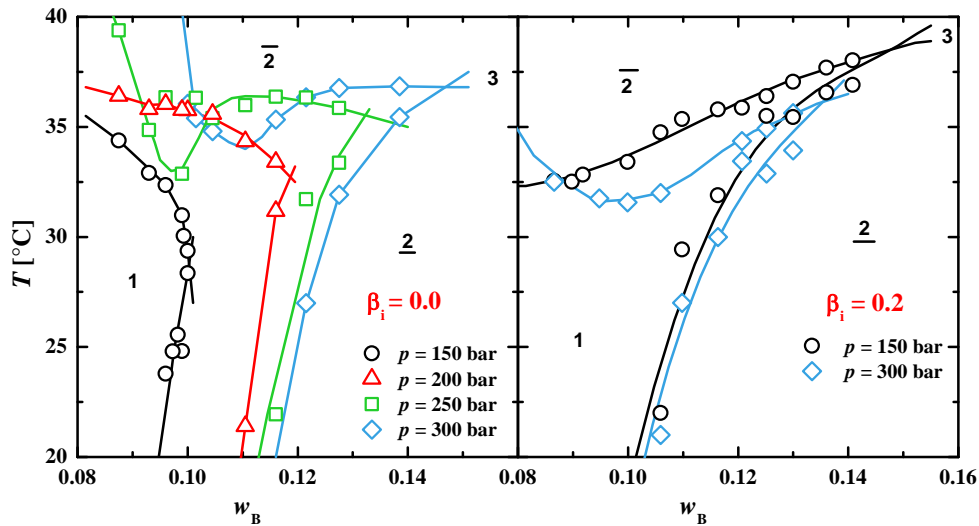


Figure 3.1: $T(w_B)$ -section of the system brine – CO₂ – Zonyl FSO 100/ Zonyl FSN 100 at $\gamma_a = 0.08$, $\delta_{\text{FSN}} = 0.75$, $\epsilon = 0.01$ and different pressures. The ability to solubilise CO₂ increases considerably with pressure (left). *Right:* Upon replacing 20 wt% of CO₂ by cyclohexane the extent of the one-phase region at $p = 150$ bar is similar to the one at $p = 300$ bar, i.e. almost the same amount of oil can be solubilised [29, 53].

The shape of the phase boundaries is analogous to that of water-rich microemulsions formulated with non-ionic surfactants and liquid oils [107, 115, 292, 293]. The microemulsion coexists with a CO₂ excess phase at low temperatures ($\underline{2}$) and with a water excess phase at high temperatures ($\bar{2}$). An extended one-phase region can be found between those states, until the maximum amount of CO₂ $w_{B,\text{max}}$ that can be solubilised is reached. The value of $w_{B,\text{max}}$ can be increased by increasing pressure. At higher w_B values a three phase region can be found, where the microemulsion coexists both with a water and a CO₂ excess phase. The emergence of the so-called loop or minimum of the upper phase boundary at $p = 250$ and 300 bar indicates that the mixture undergoes a change from weakly (no loop) to strongly (pronounced loop) structured [115] with increasing pressure. The lower phase boundary (oil emulsification failure boundary, *oefb*) ascends monotonically with the weight fraction w_B of CO₂ [113, 114]. The strong curvature of the

amphiphilic film around CO₂ at low temperatures leads to spherical, CO₂-swollen micelles in water [107, 121, 124] (see also chapter 2.1.3).

Upon the addition of cyclohexane to this microemulsion system the general phase sequence remains the same. However, the maximum amount of hydrophobic substance, *i.e.* CO₂ and cyclohexane, increases, especially at $p = 150$ bar. Here, the value for $w_{B,\max}$ at $\beta_1 = 0.2$ is almost equal for $p = 150$ bar and 300 bar.

3.1.2 Systematic SANS contrast variation

In order to probe the postulation illustrated in Figure 1.1 right a systematic small angle neutron scattering contrast variation study on the system H₂O/D₂O/NaCl – CO₂/cyclohexane – Zonyl FSO 100/Zonyl FSN 100 at $\gamma_a = 0.08$, $\delta_{\text{FSN}} = 0.75$, $w_B = 0.10$ and $T = 20^\circ\text{C}$ was performed. These measurements were carried out at the D11 instrument in Grenoble, France.

First, to determine the exact scattering length density of the technical-grade surfactants, a contrast variation of the binary mixture brine – Zonyl FSO 100/Zonyl FSN 100 at $\delta_{\text{FSN}} = 0.75$ and $\gamma_a = 0.08$ was performed, beforehand. The scattering of nine samples with different ratios of H₂O/D₂O in brine were recorded. The scattering curves are shown in Figure 3.2 left.

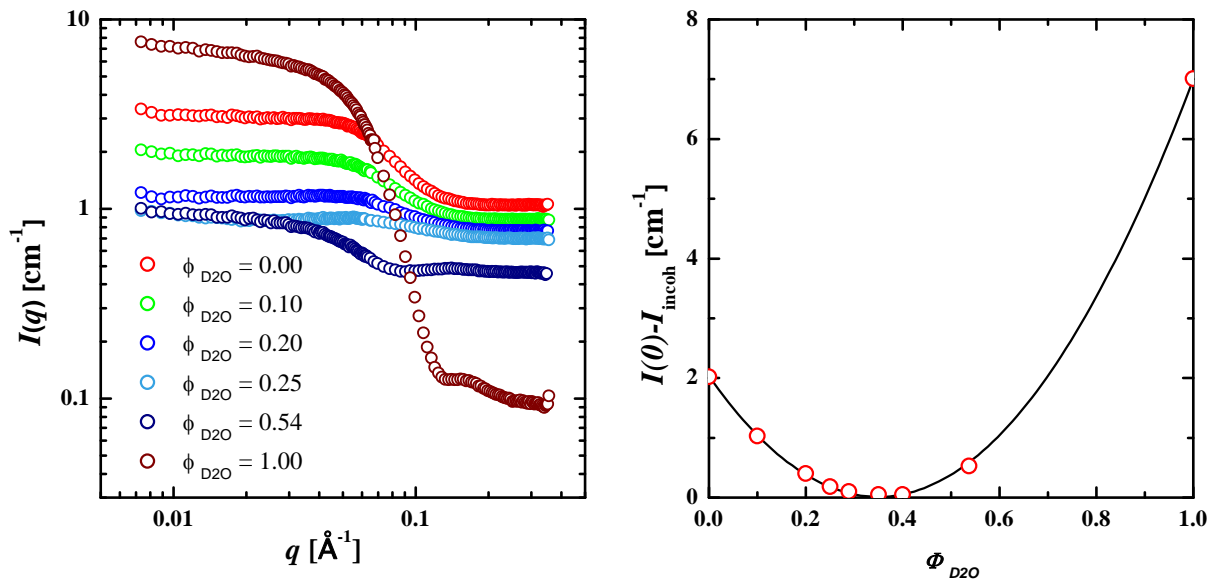


Figure 3.2: *Left:* Six out of nine scattering curves with different volume fractions of D₂O. Note that, as expected, I_{incoh} decreases with increasing $\phi_{\text{D}_2\text{O}}$. *Right:* Plot of the scattering intensity (with subtracted I_{incoh}) against the volume fraction of D₂O. The minimum of the polynomial fit is at $\phi_{\text{D}_2\text{O}} = 0.35$ [53].

To analyse the data the incoherent scattering I_{incoh} was subtracted from the forward scattering intensity, extrapolated towards $q = 0 \text{ \AA}^{-1}$ and plotted as a function of $\phi_{\text{D}_2\text{O}}$ (Figure 3.2 right). The scattering intensity reached a minimum at $\phi_{\text{D}_2\text{O}} = 0.35$, which means that the scattering length density of the surfactants is $1.84 \cdot 10^{10} \text{ cm}^{-2}$. This is slightly lower than the results of Klostermann *et al.* [34].

With the exact knowledge of the scattering length density of the surfactants four different contrast conditions on the microemulsion system were applied. A scheme of the applied contrast conditions is shown in Figure 3.3.

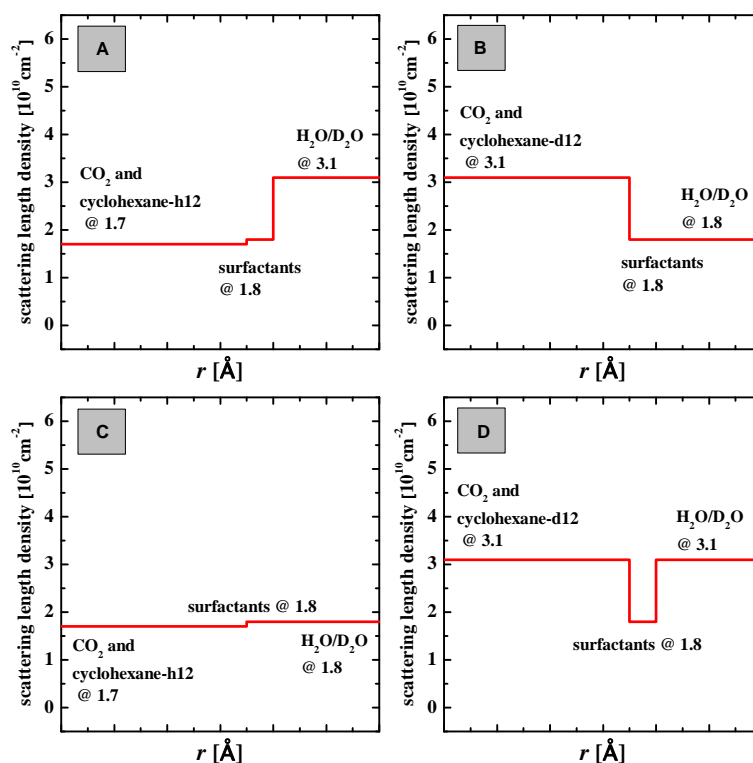


Figure 3.3: Schematic drawing of the four different contrast conditions discussed in this work, assuming a homogeneous hydrophobic phase. The scattering intensity of contrast A represents the whole micelle, whereas at the second contrast condition (B) only the hydrophobic phase contributes to the scattering intensity. The third contrast C was aimed to match all three scattering length densities. Film contrast condition was intended in contrast D. All calculations assume a temperature of 20°C and $p = 150$ bar [53].

All scattering length densities shown in Figure 3.3 in were calculated assuming that water dissolves 4 wt% of its own weight of CO_2 and that 4 wt% of the surfactants are solved in the hydrophobic phase. This is a rather low monomeric solubility of the fluorinated surfactants in the CO_2 /cyclohexane mixture since in pure CO_2 11 wt% are dissolved [34]. Thereby, the influence of pressure was neglected for both trends. Furthermore, for the calculation of the core SLD a homogeneous distribution was assumed, although this is in contradiction to the hypothesis. The scattering length densities of all used components are shown in Table 3-1 for a better overview. Except for the SLD of the surfactants all values were calculated using the NIST scattering length density calculator [224].

Table 3-1: Overview of the scattering length densities of the different compounds used for the calculation of the contrast conditions. The SLD of all components except the surfactants were calculated using the NIST scattering length density calculator.

compound	scattering length density [10^{10} cm^{-2}]
H ₂ O	-0.56
D ₂ O	6.34
surfactants	1.84
CO ₂ @ 150 bar, 20°C	2.31
cyclohexane-h12	-0.28
cyclohexane-d12	6.61

Protonated cyclohexane-h12 was used in contrast condition A, leading to a scattering length density of $1.7 \cdot 10^{10} \text{ cm}^{-2}$ of the mixture of CO₂ and cyclohexane. This is very similar to the scattering length density of the surfactants. The SLD of the bulk was adjusted to be $3.1 \cdot 10^{10} \text{ cm}^{-2}$, using a volume fraction $\phi_{\text{D}_2\text{O}} = 0.54$ in the H₂O/D₂O mixture. Applying this contrast condition, the hydrophobic phase as well as the surfactant film contribute to the total scattering intensity $I(q)$.

In contrast to that, the second contrast condition (B) was applied to achieve only core scattering contributions. Therefore, deuterated cyclohexane-d12 was used instead of protonated cyclohexane. The core SLD was estimated to be $3.1 \cdot 10^{10} \text{ cm}^{-2}$ at 20°C and 150 bar. The scattering length density of the bulk was adjusted to match that of the surfactants by mixing H₂O and D₂O at $\phi_{\text{D}_2\text{O}} = 0.35$.

In order to assess the quality of the matchings, at the third contrast (C) both the core and brine composition were chosen to match the scattering length densities of the surfactants. For this contrast condition protonated cyclohexane-h12 and $\phi_{\text{D}_2\text{O}} = 0.35$ was applied.

The fourth contrast condition (D) is the so-called film contrast condition, which is especially sensitive to scattering length densities. Here, only the amphiphilic film contributes to the total scattering intensity $I(q)$ if the SLD of core and bulk are the same. Thus, deuterated cyclohexane-d12 was used in combination with $\phi_{\text{D}_2\text{O}} = 0.54$, adjusting both SLDs to $3.1 \cdot 10^{10} \text{ cm}^{-2}$. As the scattering intensity is proportional to the volume of the scattering substance and the volume fraction of the surfactant at the interface is around 5%, the scattering intensities here are expected to be rather low.

The according scattering curves together with the fitting functions using the form factor for polydisperse spheres $P_{\text{droplet}}(q)$ (Eq. 2-45) in combination with the polydisperse Percus-Yevick structure factor $S_{\text{PY}}(q)$ (Eq. 2-54) are shown in Figure 3.4. Note that the incoherent scattering background was subtracted from the scattering curves at $p = 100, 150$ and 200 bar.

The scattering curves of the contrast conditions A, B and C show the typical features found for polydisperse spherical droplets recorded at bulk contrast condition and in the limit of a

comparatively low particle number density. Thus, the scattering intensity is constant at low q -values and changes over to a steep q^{-4} -dependence with increasing q . The oscillations of scattering intensity at $q \approx \pi/R$ are smeared by droplet polydispersity.

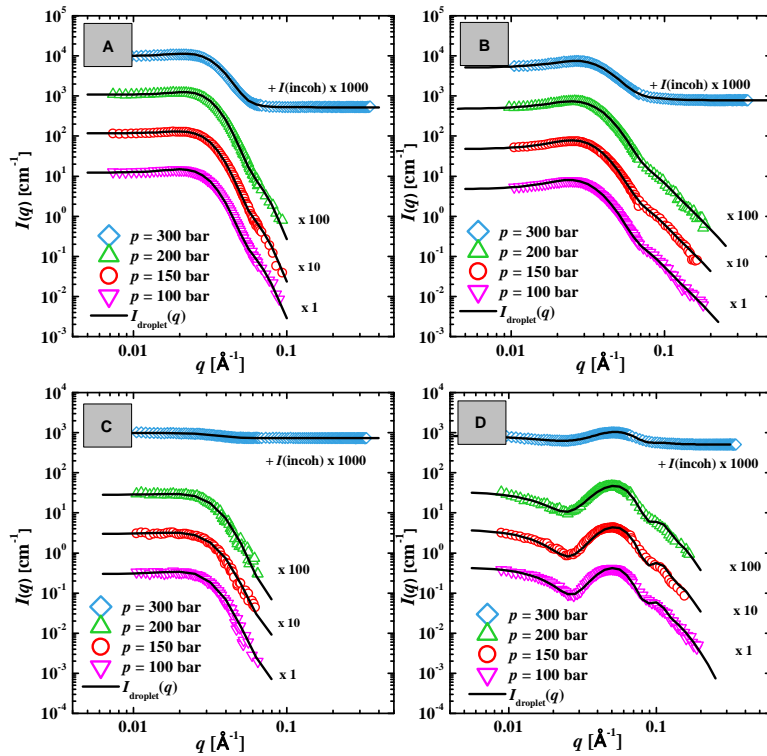


Figure 3.4: Small angle neutron scattering curves of the microemulsion system brine – CO₂/cyclohexane – Zonyl FSO 100/ Zonyl FSN 100 at $w_B = 0.10$, $\delta_{\text{FSN}} = 0.75$, $\gamma_a = 0.08$, $\beta_i = 0.2$, $T = 20^\circ\text{C}$, different pressures and the contrast conditions shown in Figure 3.3. The incoherent scattering contribution I_{incoh} was subtracted for the scattering curves recorded at 100, 150 and 200 bar. The full lines represent fitting functions using the droplet form factor $P_{\text{droplet}}(q)$ for polydispers spheres, convoluted with the Percus-Yevick structure factor $S_{\text{PY}}(q)$. Except for small but systematic deviations in contrast D the experimental scattering curves are described quantitatively [53].

The scattering intensity I_0 at $q \rightarrow 0$ strongly depends on the scattering contrast. For similar absolute values of $\Delta\rho_{\text{core}}$, as in contrast conditions A and B, the forward scattering is also similar, because the scattering intensity I_0 at $q \rightarrow 0 \text{ \AA}^{-1}$ strongly depends on the scattering contrast at similar number densities. In contrast to that, the scattering intensity at contrast conditions C and D is lower by one order of magnitude because either the scattering contrast or the volume fraction which contributes to the scattering intensity is lower. However, after subtraction of $I_{\text{incoh}}(q)$ from the scattering curves the scattering curves also for the conditions with low forward scattering show the typical q^0 and q^{-4} dependences. At film contrast condition D the oscillation at intermediate q -values becomes considerably more pronounced.

3.1.3 Data evaluation I: Model-dependent analytical fitting functions

The form factor $P_{\text{droplet}}(q)$ (Eq. 2-45) and the Percus-Yevick structure factor $S_{\text{PY}}(q)$ (Eq. 2-54) are suitable to describe the scattering intensity almost quantitatively over the entire q -range for all scattering curves shown in Figure 3.4. Small but systematic deviations can be observed in the q -region slightly higher than the oscillation, especially at contrast condition D. Here, the description of the scattering curve seems to overestimate the oscillation, indicating that the used radial density distribution function is not completely suitable to describe the distribution of CO₂ and cyclohexane qualitatively. This will be discussed in the following section.

The point of a contrast variation study is to keep the composition and temperature and thus the structure constant while varying the neutron contrast condition. The constant structure is displayed in the scattering data by constant values of hard sphere interaction radius R_{HS} and the constant polydispersity $\sigma_{\text{HS}}/R_{\text{HS}}$ compiled in Table 3-2. Here, the values obtained from the Percus-Yevick structure factor for different contrast conditions are very similar. Thus, the structure factor for this microemulsion composition at this temperature was successfully determined, which will be important later in this chapter for the GIFT procedure.

Table 3-2: Parameters for the structure factor fitting function to the scattering data (Eq. 2-54) obtained from the contrast variation of the system brine – CO₂/cyclohexane – Zonyl FSO 100/ Zonyl FSN 100 at $w_{\text{B}} = 0.10$, $\gamma_{\text{a}} = 0.08$, $\delta_{\text{FSN}} = 0.75$, $\beta_{\text{i}} = 0.2$, $T = 20^\circ\text{C}$ and various pressures. The Percus-Yevick structure factor described in section C I was used. As the general structure of the micelles is not changed within a contrast variation, the parameters at different contrast conditions are very similar [53].

P [bar]	<i>contrast A</i>		<i>contrast B</i>		<i>contrast C</i>		<i>contrast D</i>	
	R_{HS} [Å]	$\sigma_{\text{HS}}/R_{\text{HS}}$						
100	81	0.35	83	0.32	83	0.32	83	0.32
150	79	0.32	79	0.32	79	0.32	79	0.32
200	77	0.32	77	0.32	77	0.28	77	0.32
300	75	0.32	75	0.28	75	0.32	75	0.32

The structural parameters of the numerical droplet form factor $P_{\text{droplet}}(R)$ obtained from the description of the scattering data (in Figure 3.4) are summarised in Table 3-3. Comparing the parameter R_0 for $p = 100$ bar and 300 bar for each contrast it becomes obvious that the radius decreases by (8 ± 1) Å with increasing pressure. This is related to the increase of density of CO₂. Furthermore, the radii at contrast conditions B and C (both core contrasts) are approximately 6 Å smaller than at contrast condition A (core + film) in which the amphiphilic film also contributes to the scattering intensity. This value is somewhat smaller than the length of surfactant molecule which is related to the penetration of CO₂ into the surfactant chains and to the hydration of the surfactant head groups.

The best way to determine d is provided by the scattering data from film contrast condition, which indicate a thickness of the amphiphilic film between 12 and 13 Å. The values found for d are either in a reasonable range of 10 to 13 Å or very close to zero. This can be explained as follows. In the case of $d \approx 0$ Å the neutrons cannot distinguish between the amphiphilic film and the core (contrast A) or the solvent (contrast C). As a consequence the scattering length densities merge into one another to a broad transition, as indicated by high values of χ . This is especially obvious for contrast A, where at $p = 100$ bar the contrasts $\Delta\rho_{\text{core}} > \Delta\rho_{\text{film}}$ are connected to $d = 0$ Å because the SLD increase continuously from the core to the bulk. Thus, instead of a discrete step a very diffuse scattering profile with large values of χ is observed. In the case of $\Delta\rho_{\text{core}} < \Delta\rho_{\text{film}}$ at $p = 300$ bar the scattering length density runs through a minimum at the amphiphilic film. Here, neutrons can distinguish between the amphiphilic film and the core/solvent, and thus the shell thickness d was found to have a large value of 12 Å.

Table 3-3: Parameter for the droplet form factor fitting functions to the scattering data (Figure 3.4) obtained from the contrast variation of the system brine – CO₂/cyclohexane – Zonyl FSO 100/ Zonyl FSN 100 at $w_B = 0.10$, $\delta_{\text{FSN}} = 0.75$, $\beta_i = 0.2$, $T = 20^\circ\text{C}$ and various pressures. The evaluation was based on the droplet form factor described in Eq. 2-45 [53].

	p [bar]	R_0 [Å]	σ/R_0	d [Å]	χ [Å]	$\Delta\rho_{\text{core}}$ [10^{-6} Å^{-2}]	$\Delta\rho_{\text{film}}$ [10^{-6} Å^{-2}]
A	100	68	0.20	0.0	11.0	1.47	1.27
A	150	67	0.20	1.0	10.0	1.36	1.27
A	200	64	0.20	8.0	9.0	1.29	1.27
A	300	59	0.18	12.0	8.0	1.20	1.27
B	100	62	0.23	10.8	1.5	-1.49	0.25
B	150	60	0.25	10.8	1.3	-1.59	0.25
B	200	57	0.25	10.7	1.0	-1.66	0.25
B	300	54	0.25	10.7	1.0	-1.75	0.25
C	100	61	0.25	1.0	10.0	0.23	0.02
C	150	60	0.25	3.0	9.0	0.24	0.02
C	200	57	0.25	3.0	9.0	0.24	0.02
C	300	54	0.25	2.0	9.0	0.27	0.02
D	100	65	0.14	12.5	3.8	-0.58	1.27
D	150	64	0.14	12.5	3.8	-0.67	1.27
D	200	63	0.14	12.7	3.5	-0.71	1.27
D	300	59	0.16	13.0	3.0	-0.84	1.27

Upon comparing the absolute value of $\Delta\rho_{\text{core}}$ for the contrast conditions A and B at $p = 100$ bar, it becomes obvious that they are the same. This is perfectly reasonable considering the adjusted contrast conditions in Figure 3.3. At $p = 300$ bar the absolute difference from $\Delta\rho_{\text{core}}$ at 100 bar is also the same. This is because in both cases the scattering length density of the hydrophobic phase increases with increasing pressure, but in the case of contrast A the difference of the

scattering length densities becomes smaller, whereas it increases in the case of contrast B. This difference is also in agreement with the difference of scattering length densities in the case of contrast D.

Upon close investigation of the scattering curves at film contrast condition D in Figure 3.4, one notices that the first minimum shifts to lower q -values with increasing pressure. This trend, however, is not reasonable for compression since such a shift usually indicates a growth of structure. Describing the scattering curves qualitatively with the analytical fitting functions it turned out that the optimum film contrast condition was not achieved. An additional core scattering contribution which increases with increasing pressure was found to cause this shift of the minimum. As expected the mean droplet radius R_0 decreases with increasing pressure (Table 3-3).

3.1.4 Data evaluation II: Model-independent Fourier transformation

The scattering curves in Figure 3.4 were also analysed by the GIFT method developed by O. Glatter. While the determination of the particle form factor with this procedure is model-free the structure factor is required to be known if one also wants to describe the scattering intensity in the low q -range. Therefore, it is important to remember that the polydisperse Percus-Yevick structure factor for this sample was presented in the previous section (Table 3-2) and could thus easily be implemented into the calculation of the particle form factor by means of the GIFT procedure. The scattering data together with fitting functions obtained from the GIFT procedure are shown in Figure 3.5. As can be seen all scattering curves are described qualitatively over the whole q -range.

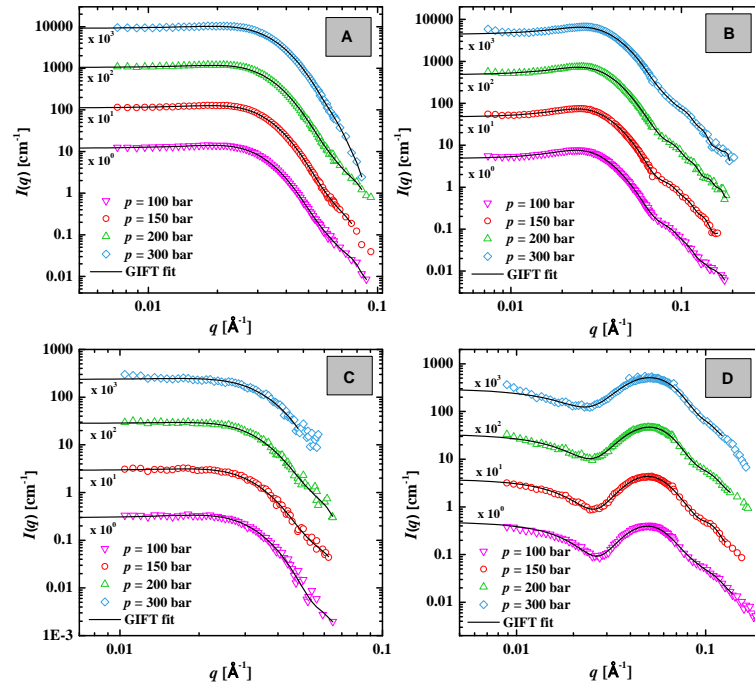


Figure 3.5: Neutron scattering curves of the microemulsion system brine – CO₂/cyclohexane – Zonyl FSO 100/Zonyl FSN 100 at $w_B = 0.10$, $\delta_{\text{FSN}} = 0.75$, $\beta_i = 0.2$, 20°C, various pressures and the contrast conditions shown in Figure 3.3. The fitting functions were calculated using the Generalised Indirect Fourier Transformation (GIFT), applying a model-free particle form factor in combination with a polydisperse Percus-Yevick structure factor with the parameters displayed in Table 3-2 [53].

Besides the fitting function the result of the first step of the GIFT procedure is the pair distance distribution function (PDDF) $p(r)$. Starting from the scattering data shown in Figure 3.5 (and Figure 3.4) the GIFT procedure was applied and the according normalised PDDFs are shown in Figure 3.6. The PDDFs of each contrast condition were normalised to the peak maximum of the PDDF at $p = 100$ bar, thus keeping the areas under the PDDFs at the right ratio.

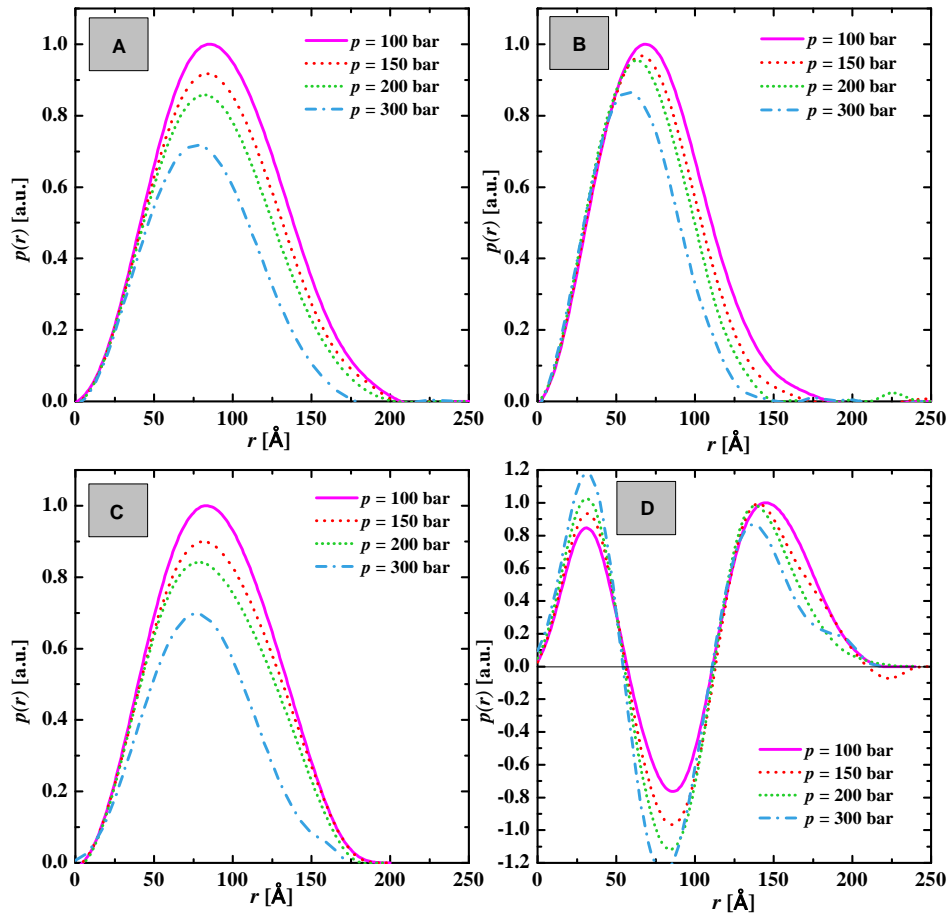


Figure 3.6: Pair distance distribution function of the microemulsion system brine – CO₂/cyclohexane – Zonyl FSO 100/ Zonyl FSN 100 at $w_B = 0.10$, $\delta_{FSN} = 0.75$, $\beta_i = 0.2$, $T = 20^\circ\text{C}$, various pressures and the contrast conditions shown in Figure 3.3, obtained from the scattering curves displayed in Figure 3.5. The PDDFs at the contrast conditions A, B and C are typical for spherical structures whereas the PDDF at contrast D is typical for inhomogeneous structures [53].

The symmetric peak of the pair distance distribution functions calculated from the scattering curves of the contrast conditions A, B and C is typical for spherical structures. Under consideration of polydispersity effects the values obtained from the PDDF are in good agreement with the parameters obtained from the fitting function (Table 3-3). The trend that the PDDF shifts to smaller radii with increasing pressure also goes well with previous results. Furthermore, comparing the maximum extension of the PDDFs obtained from contrast condition A and B, it becomes obvious that the PDDFs in the case of contrast condition B are shifted to smaller radii than the ones at contrast condition A, which can be explained by the fact that the amphiphilic film does not contribute to the scattering at contrast condition B. Also in accordance with expectations is the decreasing area of the PDDF with increasing pressure as the area is proportional to the aggregation number.

Although the PDDF in contrast condition D deviates considerably from the other PDDFs it still shows a well-known shape which is typical for inhomogeneous spheres [241]. In order to

interpret these PDDFs one has to be aware it is a statistical function which represents the rate of occurrence of different distances within one region of SLD within the micelle. For a better understanding a schematic drawing of occurring distances in a homogeneous, a hollow and an inhomogeneous sphere is given in Figure 3.7.

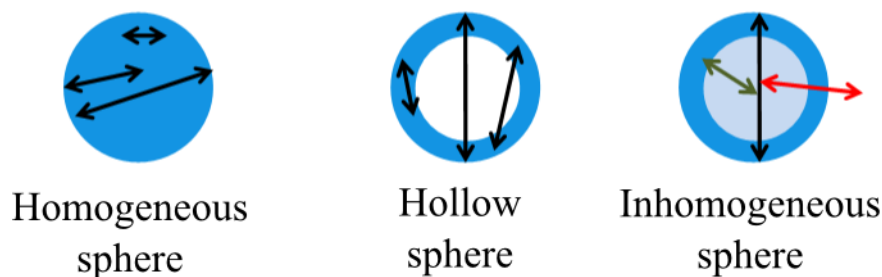


Figure 3.7: Schematic drawing of distances occurring in spheres at different contrast conditions. In homogeneous spheres all distances r within the region of the same SLD can be found, with a maximum at $r = R$ in the PDDF (left). In hollow spheres (middle) mostly distances between the outer shell contribute to $p(r)$ which leads to a shift of the PDDF to higher r -values. For inhomogeneous spheres (right) distances within the core (green arrow) and the shell (black arrow) can be found while distance between these or to the solvent do not contribute (red arrow). The shape of the PDDF also depends on the absolute values of the different compartments.

In the case of the PDDF for contrast D, the zero-crossing point of the PDDF at about 50 \AA describes the radius of the micelle, representing mostly the distances inside the core, as indicated in Figure 3.7 right by the green arrow. The second zero-crossing at about 100 \AA thus gives the diameter of the micelle. This maximum of the second peak is negative because distances from core to shell do not lie within the same volume element with the same scattering properties and are thus not accounted for. Any distance that exceeds 100 \AA can only represent shell-shell distances (long black arrow in Figure 3.7 middle and right). The position of the peaks at about 30 \AA and 80 \AA indicate that there is a change of the contrast conditions at these radii.

Since the PDDF was described earlier as a probability function it may seem strange that negative values occur. This can be explained by considering the scattering length density differences as indicated by different colours in Figure 3.7 right. Remembering Eq. 2-63 it shows that the product $\Delta\rho(r_1)\Delta\rho(r_1-r)$ also influences the PDDF. In the case of $\rho_{\text{core}} \neq \rho_{\text{bulk}} \neq \rho_{\text{shell}}$ one of the scattering length densities and thus also the product can become negative. In this case, the difference $\Delta\rho_{\text{core}}$ is negative (see Table 3-3) and thus the negative values in the PDDF can be assigned to distances within the core of the particles.

With the PDDF at hand, it is possible to apply the second step of the GIFT procedure to the data to extract the radial scattering length density profile. This is done by means of the DECON program which is part of the GIFT software package. Note that the PDDF raw data

were used instead of the normalised data shown in Figure 3.6. This procedure was applied to all contrast conditions and pressures, and the results are shown exemplarily for $p = 100$ bar and 300 bar in Figure 3.8. The profiles were normalised to the volume of the scattering particle. Note that the profiles were shifted to the applied SLD of the bulk, resulting in the intrinsic SLD. In case of contrast condition A the radial scattering length density profile was multiplied with (-1) in order to assimilate it to the schematic profile shown in Figure 3.3

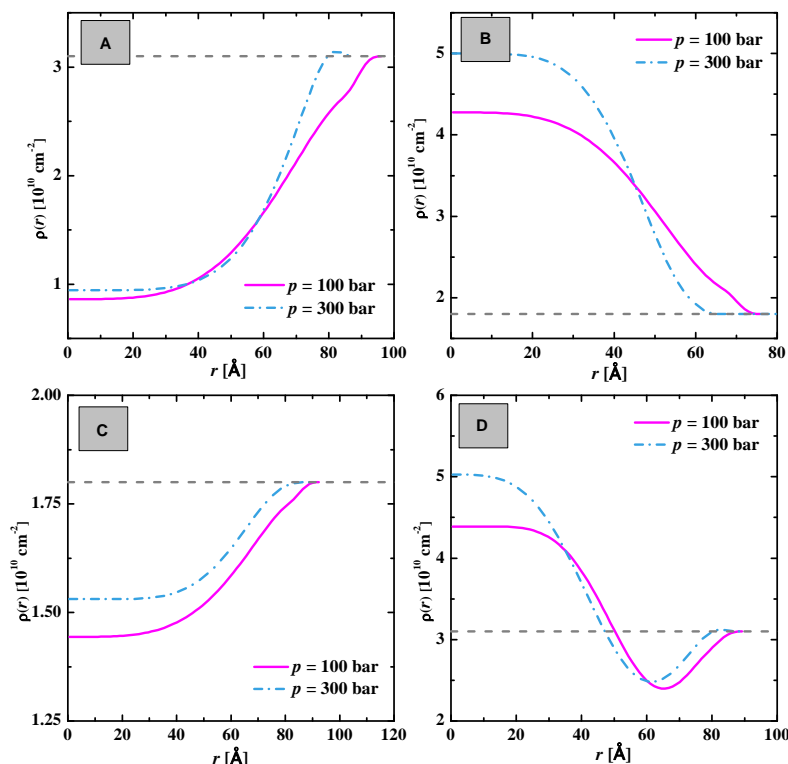


Figure 3.8: Radial scattering length density profiles deconvoluted from the PDDFs in Figure 3.6 for $p = 100$ and 300 bar and the four contrast conditions. The profiles A, B and C exhibit a homogeneous core and a wide transition range in which SLD approaches the value of the bulk. This indicates an inhomogeneous distribution of cyclohexane within the micelle, i.e. a concentration gradient. Contrast D shows a minimum which is caused by the amphiphilic film. Here, the considerably larger SLD at the core compared to the bulk is another indication of an inhomogeneous distribution of cyclohexane. The SLD profiles were shifted by the respective SLD value of the bulk [53].

The most important thing to notice in Figure 3.8 is the comparatively small homogeneous core and the wide transition range in which the SLD approaches the value of the bulk which occurs with all profiles. Using contrast A and $p = 100$ bar as an example, it can be observed that the constant scattering length density at the core of the micelle stretches only for about 45 Å, followed by a 40 Å - wide constant increase of scattering length density, until at about 90 Å the SLD of the bulk is reached. Comparing the size of these regions, the results indicate that the micelle is about semi-filled with a region of non-constant composition, since a change in SLD is a direct mirror of a change of composition. These results clearly support the hypothesis of a depletion zone of cyclohexane close to the amphiphilic film and a cyclohexane-enriched zone

at the centre of the micelle (Figure 1.1 right). A similar profile can also be observed at $p = 300$ bar. Here, the gradient region is slightly steeper than at 100 bar due to a smaller volume of the micelle.

Taking a closer look at the radial scattering length density profiles it becomes obvious that pressure influences the SLD at the core, i.e. at $r \rightarrow 0$. While at contrast conditions A and C the SLDs are very similar at $p = 100$ bar and 300 bar, ($\Delta_{\text{SLD}} = 0.09 \cdot 10^{10} \text{ cm}^{-2}$), this difference is much more pronounced at contrast conditions B and D ($\Delta_{\text{SLD}} = 0.7 \cdot 10^{10} \text{ cm}^{-2}$). This is due to two things: First, the concentration of cyclohexane at the core increases and, secondly, the density of CO_2 increases. By considering that deuterated cyclohexane-d12 was used in case of contrast B and D the higher absolute values of Δ_{SLD} can be explained by a further increased cyclohexane concentration. This is triggered by the avoidance of increasing repulsive interactions which arise due to the pressure-induced shrinkage of the micelle. In the case of protonated cyclohexane-h12 (contrast A and C), the slightly higher concentration of protonated cyclohexane (which has a negative scattering length density) at the core is partly compensated by the increase of the SLD of CO_2 . Using deuterated cyclohexane-d12, in contrast, the trend for both components is to change to higher scattering length densities, which is why the scattering contrast is more pressure-dependent in systems with deuterated cyclohexane-d12 (contrasts B and C) than in the case of cyclohexane-h12 as at the contrast conditions A and C.

A comparison of $\Delta\rho_{\text{core}}$ obtained from Figure 3.8 to the one obtained from the radial density distribution function $f_{\text{droplet}}(r)$ (Table 3-3) reveals that in all cases, the absolute values for $\Delta\rho_{\text{core}}$ obtained from the GIFT procedure are higher. This further supports the hypothesis of a cyclohexane-enriched zone at the centre of the micelle since the values for $f_{\text{droplet}}(r)$ were calculated assuming a homogeneous distribution of CO_2 and cyclohexane.

The actual distribution of CO_2 and cyclohexane at the core of the micelle can directly be calculated from the SLDs at $r = 0 \text{ \AA}$. The results indicate a cyclohexane content of $\beta_{\text{core}} \approx 0.5$ at the centre of the micelle for the scattering contrasts A, B and D. This is much larger than the value of $\beta_i = 0.20$ obtained from for a homogeneous distribution. Note that, probably due to the very low scattering contrast, contrast condition C suggests that $\beta_{\text{core}} = 0.3$. For all contrast conditions the concentration of cyclohexane at the core is slightly higher at $p = 300$ bar which is reasonable considering the smaller volume of the micelle.

Note that in all cases the radii calculated using $f_{\text{droplet}}(r)$ (Table 3-3) and the GIFT procedure are in good agreement. Furthermore, the pressure-dependent SLD differences at contrast conditions B and D are the same and the difference between the ones at A and C are only rather small. This accordance confirms the reliability of the results.

The scattering length density profiles of contrast D display a minimum between 60 and 70 Å which is expected for film contrast condition [130] and stems from the amphiphilic film. However, the second scattering contribution from core scattering becomes obvious here, as the SLD at the core of the micelle deviates considerably from the bulk material. This contribution is also one of the reasons for the deviation of the PDDFs from the others. Considering the zero crossing points of the PDDF at 30 Å and 80 Å it becomes obvious in $\Delta\rho(r)$ in Figure 3.8 that the SLD at the core of the micelle is constant up to about 30 Å and that the change at 80 Å represents the transition from micelle to bulk material. In accordance with the calculated trend of $\Delta\rho_{\text{core}}$ (Table 3-3) the SLD difference between core and bulk increases with increasing pressure. The absolute values, however, differ considerably, which is probably because of the re-distribution of deuterated cyclohexane which is considerably underestimated in the analytical fitting procedure. However, the dimension of non-constant scattering intensity over half of the micelle radius is very obvious here.

To evaluate the quality of the GIFT procedure the first step is to compare the fitting functions calculated by GIFT to the actual scattering curves which can be seen in Figure 3.5.

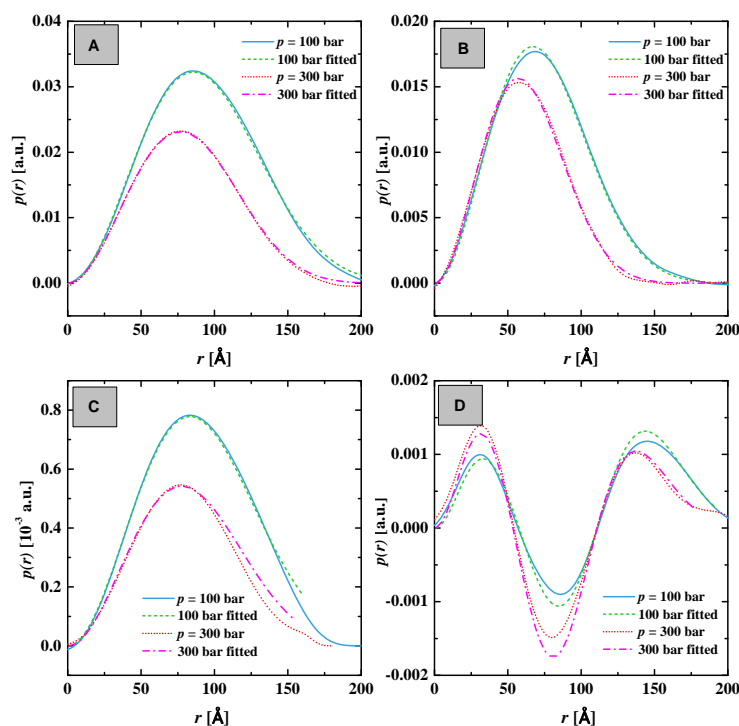


Figure 3.9: The PDDFs as shown in Figure 3.6, described by a fitting function in the frame of the DECON procedure. The fitting functions describe the data completely, thus indicating a high quality and reliability of the GIFT procedure and the results.

The second step, the deconvolution of the PDDF to the scattering length density distribution, is also combined to a fitting procedure, namely the description of the PDDF calculated in the first step. Thus, if both fitting procedures generate a good description of the data or function,

respectively, it can be concluded that the results are reasonable. The fitting curves to these PDDFs are shown in Figure 3.9. As can be seen the PDDFs are described qualitatively over the whole r -range, which, in combination with the perfectly fitted scattering curves in Figure 3.5, clearly shows that the results of the GIFT procedure and the DECON deconvolution are of high quality.

3.1.5 Measurements at elevated temperature and w_B

As the film contrast condition was not achieved during the contrast variation series another approach was performed at the D22 instrument at a slightly higher temperature ($T = 23^\circ\text{C}$) and w_B ($w_B = 0.11$) whereby the bulk scattering length density was adjusted to $3.02 \cdot 10^{10} \text{ cm}^{-2}$. The scattering curves and model fitting functions were measured and described by A. Müller [29]. The schematic contrast condition is shown in Figure 3.10 A, the according scattering curves in Figure 3.10 B. The fitting functions in Figure 3.10 B were calculated using the droplet form factor with $f_{\text{droplet}}(r)$ described in Eq. 2-45 in combination with the Percus-Yevick (Eq. 2-54) and the Ornstein-Zernicke structure factor (Eq. 2-55). The use of the Ornstein-Zernicke structure factor emerges due to the higher temperature which is closer to the critical point than the measurements discussed before.

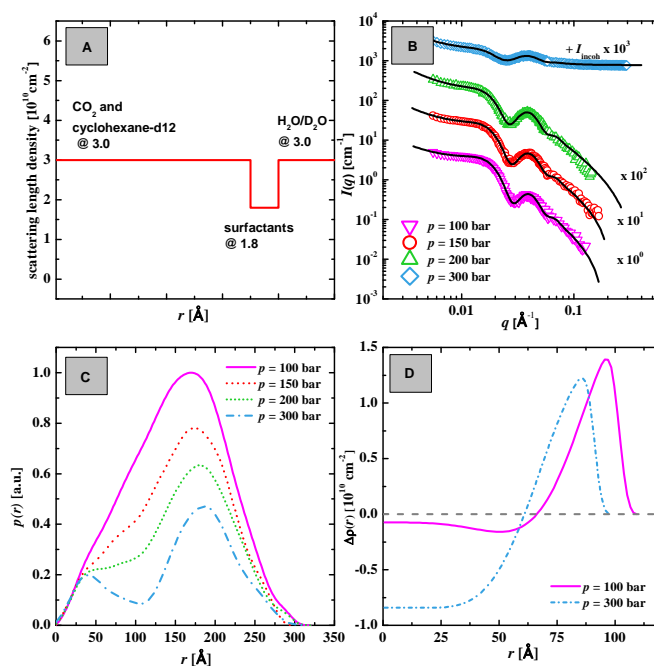


Figure 3.10: Summarised results of scattering experiments and GIFT-analysis of the system brine – CO_2 /cyclohexane – Zonyl FSO 100/ Zonyl FSN 100 at $w_B = 0.11$, $\delta_{\text{FSN}} = 0.75$, $\beta_i = 0.2$ and $T = 23^\circ\text{C}$. Schematic drawing of the contrast condition (A), calculated for $p = 100$ bar and $T = 23^\circ\text{C}$, and the scattering curves together with the according fitting functions at various pressures (B) [29]. The PDDFs are shown in C, which were used for the calculation of the scattering length density distribution (D).

The PDDF for $p = 100$ bar in Figure 3.10 C is shifted to higher r -values and thus differs from the other pair distance distribution functions for homogeneous spheres in Figure 3.6. The shape of this PDDF is typical for hollow spheres and a similar ones were already reported for microemulsions at film contrast condition [34, 130]. However, the PDDFs at higher pressures deviate also from the film contrast condition and change with increasing pressure to a PDDF with two peaks, thus resembling more and more PDDFs for inhomogeneous particles as shown in Figure 3.6 D. This is probably connected to the increasing scattering contribution of $\Delta\rho_{\text{core}}$ considering also the parameters of the numerical fitting functions of the scattering data in Figure 3.10 B (see Table 3-4). Here, it shows that the optimum film contrast condition was achieved at $p = 100$ bar but that at higher pressures a second scattering contribution from core scattering arises. This is reflected by the second peak in the PDDF. As the core scattering contribution is rather small, these data are a good example to follow a transition from hollow sphere to inhomogeneous particle via the PDDF. This finding is also interesting regarding the PDDF found for the non-perfect film contrast condition in Figure 3.6 D in which $\Delta\rho_{\text{core}}$ is considerably higher than here. Thinking of the higher difference between $\Delta\rho_{\text{core}}$ and $\Delta\rho_{\text{film}}$, one can imagine that the minimum between the two peaks (Figure 3.10 C, 300 bar) extends with increasing $\Delta\rho_{\text{core}}$ up to a PDDF like the ones shown in Figure 3.6 D.

Table 3-4: Overview of the fitting parameter of the droplet form factor and the Percus-Yevick structure for the scattering curves of the system brine – CO₂/cyclohexane – Zonyl FSO 100/ Zonyl FSN 100 at $w_B = 0.11$, $\delta_{\text{FSN}} = 0.75$, $\beta_i = 0.2$, $T = 23^\circ\text{C}$ and various pressures (shown in Figure 3.10 B) [29]. Note that the parameters of the Ornstein-Zernicke structure factor are not shown.

p [bar]	R_0 [Å]	σ/R_0	χ [Å]	d [Å]	$\Delta\rho_{\text{core}}$ [10^{-6} Å^{-2}]	$\Delta\rho_{\text{film}}$ [10^{-6} Å^{-2}]	R_{HS} [Å]	$\sigma_{\text{HS}}/R_{\text{HS}}$
100	102	0.17	3.0	10	0.00	1.60	120	0.3
150	100	0.17	2.0	10	-0.07	1.60	120	0.3
200	99	0.17	1.5	10	-0.13	1.60	120	0.3
300	95	0.17	0.5	10	-0.22	1.60	120	0.3

Considering the scattering length density profile of the film contrast condition (Figure 3.10 D), the emergence of the second peak in the PDDF at the non-optimum film contrast condition in Figure 3.6 for contrast D becomes clear, as the second scattering contrast is very obvious at $p = 300$ bar. Here, the shape of the peak is especially interesting, as the distortion of the peak at $p = 300$ bar indicates that the gradient is more pronounced at higher pressures. It is also interesting to note that the distortion of the peak occurs only at the inside of the micelle, indicating that the SLD profile is more step-like from surfactants to the brine solution. The minimum in the SLD profile in Figure 3.10 D at $p = 100$ bar for the GIFT results is probably due to instabilities during the calculation.

3.1.6 Conclusion

The results of the contrast variation study and the GIFT procedure indicate very clearly that the microemulsion system type brine – CO₂/cyclohexane – Zonyl FSO 100/ Zonyl FSN 100 does *not* consist of microemulsion droplets which are homogeneously filled with CO₂ and cyclohexane. This is clearly shown by the large region of non-constant scattering length density in Figure 3.8 which stretches over half of the micelle radius. Thus, the hypothesis of a depletion zone of cyclohexane close to the surfactants and an enrichment of cyclohexane at the centre of the micelle (Figure 1.1 right) was clearly validated. The reason for the formation of the depletion zone can be found on one hand in the repulsive interactions of cyclohexane and the fluorinated surfactant tails. On the other hand, the miscibility gap of CO₂ and protonated substances lies at considerably higher pressures than the ones with comparable perfluorinated alkanes [294, 295] which also confirms the preferred interactions. These results become especially interesting if one compares them to the results from Klostermann *et al.* who investigated microemulsions of the type brine – CO₂ – Zonyl FSO 100/ Zonyl FSN 100 at very similar parameters [34] ($\gamma_a = 0.06$ instead of 0.08, different lot number of Zonyl FSN 100, higher temperature). For a micelle with a mean radius of $r \approx 115$ Å they found a constant scattering length density for about 95 Å, followed by a steep decrease of scattering length density difference for about 20 Å, onto the constant scattering length density of the bulk phase (Figure 3.11 left).

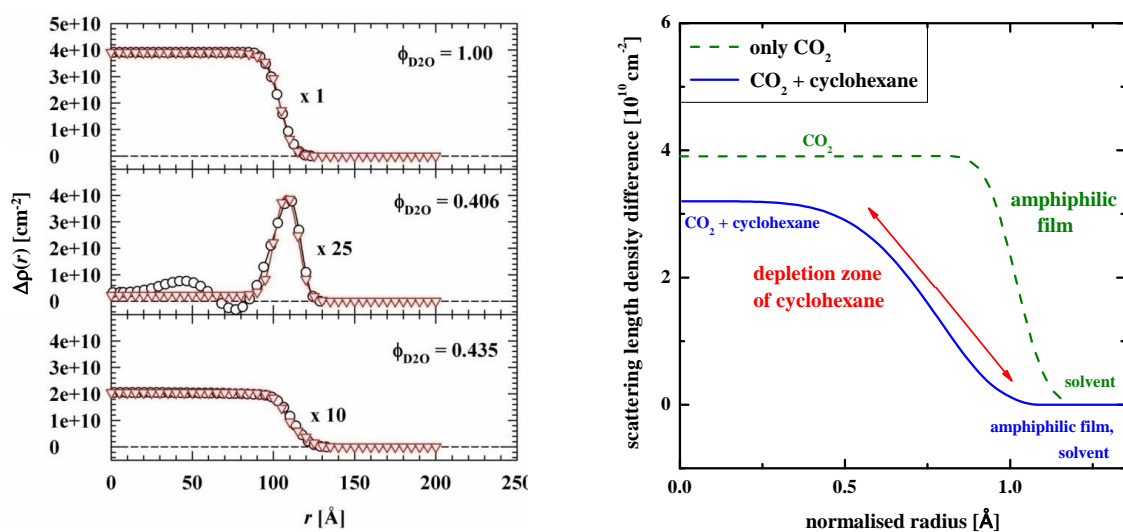


Figure 3.11: *Left:* SLD profiles of the microemulsion H₂O/D₂O/NaCl – CO₂ – Zonyl FSO 100/ Zonyl FSN 100 at $\gamma_a = 0.06$, $w_B = 0.10$, $p = 220$ bar and $T = 31.1$ °C for different scattering contrasts. Both GIFT results (circles) and the analytical density profiles $\Delta\rho_{\text{droplet}}(r)$ are shown (triangles). Both profiles were scaled to the scattering contrast of the different microemulsion sub-phases. For a better overview the profiles at $\phi_{D2O} = 0.406$ and 0.435 were multiplied with a constant factor of 25 and 10, respectively. Taken from [34]. *Right:* Comparison of the SLD profile of a microemulsion system without cyclohexane studied by Klostermann *et al.* [34] (green) and the system with 20 wt% cyclohexane (blue). The x values are normalised to the radius of the respective system. It can clearly be seen that the system with cyclohexane displays a wide transition range which is not present in the system without cyclohexane [53].

In order to see the differences more clearly Klostermann's SLD profile at $\phi_{D2O} = 1$ is plotted together with the SLD profile for contrast B at $p = 100$ bar in Figure 3.11 right. For this plot the radius values on the x-axis were normalised to the radius of the respective microemulsion system so that the dimension of the transition ranges can be compared more easily. The transition range is considerably more pronounced in the system with cyclohexane which further validates the proposed depletion zone of cyclohexane close to the amphiphilic film. Note that the absolute values of SLD at the y-axis cannot be compared since the contrast conditions are different.

Comparably to the data shown by Klostermann *et al.* in Figure 3.11 left, it was also tried to describe the scattering length density distribution functions shown in Figure 3.8 by means of the radial density distribution function $f_{\text{droplet}}(r)$. Figure 3.12 shows, however, that this is not possible because the parameter χ can only account for symmetry diffusivities. Thus, the SLD profile can be described satisfactorily for small radii but the position of the maximum of the $f_{\text{droplet}}(r)$ function deviates considerably. Furthermore, the fitting function $f_{\text{droplet}}(r)$ overestimates the diffusivity for large values of r , i.e. the hydrophilic part of the surfactant which is penetrated by solvent molecules. This overestimation of the diffusivity is also the reason why $f_{\text{droplet}}(r)$ is not completely appropriate to describe the scattering curves shown in Figure 3.4 over the whole q -range.

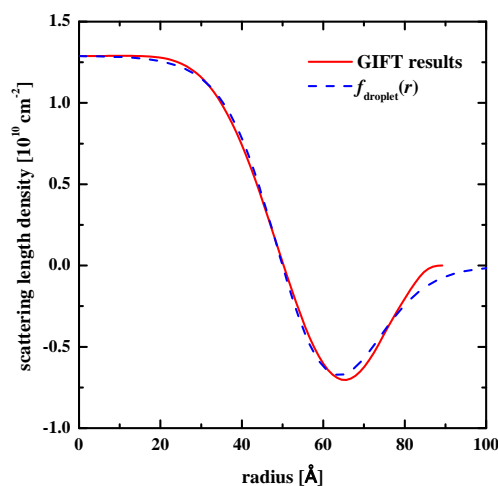


Figure 3.12: Scattering length density profile of scattering contrast D at $p = 100$ bar (red solid line) calculated using the GIFT method and the DECON program package. The radial density distribution profile $f_{\text{droplet}}(r)$ (blue dashed line) was fitted to these data which is clearly not entirely possible. Although the GIFT results are well described for small radii the peak maximum of the $f_{\text{droplet}}(r)$ function is at a different position and the diffusivity of the surfactants towards the solvent is overestimated.

3.2 Kinetics of structural changes of CO₂-microemulsions

In previous studies the microstructure of microemulsions of the type water – CO₂ – fluorinated surfactants was investigated [36, 163]. In the last years also the microstructure of the system H₂O/NaCl – CO₂ – Zonyl FSO 100/Zonyl FSN 100 was elucidated, which is, except for the hydrophobic additive cyclohexane, very similar to the system studied here [34, 35].

It is obvious that the kinetics of such a microemulsion shifts into focus to support processes which depend on the speed of structural changes, such as for example the POSME procedure. Regarding the formation kinetics of a CO₂ microemulsion with fluorinated surfactants an interesting piece of work was published by Thurecht *et al.* [165]. They used high pressure self diffusion ⁹F-NMR to follow the diffusion coefficient of the surfactants. They found that the surfactant tails exhibit greater mobility with increasing time after pressurisation of a water – CO₂ –surfactant mixture to 300 bar and 40°C.

Only very recently, also the kinetics of structural changes of a CO₂-in-brine microemulsion stabilised by the Zonyl FSO 100/ Zonyl FSN 100 mixture was examined by performing pressure jumps. This study showed that the change from a spherical microemulsion droplet to a cylindrical micelle, induced by a sudden pressure jump, occurs in the order of one second [56]. A. Müller investigated not only the structural changes within the one-phase microemulsion but also the demixing kinetics by performing pressure jumps to a pressure at which the CO₂-in-brine microemulsion coexists with an excess CO₂-phase [29]. By studying one microemulsion without and one with cyclohexane it turned out that the substitution of 20% CO₂ by cyclohexane decelerates the demixing by one order of magnitude. Based on these results, the influence of different amounts of cyclohexane on phase behaviour and microstructure, the kinetics of structural changes between thermodynamically stable states as well as the demixing kinetics are systematically investigated in this work.

3.2.1 Phase behaviour and microstructure

The phase behaviour of the systems H₂O/NaCl – CO₂/cyclohexane – Zonyl FSO 100/ Zonyl FSN 100 at $\delta_{\text{FSN}} = 0.75$ and $\varepsilon = 0.01$ was for $\beta_i = 0.0$ and 0.2 (β_i : mass fraction of cyclohexane in the mixture of cyclohexane and CO₂ solubilised inside the micelles (see Eq. 3-1)) already shown in Figure 3.1. In order to systematically investigate the influence of cyclohexane on the phase behaviour the temperature- and pressure-dependent $T(w_B)$ -sections recorded at $\gamma_a = 0.08$ are presented for $\beta_i = 0.10$, 0.15 and 0.25 in this chapter. Alongside with each phase diagram scattering curves are shown which were recorded at an overall CO₂/cyclohexane mass fraction $w_B = 0.10 \pm 0.01$, $T = 28^\circ\text{C}$ and different pressures. The parameters chosen allow to compare the results obtained in this work with the ones found for the cyclohexane-free system by Müller [29]. The rather large error in w_B can on one hand be explained by the low amount of the CO₂/cyclohexane mixture which is used in a water-rich microemulsion system and is on the other hand due to the filling procedure of CO₂ into the view cell.

Since the determination of volume of CO₂ is performed by eye (see section 7.2.1) there are always experimental errors, especially since the surface curvature of the aqueous surfactant mixture and cyclohexane droplets on top further complicate the determination of the CO₂-volume.

The phase behaviour of the $\beta_i = 0.10$ system together with the respective scattering curves is shown in Figure 3.13. The phase behaviour of a microemulsion with CO₂ is analogous to that of non-ionic microemulsions containing liquid oils [107, 115]. Thus, at low temperatures a CO₂-in-water microemulsion phase coexists with a CO₂ excess phase ($\underline{2}$). At high temperatures a water-in-CO₂ microemulsion coexists with a water excess phase ($\bar{2}$). At intermediate temperatures a one-phase region can be found. The intersection of the emulsification failure boundary (lower phase boundary) and the near-critical upper boundary characterises the maximum amount of oil ($w_{B,max}$) which can be solubilised at the adjusted mass fraction γ_a of surfactant in the brine/ surfactant mixture. As can be seen, $w_{B,max}$ increases with increasing pressure. The same trend was also observed for the system without cyclohexane. The presence of cyclohexane is reflected by the fact that the one-phase region becomes narrower compared to the system without cyclohexane. This means that the oil/ surfactant tail interactions are more temperature-sensitive. Furthermore, the $w_{B,max}$ -values of the cyclohexane-containing system are slightly larger than the ones of the cyclohexane-free system (see Figure 3.1 left). This, compared to the balanced CO₂-microemulsions (equal volumes of brine and CO₂), small effect can be expected because the amount of cyclohexane is considerably smaller in water-rich c/w-microemulsions.

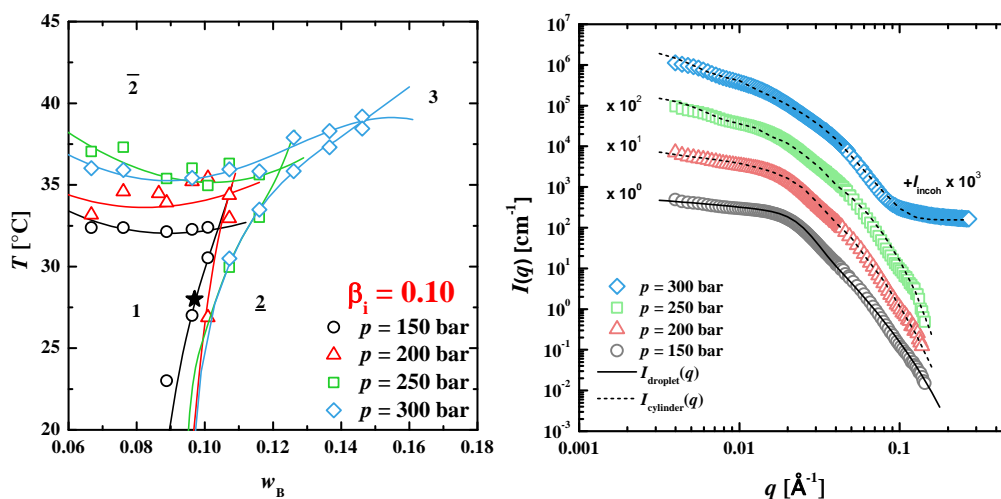


Figure 3.13: *Left:* Temperature and pressure-dependent phase behaviour of the system brine – CO₂/ cyclohexane – Zonyl FSO 100/ Zonyl FSN 100 ($\delta_{\text{FSN}} = 0.75$, $\varepsilon = 0.01$ and $\beta_i = 0.10$) as a function of the overall oil mass fraction w_B . As observed for the system without cyclohexane (Figure 3.1) the efficiency of the system increases with increasing pressure which is due to improved interactions of the fluorinated surfactant tails and CO₂. The star indicates the point at which the scattering curves were recorded. *Right:* Pressure dependent scattering curves recorded at $w_B = 0.1$ and $T = 28^\circ\text{C}$ as indicated by the star in the phase diagram left. While the scattering curve at $p = 150$ bar can be described using a droplet form factor the micelles show an elongated cylindrical shape at higher pressures.

As was also observed for the microemulsion system without cyclohexane at the same overall oil mass fraction w_B and at the same temperature [29, 56] the analysis of the SANS scattering curves reveal a spherical structure at $p = 150$ bar and elongated, cylindrical micelles at higher pressures (see Table 3-5). Thus, the scattering curve at $p = 150$ bar is typical for polydisperse spheres, as a constant scattering intensity can be observed for low q -values which is followed by a q^{-4} dependence at higher q -values. The high degree of smearing of the oscillation at $q \approx \pi/R$ indicates high polydispersity. The slight increase of scattering intensity at low q -values is caused by the proximity of the upper near-critical phase boundary which causes critical scattering contributions. At $p \geq 200$ bar a q^{-1} decrease instead of constant scattering intensity can be observed in the region $0.004 \text{ \AA}^{-1} \leq q \leq 0.013 \text{ \AA}^{-1}$ which is characteristic for the scattering pattern of elongated structures [296].

Thereby, the elongation is much more pronounced compared to the system without cyclohexane where the radius decreases from 57 \AA to 48 \AA upon increasing the pressure from 200 to 300 bar while simultaneously the length of the cylinder increases from 170 \AA to 200 \AA [56]. In the case of $\beta_i = 0.10$, the micelles seem to grow in length and between 250 and 300 bar also in radius (see Table 3-5). This is in accordance with the results of Müller for the system at $\beta_i = 0.20$ [29] where, however, the elongation of micelles is less pronounced. Since here, in contrast to the system without cyclohexane, the upper phase boundary at $p \geq 200$ bar is located at a temperature which is more than 5 K higher than the temperature of the measurement, no Ornstein Zernicke structure factor has to be used to describe the scattering curves of elongated micelles.

Upon close examination of the scattering curves and the respective fitting functions in the region $0.03 \text{ \AA}^{-1} \leq q \leq 0.10 \text{ \AA}^{-1}$ one finds systematic deviations in form of an underestimation of the scattering intensity in the lower part of this region and an overestimation in the high q -region. Note that for all scattering curves a neutron wavelength of 11.5 \AA was used for the low q -region and a wavelength of 6 \AA for the high q -region. Since multiple scattering is wavelength dependent it is possible that it affects mostly the scattering curve recorded at 11.5 \AA [297]. Thus, the increased intensity at intermediate q -values may be attributed to double scattering. The existence of a second “wiggle”, however, which occurs at a q -value considerably larger than twice of the q -value of the first “wiggle”, excludes multiple scattering. Furthermore, the fraction of double scattering for neutrons with 6 \AA and a sample transmission of 76% is expected to be rather small. Thus, this second “wiggle” might be attributed to an instrumental problem.

Another interesting trend can be observed considering the scattering length density difference $\Delta\rho_{\text{core}}$ which decreases with increasing pressure. This means that the scattering length density of the core increases with increasing pressure which can be explained by the higher concentration of protonated cyclohexane at the centre of the micelle as described in section 3.1.4.

Table 3-5: Fit parameters obtained from the analysis of the pressure-dependent scattering curves shown in Figure 3.13 right which correspond to the system brine – CO₂/cyclohexane – Zonyl FSO 100/ Zonyl FSN 100 at $\delta_{\text{FSN}} = 0.75$, $\varepsilon = 0.01$, $\beta_i = 0.10$, $w_B = 0.10$, $\gamma_a = 0.08$ and $T = 28^\circ\text{C}$. The scattering curve at $p = 150$ bar was described using a model for spherical droplets (convoluted with $I_{\text{OZ}}(q)$ whereby $I_{\text{OZ}}(0) = 0.7 \text{ cm}^{-1}$ and $\xi = 300 \text{ \AA}$) while at higher pressure the cylindrical model was used.

p [bar]	R_0 [\AA]	σ/R_0	L [\AA]	χ [\AA]	d [\AA]	$\Delta\rho_{\text{core}}$ [10^{-6} \AA^{-2}]	$\Delta\rho_{\text{film}}$ [10^{-6} \AA^{-2}]	R_{HS} [\AA]	$\sigma_{\text{HS}}/R_{\text{HS}}$
150	80	0.45	--	5	17	3.80	4.20	80	0.45
200	65	0.45	190	7	17	3.60	4.20	65	0.45
250	55	0.45	750	7.5	17	3.20	4.20	55	0.40
300	85	0.45	900	8.5	17	2.60	4.20	85	0.35

Increasing β_i from $\beta_i = 0.10$ to $\beta_i = 0.15$ slightly influences the phase behaviour, as shown in Figure 3.14 left. Thus, the efficiency at pressures between 150 bar and 250 bar marginally increases whereas the efficiency at $p = 300$ bar decreases compared to $\beta_i = 0.10$ (Figure 3.13 left). Furthermore, the oil emulsification failure (lower) boundaries shift to higher oil mass fractions in all cases. Thus, with increasing distance to the composition of the SANS sample conditions elongated structures can be expected and are indeed found.

Upon describing the SANS scattering curves the same problem as described above was encountered, more precisely an increased intensity at intermediate q -values followed by a “wiggle” of intensity near $q \approx 0.1 \text{ \AA}^{-1}$. With this system, however, this effect is even more pronounced than for the system with $\beta_i = 0.10$. Thus, at $p = 250$ bar and $p = 300$ bar a description of the scattering curve with a cylindrical droplet form factor was not possible. Taking a closer look at the power laws of the scattering curve at $p = 300$ bar it turned out that there is no clear q^{-4} -dependence. Instead, in the region $0.0177 \text{ \AA}^{-1} \leq q \leq 0.375 \text{ \AA}^{-1}$ a power law of $q^{-3.1}$ was found and for $0.0517 \text{ \AA}^{-1} \leq q \leq 0.0793 \text{ \AA}^{-1}$ the q -dependence is proportional to $q^{-5.4}$.

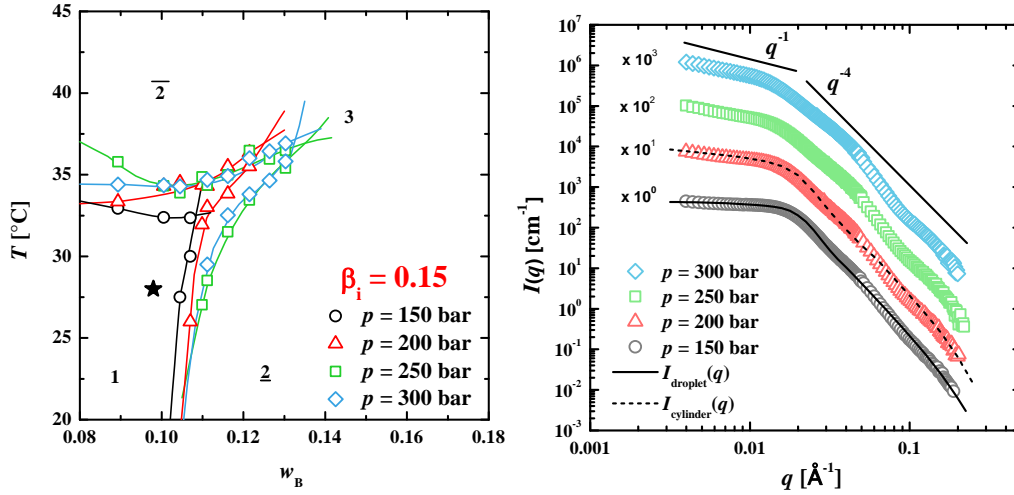


Figure 3.14: *Left:* Phase behaviour of the system brine – CO₂/cyclohexane – Zonyl FSO 100/ Zonyl FSN 100 ($\gamma_a = 0.08$, $\delta_{\text{FSN}} = 0.75$, $\varepsilon = 0.01$ and $\beta_i = 0.15$) as a function of temperature and the overall oil mass fraction w_B for different pressures. As observed for the previous systems with lower cyclohexane content the efficiency of the system increases with increasing pressure. The gaps between the efficiency points $w_{B,\text{max}}$, however, become smaller for $p = 200$, 250 and 300 bar. The star indicates the point at which the scattering curves were recorded. *Right:* Scattering curves corresponding to the star in the phase diagram at the left hand side. Spherical droplets are present at $p = 150$ bar but with increasing pressure the micelles elongate to cylindrical droplets at $p = 200$ bar. Note that it was not possible to describe the scattering curves at $p = 250$ and 300 bar with a cylindrical droplet form factor because the scattering curves do not have a clear q^{-4} dependence at intermediate q .

The scattering curves at $p = 150$ bar and 200 bar were described with a spherical and a cylindrical droplet form factor, respectively. The according parameters are shown in Table 3-6. There, it can be seen that the transition from spherical droplets to elongated droplets is connected to a decrease of radius which was also observed for the scattering curves obtained from the system at $\beta_i = 0.10$.

Table 3-6: Fit parameters to the scattering curves shown in Figure 3.13 for $p = 150$ bar and 200 bar which correspond to the system brine – CO₂/cyclohexane – Zonyl FSO 100/ Zonyl FSN 100 at $\delta_{\text{FSN}} = 0.75$, $\beta_i = 0.15$, $w_B = 0.1$ and $T = 28^\circ\text{C}$.

p [bar]	R_0 [Å]	σ/R_0	L [Å]	χ [Å]	d [Å]	$\Delta\rho_{\text{core}}$ [10 ⁻⁶ Å ⁻²]	$\Delta\rho_{\text{film}}$ [10 ⁻⁶ Å ⁻²]	R_{HS} [Å]	$\sigma_{\text{HS}}/R_{\text{HS}}$
150	95	0.40	--	3.5	10	3.6	4.2	95	0.40
200	90	0.40	140	10	3.8	3.2	4.2	90	0.40

In order to obtain structural information from the scattering curves at $p = 250$ and 300 bar the GIFT procedure was applied for all scattering curves shown in Figure 3.14 right. The resulting fitting functions and the pair distance distribution functions are shown in Figure 3.15.

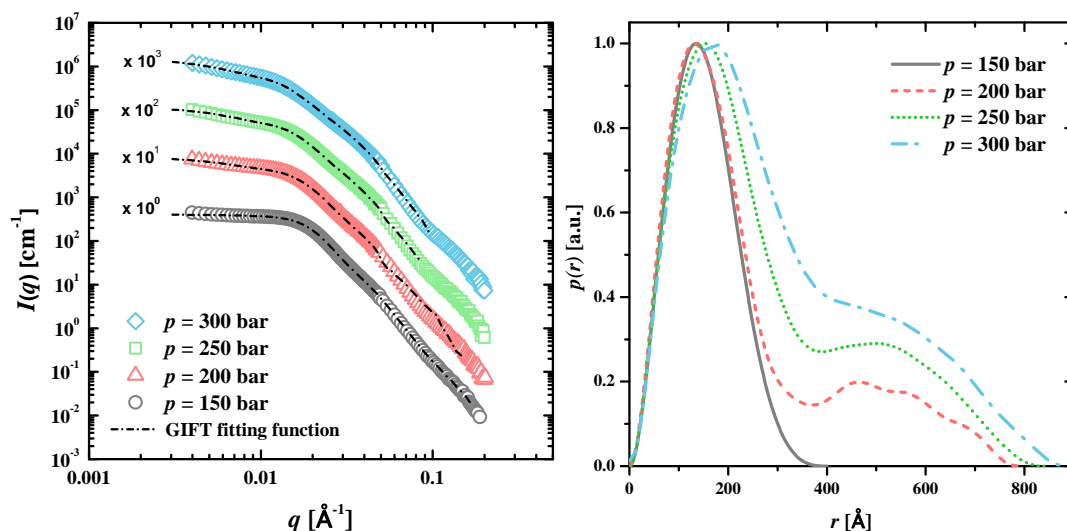


Figure 3.15: *Left:* SANS scattering curves obtained from the microemulsion system brine – CO₂/cyclohexane – Zonyl FSO 100/ Zonyl FSN 100 ($\gamma_a = 0.08$, $\delta_{\text{FSN}} = 0.75$, $\varepsilon = 0.01$ and $\beta_i = 0.15$) at $w_B = 0.10$ and $T = 28^\circ\text{C}$, as shown in Figure 3.14 right. Here, the fitting functions were calculated by means of the GIFT procedure. *Right:* Pair distance distribution functions according to the analysis of the scattering curves. While the single peak at $p = 150$ bar clearly points to spherical structures the PDDFs at higher pressures resemble the ones known for dimer prolate ellipsoids [298].

As expected, the PDDF obtained from the scattering curve at $p = 150$ bar displays a single peak which is a clear evidence for spherical droplets. The PDDFs at higher pressures, however, indicate the presence of at least one further distance. Since the PDDF for cylindrical droplets shows a single peak with its maximum is shifted to higher r -values than its mean radius, the PDDFs shown in Figure 3.15 right indicate that the present structures are not of cylindrical shape. Comparing these PDDFs to literature one finds a resemblance to PDDFs obtained from prolate ellipsoid dimers which orient in a linear arrangement [298]. Thus, the first peak indicates the radius of one prolate ellipsoid and the second peak the length of the dimer arrangement. The existence of such a type of structure this would explain the deviations from the cylindrical droplet form factor (also for the scattering curves recorded at $\beta_i = 0.10$). However, note that it was not possible to describe the scattering curves satisfactorily at $q \geq 0.1 \text{ \AA}^{-1}$. This strongly supports the hypothesis that the oscillation of scattering intensity in the high q -regime stems from an instrumental problem rather than from the structure because if it was caused by the structure the GIFT procedure should be able to account for that. Furthermore, since the increased scattering intensity around $q \approx 0.045 \text{ \AA}^{-1}$ is assumed to be caused by multiple scattering the interpretation of the PDDF should be treated carefully.

Increasing the cyclohexane content further to $\beta_i = 0.25$ the pressure-dependent phase behaviour of the microemulsion system changes. While the efficiency, i.e. $w_{B,\text{max}}$, does not seem to change much compared to $\beta_i = 0.15$, so do the phase boundaries. Obviously, the width of the one phase region decreases considerably. This trend is especially pronounced at $p = 150$ bar where at the composition of

the SANS sample a two-phase region exists. The lower phase boundaries at higher pressure are also distinctly less steep. Thus, the distance between star (SANS sample) and *efb* is considerably smaller than for $\beta_i = 0.25$, which is very likely the reason why spherical droplet structures are present at $p = 200\text{--}300$ bar (see Figure 3.16 right).

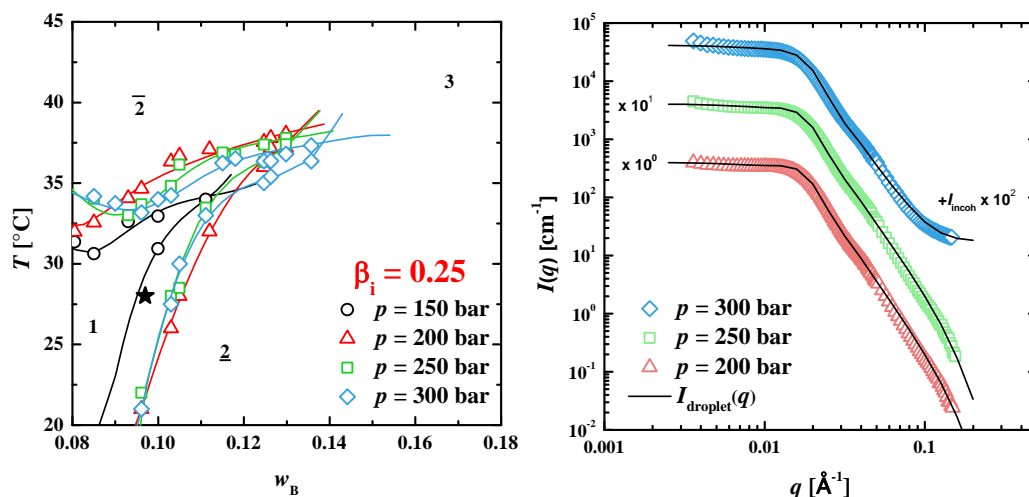


Figure 3.16: *Left:* Pressure-dependent phase behaviour of the system brine – CO₂/cyclohexane – Zonyl FSO 100/ Zonyl FSN 100 ($\gamma_a = 0.08$, $\delta_{\text{FSN}} = 0.75$, $\varepsilon = 0.01$ and $\beta_i = 0.25$) as a function of temperature and the overall oil mass fraction w_B . The one-phase regions are considerably narrower compared to the previously discussed systems with lower cyclohexane content. Here, the efficiency of the system is highest for $p = 200$ bar. The star indicates the composition at which the scattering curves were recorded. *Right:* Scattering curves according to the composition and temperature of the star in the phase diagram. At all pressures spherical droplets are present.

All scattering curves in Figure 3.16 right were described by a combination of the spherical droplet form factor and the Percus-Yevick structure factor. Thereby, the size of the droplets slightly decreases with increasing pressure which is connected to the density change of CO₂. However, since 25 wt% of CO₂ were replaced by cyclohexane here, the compressibility is lower compared to the system without cyclohexane. Because high numerical values were found for both d and χ it is likely that χ describes the concentration gradient of cyclohexane rather than the diffusivity of the amphiphilic film, as discussed in section 3.1.6. As was observed for the system at $\beta_i = 0.15$ it is also the case here that $\Delta\rho_{\text{core}}$ decreases with increasing pressure due to the higher concentration of cyclohexane at the centre of the micelle. The high polydispersity of the microemulsion system is reflected in the scattering curve by the oscillation in the medium q -range which is hardly pronounced. This can also be seen by the high polydispersity index of 40 % (see Table 3-7).

Table 3-7: Fit parameters to the scattering curves shown in Figure 3.16 for various pressures which correspond to the system brine – CO₂/cyclohexane – Zonyl FSO 100/ Zonyl FSN 100 at $\gamma_a = 0.08$, $\delta_{\text{FSN}} = 0.75$, $\varepsilon = 0.01$, $\beta_i = 0.25$, $w_B = 0.10$ and $T = 28^\circ\text{C}$. The droplet form factor in combination with the Percus-Yevick structure factor was used to describe all scattering curves.

p [bar]	R_0 [Å]	σ/R_0	χ [Å]	d [Å]	$\Delta\rho_{\text{core}}$ [10^{-6}Å^{-2}]	$\Delta\rho_{\text{film}}$ [10^{-6}Å^{-2}]	R_{HS} [Å]	$\sigma_{\text{HS}}/R_{\text{HS}}$
200	106	0.40	5.0	13	2.6	4.2	106	0.45
250	105	0.40	5.0	13	2.5	4.2	105	0.45
300	104	0.38	5.2	13	2.4	4.2	104	0.45

Comparing the $T(w_B)$ phase diagrams at different cyclohexane contents one finds that the efficiency boosting as described in section 3.1.1 for balanced microemulsions also occurs for water-rich microemulsions (Figure 3.17 right), especially in the case of $p = 150$ bar as can be seen in Figure 3.17 left. The trend of improved efficiency is, however, much less pronounced for diluted than for balanced microemulsions (compare Figure 1.1 left), especially in the case of $p = 300$ bar. For $p = 150, 200$ and 250 bar a general increase of $w_{B,\text{max}}$ with increasing cyclohexane content can be observed. This trend is slightly weaker for $p = 200$ bar and even less obvious for 250 bar. At $p = 300$ bar, even a small decrease of $w_{B,\text{max}}$ with increasing $\beta_i =$ can be observed.

The system at $p = 150$ bar reaches its maximum efficiency at $\beta_i = 0.20$ which is very similar to the trend observed with balanced microemulsions (see Figure 1.1 left). Furthermore, the increase of efficiency is highest at $p = 150$ bar and lowest at $p = 300$ bar which is connected to the higher density of CO₂ at higher pressure. Since CO₂ functions a buffer layer between cyclohexane and the fluorinated surfactant tails it is reasonable that this layer is thinner at high densities, i.e. at 300 bar, leading to a less efficient system compared to a micelle with a larger layer. However, the comparably low number of data points and the high errors of w_B make it difficult to reliably interpret Figure 3.17 right.

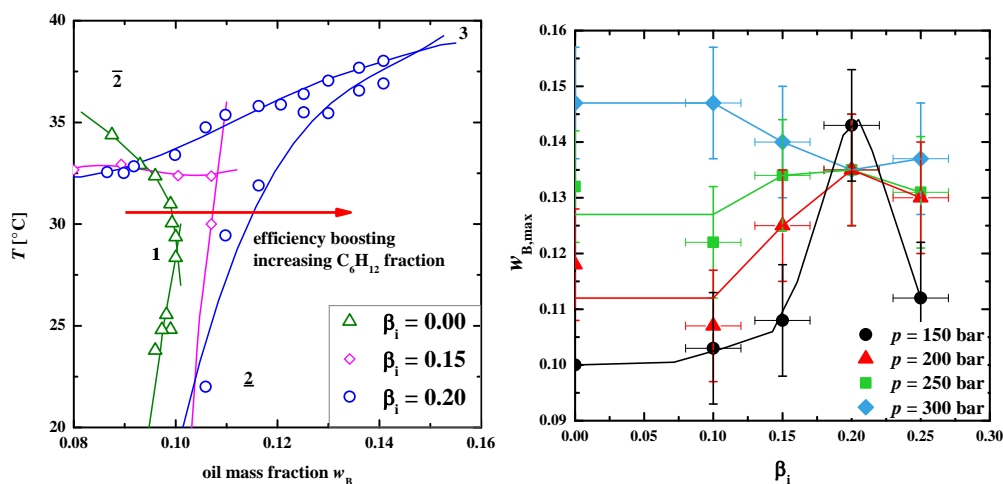


Figure 3.17: *Left:* Comparison of $T(w_B)$ sections of the system brine – CO₂/cyclohexane – Zonyl FSO 100/ Zonyl FSN 100 at $\gamma_a = 0.08$, $\delta_{FSN} = 0.75$, $\varepsilon = 0.01$, $p = 150$ bar and different mass fractions β_i of cyclohexane in the hydrophobic phase. $w_{B,max}$ increases with increasing cyclohexane mass fraction β_i . *Right:* Comparison of the points of maximum efficiency $w_{B,max}$ of the systems previously discussed at four different pressures. For $p = 150$ bar a strong increase of efficiency with increasing β_i can be observed, which is less pronounced at 200 and 250 bar. At $p = 300$ bar, in contrast, a slight decrease of efficiency was found.

Another very interesting trend becomes obvious if the radius of the spherical droplets at $p = 150$ bar (200 bar in the case of $\beta_i = 0.25$) is plotted against the cyclohexane mass fraction β_i within the hydrophobic phase, as shown in Figure 3.18 left. Thereby, the radius of the spherical micelles found at $p = 150$ bar increases linearly with increasing cyclohexane content. This is surprising because the overall oil mass fraction was kept constant. Since the overall interface area remains constant in first approximation (the amount of surfactant is not changed) this increase in radius must be connected to a decrease of particle number density. In order to verify this trend the respective scattering curves are shown in Figure 3.18 right. The increase of forward scattering intensity upon addition of cyclohexane immediately shows that the droplets at $\beta_i = 0.00$ are smaller compared to the systems with cyclohexane. The fact that the scattering curves with cyclohexane have a similar forward scattering intensity can be explained by considering that the scattering increase of larger droplets is compensated by a lower core scattering contrast $\Delta\rho_{core}$ with increasing β_i . The position of the characteristic oscillations shifts to lower q -values with increasing β_i as indicated by the arrows in Figure 3.28 right. Furthermore, the scattering intensity in the medium q -range slightly shifts to lower q -values. Both trends indicate a trend towards larger droplets. Considering the depletion zone of cyclohexane close to the surfactants (see section 3.1) it is possible that larger droplets form because they can hold considerable higher amounts of cyclohexane. Thereby, the smaller surface-to-volume ratio also reduces the interaction regions of cyclohexane and fluorinated surfactants. Furthermore, it is possible that the presence of cyclohexane at the centre of the micelles leads to a higher bending rigidity of the amphiphilic film. This would also explain the improved efficiency and the larger structures [299].

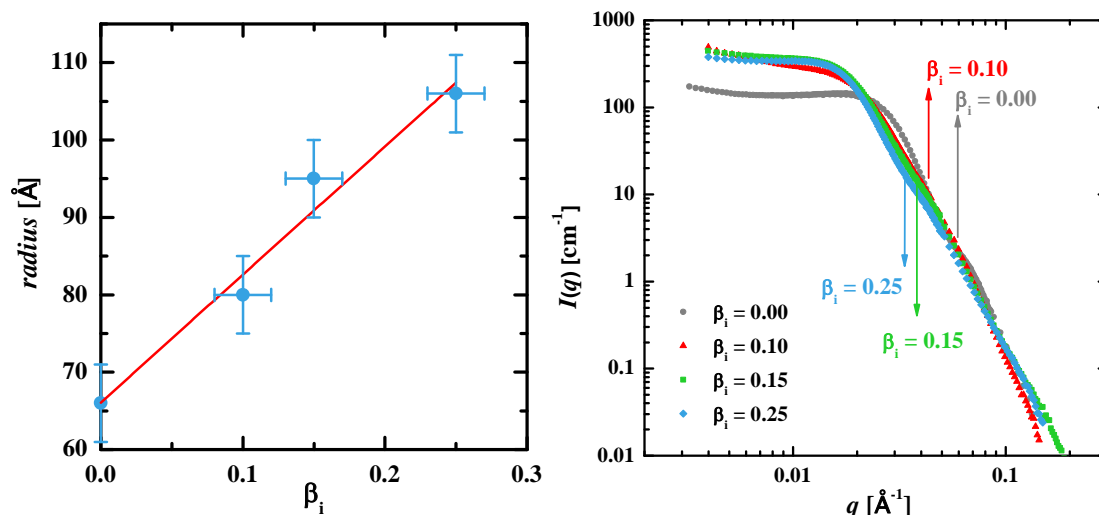


Figure 3.18: *Left:* Plot of the spherical droplet radius obtained from fitting scattering curves of the system brine – CO₂/cyclohexane – Zonyl FSO 100/ Zonyl FSN 100 at $\gamma_a = 0.08$, $\delta_{FSN} = 0.75$, $\varepsilon = 0.01$, $p = 150$ bar ($p = 200$ bar at $\beta_i = 0.25$), $w_B = 0.10$ and $T = 28^\circ\text{C}$ and different mass fractions β_i . The droplet radius depends linearly on the amount of cyclohexane in the hydrophobic phase (red fitting function). *Right:* In order to verify the trend shown left the respective scattering curves are plotted together. The forward scattering intensity increases upon addition of cyclohexane. Furthermore, both the characteristic oscillations as well as the scattering intensity in the medium q -range shift to lower q -values and thus to larger structures with increasing β_i .

3.2.2 Pressure jumps within the thermodynamically stable state

Based on the investigation of the microstructure the discussed microemulsion systems ($\beta_i = 0.10, 0.15$ and 0.25) were also used to investigate the influence of cyclohexane on the kinetics of structural changes as a response to a sudden pressure jump within the thermodynamically stable state of the microemulsion.

Thus, the first kinetic experiment was performed on the system brine – CO₂/ cyclohexane – Zonyl FSO 100/ Zonyl FSN 100 ($\gamma_a = 0.08$, $\delta_{FSN} = 0.75$, $\varepsilon = 0.01$) at $w_B = 0.10$, $\beta_i = 0.10$ and $T = 28^\circ\text{C}$ using the stroboscopic high-pressure SANS cell (see section 2.4.5). The pressure jumps were adjusted to be between $p_{\text{high}} = 300$ bar and $p_{\text{low}} = 150$ bar whereby each pressure was held for 2.5 s, meaning that the duration of one pressure cycle was 5 s and thus had a frequency of 0.2 Hz. Since the experiment was performed using LISTMODE data acquisition (see chapter 2.4.6) it was not necessary to define a time resolution prior to the experiment. The scattering curves as a function of time are shown in Figure 3.19. Thereby, negative times correspond to $p = 300$ bar, the time of the pressure jump was set to zero and positive times consequently refer to $p = 150$ bar. For this plot a rather low time resolution of $t_S = 0.2$ s was applied. As can be seen especially the forward scattering intensity strongly increases after the pressure jump from 150 bar to 300 bar which is consistent with the results obtained from static measurements (Figure 3.13) and can be explained by a change from spherical to elongated microemulsion droplets. Furthermore, considering the intermediate q -range, it is possible to

follow the vanishing of the so-called shoulder of the scattering curve which defines the transition to the q^{-4} dependence of the scattering intensity. The major decrease of forward scattering intensity after the pressure jump to $p = 150$ bar cannot be resolved with this time resolution. However, a slight change of scattering intensity at very low q -values is noticeable at the end of the pressure cycle. The development of the shoulder of the scattering intensity seems to occur on a similar time scale as its vanishing.

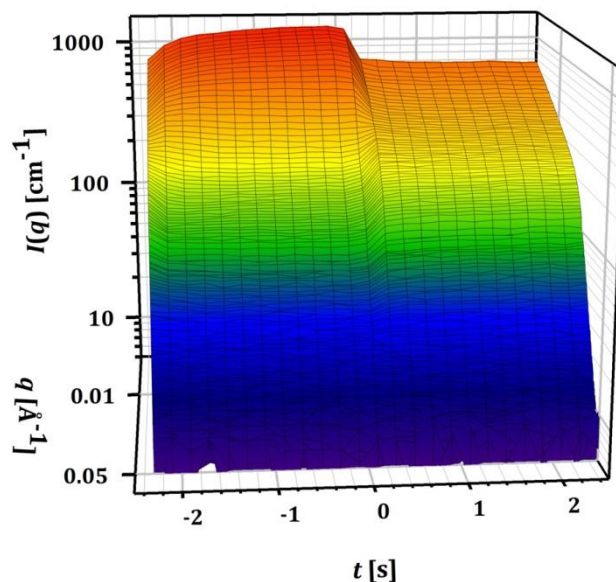


Figure 3.19: Pressure-dependent scattering curves as a function of time for the microemulsion system $D_2O/NaCl - CO_2/cyclohexane - Zonyl\ FSO\ 100/ Zonyl\ FSN\ 100$ ($\gamma_a = 0.08$, $\delta_{FSN} = 0.75$, $\varepsilon = 0.01$) at $\beta_1 = 0.10$, $w_B = 0.10$ and $T = 28^\circ C$. The pressure cycle starts at $p = 300$ bar at $t = -2.5$ s, until after 2.5 s at $t = 0$ s the pressure is changed to 150 bar for 2.5 s. A time resolution of 0.2 s was applied.

In order to follow the kinetic processes in more detail selected scattering curves from Figure 3.19 are shown in Figure 3.20. Comparing the scattering curve shortly after the pressure jump to 300 bar (blue) one finds that the scattering curve recorded 0.3 s after the pressure jump already displays characteristic features of elongated structures, for example a more gradual turnover to the q^{-4} dependence at high q -values. It is clearly visible that the reorganisation in the following 2 s (to the scattering curve recorded 2.2 s after the pressure jump (green) leads to a considerable change of scattering intensity especially in the low q -region. Comparing this behaviour to the scattering curves recorded 0.3 s (red) and 2.3 s (violet) after the pressure jump to $p = 150$ bar one finds that the difference of scattering behaviour is considerably lower between these two scattering curves, indicating that the breakdown of long elongated structures is faster than its rebuilding. This is consistent with results found for the reference system without cyclohexane [56]. The slight decrease of scattering intensity in the low q -region at $p = 150$ bar occurs with a power law of less than q^{-1} and can be attributed to critical scattering, as was also observed for the static scattering curve (Figure 3.13).

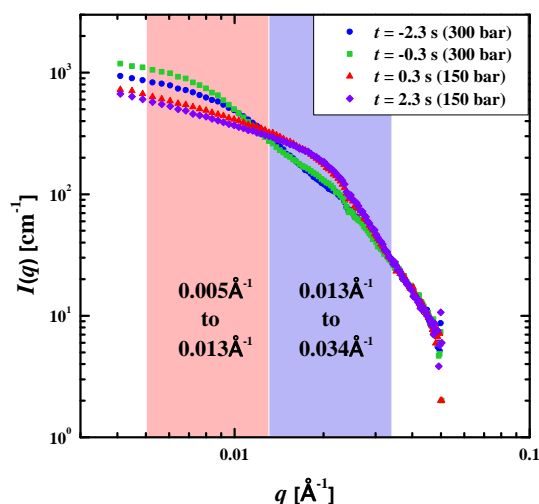


Figure 3.20: Selected scattering curves of the same system from the pressure jump from 300 bar to 150 bar (Figure 3.19). The blue and green scattering curves are recorded at $p = 300$ bar, 0.2 s (blue) and 2.2 s (green) after the pressure jump to 300 bar, respectively, as indicated by negative times. The red and violet scattering curves correspond to 0.2 s (red) and 2.2 s (violet) after the pressure jump to 150 bar. The scattering curves have an isosbestic point at $q = 0.013 \text{ \AA}^{-1}$ and overlap for $q \geq 0.034 \text{ \AA}^{-1}$.

In order to quantitatively follow the structural changes shown in Figure 3.19 it is useful to analyse the scattering intensity recorded for different q -ranges. Prior to integrating the intensity the appropriate q -ranges have to be defined. As the results of these experiments are supposed to be compared to the reference system without cyclohexane it is reasonable to apply the same q -ranges [56]. By comparing the scattering curves of the kinetic measurement (see Figure 3.20) an isosbestic point at $q = 0.013 \text{ \AA}^{-1}$ was identified as well as an overlap for $q \geq 0.034 \text{ \AA}^{-1}$. Therefore, the q -regions $0.005 \text{ \AA}^{-1} \leq q \leq 0.013 \text{ \AA}^{-1}$ and $0.013 \text{ \AA}^{-1} \leq q \leq 0.034 \text{ \AA}^{-1}$ were used for analysing the time-dependent scattering behaviour. The results of these integrations together with the plot shown in Figure 3.19 at a slightly different perspective are shown in Figure 3.21 where the normalised integrated intensity ($ni(t)$) is plotted as a function of time for the two q -ranges. For a better clarification the pressure profile for the pressure jump, which of course also applies for the scattering curves shown left, is shown at the top.

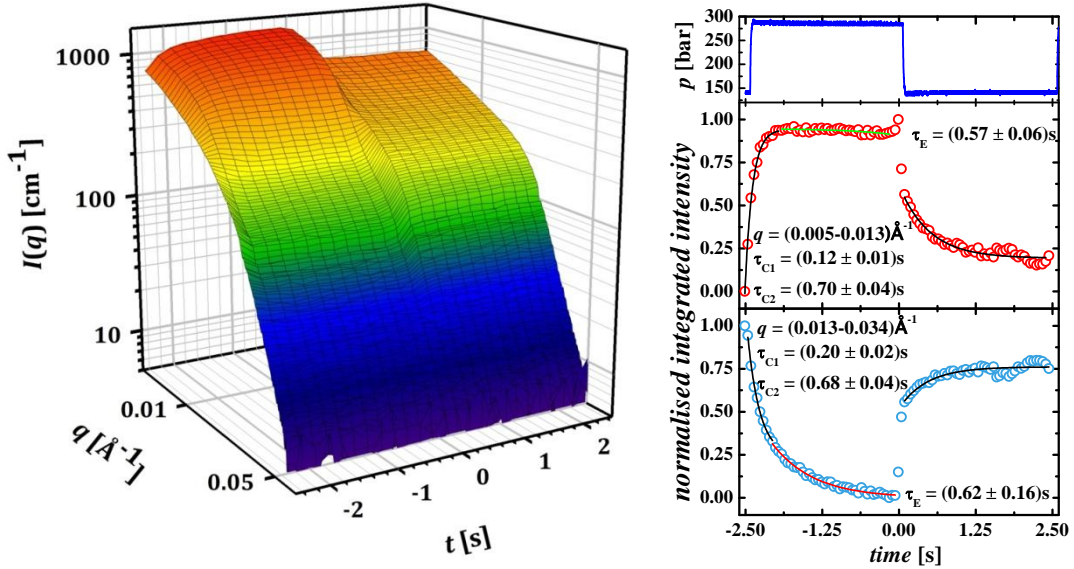


Figure 3.21: *Left:* 3D-plot of scattering curves recorded during a pressure-jump from $p = 150$ bar to $p = 300$ bar as a function of time for the system $D_2O/NaCl - CO_2/cyclohexane - Zonyl FSO 100/ Zonyl FSN 100$ ($\gamma_a = 0.08$, $\delta_{FSN} = 0.75$, $\varepsilon = 0.01$) at $\beta_i = 0.10$, $w_B = 0.1$ and $T = 28^\circ C$, as shown in Figure 3.19 from a different perspective. *Right:* Normalised integrated intensity as a function of time for two q -ranges ($0.005 \text{ \AA}^{-1} \leq q \leq 0.013 \text{ \AA}^{-1}$ (red) and $0.013 \text{ \AA}^{-1} \leq q \leq 0.034 \text{ \AA}^{-1}$ (blue)) with a time resolution of $t_S = 0.05$ s. The lines represent exponential fits of the form $y \sim \exp(-t/\tau)$ whereby the respective time constants τ for compression (τ_C) and expansion (τ_E) are shown in the graph. Note that the pressure profile applies for both $nii(t)$ and the plot at the left.

The course of normalised integrated intensity was found to be of exponential dependence and was fitted according to

$$nii(t) \propto 1 - e^{-\frac{t}{\tau}} \quad \text{Eq. 3-2}$$

if the intensity increases and according to

$$nii(t) \propto e^{-\frac{t}{\tau}} \quad \text{Eq. 3-3}$$

in the case of decreasing intensity with τ being the respective time constant.

Using Eq. 3-2 and Eq. 3-3 it was possible to describe the $nii(t)$ shown in Figure 3.21 right, i.e. time constants for the relaxation processes could be determined. However, the dependence of $nii(t)$ in the low q -regime after compression could not be described with a mono-exponential fitting function but two fits were necessary. The two time constants τ_{C1} and τ_{C2} indicate that a first and fast process occurs which can be interpreted as the initial elongation and merging of spherical droplets to several small, polydisperse micelles. The second, slower process with negative amplitude can thus be considered a reordering process and further elongation. This is also indicated by the scattering curves shown in Figure 3.20, where the forward scattering intensity decreases with time. Here, the micelles seem to be much longer at $t = -0.3$ s than at $t = -2.3$ s. Regarding the processes described by the second q -regime one finds that here, in contrast, it is possible to describe the time-dependence of $nii(t)$ with a single exponential fit with a time constant of $\tau_C = 0.56 \pm 0.02$ (fit not shown). This is another indication that the

elongation of the structure takes place all the time at this pressure and is not a fast process. Considering the two processes which occur in the low q -range it is also possible to describe the $iii(t)$ with two fitting functions as shown in Figure 3.21 right.

The processes after expansion could be described with a single exponential function for both q -regimes which is an indication that the breakdown of elongated structures occurs more homogeneously. Furthermore, the time constants for both q -regions are in a similar range which points to the same direction. The results for the system without cyclohexane lead to the assumption that the breakdown of elongated structures occurs faster than 0.1 s and that the observed processes with a time constant of $\tau_E = (0.52 \pm 0.05)$ s represent minor reordering processes such as reducing polydispersity. Since here it is also the case that the difference between the scattering curves are very small (see Figure 3.20 right) it can be assumed that also reordering processes are observed. Note that it was not possible to include the first two data points after expansion into the fitting functions.

Therefore, another pressure jump experiment was performed with a shorter pressure cycle in order to investigate the processes which happen right after expansion in more detail. For this experiment the pressure p_{high} was set to 280 bar and the pressure p_{low} to 140 bar. The scattering curves as a function of time are shown in Figure 3.22.

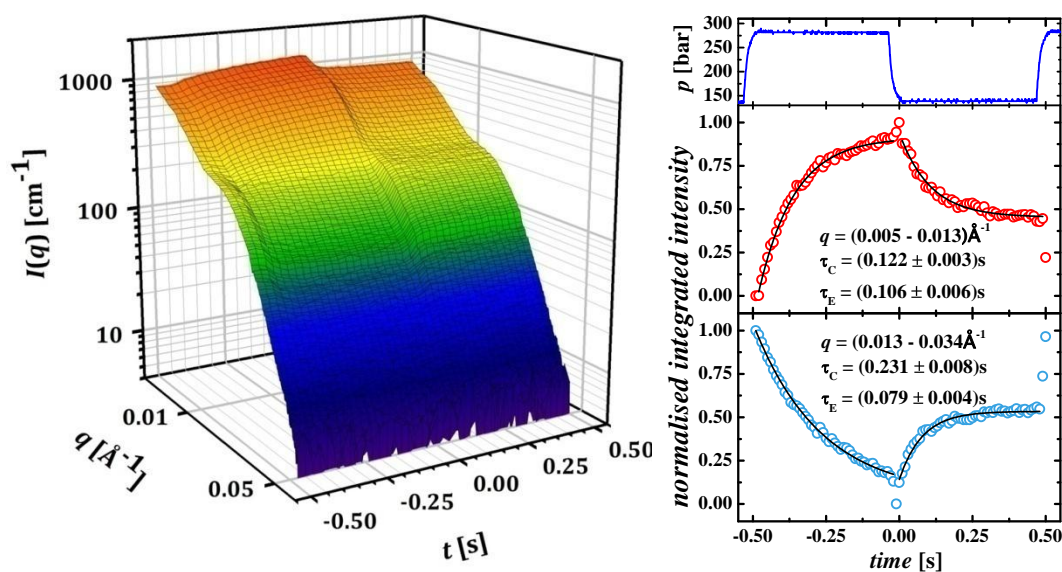


Figure 3.22: *Left:* Pressure-dependent scattering curves as a function of time for the system $\text{D}_2\text{O}/\text{NaCl} - \text{CO}_2/\text{cyclohexane} - \text{Zonyl FSO 100}/\text{Zonyl FSN 100}$ ($\gamma_a = 0.08$, $\delta_{\text{FSN}} = 0.75$, $\varepsilon = 0.01$) at $\beta_i = 0.10$, $w_B = 0.10$ and $T = 28^\circ\text{C}$. The pressure cycle was adjusted to start at $p_{\text{high}} = 280$ bar and that pressure was held for 0.5 s until the pressure jump (at $t = 0$ s) occurs to $p_{\text{low}} = 140$ bar which was also held for 0.5 s. For this plot a time resolution of $t_S = 0.025$ ms was applied. *Right:* Normalised integrated intensity as a function of time for two different q -regions as indicated in the plot with a time resolution of 0.01 s. The data were fitted with an exponential function of the form $y \sim \exp(-t/\tau)$. The according time constants are shown in the graph. The pressure profile shown at the top applies also for the plot shown left.

The scattering curves in Figure 3.22 left at $p = 140$ bar indicate that the equilibrium state is not yet reached at the end of the pressure cycle which can be explained by the shorter time the system was kept at this pressure compared to the previous experiment. Considering the $n_{ii}(t)$ shown in Figure 3.22 right this also seems to be valid for the system at $p = 300$ bar, as there is no plateau of the scattering intensity which would indicate a thermodynamically stable state. The time constants for the processes after compression match the ones which were found in the previous experiment for both q -regions. This is especially interesting in the case of the low q -region for which the two time constants describing the fast process are exactly the same, which validates the procedure of two fitting functions instead of one in the case of medium q -values. This indicates that the second pressure jump as shown in Figure 3.22 describes the first 500 ms of the pressure jump shown in Figure 3.21. Regarding the processes after expansion it turned out that the immediate processes occur on a time scale of 0.1 s in the low q -range and with a time constant of 80 ms in the medium q -range. This confirms the assumption which was previously published that the breakdown of elongated structures is faster than 0.1 s [56]. Scattering curves recorded right after expansion are shown in Figure 3.23 right. Before taking a close look at these one needs to consider that the pressure jump itself needs about 30 ms to be completed. Thus, the scattering curve which is described to be recorded at $t = 0.025$ s is likely to correspond to non-constant pressure.

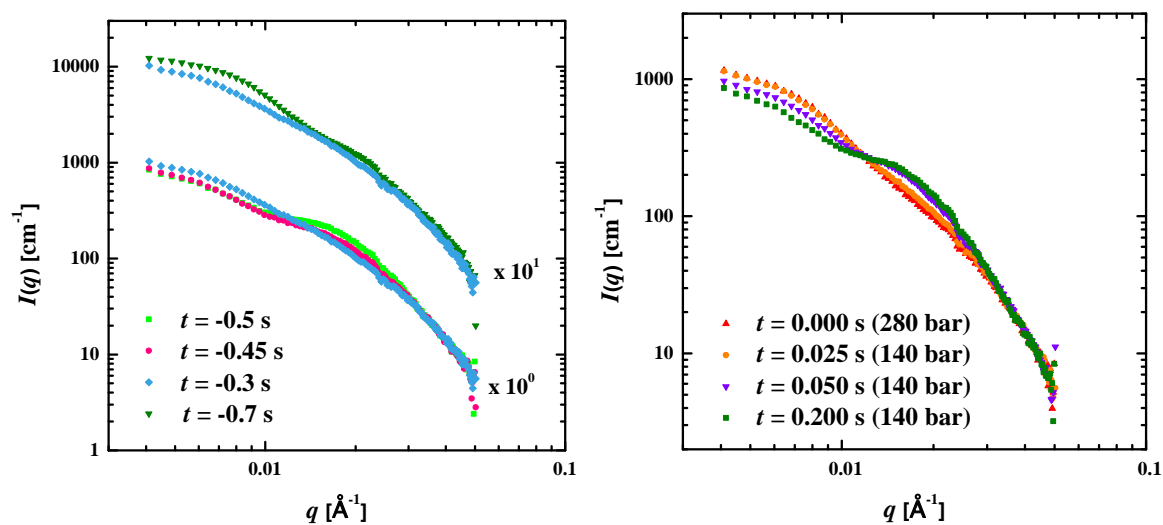


Figure 3.23: *Left:* Selected scattering curves from the pressure jump described in Figure 3.22 (time resolution $t_s = 0.25$ s) recorded at ($t = -0.5$ s) and slightly after compression ($t = -0.45$ and -0.3 s). The increase of intensity in the low q -regime is clearly connected to an elongation process which can be seen by the vanishing of the scattering shoulder at intermediate q -values. Comparing this scattering curve to one recorded 1.8 s after the pressure jump (green downward triangles, $t = -0.7$ s, taken from Figure 3.19) shows that the second process displays ordering processes. *Right:* Selected scattering curves from the pressure jump described in Figure 3.22 (time resolution $t_s = 0.25$ s) recorded before the pressure jump to 150 bar ($t = 0.0$ s, red triangles), during the pressure jump ($t = 0.025$ s, orange circles) which takes about 30 ms to be completed, and at $t = 0.05$ s after the pressure jump (violet downward triangles). This scattering curve is already very close to the one recorded after $t = 0.2$ s and shows a clear transition to the q^{-4} dependence at higher q -values.

The first scattering curve at constant pressure, at $t = 0.05$ s, already shows the distinct scattering shoulder before the q^{-4} dependence occurs in the higher q -regime. This shoulder becomes more pronounced with time. The fact that the shoulder is already present after 50 ms means that indeed the breakdown of elongated structures to sphere-like droplets is very fast.

Figure 3.23 left shows selected scattering curves at $p = 300$ bar, i.e. after compression. The lower scattering curves represent the structural changes at times close to the pressure jump which takes place at $t = -0.5$ s. The following scattering curves at $t = -0.45$ s and -0.3 s nicely show the process of elongation as the scattering shoulder which is characteristic for spherical structures vanishes and simultaneously the forward scattering increases. However, this scattering curve does not show any characteristic oscillations which can give information on the length scale of the structure which indicates a high polydispersity of the system. Only by means of scattering curves recorded much later after the pressure jump (1.8 s, $t = -0.7$, taken from Figure 3.19) one finds characteristics such as an oscillation. This clearly shows that the second process detected by the $nii(t)$ in Figure 3.21 describes reordering and homogenisation processes.

After having investigated the system with 10 wt% cyclohexane the next experiment was to apply a comparable pressure jump to the microemulsion with 15 wt% cyclohexane in the hydrophobic phase. Analogously to the experiment at $\beta_i = 0.10$ shown in Figure 3.19 and Figure 3.21 the pressure jump at $\beta_i = 0.15$ was performed from 280 bar to 140 bar whereby each pressure was held for 2.5 s. At these conditions, the microemulsion also undergoes structural changes from spherical to elongated droplets (see Figure 3.14). The resulting scattering curves as a function of time together with the normalised integrated intensities for two different q -regions are shown in Figure 3.24. The q -regions are the same ones as applied for the previous system and the reference system. The pressure jump at $t = 0$ s is easily visible by the abrupt change of forward scattering intensity in the 3D-plot.

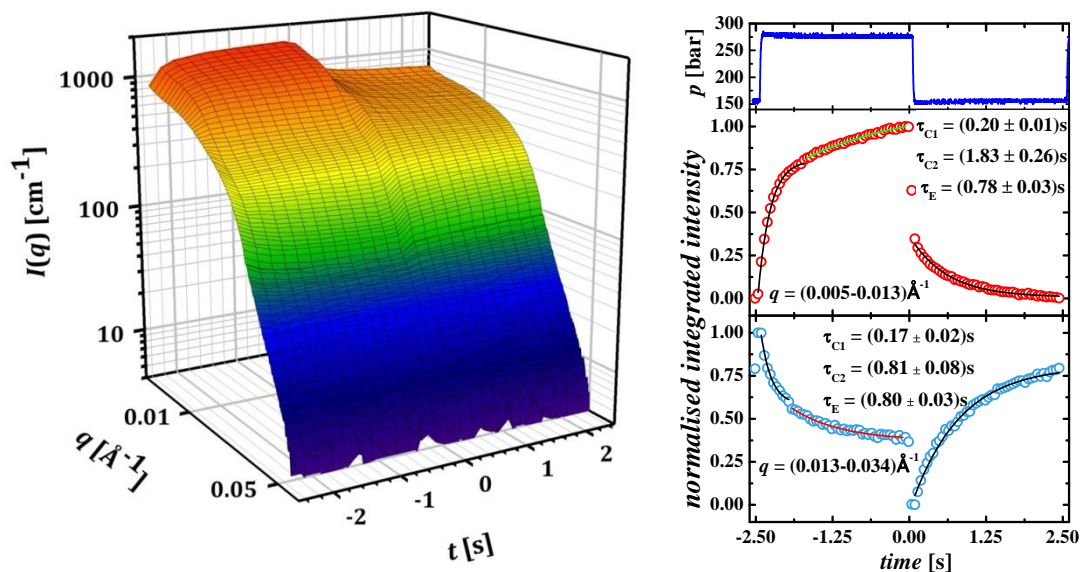


Figure 3.24: *Left:* Pressure-dependent scattering curves as a function of time for the system $\text{D}_2\text{O}/\text{NaCl} - \text{CO}_2/\text{cyclohexane} - \text{Zonyl FSO 100}/\text{Zonyl FSN 100}$ ($\gamma_a = 0.08$, $\delta_{\text{FSN}} = 0.75$, $\varepsilon = 0.01$) at $\beta_i = 0.15$, $w_B = 0.10$ and $T = 28^\circ\text{C}$. The pressure jump from $p = 300$ bar to $p = 150$ bar was set to $t = 0$ s. Each pressure was held for 2.5 s whereby a time resolution of 0.2 s was applied. *Right:* Pressure profile (top) together with the normalised integrated intensity with a time resolution of 0.05 s as a function of time for two q -ranges ($0.005 \text{ \AA}^{-1} \leq q \leq 0.013 \text{ \AA}^{-1}$ (red) and $0.013 \text{ \AA}^{-1} \leq q \leq 0.034 \text{ \AA}^{-1}$ (blue)). The error bars are within the size of the symbols. The lines represent exponential fits with $y \sim \exp(-t/\tau)$. Note that for the processes after compression two exponential fits were necessary to describe the changes of scattering intensity.

As was observed for the system at $\beta_i = 0.10$ it was also not possible to describe the $nii(t)$ in the low q -region by a mono-exponential fitting function. Two functions were necessary which clearly points to a similar process as described for the previous experiment, meaning that first disordered elongation processes happen before the system equilibrates to a less polydisperse state. This is also the reason why the $nii(t)$ in the medium q -range were fitted with two exponential fits rather than one which is also possible and leads to a time constant of $\tau_C = 0.44 \pm 0.02$ s (fit not shown). Note that the description of the time-dependent change of $nii(t)$ after expansion with a mono-exponential function again excludes two data points, i.e. a time period of 100 ms, at both q -regimes. Since the scattering curves in Figure 3.24 left display the characteristic shoulder right after the pressure jump it can be assumed that the formation of spherical droplets occurs on a time scale comparable to the previous experiment. The time constants for these processes are slightly higher than for the system at $\beta_i = 0.10$, indicating that the reordering process is slower here. Since reordering processes likely include diffusion processes of hydrophobic substance between micelles it seems reasonable that this process is slower at a higher cyclohexane content since the solubility of cyclohexane in water is much lower than the one of CO_2 in water.

The microemulsion system with 25 wt% cyclohexane in the hydrophobic phase differs considerably from the other two described systems. The analysis of phase behaviour and the

static scattering curves shown in Figure 3.16 revealed that at the chosen parameters of $w_B = 0.10$ and $T = 28^\circ\text{C}$ no one-phase region was found at $p = 150$ bar. Hence, the pressure jump experiment could not be performed at $p_{\text{high}} = 300$ bar and $p_{\text{low}} = 150$ bar since this would lead to a demixing of the microemulsion which was not sought to achieve in the series of experiments. Therefore, the pressure p_{low} was adjusted to 200 bar where a thermodynamically stable one-phase region exists, and all other parameters were kept constant. The results in form of a 3D-plot of the scattering intensity are shown in Figure 3.25 left, together with the respective pressure profile and normalised integrated intensities (right). The investigation of the microstructure already showed that spherical structures are present at all pressures (see Figure 3.16). Although these droplets have a slightly different size the general microstructure is the same, which is the reason why the difference of scattering intensity in Figure 3.25 is very low at different pressures.

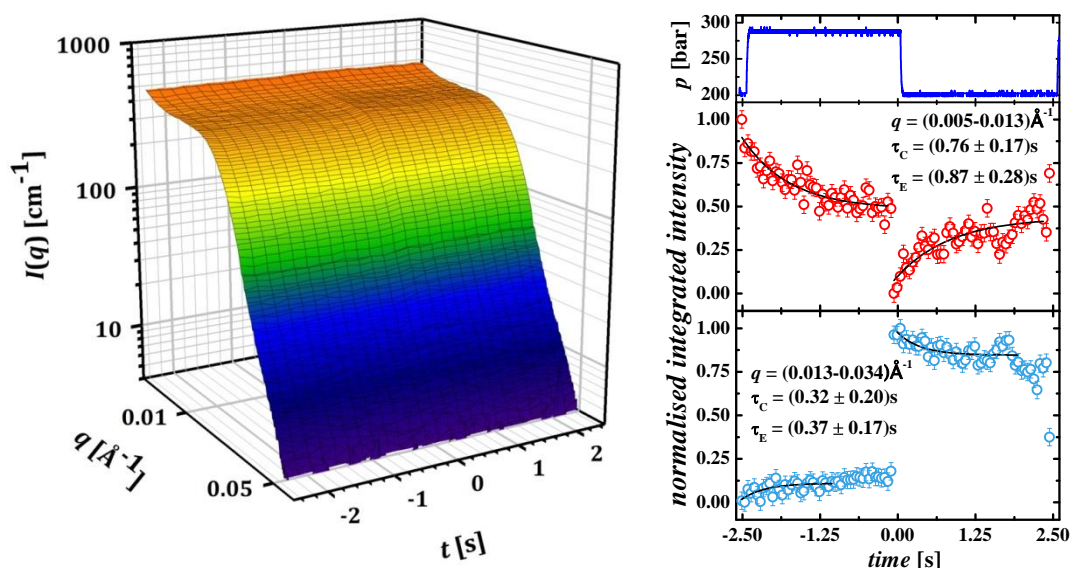


Figure 3.25: *Left:* Scattering curves at two different pressures as a function of time for the system $\text{D}_2\text{O}/\text{NaCl} - \text{CO}_2/\text{cyclohexane} - \text{Zonyl FSO 100}/\text{Zonyl FSN 100}$ ($\gamma_a = 0.08$, $\delta_{\text{FSN}} = 0.75$, $\varepsilon = 0.01$) at $\beta_i = 0.25$, $w_B = 0.10$ and $T = 28^\circ\text{C}$. The pressure cycle starts at $p = 290$ bar at $t = -2.5$ s, until after 2.5 s at $t = 0$ s the pressure is changed to 200 bar for 2.5 s. A time resolution of 0.2 s was applied. Obviously, the scattering intensity does not change much between the different pressures. *Right:* Normalised integrated intensity (time resolution 0.05 s) as a function of time for two q -ranges ($0.005 \text{ \AA}^{-1} \leq q \leq 0.013 \text{ \AA}^{-1}$ (red)) and $0.013 \text{ \AA}^{-1} \leq q \leq 0.034 \text{ \AA}^{-1}$ (blue)). The pressure profile which is also valid for the plot at the left is shown at the top. The black lines represent exponential fits proportional to $\exp(-t/\tau)$. Since the amplitude of the change is very low (see 3D-plot left) the data points scatter very much and thus the errors of the fitting functions are high.

Although the scales of $nii(t)$ in Figure 3.25 right range from 0 to 1 the amplitude of difference of scattering intensity is rather low, as can be seen by the scattering curves shown left. This low amplitude is also the reason why the data points vary a lot among each other compared to the previous systems. Nevertheless, it was possible to describe the time-dependency of the scattering intensity with mono-exponential fitting functions, whereby one function was

sufficient in all cases. The lack of a first, fast process visible after compression in the low q -region is very likely due to the fact that the microstructure does not undergo a change to elongated structures here, as was the case for the other systems. The time constants found for this experiment are in the range of the previous results, indicating that mainly reordering processes are observed here.

3.2.3 Influence of cyclohexane on changes of microstructure

The kinetics of pressure-induced structural changes of the system $D_2O/NaCl - CO_2/cyclohexane - Zonyl\ FSO\ 100/ Zonyl\ FSN\ 100$ ($\gamma_a = 0.08$, $\delta_{FSN} = 0.75$, $\varepsilon = 0.01$) at $w_B = 0.10$, $T = 28^\circ C$, studied at three cyclohexane contents $\beta_i = 0.10, 0.15$ and 0.25 were described in section 3.2.2. These experiments were performed within the thermodynamically stable region and composition and temperature of these experiments were adjusted to be comparable to previous results of the cyclohexane-free system [29, 56] and the system with 20 wt% cyclohexane at similar conditions. The system at $\beta_i = 0.25$ consists of spherical structures at all pressures and thus is different from the others where elongated structures can be found at $p \geq 200$ bar. Table 3-8 summarises all time constants for pressure jumps within the thermodynamically stable state. The q -regimes $0.005 \text{ \AA}^{-1} \leq q \leq 0.013 \text{ \AA}^{-1}$ and $0.013 \text{ \AA}^{-1} \leq q \leq 0.034 \text{ \AA}^{-1}$ were set due to an isosbestic point at $q \approx 0.013 \text{ \AA}^{-1}$.

Table 3-8: Overview of time constants obtained from pressure jumps within the thermodynamically stable state of the system $D_2O/NaCl - CO_2/cyclohexane - Zonyl\ FSO\ 100/ Zonyl\ FSN\ 100$ ($\gamma_a = 0.08$, $\delta_{FSN} = 0.75$, $\varepsilon = 0.01$) at $w_B = 0.10$, $T = 28^\circ C$ and for different values of $\beta_i = 0.00, 0.10, 0.15, 0.20$ and 0.25 . The time constants for the systems at $\beta_i = 0.10, 0.15$ and 0.25 are also displayed in the respective graphs in section 3.2.2 whereas the values for $\beta_i = 0.00$ and 0.20 were taken from [56] and [29]. Note that the data in [29] for $\beta_i = 0.20$ were re-evaluated.

β_i	w_B	T [°C]	p_{high} [bar]	p_{low} [bar]	$0.005 \text{ \AA}^{-1} \leq q \leq 0.013 \text{ \AA}^{-1}$		$0.013 \text{ \AA}^{-1} \leq q \leq 0.034 \text{ \AA}^{-1}$	
					$\tau_{compression}$ [s]	$\tau_{expansion}$ [s]	$\tau_{compression}$ [s]	$\tau_{expansion}$ [s]
0.00	0.10	28	300	150	0.63 ± 0.05	0.52 ± 0.05	0.59 ± 0.05	< 100 ms
0.10	0.10	28	300	150	0.12 ± 0.01	0.11 ± 0.01	0.20 ± 0.02	0.080 ± 0.004
					0.70 ± 0.04	0.57 ± 0.06	0.68 ± 0.04	0.62 ± 0.16
0.15	0.10	28	300	150	0.20 ± 0.01	0.78 ± 0.03	0.17 ± 0.02	0.80 ± 0.03
					1.8 ± 0.30		0.81 ± 0.08	
0.20	0.12	32.5	300	150	0.29 ± 0.01	1.18 ± 0.05	0.26 ± 0.01	1.11 ± 0.05
					1.05 ± 0.15		0.40 ± 0.04	
0.25	0.10	28	300	200	0.76 ± 0.17	0.87 ± 0.28	0.32 ± 0.23	0.37 ± 0.17

The time constants in Table 3-8 as a function of cyclohexane content β_i are shown graphically in Figure 3.26. There, two basic trends become obvious. Considering the process after expansion (blue hollow squares) it becomes obvious that this process is systematically

decelerated with increasing cyclohexane content, up to a factor of 2 at $\beta_i = 0.20$. Since the breakdown of elongated structures to spherical droplets is too fast for observation this process is likely the formation of spherical droplets from cylinder fragments. Note that the data points for $\beta_i = 0.25$ represent a sphere-sphere transition rather than the transition from elongated to spherical structures which is why these data points should not be considered.

In most cases two time constants can be found after compression. The first time constant (filled red circles) for almost all systems containing cyclohexane is lower than the one found for the reference system. With increasing cyclohexane concentration, however, a deceleration trend can be observed, leading to the assumption that the process described here might not be resolved at $\beta_i = 0.00$. From the scattering curves it is assumed that this process represents the elongation of spherical droplets and first merging processes.

The time constants of the second, slower process are in the range of the one found for the reference system (hollow purple circles). This process is assumed to be ordering to less polydisperse spheres. A deceleration can only be found up to 15 wt% cyclohexane. Here, however, the higher temperature at $\beta_i = 0.2$ might trigger a faster process.

Considering the results for both q -regions and both pressure jumps, one can state that structural changes from elongated to spherical droplets, and vice versa, are systematically decelerated by cyclohexane for microemulsions of the type brine – CO₂/cyclohexane – fluorinated surfactants.

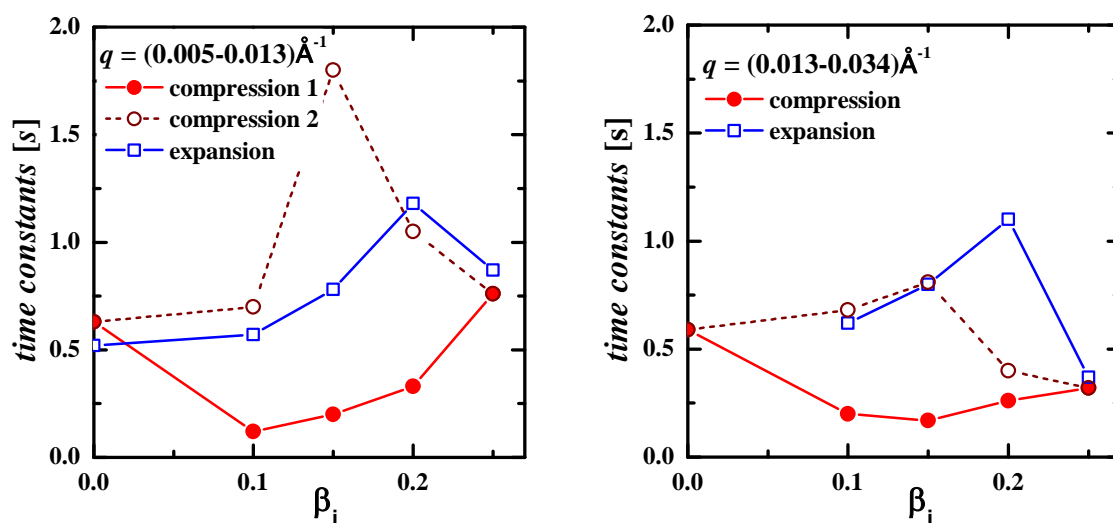


Figure 3.26: Graphical overview of different time constants obtained from pressure jumps with the system D₂O/NaCl – CO₂/cyclohexane – Zonyl FSO 100/ Zonyl FSN 100 ($\gamma_a = 0.08$, $\delta_{FSN} = 0.75$, $\varepsilon = 0.01$) at similar composition and temperature and various cyclohexane contents β_i for two different q -regions. Thereby, the expansion (blue hollow squares) represents the breakdown of elongated structures to spherical droplets, which are obviously decelerated with increasing cyclohexane content. After compression, two processes can be observed. While the first and fast process (red filled circles) happens faster than the process at the reference system the second process displays time constants in the same range or higher. Especially the first process is decelerated with increasing β_i . The data at $\beta_i = 0.25$ represent a sphere-sphere transition and can thus not be compared.

3.2.4 Pressure jumps to thermodynamically unstable states

Starting from the points marked with a star in the phase diagrams in the section 3.2.1 the demixing kinetics of the respective microemulsions were investigated by performing pressure jumps to $p = 70$ bar. At this pressure, composition and temperature a CO₂-in-water microemulsion coexists with a CO₂-excess phase in all systems. Similar to the previous chapter the composition and the temperature were kept constant in order to allow comparing all systems to the cyclohexane-free system. This time, however, the structure at p_{high} , i.e. at the thermodynamically stable state, consists of spherical droplets in all cases.

Thus, the first pressure jump experiment was performed at the system with 10 wt% cyclohexane in the hydrophobic phase. p_{high} was adjusted to 150 bar and p_{low} to 70 bar which is in a two-phase region of the microemulsion system. Each pressure was kept for 2.5 s. The scattering curves at different pressures and as a function of time are shown in Figure 3.27. As can be seen the forward scattering intensity constantly increases after the pressure jump to 70 bar at $t = 0.0$ s. Furthermore, the scattering shoulder in the medium q -range disappears after the pressure jump.

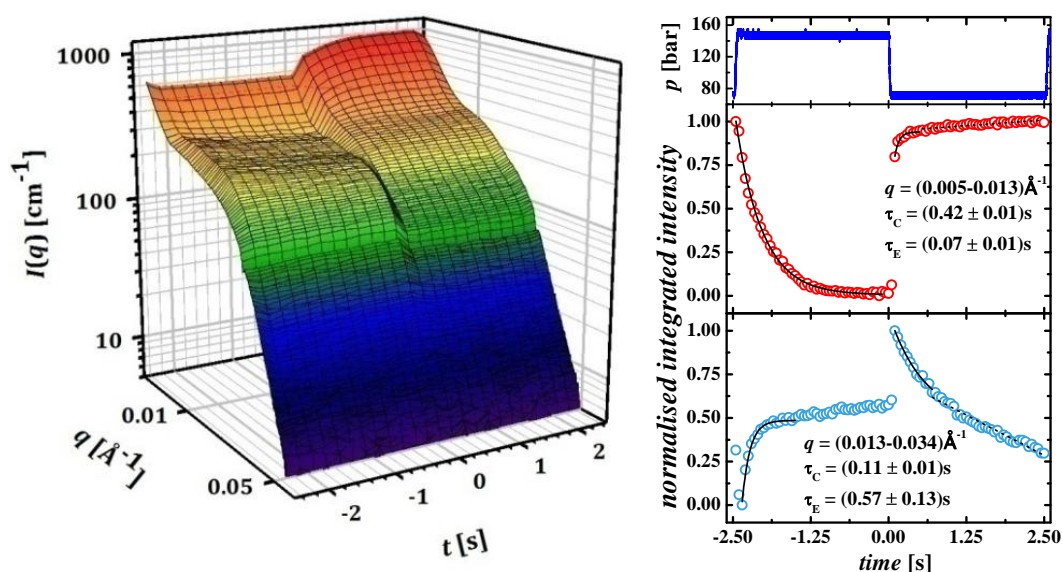


Figure 3.27: *Left:* Pressure-dependent scattering curves as a function of time for the system D₂O/NaCl – CO₂/cyclohexane – Zonyl FSO 100/ Zonyl FSN 100 ($\gamma_a = 0.08$, $\delta_{\text{FSN}} = 0.75$, $\varepsilon = 0.01$) at $\beta_i = 0.10$, $w_B = 0.10$ and $T = 28^\circ\text{C}$. Starting at $p = 300$ bar at $t = -2.5$ s this pressure was held for 2.5 s so that the pressure is changed to 150 bar at $t = 0$ s and also held for 2.5 s. A time resolution of 0.2 s was applied. *Right:* Normalised integrated intensity as a function of time for two q -ranges ($0.005 \text{ \AA}^{-1} \leq q \leq 0.013 \text{ \AA}^{-1}$ (red) and $0.013 \text{ \AA}^{-1} \leq q \leq 0.034 \text{ \AA}^{-1}$ (blue)) with a time resolution of 0.05 s, together with the pressure profile (top). The black lines represent exponential fits proportional to $\exp(-t/\tau)$ whereby the respective time constants τ for compression (τ_c) and expansion (τ_e) are shown in the graph. The dashed line indicates a region of linear dependency which will be discussed later in this section. Note that the error bars lie within the symbol size.

The time-dependent normalised integrated intensities ($nii(t)$) for two different q -regimes are shown in Figure 3.27 right and the integration limits are the same ones applied in the previous chapter. The time

constants for the process after compression indicate that the spherical droplet structure at $p = 150$ bar is reformed on a time scale of less than half a second. The processes after expansion, however, seem to be of completely different nature. While the first data points after expansion can be described by an exponential function this process is followed by a linear decrease of the scattering intensity in the medium q -range and a linear increase of intensity in the low q -range. The time constants for the exponential process indicate that the process followed at low q which represents the formation of large emulsion droplets occurs much faster than the process observed in the medium q range. This is reasonable considering that already few emulsion droplets influence the forward scattering intensity whereas the vanishing of the droplet structure requires that most of the microemulsion droplets form emulsion droplets before the scattering shoulder diminishes.

The second experiment was performed on the microemulsion system containing 15 wt% cyclohexane in the hydrophobic phase. Again, the time-dependent scattering curves at $p_{\text{high}} = 160$ bar and $p_{\text{low}} = 70$ bar are shown together with the $nii(t)$ in Figure 3.28. The scattering curves show that the forward scattering intensity increases immediately after expansion while the scattering intensity after compression remains constant, indicating a thermodynamically stable state at p_{high} .

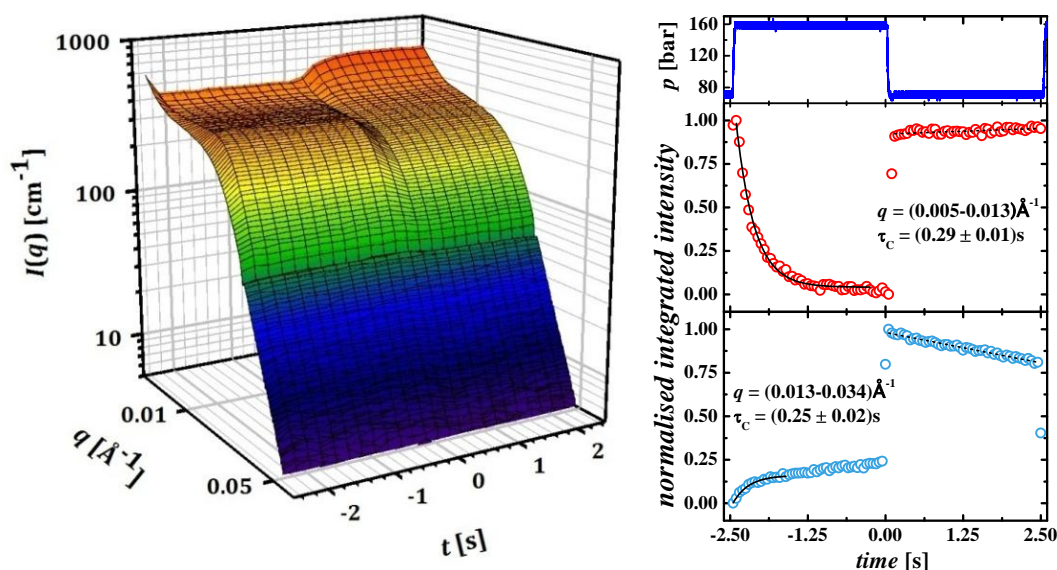


Figure 3.28: *Left:* 3D-plot of scattering curves as a function of time for the system $\text{D}_2\text{O}/\text{NaCl} - \text{CO}_2/\text{cyclohexane} - \text{Zonyl FSO 100}/\text{Zonyl FSN 100}$ ($\gamma_a = 0.08$, $\delta_{\text{FSN}} = 0.75$, $\varepsilon = 0.01$) at $\beta_1 = 0.15$, $w_B = 0.10$ and $T = 28^\circ\text{C}$. Starting at $p = 160$ bar for 2.5 s, the pressure jump was set to happen at $t = 0$ s to 70 bar which was held for 2.5 s. The scattering curves are shown with a time resolution of 0.2 s. *Right:* Time-dependent normalised integrated intensity with a time resolution of 0.05 s shown for two different q -regions. The pressure profile at the top applies also to the plot at the left. The black lines represent exponential fits proportional to $\exp(t/\tau)$. The dashed line indicates a region of linear dependency which will be discussed later in this section. Note that the error bars are smaller than the symbols.

The $nii(t)$ as a function of time (Figure 3.28 right) show a linear dependency of the scattering intensity immediately after expansion, indicating that the demixing process starts as soon as p_{low} is reached. The

relaxation after compression back to the thermodynamically stable state can be described with a single-exponential fitting function for both q -regions, leading to time constants for this process which are in the same order of magnitude of about 0.3 s.

The third pressure jump to the thermodynamically unstable state was performed with the microemulsion system at $\beta_i = 0.25$. Since the examination of the phase behaviour showed that this system is not in a one-phase region at $w_B = 0.10$ and $p = 150$ bar (see Figure 3.16) the pressure cycle was slightly changed in comparison to the previous experiment. Thus, p_{high} was adjusted to be 200 bar in order to ensure a stable microstructure at this point of the pressure cycle. Since it was assumed that this experiment should result in a jump deeper into the two-phase region p_{low} was slightly modified to $p_{\text{low}} = 75$ bar. The times at each pressure were kept at the same values as the pressure jumps discussed above. Figure 3.29 left shows the time-dependent scattering curves obtained from this experiment. As can already be seen here the forward scattering intensity decreases after compression which is the opposite trend compared to the experiments at $\beta_i = 0.10$ and 0.15. However, compared to the measurements shown in Figure 3.27 and Figure 3.28 the amplitude of change of the scattering intensity is also very low.

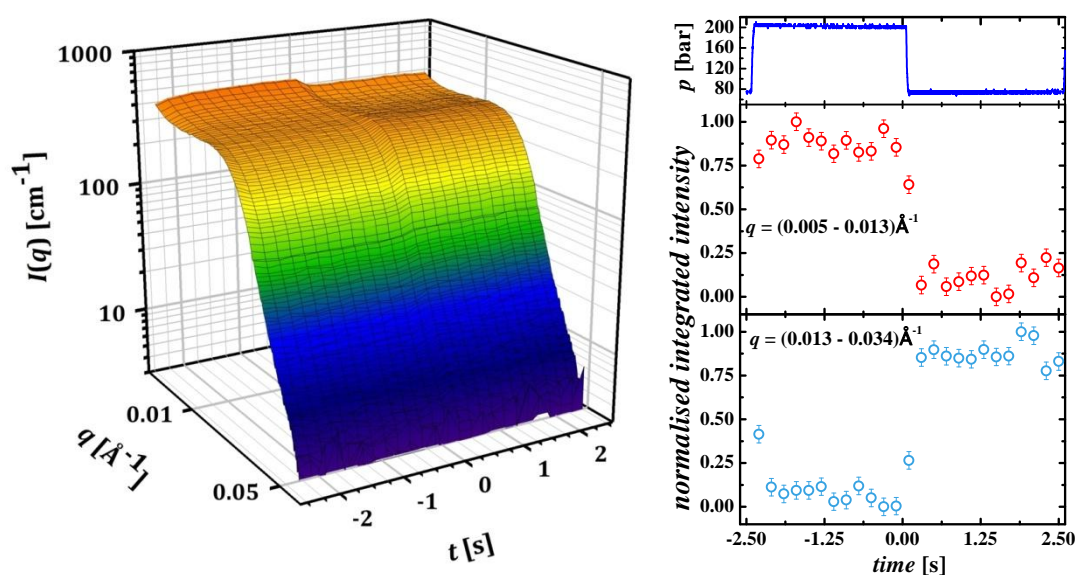


Figure 3.29: *Left:* Scattering curves with a time resolution of 0.2 s recorded after pressure jumps as a function of time for the system $\text{D}_2\text{O}/\text{NaCl} - \text{CO}_2/\text{cyclohexane} - \text{Zonyl FSO 100}/ \text{Zonyl FSN 100}$ ($\gamma_a = 0.08$, $\delta_{\text{FSN}} = 0.75$, $\varepsilon = 0.01$) at $\beta_i = 0.25$, $w_B = 0.10$ and $T = 28^\circ\text{C}$. The pressure cycle starts at $p = 200$ bar at $t = -2.5$ s, until at $t = 0$ s a pressure jump to 75 bar is performed and hold for 2.5 s. As was observed for the pressure jump from 200 to 300 bar (Figure 3.25) the change of scattering intensity is very low at different pressures. *Right:* Normalised integrated intensity as a function of time for two q -ranges ($0.005 \text{ \AA}^{-1} \leq q \leq 0.013 \text{ \AA}^{-1}$ (red) and $0.013 \text{ \AA}^{-1} \leq q \leq 0.034 \text{ \AA}^{-1}$ (blue)). A time resolution of 0.2 s was applied because the values of normalised integrated intensity scatter very much due to the low change of scattering intensity upon the pressure jump (see left). It was not possible to applied exponential fits to the normalised integrated intensity.

The same opposing behaviour can be found considering the $nii(t)$ shown in Figure 3.29 right. Because the scattering intensity changes only slightly after the pressure jumps the time resolution for this plot was chosen to be 0.2 s in order to obtain more reliable data points. Nevertheless, the data points are considerably noisy and do not allow for any time-dependent description of the scattering intensity. It was assumed that either a pressure of 75 bar was too high to induce fast demixing, especially because the oil excess phase is very small, or that the sought demixing with this system occurs on a much longer time scale compared to the other systems. Thus, another experiment was performed in which the pressure p_{low} was lowered to $p_{\text{low}} = 65$ bar in order to jump deeper into the two-phase region and thus trigger a faster demixing process. It needs to be considered that the density of CO_2 changes very much around this pressure which implies that the bellow needs to shrink considerably more to transfer a pressure as low as 65 bar. In order to prevent damage of the bellow the pressure p_{high} was slightly adjusted to 180 bar instead of 200 bar to counteract the size change of the bellow a little. The times of the pressure cycle were kept at 2.5 s at each pressure as in previous measurements. The scattering curves as a function of time obtained from this modified experiment are shown in Figure 3.30 left. Taking a very close look at the scattering curves at $p = 65$ bar, i.e. at $t > 0$ s one finds a small but systematic increase in forward scattering intensity with time, indicating that indeed demixing was achieved with this experiment. The expected linear dependency of $nii(t)$ (Figure 3.30 right) is noticeable, although the amplitude is low, which also indicates slower demixing processes.

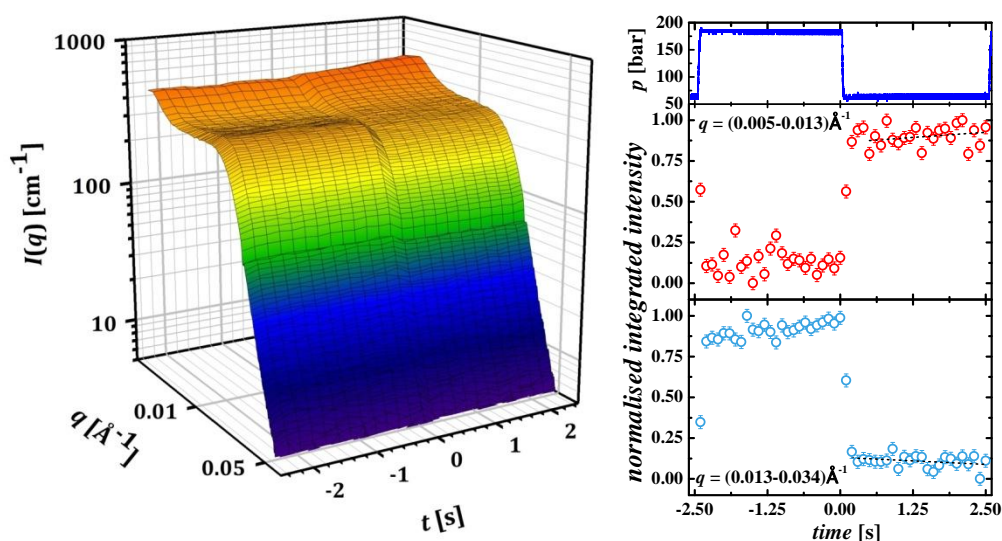


Figure 3.30: *Left:* Time and pressure-dependent scattering curves for the system $\text{D}_2\text{O}/\text{NaCl} - \text{CO}_2/\text{cyclohexane} - \text{Zonyl FSO 100}/ \text{Zonyl FSN 100}$ ($\gamma_a = 0.08$, $\delta_{\text{FSN}} = 0.75$, $\varepsilon = 0.01$) at $\beta_i = 0.25$, $w_B = 0.10$ and $T = 28^\circ\text{C}$. Starting at a high pressure of 180 bar for 2.5 s the pressure jump is performed at $t = 0$ s to $p_{\text{low}} = 65$ bar which was also kept for 2.5 s. As was observed for the pressure jump from 200 to 300 bar (Figure 3.25) the change of scattering intensity is very low at different pressures. *Right:* Normalised integrated intensity as a function of time for two q -ranges. A low time resolution of 0.1 s was applied because the values of normalised integrated intensity scatter very much due to the low change of scattering intensity upon the pressure jump (see left). It was not possible to apply exponential fits to the normalised integrated intensity.

3.2.5 Influence of cyclohexane on kinetics of demixing processes

After having characterised structural changes within the thermodynamically stable states of the microemulsion systems $D_2O/NaCl - CO_2/cyclohexane - Zonyl\ FSO\ 100/ Zonyl\ FSN\ 100$ ($\gamma_a = 0.08$, $\delta_{FSN} = 0.75$, $\varepsilon = 0.01$) at $w_B = 0.10$ and $T = 28^\circ C$ and three cyclohexane contents $\beta_i = 0.10, 0.10$ and 0.25 the influence of cyclohexane on kinetics of the structural changes was studied recording the scattering behaviour after pressure jumps to a thermodynamically unstable state, i.e. to $p_{low} = 70$ bar (section 3.2.4). Thereby, it turned out that the integrated scattering intensity after expansion increases linearly in the low and decreases linearly in the intermediate q -regime. The origin of the linear dependency of scattering intensity can be explained by considering the relation of radius and time for diffusive phase separation by growing processes [300-302].

$$R(t) \propto \sqrt[3]{t} \quad \text{Eq. 3-4}$$

which shows that the radius is proportional to the third root of time. In order to connect this time-dependence to the scattering intensity the relation of radius and I_0 needs to be included, which for discrete aggregates can be described by

$$I_0 \propto \phi_{disp} R^3 \quad \text{Eq. 3-5.}$$

Assuming that the volume fraction of the dispersed phase ϕ_{disp} remains constant it directly follows that

$$I_0 \propto t \quad \text{Eq. 3-6}$$

i.e. that the expansion-induced phase separation should lead to a linear increase of the scattering intensity with time. Note that Ostwald ripening and coagulation follow the same time law (Eq. 3-4) so that it is not easy to distinguish between these [302, 303].

The pressure jump leads to a change of relative position of the sample composition to the phase boundary. This new position, i.e. the new parameters, leads to a different spontaneous curvature of the amphiphilic film and thus renders the system unstable. Furthermore, the pressure jump also leads to a sudden increase of the volume of the CO_2 droplets and to an increase of the surface area. Smoluchowski's rapid coagulation theory for number densities of order $10^{15} - 10^{16}$ microemulsion droplets per cm^3 predicts a half-time of less than a millisecond. Thus, it can be concluded that the jump of scattering intensity immediately after the pressure jump (see plots of $n_{ii}(t)$ vs. t in the previous section) is not only connected to the change of CO_2 scattering length density but that it also includes a change of the particle number density caused by coagulation and nucleation processes.

The new pressure parameters demand a different, i.e. higher, spontaneous curvature of the amphiphilic film. This means that the microemulsion droplets have to shrink. At the same time

the total interfacial area must remain constant. This requires that the number density of microemulsion droplets must increase. The mechanism of these structural changes is presumably fusion and fission with more fission than fusion but is not clear at this point.

Based on the isosbestic points of the scattering curves the normalised scattering intensity as a function of time was determined for two different q -regions. Here, the increase of scattering intensity in the low q -regime is caused by the growth of large emulsion droplets which highly contribute to the overall scattering intensity due to their large volume. The intermediate q -regime represents the shrinking of the microemulsion droplets where the decrease in radius apparently overcompensates the fact that the particle number density increases.

A mechanism similar as described above was already discussed in 1997 by Olsson *et al.* [304]. Performing shallow temperature quenches to a non-ionic microemulsion they found that small temperature quenches which only slightly traverse the phase boundary result in metastable states with very slow coarsening of microemulsion droplets as observed by turbidity measurements. With larger quenches, though, coarsening occurs much faster, i.e. on a time scale of minutes rather than hours. They also recognised that although the curvature of growing emulsion droplets decreases, where increasing is favoured, a few large droplets have to be tolerated in order to let the majority of droplets decrease in size [304]. Furthermore, Olsson *et al.* argue that the overall number of droplets increases due to the conservation of interfacial area. Later a more mathematical approach to this problem was published, describing nucleation processes in a microemulsion system from which an oil excess phase separates [305]. A nucleation barrier for moderately deep quenches is discussed as well as the nucleation kinetics. Another very interesting temperature jump was performed by Deen *et al.* with a Peltier temperature controller whereby the quench was performed in about 30 s [173, 306]. By means of SAXS scattering curves which were measured in regular intervals a 3D-plot of $I(q, t)$ was generated, comparable to the plots shown in the previous section. Deen *et al.* find a linear dependency between R_G and $t^{1/3}$ which is discussed in detail. By using a combination of a prolate ellipsoid and polydisperse sphere form factors they were able to describe the scattering curves, finding that a second contribution from the emulsion droplets arises with time and that the radius of the microemulsion droplets decreases from 76 Å to 51 Å within 45 minutes. Remarkably, the polydispersity is very low ($\sigma = 0.135$) compared to CO₂-microemulsions where $\sigma = 0.30$ is very common. Due to the high polydispersity it was not possible to follow the growth of the emulsion droplets in such a detailed way or to extract droplet sizes from the scattering curves. Furthermore, the structural changes happen on a much faster time scale here in the case of CO₂ microemulsions which makes the analysis even more difficult. Although surface and volume considerations are briefly mentioned by Olsson *et al.* they are not discussed in detail. The experiments performed by Olsson *et al.* and Deen *et al.* reveal

coarsening processes on a time scale of minutes. For the CO₂-microemulsions described in this work we have a much faster process, which can be followed because our pressure jump is much faster than their temperature jump.

To explain the differences in coarsening time constants results obtained by Volmer *et al.* can be considered which indicate that the processes observed after a temperature quench to a thermodynamically unstable region can be ascribed to three different stages [307]. They term the first stage the t_1 -phase, which means that a burst of large oil droplets is observed which grow in size about three orders of magnitude within few seconds. They also describe a second step in which actual phase separation to a clear excess phase occurs but on a time scale of up to 8 minutes. The third stage according to Volmer *et al.* is termed equilibration of the excess phase in which the excess phase grows in volume. Assuming that the effects of temperature and pressure jumps are comparable the processes described in the previous chapters seem to be mainly the growth of emulsion droplets, as was observed by the increase of intensity in the low q -regime. In the medium q -range two processes are expected according to this mechanism: the shrinking of microemulsion droplets and the increase of particle number density. Considering that these processes lead to opposite trends regarding the scattering intensity, it seems reasonable that the decrease of intensity is governed by the volume fraction of oil transferred to the emulsion droplets.

In order to quantify the effect of cyclohexane on the demixing kinetics the $n_{ii}(t)$ -data described in section 3.2.4 were normalised (for details see chapter 7.4). The linear regions of normalised $n_{ii}(t)$ were plotted together as shown in Figure 3.31 for the intermediate q -regime. Since the integrated intensity below the whole scattering curve must remain constant (except for the change of scattering length density) it follows that, if the intensity increases in the low q -regime (Eq. 3-6) it must decrease in the intermediate q -regime, which is indeed the case due to vanishing of microemulsion droplets.

Considering the different slopes of the linear fits to the normalised scattering intensity it becomes obvious that the slope is steepest at $\beta_i = 0.00$ and most shallow for $\beta_i = 0.25$, which translates to a fast process in the cyclohexane-free system and a slow process for the system with 25wt% cyclohexane in the hydrophobic phase. Plotting the slopes versus the cyclohexane content β_i one finds that the dependency can be described by a mono-exponential fitting function with an exponential constant of $z = 0.059 \pm 0.004$. Thus, the speed of the demixing process can be systematically influenced by substituting CO₂ by cyclohexane. Comparing the absolute values one finds that the demixing speed at $\beta_i = 0.0$ can be reduced to 20% of its initial value replacing only 10% of CO₂ by cyclohexane ($\beta_i = 0.10$) and even to 3% at $\beta_i = 0.25$.

The comparability of the discussed systems is given by the fact that all demixing processes were performed at similar conditions. Furthermore, the demixing process was in all cases induced by starting from spherical structures.

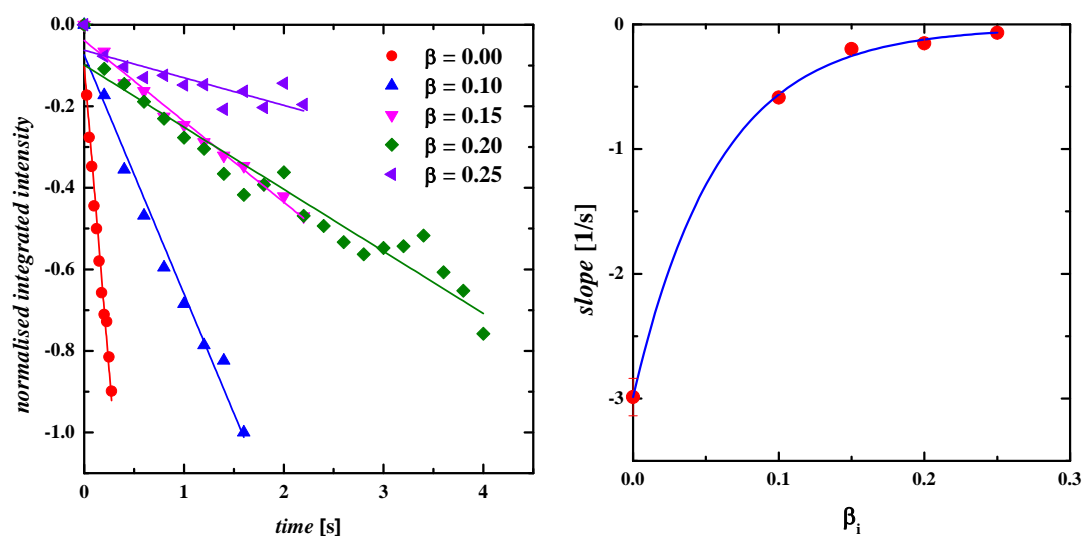


Figure 3.31: *Left:* Linear regions of normalised scattering intensity as described in section 3.2.4 for the intermediate q range $0.013 \text{ \AA}^{-1} \leq q \leq 0.034 \text{ \AA}^{-1}$. While $nii(t)$ decreases (vanishing of the correlation peak) rapidly with t this process is considerably slowed down by successively increasing the cyclohexane content in the hydrophobic phase. *Right:* Plot of the slopes shown left against the cyclohexane mass fraction β_i . The dependency can be described by a mono-exponential function with an exponential constant $z = 0.059 \pm 0.004$. This constant, however, does not give any absolute information on the demixing speed and can only be used to describe the data shown left.

One difference among the systems is the droplet size which increases with increasing cyclohexane content (Figure 3.18). Since systems with larger droplets have a lower number density the probability of coagulating is lower which slows down demixing. The droplet size, however, is influenced by cyclohexane, which in the end is responsible for the slower kinetics. Diffusive processes like Ostwald ripening are also slowed down due to the low monomeric solubility of cyclohexane in water. This effect was reported to reduce Ostwald ripening processes [301, 308] and is probably the main reason for the deceleration of demixing.

The kinetics might also be influenced by the change of volume after expansion which is smaller for a system containing less CO_2 . A smaller change of volume points to slower ageing processes. Thus, a droplet with a radius of 66 \AA at $p = 150 \text{ bar}$ increases its volume by 28% upon expansion whereas one filled with 25 wt% cyclohexane and 75 wt% CO_2 increases only by 19% in volume. Thereby, the relative change of radius upon expansion equals an increase of 5% for all cyclohexane concentrations.

3.3 The TISANE option

3.3.1 TISANE experiments: State of the art

Only recently, Bender *et al.* finished a manuscript on the first experimental data obtained by SANS using the TISANE mode [309]. Previously published data were simulations. Bender *et al.* investigated the response of a colloidal dispersion of nickel nanorods to an oscillating magnetic field which represents the required stroboscopic change of scattering property and is the equivalent to pressure jumps. In contrast to pressure jumps, it is possible to oscillate a magnetic field with frequencies of several thousand Hz. The maximum sample frequency presented in this manuscript is 3000 Hz which corresponds to a chopper frequency of about 4100 Hz.

At the outset of this work the maximum frequency of pressure cycles was 4.5 Hz. Therefore, TISANE experiments were performed with a sample frequency of 4.340 Hz. This is connected to a detector frequency of 2.609 Hz. Although these conditions fulfil the TISANE requirements the results suffered from various problems.

On one hand, the parameters mentioned above do not completely satisfy the TISANE requirements ($f_{\text{sample}} = 4.340$ Hz instead of 4 Hz) which is due to the fact that the electronics of the SHP-SANS cell finished one pressure cycle before waiting for the next trigger signal. By performing various experiments it turned out that a few ms after the finished pressure cycle were necessary for the SHP-SANS cell to start the next pressure cycle with the next trigger signal. Furthermore, it showed that the rotational speeds of 14 and 28 rpm were too slow for the chopper wheels to keep a constant velocity since the chopper is designed to operate at several thousand Hz. Irregularities of the chopper mean that the neutron beam approaching the sample is of fluctuating intensity.

Overall, the main result from these measurements was that both the electronic communication as well as the frequency of the pressure jumps need to be improved, especially since it was shown by Bender *et al.* that the TISANE principle can be successfully applied at high frequencies [309].

3.3.2 Improvements of the SHP-SANS cell

The maximum pressure jump frequency was 4.5 Hz at the outset of this work. Thereby, the pneumatic valves controlling the opening and closing of the hydraulic valves were the limiting factor. This was determined by lowering the opening times of the valves until the pressure was not transferred to the sample any more, i.e. until the opening time was too short to open the valves. In order to improve the time needed to transfer the pressure jump the valves were modified as shown in Figure 3.32. Beforehand, the functioning of such a valve is briefly described.

The part of the valve which connects or disconnects the bellow from the hydraulic pump is the ball valve which, depending on its position, allows or prevents the contact of bellow and pump through

flow of hydraulic oil. The position of the ball valve can be changed by the pneumatic setup at the top. The ball is connected to a toothed wheel by a rod. This wheel is clicked into a gear rack which is connected to a movable disk in the air storage room (black part of the valves in Figure 3.32). By applying an impulse of pressurised air from the side of the valve, as indicated by the blue arrows in Figure 3.32, the disk is moved to the back (right) side, which brings the ball valve to an open position. Applying the impulse of pressurised air from the back side of the valve has the opposite effect: The disk is moved to the front (left) and the toothed wheel turns the ball valve to a closed position.

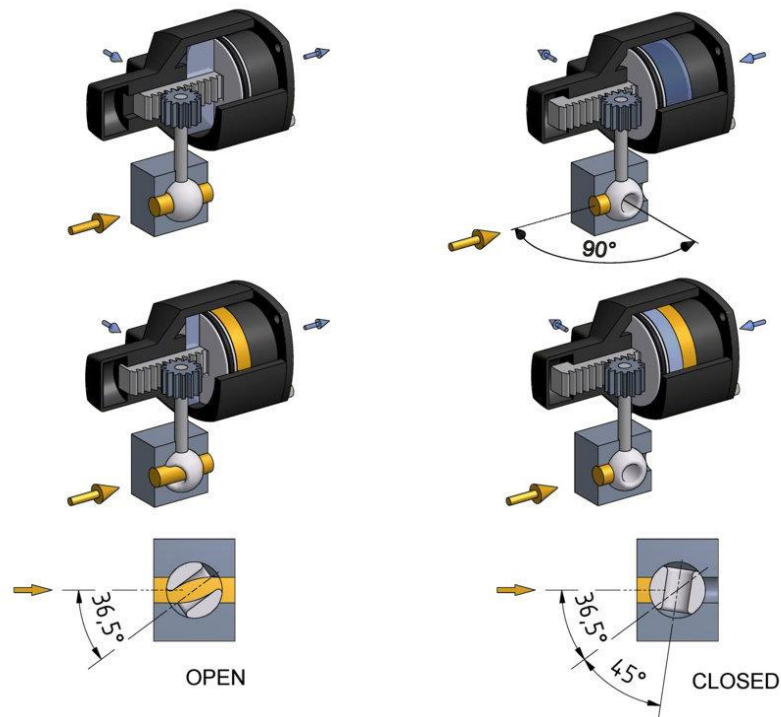


Figure 3.32: Technical drawing of the hydraulic valves which connect the bellow to the hydraulic pump, prepared by the internal mechanical workshop. *Top valves:* The oil canal is open if the ball valve channel is aligned with the flow (top left). It is closed if it is in a position perpendicular to the flow of hydraulic oil (top right). Thus, the ball valve needs to be turned by 90° to be opened. *Bottom Valves:* A metal disk is inserted inside the pneumatic part of the valve which limits the possible positions of the ball valve. Here, the valve is open if it is turned by an angle of 36.5° from the flow direction, and closed if its position is 45° from the open position, as indicated in the 2D drawing at the bottom.

The modification of the valves consists of inserting a metal disk into the upper, pneumatic part of the valve that limits the way the movable disks can be pushed in either direction. Thus, the new opening position is reached if the ball valve is positioned at an angle of 36.5° to the direction of the flow. Therefore, the ball valve needs to be turned only by 45° instead of 90° . Although the opening for the hydraulic oil to flow through is considerably narrower compared to the ball valve at the completely open position it was thoroughly tested that the opening allows enough oil to flow through to enable any desired pressure jump.

The new orientation of the valves also has the additional advantage that less air is needed at the top of the valve to induce the opening or closing, respectively. This can also be a limiting factor since the valves are not air-tight at the top and thus an enormous amount of compressed air is needed to switch the valves, especially at higher frequencies.

The new orientation of the valves enabled pressure jumps with a frequency of 19.2 Hz for a non-compressible sample. Thereby, the minimum opening times of the valves were found to be 13 ms and thus the whole pressure cycle took 222 ms to be completed if equal times for 'valve open' and 'valve closed' are chosen. However, it turned out that the response of the bellow with samples with a high compressibility, such as CO₂, is much slower due to the fact that the change of size the bellow performs is much higher. Therefore, the maximum frequency for microemulsions containing 10 wt% CO₂ was 10 Hz in August 2013. This is an improvement of more than a factor 2.

To further improve the cell four pneumatic valves instead of two were implemented into the setup, whereby two pneumatic valves control one hydraulic ball valve. Thereby, one pneumatic valve applies the impulse to open the ball valve whereas the other one controls the closing of this ball valve. This enables the ball valves to switch faster because each valve has more time to be refilled with compressed air after releasing an impulse.

Furthermore, the inner part of the SHP-SANS cell was modified so that the volume is smaller by about 6 mL compared to the previous cell. A smaller overall volume means a lower amount of compressible substance (CO₂) which in turn means that the bellow has to elongate or shrink less to transfer the desired pressure.

Combining the smaller sample volume with the newly implemented valves a frequency as high as 22.7 Hz was possible using water as an incompressible sample. Thereby, the minimum opening times of the valves was improved to 11 ms. To stress the enormous improvement the pressure profile of a pressure jump with 22.7 Hz is shown together with the maximum frequency at the outset of this work in Figure 3.33.

The frequency of 22.7 Hz is, however, only possible with incompressible substances. The fastest pressure jump which can be applied to a sample containing 10 wt% CO₂ is 19.2 Hz, with the four times being 13 ms each. This is an improvement of a factor of 3.8 compared to the start of this work and also an improvement of a factor of almost 2 compared to the last measurements in August 2013.

After that, however, the potential for further improvement is likely very low. The switching times of the valves have probably reached a minimum, and the experiment will always be limited by the flow rate of the hydraulic oil. Only a considerable reduction of the sample volume offers the possibility for further improvement, but this challenge is difficult to reconcile with the requirement of a good mixing of the microemulsion sample.

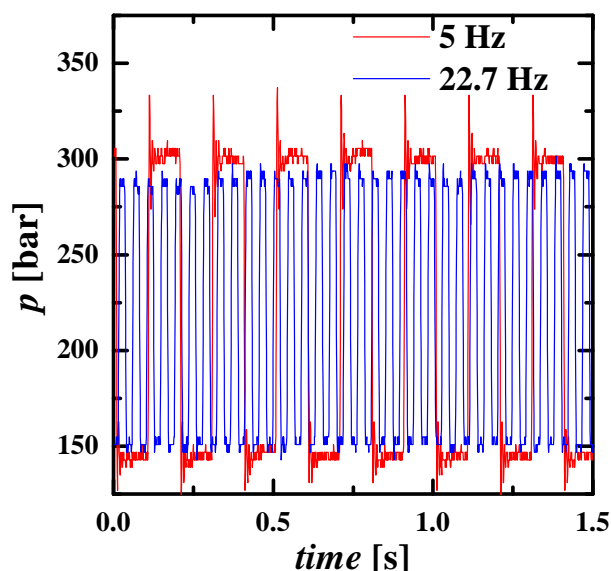


Figure 3.33: Comparison of pressure profiles at two different frequencies. While the red line indicates the highest possible frequency at the outset of this work (5 Hz) this was improved to 22.7 Hz (blue line).

3.3.3 Applying the TISANE option to microemulsions

The TISANE option was tested with the microemulsion system $D_2O/NaCl - CO_2/cyclohexane - Zonyl\ FSO\ 100/ Zonyl\ FSN\ 100$ ($\gamma_a = 0.08$, $\delta_{FSN} = 0.75$, $\varepsilon = 0.01$) at $w_B = 0.10$, $T = 28^\circ C$ and $\beta_i = 0.10$ (characterisation see Figure 3.13). Thereby, the pressure jump was fixed to be from $p_{high} = 250$ bar to $p_{low} = 150$ bar for all experiments shown in the following. First, a measurement applying the LISTMODE counting mode with a sample frequency of 9.77 Hz was performed for comparison. Second, a TISANE experiment was applied with the same sample frequency and a detector frequency of $f_{detector} = 6.36$ Hz. The second chopper wheel was rotated at a speed of 17 rpm which complies with the TISANE conditions. Note that it was not possible to deploy both chopper wheels due to a technical problem with the first chopper wheel. The normalised integrated intensities obtained from these two experiments as a function of $time \cdot f_{detector}$ are shown in Figure 3.34.

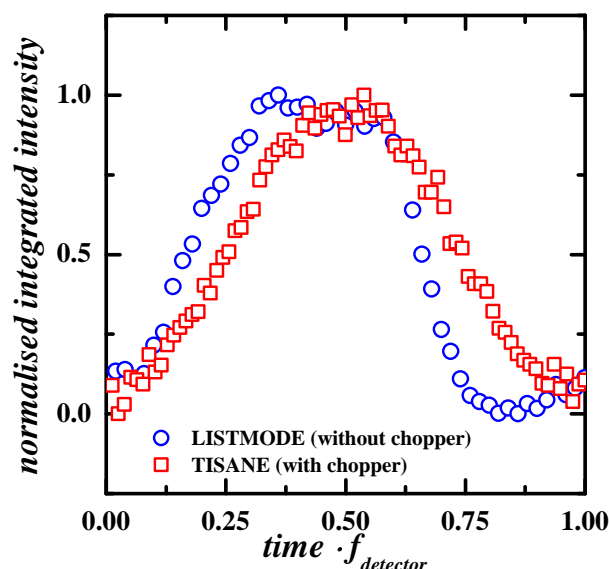


Figure 3.34: Comparison of two measurements at the same sample frequency ($f_{\text{sample}} = 9.77$ Hz) for a pressure jump from $p_{\text{high}} = 300$ bar to $p_{\text{low}} = 200$ bar, performed with the microemulsion system $\text{D}_2\text{O}/\text{NaCl} - \text{CO}_2/\text{cyclohexane} - \text{Zonyl FSO 100}/\text{Zonyl FSN 100}$ ($\gamma_a = 0.08$, $\delta_{\text{FSN}} = 0.75$, $\varepsilon = 0.01$) at $w_B = 0.1$, $T = 28^\circ\text{C}$ and $\beta_i = 0.10$. The first measurement was performed with a usual LISTMODE count without the chopper (blue circles) while the second experiment was performed at TISANE conditions (red squares) with a detector frequency of $f_{\text{detector}} = 6.37$ and a rotational speed of the second chopper disk of 17 rpm. Although a plateau at high scattering intensity can also be observed for the TISANE measurement it is smeared out and the peak shape is very different.

The results in Figure 3.34 of the two experiments differ considerably from each other. While the results obtained from a common LISTMODE experiment show a plateau of scattering intensity both at high scattering intensity (starting at $\text{time} \cdot f_{\text{detector}} \approx 0.3$) as well as at low scattering intensity (starting at $\text{time} \cdot f_{\text{detector}} \approx 0.75$) the first plateau is considerably shorter in the TISANE experiment, the second plateau is hardly noticeable and the peak of scattering intensity is considerably broader. Despite these differences, this result represents a major improvement compared to the TISANE experiments with a maximum sample frequency of 4.5 Hz. Here, the plateau of scattering intensity is noticeable and not completely smeared out, which clearly points to the fact that the TISANE conditions were almost met. To identify the remaining problems more test experiments were performed. First, the experiment shown in Figure 3.34 was reproduced successfully (Figure 3.35 left).

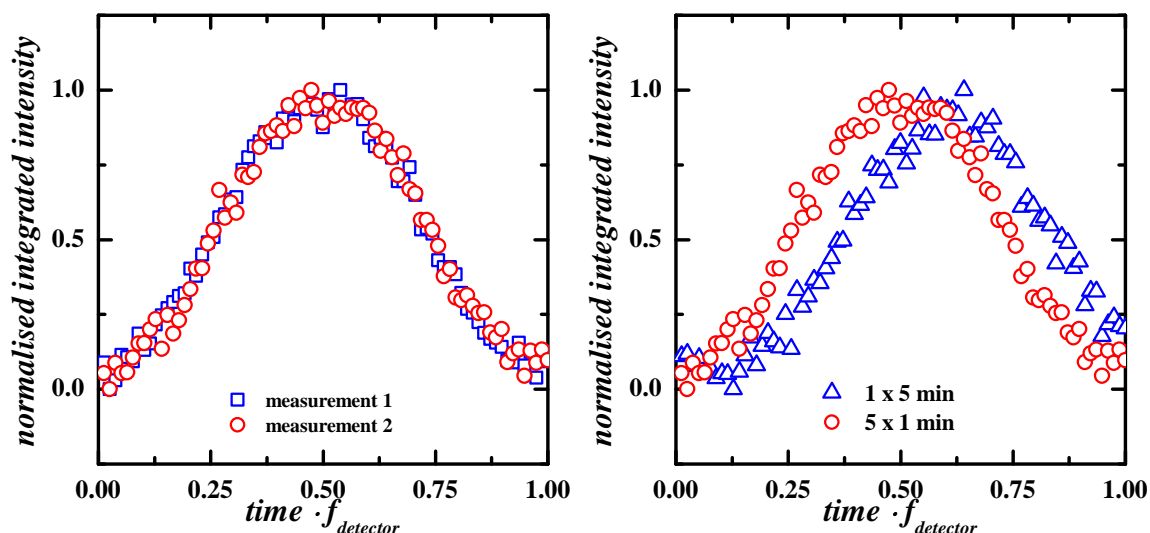


Figure 3.35: *Left:* Comparison of two separately performed TISANE experiments with $f_{\text{sample}} = 9.77$ Hz, $f_{\text{detector}} = 6.37$ Hz and a rotational speed of the second chopper disk of 17 rpm. Both experiments led to exactly the same results. *Right:* Comparison of different counting modes. While the blue triangles represent one measurement of 5 minutes the red squares show the result of a loop measurement of 5 measurements which each lasts 1 minute. This loop function allows for the devices to synchronise every minute which obviously improves the result since the peak in the single 5-minute measurement is considerably more smeared out. Note that the red circles in both plot represent the same measurement.

To test the synchronisation of the devices acquisition of data was varied. The first measurement was performed continuously for 5 minutes while the second measurement was divided into 5 single measurements each lasting 1 minute. Such a loop-function means that all devices are synchronised every minute. The results shown in Figure 3.35 right differ considerably from each other, indicating that the frequencies of chopper, sample and detector drift apart with time. This may be one reason for the discrepancy of the TISANE and the LISTMODE experiment as shown in Figure 3.34.

Another problem is the frequency of the chopper wheels. To meet the TISANE conditions with a maximum sample frequency of 10 Hz the chopper wheel should rotate with a velocity of 17 rpm. This is very low since the wheels are designed to rotate at a speed of several thousand rpm. To test the evenness of the chopper rotation a TISANE experiment without pressure jumps was performed so that the scattering properties do change with time. Any deviations of the scattering intensity detected in this experiment can thus be attributed to irregularities of the chopper rotation. The results are shown in Figure 3.36. Clearly there are considerable fluctuations of intensity, as in each experiment a peak of scattering intensity is noticeable. On top of that, these peaks have completely different shapes for different experiments. Since a reproducible intensity is a precondition for TISANE experiments these fluctuations are likely to prevent the results from being reliable. Since the fluctuations are caused by the low and thus unstable rotational speed of the chopper wheel the only solution towards a more constant neutron beam is a higher chopper frequency which in turn requires a higher sample frequency.

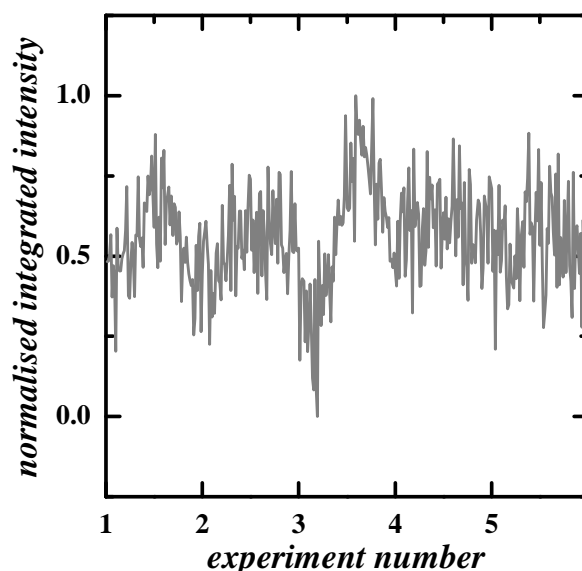


Figure 3.36: Comparison of the scattering intensity recorded at TISANE counting mode but without a pressure jump so that the scattering intensity should not change with time. Five experiments, each lasting one minute, are shown next to each other. While experiment one displays a peak of scattering intensity experiment 3 starts with a considerably loss of intensity, which indicates that the rotational speed of the chopper disks (17 rpm) is not stable and thus not reliable.

The low chopper frequency is also the reason for the observed smearing of the signal since the chopper frequency is directly connected to the time resolution of a TISANE experiment. Thereby, the time resolution scales inversely with the chopper frequency which means that such a low frequency as applied here leads to only a high time resolution [310]. The time resolution can be calculated according to

$$\Delta t = \frac{DC}{f_{\text{detector}}} \quad \text{Eq. 3-7}$$

where the duty cycle (DC) is defined as

$$DC = \frac{\Delta t_c}{2T_C} \quad \text{Eq. 3-8.}$$

Here, Δt_c is the opening time of the chopper (in this case $12 \cdot 1.577$ ms) and T_C is the rotational time of the chopper wheel (for 17 rpm $T_C \approx 3.53$ s). Thus the duty cycle is 0.22 and subsequently the time resolution is about 43 ms. This leads to a smearing of the signal.

The time resolution of a common kinetic experiment can be calculated according in to

$$\Delta t = \frac{\Delta \lambda \cdot L_{SD}}{4} \quad \text{Eq. 3-9.}$$

where L_{SD} is the sample-to-detector distance (11.2 m). The wavelength distribution is specified by the ILL to 0.1, i.e. $0.1 \cdot 6 \text{ \AA} = 0.6 \text{ \AA}$. Thus, the time resolution is 1.7 ms which is 25 times better than for a comparable TISANE experiment. Finally, it should be noted that for the sample frequencies which are so far possible a common kinetic experiment without a pulsed neutron beam leads to considerably more reliable results.

3.4 Conclusion

Microemulsions containing near or supercritical CO₂ are of interest for both fundamental research and technical applications. A new way to improve the efficiency of non-biodegradable and therefore environmentally questionable fluorinated surfactants to formulate balanced CO₂-microemulsions was found. This is obtained by partially replacing CO₂ by cyclohexane. Thus, the substitution of 20 wt% of CO₂ by cyclohexane reduces the amount of surfactant needed to formulate a one-phase microemulsion by a factor of two to five, depending on the pressure. However, at first sight this result is surprising because cyclohexane and the fluorinated alkyl chains of the surfactants are not compatible. Therefore, it was postulated that the distribution of cyclohexane within CO₂ is not homogeneous but that a depletion zone of cyclohexane close to the surfactants forms to spatially avoid repulsive interactions.

To verify this hypothesis SANS experiments were performed using the contrast variation technique, which is known to be a powerful tool not only to investigate the microstructure but also the spatial distribution of the various components in microemulsion domains. The scattering data of a fluorinated CO₂-microemulsion with 20 wt% cyclohexane in the hydrophobic phase recorded at four different pressures and four contrasts could be almost quantitatively described using the form factor $P_{\text{droplet}}(q)$ of polydisperse spherical droplets and the polydisperse Percus-Yevick structure factor $S_{\text{PY}}(q)$. Small but systematic deviations observed for q -values slightly larger than the position of the oscillation already indicate that the used radial density distribution function is not able to describe the distribution of CO₂ and cyclohexane inside the micelle quantitatively.

The pair distance distribution functions (PDDFs) were obtained applying the Generalised Indirect Fourier Transformation (GIFT) and were subsequently deconvoluted to radial scattering length density distribution profiles. In all cases, instead of a nearly constant scattering length density, a density profile that varies systematically over half of the droplet radius was detected. These results confirm the hypothesis of a concentration gradient within the micelle. While cyclohexane is concentrated at the centre of the swollen micelle ($\beta_{\text{core}} \approx 0.5$ instead of 0.2 for a homogeneous distribution), it is depleted close to the fluorinated amphiphilic film. Hence, it was elucidated that the observed unexpected efficiency boosting of CO₂-microemulsions is caused by an improvement of the CO₂-surfactant interactions triggered through repulsive interactions between cyclohexane and the fluorinated surfactant chains.

Furthermore, systems containing 10, 15 and 25 wt% cyclohexane in the hydrophobic phase were investigated regarding their phase behaviour and microstructure. It was found that the efficiency boosting described above for balanced microemulsion exists also for diluted microemulsions at $p \leq 250$ bar but in a less pronounced way. Comparing the radii of spherical

droplets found at $p = 150$ bar for cyclohexane contents $\beta_i = 0.00, 0.10,$ and 0.15 and at $p = 200$ bar for $\beta_i = 0.25$ it turned out that the droplet radius linearly increases with β_i . This can be ascribed to the lower surface-to-volume ratio which provides better spatial possibilities for cyclohexane and fluorinated surfactant tails to avoid repulsive interactions.

Furthermore, the kinetics of structural changes as a response to sudden pressure jumps were investigated by utilising the improved stroboscopic high-pressure SANS cell. Thereby, pressure jumps from elongated to spherical droplets, both at a thermodynamically stable state, were performed. It turned out that the breakdown of elongated droplets to cylinder fragments and subsequently to spherical structures after expansion is slowed down by a factor of two if 20 wt% of CO_2 are substituted by cyclohexane. Regarding the inverse process, i.e. the accumulation of spherical droplets with subsequent reordering to elongated micelles, seems to be accelerated by the same factor. Thereby, it needs to be considered that the process to which the new values were compared might not be the accumulation but the reordering process.

Another set of pressure jumps to the thermodynamically unstable region was performed, thus inducing demixing. Thereby, a linear decrease of the scattering intensity in the medium q -range ($0.013 \text{ \AA}^{-1} \leq q \leq 0.034 \text{ \AA}^{-1}$) was found as well as a linear increase for the low q -region ($0.005 \text{ \AA}^{-1} \leq q \leq 0.013 \text{ \AA}^{-1}$). While the low q -regime represents droplet growth processes due to the growth of emulsion droplets the medium q -regime can be used to follow the breakdown of the microemulsion microstructure. The pressure jump induces a shift of the phase boundary to lower w_B , thus also influencing the curvature of the amphiphilic film in such a way that smaller droplets of the coexisting microemulsion are favoured. Since the overall interfacial area must remain constant the reduction of microemulsion droplets must occur together with an increase of the droplet number while the few emulsion droplets simultaneously grow in size. The comparably much higher volume fraction of the large emulsion droplets, however, is responsible for the fact that the scattering curves reflect mostly their contribution. Normalising the linear regions in the intermediate q -range showed that cyclohexane systematically decelerates the demixing process whereby the dependency can be described by means of an exponential function. The fact that demixing is decelerated at all is very likely due to the presence of a second dispersed phase component, i.e. cyclohexane, which is insoluble in the continuous phase. The difference in droplet size (larger droplets with increasing β_i) likely further promotes deceleration because ageing processes, especially coagulation, are slower for larger droplets. This, the lower number density of droplets at high β_i and the lower monomeric solubility of cyclohexane in water combined probably lead to the observed deceleration. The obtained time constants are in the order of seconds which is very fast compared to time constants reported for coarsening processes upon a temperature quench, which are in the order of minutes [173, 311]. This indicates that the processes observed here mainly represent

nucleation of microemulsion droplets to emulsion droplets and their growth by diffusive transfer of hydrophobic components from microemulsion to emulsion droplets.

Applying the TISANE option with a maximum sample frequency of 10 Hz for the first time led to a reasonable result. However, a smearing of the signal also indicates that the frequency is still too slow for optimum TISANE conditions. The time resolution at these parameters is about 25 times higher than a comparable kinetic measurement without chopper. Thus, the SHP-SANS cell was further improved to currently enable pressure jumps with a maximum frequency of 22.7 Hz which will soon be tested in TISANE experiments.

4 Influence of hydrostatic pressure on PNIPAM particles

The influence of stimuli like salt [312], surfactants [313, 314], pH [69] and solvent composition on PNIPAM particles is well examined. Using hydrostatic pressure as a stimulus for PNIPAM particles has so far only been investigated by Lietor-Santos *et al.* [67, 68, 315]. They show that the application of drastic hydrostatic pressure (up to 5000 bar) leads to a deswelling of the particles. Thus, they postulated that hydrostatic pressure has the same effect on the particles as an increase of temperature [67]. The measurements were, however performed at 25°C which is rather far away from the volume phase transition temperature (VPTT). This chapter shows that the influence of pressure has a delaying effect on the VPTT, which is the opposite effect of the one postulated by Lietor-Santos *et al.*. However, only recently Reinhardt *et al.* [75] published a neutron reflectivity study on the effect of moderately elevated pressure on thermoresponsive polymer brushes (polystyrene-*b*-poly 2-(dimehtylamino)ethylmethacrylate) on a silicon waver. They found that the VPTT can be postponed by about 1 K per 100 bar which, as this chapter will show, is in good agreement with the measurements on PNIPAM particles presented in this work.

In contrast to the well-known temperature dependence of the radius of PNIPAM particles there are only few publications on the kinetics of the structural transition. Admittedly, measuring kinetics due to a change of temperature provides experimental challenges. While a fast increase of temperature can be achieved by Joule-heating using a laser [70, 72] or by magnetic heating (if PNIPAM particles are coated onto magnetic particles) the reverse process, i.e. a fast cooling, is a challenge. Most publications on this topic simply switch thermostats to induce the temperature change [316-318] which is not a fast temperature jump. Furthermore, with this method it is difficult to distinguish between the kinetics of the temperature change and the response of the sample.

4.1 PNIPAM particles at elevated hydrostatic pressure

In order to systematically study the influence of hydrostatic pressure on PNIPAM particles five different particles were synthesised via emulsion polymerisation. By varying the crosslinker and surfactant content different particles were produced, as shown in. Figure 4.1.

After synthesis the particles were dialysed against distilled water for four days to remove the surfactant from the polymer dispersion, changing the water twice a day.

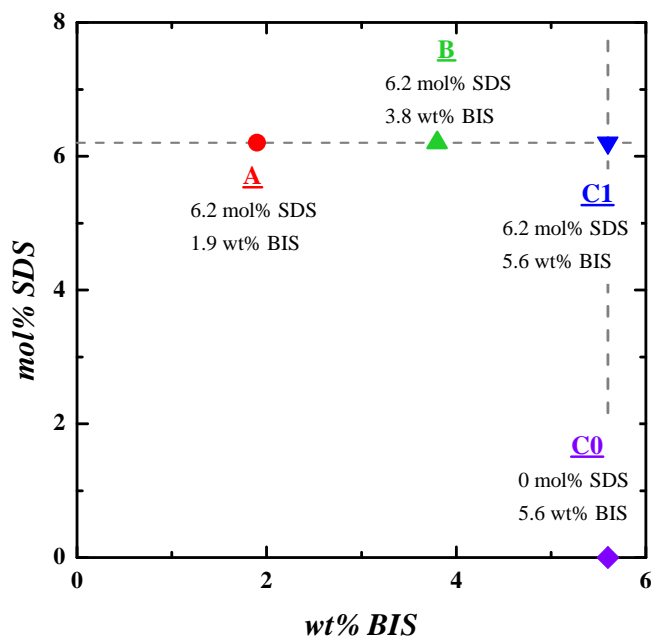


Figure 4.1: Overview of the different particles which are characterised in the following. The amount of crosslinker BIS was varied so that particles with 1.9 wt% (A, red circle), 3.8 wt% (B, green upward triangle) and 5.6 wt% (C1, blue downward triangle) were obtained via emulsion polymerisation with 6.2 mol% SDS. In order to study the effect of size and polydispersity the particles with 5.6 wt% crosslinker were synthesised again without surfactant (C0, violet diamond). The amounts of water, NIPAM monomer and radical initiator were the same for all particles.

4.1.1 Dynamic light scattering

The most common way to study the swelling behaviour of PNIPAM microgel particles is by dynamic light scattering measurements at different temperatures. Plotting the hydrodynamic radius against temperature in a range from 25 to 40°C one finds a linear decrease of the radius at low temperature [319]. This turns over to a non-linear decrease of R_h over a temperature range of about 5 K around the VPTT and finally results in a constant radius at temperatures well above the VPTT. The same was found for PNIPAM particles with 5.6 wt% crosslinker synthesised in the presence of 6.2 mol% SDS (particles C1 in Figure 4.1) both at normal pressure as well as at $p = 300$ bar (see Figure 4.2 left).

The derivatives in Figure 4.2 right are used to determine the VPTT for the respective pressure with a higher accuracy. Thus, the VPTT of the particles with 5.6 wt% crosslinker was determined to be 34°C at atmospheric pressure and 36.5°C at $p = 300$ bar. Obviously, the VPTT is shifted by 2.5 K upon application of 300 bar. The sharpness of the peaks in Figure 4.2 right shows that the transition occurs within a smaller temperature frame at atmospheric pressure than at 300 bar which may be due to competing interactions. For this analysis it is also interesting to compare the slopes of the different regions of temperature dependence in Figure 4.2. Thus, the decrease of the hydrodynamic radius at $p = 1$ bar in the range from 25 to 30°C is -0.75 nm/K and -0.48 nm/K at 300 bar. The slopes in the transition region differ between -15 nm/K at 1 bar (for 33-35°C) and -11 nm/K at 300 bar (for 34.5 to

37°C) which clearly shows that the transition is sharper at atmospheric pressure. Note that the slopes scale with a factor of 1.5 in both cases.

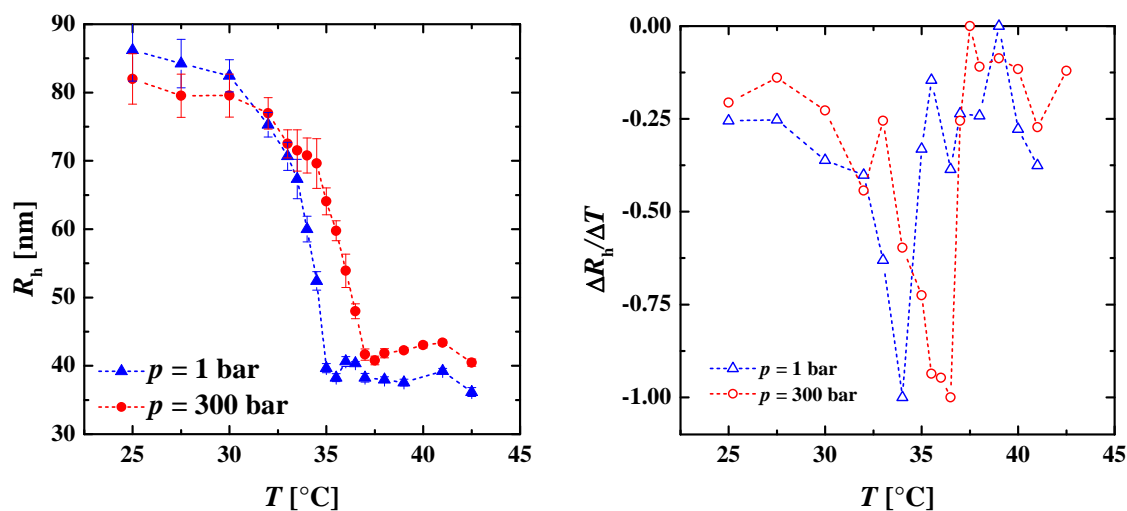


Figure 4.2: *Left:* Plot of the hydrodynamic radius of particles C1 as a function of temperature for atmospheric pressure (blue triangles) and at $p = 300$ bar (red circles) to demonstrate the swelling behaviour. *Right:* Using the derivative of the plot at the left for the determination of the VPTT one finds that the VPTT is at 34°C at $p = 1$ bar and at 36.5°C at $p = 300$ bar.

The hydrodynamic radius at temperatures below the VPTT is smaller at high pressure, which is in consistence with the results of Lieter-Santos *et al.* [67]. This can be explained simply by imagining that the particles are compressed at high pressure, although Lieter-Santos interpret their data as deswelling. The cancelling effect of pressure on the VPTT leads to higher radii at temperatures around the VPTT at high pressure. At temperatures well above the VPTT it turns out that the particles have almost the same size at both pressures whereby the radii at $p = 300$ bar are approximately 4 nm larger than at atmospheric pressure, probably due to remaining pressure-induced swelling. Note that the swelling ratio i.e. the differences in radius at temperatures below and above the VPTT is slightly higher at atmospheric pressure than at elevated pressure (only 90% of the swelling at 1 bar).

The reason for the cancellation effect is argued in literature to be due to hydrophobically associated homopolymers which form solvent-inaccessible cavities. Upon applying higher pressures the energy barrier for solvent molecules to enter these cavities can be overcome, which leads to a better hydration of the polymer and thus higher volume phase transition temperatures [75].

The same particles were synthesised again without surfactant (particles C0) since a synthesis without surfactant is known to lead to a broader distribution of the resulting particle radius (see section 2.3.1). Thus, the influence of size and polydispersity (will be discussed with Figure 4.4) on the swelling behaviour can be investigated. The temperature and pressure dependent DLS results which are shown in Figure 4.3 reveal that the VPTT is slightly affected as the according temperatures determined in Figure 4.3 right are approximately by 1 K higher than the ones shown in Figure 4.2. Thus the VPTT was estimated to be 35°C at atmospheric pressure and 37.5°C at 300 bar.

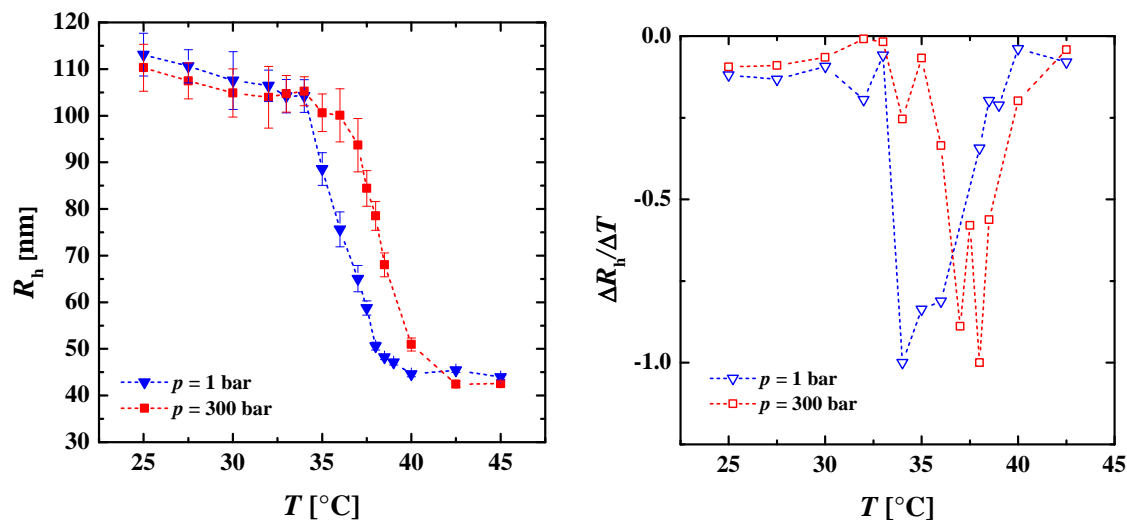


Figure 4.3: *Left:* Plot of the hydrodynamic radius of particles C0 as a function of temperature for normal pressure (blue downward triangles) and at $p = 300$ bar (red squares), indicating the swelling behaviour. *Right:* The derivatives of these swelling curves are used to determine the VPTT for the respective pressure which is located at 35°C at atmospheric pressure and at 37.5°C at 300 bar.

In contrast to the derivatives shown in Figure 4.2 the ones for the particles synthesised without surfactant (Figure 4.3 right) show a much broader peak which is very likely caused by polydispersity effects. Since the amount of surfactant is the only difference the fact that the VPTT at both pressures is slightly higher in this case is assumed to be due to both the higher hydrodynamic radii and the higher polydispersity. It is also interesting to note that the particles which were synthesised with surfactant have a radius of 38 nm at atmospheric pressure and at $T > \text{VPTT}$ whereas the particles from the surfactant-free synthesis have an average radius of about 45 nm. This is due to larger emulsion droplets in the surfactant-free polymerisation.

Comparing the swelling degree of both particles one finds that the swelling ratio is almost the same, as the particles shown in Figure 4.2 swell by about 50 nm (a factor of 2.2) and the ones shown in Figure 4.3 by about 55 nm (a factor of 2.3). This trend is, however, expected, since the main parameter which influences the degree of swelling is the crosslinker content [62] which is the same (5.6 wt%) for both particles.

To evaluate the polydispersities the CONTIN analysis for a DLS measurement at 40°C and atmospheric pressure can be compared (see Figure 4.4). As expected, it is obvious that the relaxation rate distribution is much broader in the case of the particles which were synthesised in a surfactant-free way.

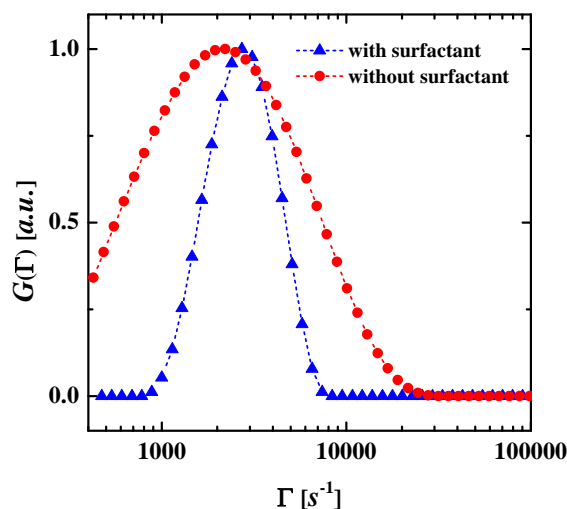


Figure 4.4: Distribution of relaxation rates Γ for two different particles with 5.6 wt% crosslinker where one particle batch was synthesised with and the other without surfactant. The rates were computed by a CONTIN analysis of a DLS measurement at 40°C and 90°. Very obviously the distribution rates in the case of synthesis without surfactant is much broader, implying a higher polydispersity of these particles.

Beside the variation of the surfactant content also the amount of crosslinker was varied. Thus, particles with 1.9 wt% and with 3.8 wt% crosslinker were prepared with 6.2 mol% SDS during polymerisation. The results of DLS measurements at atmospheric pressure as well as at $p = 300$ bar are shown in Figure 4.5.

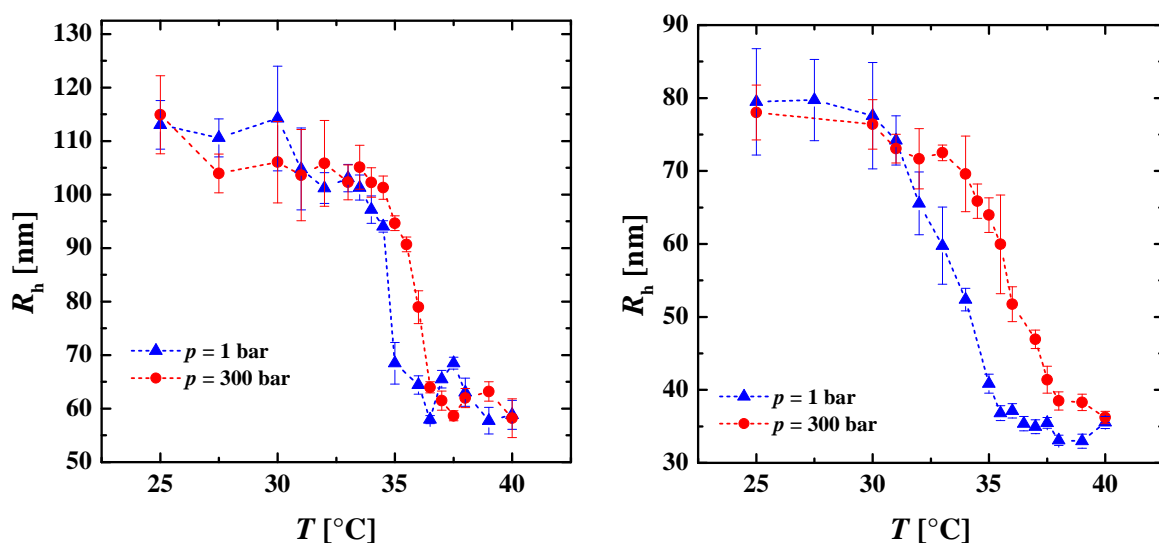


Figure 4.5: Plot of the hydrodynamic radius of particles A with 1.9 wt% crosslinker (left) and B with 3.8 wt% crosslinker (right) versus temperature at atmospheric pressure (blue triangles) and at $p = 300$ bar (red circles). The VPTT was determined by means of a derivative plot (not shown) to be 34.5°C (particles A) and 34°C (particles B) at atmospheric pressure and 36°C for both particles at 300 bar.

The low crosslinker content of the particles A (1.9 wt%, left) is probably the reason why the particles are of comparably high radius also at high temperatures, since the low crosslinker content may also lead to a lower particle number density since the crosslinker polymerises faster than the NIPAM monomer [320, 321].

Comparing the VPTTs of the particles with different crosslinker contents one finds that the VPTT does not change considerably within this variation and can be found at 34°C for the particles containing 3.8 wt% and 5.6 wt% crosslinker and at 34.5°C for the particles containing 1.9 wt% crosslinker. Considering also the difference of VPTTs among the particles with different crosslinker contents one finds a systematic trend of linearly increasing difference of the VPTTs at atmospheric pressure and 300 bar with increasing crosslinker content. The values are compared in Table 4-1.

Table 4-1: Overview of volume phase transition temperatures of PNIPAM particles with different crosslinker content at atmospheric pressure and at $p = 300$ bar. As can be seen the temperature difference ΔT increases with increasing crosslinker content.

particles	crosslinker content [wt%]	VPTT [°C]	VPTT [°C]	ΔT [K]
		$p = 1$ bar	$p = 300$ bar	
A	1.9	34.5	36.0	1.5
B	3.8	34.0	36.0	2.0
C1	5.6	34.0	36.5	2.5
C0	5.6	35.0	37.5	2.5

Considering the swelling degree one finds a systematic trend. While the particles with 5.6 wt% crosslinker undergo a change from about 85 nm to 40 nm ($\Delta R_h = 45$ nm), this effect is more pronounced for the particles containing 3.8 wt% crosslinker which shrink from 80 nm to 32 nm ($\Delta R_h = 48$ nm). The biggest change of size can be found for the particles with 1.9 wt% crosslinker (110 nm to 60 nm) which shrink by 50 nm. This trend is well-known [62].

4.1.2 Small Angle Neutron Scattering

In order to investigate not only the hydrodynamic radius but also the internal structure of the particles small angle neutron scattering (SANS) measurements at different temperatures and pressures were performed. Figure 4.6 shows the neutron scattering curves of PNIPAM particles C1 with 5.6 wt% crosslinker at constant atmospheric pressure (left) and at constant temperature and different pressures (right). The temperature dependence of the hydrodynamic radius is shown in Figure 4.2. The scattering curves were described according to Eq. 2-57 and Eq. 2-58, i.e. by a combination of a spherical, a Lorentzian and a Gaussian scattering contribution whereby the Gaussian contribution was only used at temperatures at or below the VPTT.

The temperature-dependent scattering curves show a clear trend to higher scattering intensities with increasing temperature. This is due to the increasing scattering contrast. The forward scattering intensity of the pressure-dependent scattering curves at $T = 36.5^\circ\text{C}$ (Figure 4.6 right) decreases with increasing pressure which is expected since the particles become more hydrated with increasing pressure, thus losing scattering contrast. The fitting parameters are given in Table 4-2.

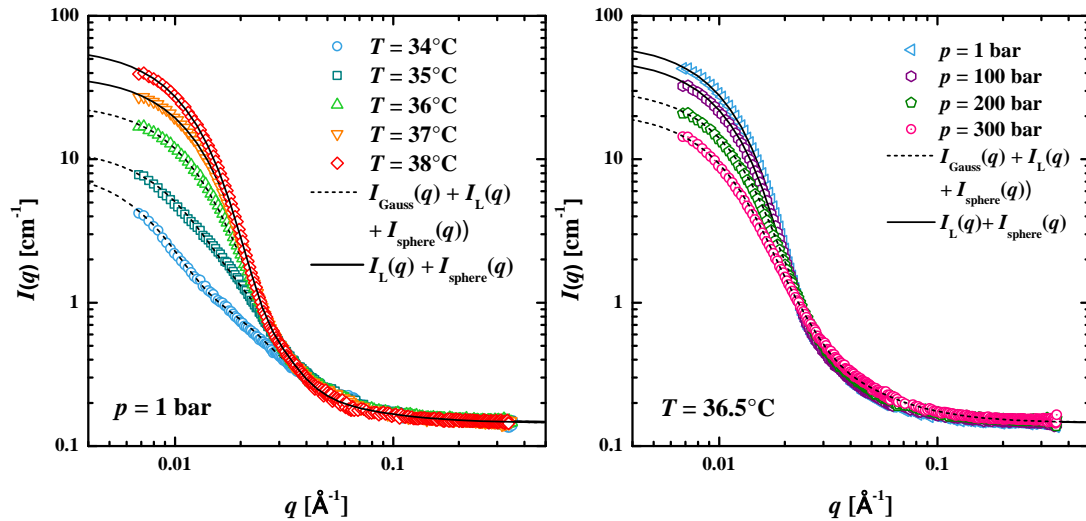


Figure 4.6: *Left:* Temperature-dependent scattering curves of PNIPAM particles C1 (0.5 wt% in D₂O). While for the scattering curves at $T \geq 37^\circ\text{C}$ the spherical droplet form factor in combination with the Lorentzian was applied the scattering curves at lower temperature were described with an additional Gaussian contribution. *Right:* Scattering curves for the same PNIPAM particles at a constant temperature of 36.5°C and different pressures. With increasing scattering contribution of the gel network a Gaussian scattering contribution was taken into account for $p \leq 200$ bar to describe the scattering curves.

Table 4-2: Overview of fit parameters to describe the scattering curves shown in Figure 4.6 of PNIPAM particles C1. The scattering intensity $I_{\text{sphere}}(q)$ was used in combination with the Lorentzian shape $I_{\text{L}}(q)$ at temperatures above the VPTT. At temperatures at or below the VPTT the Gaussian contribution $I_{\text{Gauss}}(q)$ was also taken into account. Note that the scattering curves at .5 temperatures are not shown.

parameter		sphere form factor			Lorentzian		Gaussian	
T [$^\circ\text{C}$]	p [bar]	R_0 [\AA]	σ/R_0	$\Delta\rho$ [10^{-6}\AA^{-2}]	$I_{\text{L}}(0)$ [cm^{-1}]	ξ_{L} [\AA]	$I_{\text{Gauss}}(0)$ [cm^{-1}]	Λ [\AA]
34.0	1	190	0.38	0.14	0.38	36.5	0.8	83
34.5	1	175	0.37	0.17	0.40	37.5	1.3	88
35.0	1	158	0.35	0.255	0.45	40	2.2	90
35.5	1	146	0.34	0.370	0.48	44	3.1	97
36.0	1	140	0.33	0.505	0.55	47	5.0	110
36.5	1	135	0.33	0.625	0.70	60	7.0	124
37.0	1	130	0.32	0.70	0.09	17	--	--
38.0	1	135	0.32	1.00	0.05	17	--	--
36.6	1	148	0.28	1.03	0.05	14	--	--
36.6	100	142	0.33	0.82	0.165	31	--	--
36.6	200	142	0.33	0.565	0.68	55	5.2	123
36.6	300	142	0.36	0.425	0.57	44	2.7	108

The increasing contribution of $\Delta\rho$ with increasing T clearly points to an increase of scattering contribution of the sphere. The absolute value of $\Delta\rho$ is, however, rather low for all scattering curves. Hellweg *et al.* found that PNIPAM can be matched by a mixture of 10 % H₂O and 90 % D₂O, resulting in a SLD of about $0.13 \cdot 10^{-6} \text{\AA}^{-2}$ [322]. The monomer has a scattering length density of

$0.74 \cdot 10^{-6} \text{ \AA}^{-2}$. Thus, if the particles were in pure D_2O the scattering contrast should be about $6 \cdot 10^{-6} \text{ \AA}^{-2}$ for completely dehydrated particles. Considering that water molecules inside the polymer decrease the scattering contrast this value is likely a bit lower. However, the results indicate that the substitution of 90 % of H_2O by D_2O is not sufficient for a good scattering contrast.

Furthermore, the radius of the particles continuously decreases with increasing temperature. Comparing the values of R_0 and R_h (Figure 4.2) one finds a difference of almost 30 nm. This is reasonable since DLS measures the hydrodynamic radius whereas SANS tends to describe only the core of the scattering particle [323].

The parameters of the Lorentzian and the Gaussian scattering also increase with increasing temperature until at 37°C and higher temperatures their contribution breaks down. A plot of $I_L(0)$ and ξ_L , respectively, versus temperature is shown in Figure 4.7. It can be seen that the absolute values of both increase upon approaching 36.5°C while both contributions are considerably smaller at higher temperatures. This trend is known in literature [318].

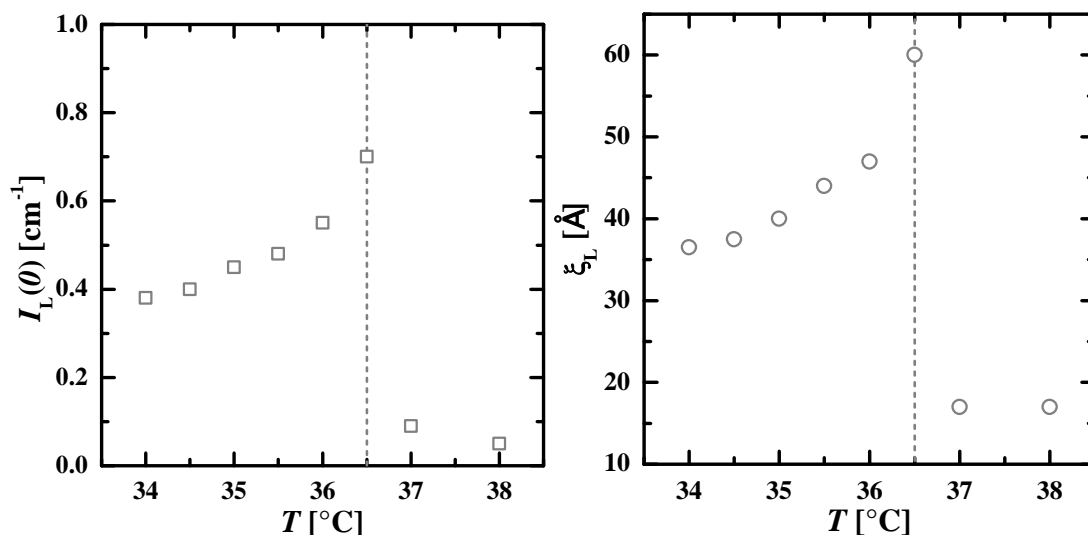


Figure 4.7: Plot of the fitting parameter $I_L(0)$ (left) and ξ_L (right) of the Lorentzian scattering contribution to the scattering curves of PNIPAM particles C1 (Figure 4.6). The values of both parameters increase up to 36.5°C . At higher temperatures the contribution of both breaks down.

The data shown in Figure 4.7 clearly indicate that the VPTT is at 36.5°C which is 2.5 K higher than the value found from DLS (see Table 4-1). A similar discrepancy becomes obvious if the scattering curves at 36.5°C and various pressures (Figure 4.6 right, measured in the SHP-SANS cell) are compared to the scattering curves at various temperatures (Figure 4.6 left, measured in a Hellma cuvette). The scattering curve at 1 bar and 36.5°C should have a shape and forward scattering comparable to the scattering curve obtained at 36°C or 37°C . This is not the case. Considering, the scattering curve at $p = 300$ bar shows a similar forward scattering intensity as the one recorded at $p = 1$ bar and 38°C . Thus, there seems to be a temperature discrepancy between the two sample holders. While the temperature probe is permanently installed into the SHP-SANS cell the one for the

Hellma cuvette sample holder is inserted manually. Furthermore, the temperature inside the SHP-SANS cell was double checked and verified by inserting the same temperature probe which was used for the cuvette holder directly into the sample volume. Thus, the temperatures obtained for the temperature variation are not correct, whereby the scattering curves indicate that the actual temperature was about 2.5°C lower than specified.

Temperature and pressure dependent SANS experiments were also performed on the polydisperse particles synthesised without surfactant. The resulting scattering curves together with the fitting functions are shown in Figure 4.8. Only the scattering curve at $T = 37^\circ\text{C}$ and $p = 1$ bar (Figure 4.8 right), recorded in the SHP-SANS cell, was described by the droplet form factor and the Lorentzian whereas for all other scattering curves also a Gaussian contribution was found. The results of the fitting functions are shown in Table 4-3.

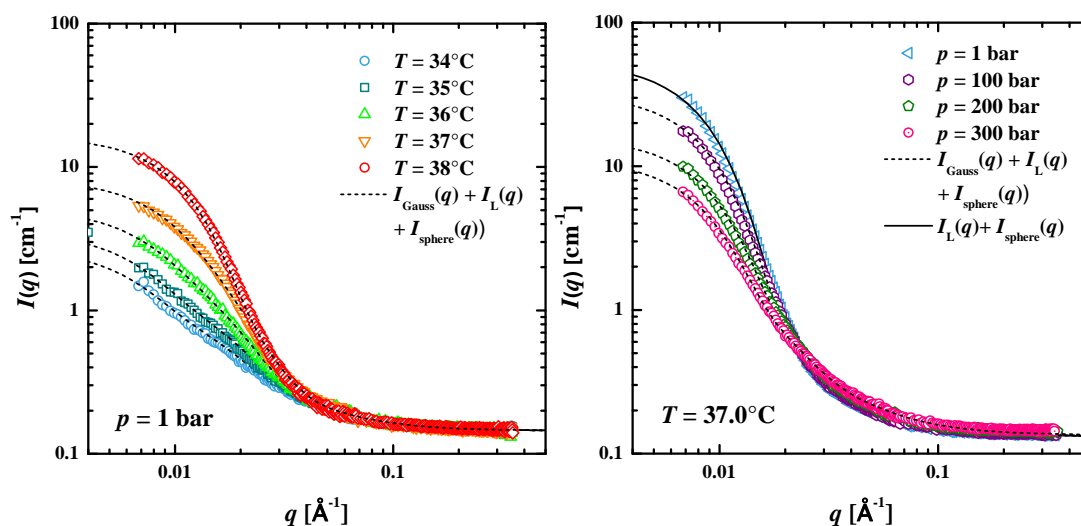


Figure 4.8: SANS data of PNIPAM particles C0, at atmospheric pressure and different temperatures (left) and at 37.0°C and at different pressures (right). Only the scattering curve at $p = 1$ bar and 37°C (right) was described without a Lorentzian scattering contribution. The scattering intensity increases with increasing temperature (left) while the slope changes from q^{-2} to q^{-4} . With increasing pressure (right) the scattering intensity decreases as the particles become more hydrated and thus loose scattering contrast.

Basically, the same trends as described for the scattering curves of the particles C1 with 5.6 wt% crosslinker and synthesised with surfactant (Figure 4.6) can be observed. Thus, the forward scattering increases with increasing temperature and decreases with increasing pressure. Comparing the scattering curves recorded in two different sample holders one again finds a discrepancy since the scattering curves both recorded at 1 bar and 37°C are considerably different. Considering that the temperatures displayed left were about 2.5 K lower than specified it is reasonable that for all scattering curves a Gaussian contribution was found. The breakdown of this contribution only occurs at temperatures exceeding the VPTT. Since the VPTT was determined to be 35°C by means of DLS (see Table 4-1) it follows that the scattering curve at (apparent) $T = 38^\circ\text{C}$ is actually only slightly above the VPTT. This is also indicated by the Lorentzian fitting parameter shown in Table 4-3. As was shown in

Figure 4.7 the Lorentzian contribution becomes considerably weaker at $T > \text{VPTT}$ which can be found at an alleged temperature of 37°C. This is 2 K higher than the VPTT determined by DLS.

Comparing the fitting parameters shown in Table 4-2 and Table 4-3 one basically observes the same trends. As expected from DLS results the particles synthesised without surfactant are somewhat larger and display higher polydispersities. Unfortunately, the scattering contrast for these particles is even lower than the one found for the previously discussed particles. This is probably due to small differences of the exact amounts of H₂O which were substituted by D₂O.

Table 4-3: Overview of the parameters used to describe the scattering curves shown in Figure 4.6 of PNIPAM particles C0. The scattering intensity $I_{\text{sphere}}(q)$ was used in combination with the Lorentzian $I_L(q)$ and the Gaussian intensity $I_G(q)$ for all scattering curve except the one $p = 300$ bar which was described without a Gaussian contribution. Note that the scattering curves at .5 temperatures are not shown.

parameter		sphere form factor			Lorentzian		Gaussian	
T [°C]	p [bar]	R_0 [Å]	σ/R_0	$\Delta\rho$ [10^{-6} Å^{-2}]	$I_L(0)$ [cm^{-1}]	ξ_L [Å]	$I_{\text{Gauss}}(0)$ [cm^{-1}]	Λ [Å]
34.0	1	205	0.38	0.050	0.40	47	0.60	120
35.0	1	200	0.38	0.065	0.48	50	0.85	117
35.5	1	192	0.37	0.070	0.52	53	1.00	115
36.0	1	188	0.37	0.095	0.60	57	1.40	110
36.5	1	182	0.36	0.125	0.75	65	1.78	108
37.0	1	160	0.35	0.180	0.90	73	2.40	108
37.5	1	140	0.35	0.300	0.22	35	2.40	102
38.0	1	140	0.35	0.505	0.15	27	1.05	90
37.0	1	170	0.34	0.550	0.08	20	--	--
37.0	100	160	0.34	0.450	0.12	22	0.30	85
37.0	200	165	0.34	0.330	0.18	25	0.54	85
37.0	300	170	0.34	0.240	0.40	40	0.60	95

A temperature and pressure variation was also performed for the particles containing 1.9 wt% crosslinker. The scattering curves shown in Figure 4.9 show the expected trends of increasing forward scattering intensity with increasing temperature. Increasing the pressure leads to a decrease of scattering intensity due to a higher degree of hydration of the particles which results in a lower scattering contrast.

Comparing the scattering curves at $p = 1$ bar and $T = 36^\circ\text{C}$ it is again obvious that they do not correspond to the same structure. The forward scattering intensity of the scattering curve recorded at $p = 300$ bar is comparable to the one at the alleged same temperature at atmospheric pressure. For the description of this scattering curve the Gaussian contribution was taken into account, indicating that the VPTT is traversed or very close.

In contrast to previous findings the fitting parameter R_0 (see Table 4-4) increases again at temperatures higher than the VPTT. In order to understand this effect the polymerisation kinetics need to be taken

into account. It is known that the polymerisation rate of the crosslinker BIS is higher than the one of the NIPAM monomer [320, 321], leading to polymer particles with a higher crosslinker density at the centre of the particle. This effect is probably more pronounced at low crosslinker concentrations. From a neutron point of view that means that only a small core is detected whereas a large amount of non-crosslinked hydrated polymer chains remain undetected due to their high degree of hydration. Upon increasing the temperature these chains fold onto the core. Although the core also shrinks with increasing temperature this effect seems to be compensated by the accumulation of polymer chains around the core, leading to an increase of radius.

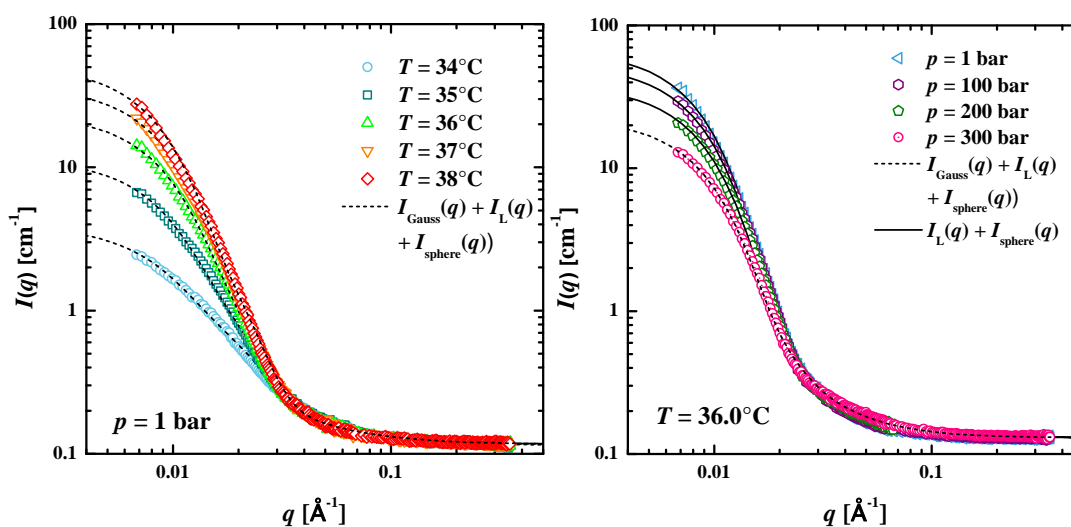


Figure 4.9: *Left:* SANS scattering curves at atmospheric pressure and different temperatures of PNIPAM particles A. With increasing temperature the forward scattering intensity increases mainly due to the better scattering contrast. All curves were described using the combination of the Gaussian, Lorentzian and sphere contribution. *Right:* SANS scattering curves of the same particles at $T = 36^\circ\text{C}$ and pressures between 1 bar and 300 bar. The scattering curves at $p \leq 200$ bar were described by means of a sphere form factor and the Lorentzian contribution whereas the Gaussian scattering intensity was also taken into account to describe the scattering curve at $p = 300$ bar.

As observed for the previous particles the scattering contrast is very low. This is again probably due to the fact that H_2O was not completely substituted by D_2O . Although the forward scattering intensity at an alleged temperature of 38°C is comparably high the Gaussian scattering contribution gives rise to the assumption that the VPTT was only slightly traversed.

Table 4-4: Overview of fit parameters to the scattering curves shown in Figure 4.9 of PNIPAM particles A. The scattering intensity $I_{\text{sphere}}(q)$ was used in combination with the Lorentzian $I_L(q)$ and the Gaussian intensity $I_G(q)$ for scattering curves below the VPTT. The scattering curves at .5 temperatures are not shown in Figure 4.9.

parameter		sphere form factor			Lorentzian		Gaussian	
T [°C]	p [bar]	R_0 [Å]	σ/R_0	$\Delta\rho$ [10^{-6} Å $^{-2}$]	$I_L(\mathbf{0})$ [cm $^{-1}$]	ξ_L [Å]	$I_{\text{Gauss}}(\mathbf{0})$ [cm $^{-1}$]	Λ [Å]
34.0	1	198	0.36	0.12	0.20	35	0.8	88
34.5	1	166	0.36	0.19	0.22	39	1.1	93
35.0	1	164	0.36	0.23	0.25	44	1.6	101
35.5	1	163	0.36	0.31	0.32	50	2.0	109
36.0	1	160	0.37	0.34	0.44	62	2.5	115
36.5	1	163	0.38	0.38	0.10	25	2.5	108
37.0	1	163	0.36	0.44	0.09	22	2.8	107
37.5	1	169	0.36	0.46	0.06	18	3.0	110
38.0	1	172	0.36	0.47	0.06	18	3.4	112
36.0	1	178	0.32	0.61	0.035	14.5	--	--
36.0	100	170	0.34	0.55	0.040	16	--	--
36.0	200	162	0.35	0.49	0.080	23	--	--
36.0	300	160	0.35	0.39	0.400	54	0.9	130

4.1.3 Static light scattering

The temperature-dependent scattering behaviour of PNIPAM particles A, C1 and C0 was investigated with static light scattering (SLS) measurements at different temperatures (see Figure 4.10). Here, despite the title of this chapter these measurements were only performed at atmospheric pressure. The scattering intensities for the particles C1 (5.6 wt% crosslinker, synthesised with surfactant), display the same trend (not shown).

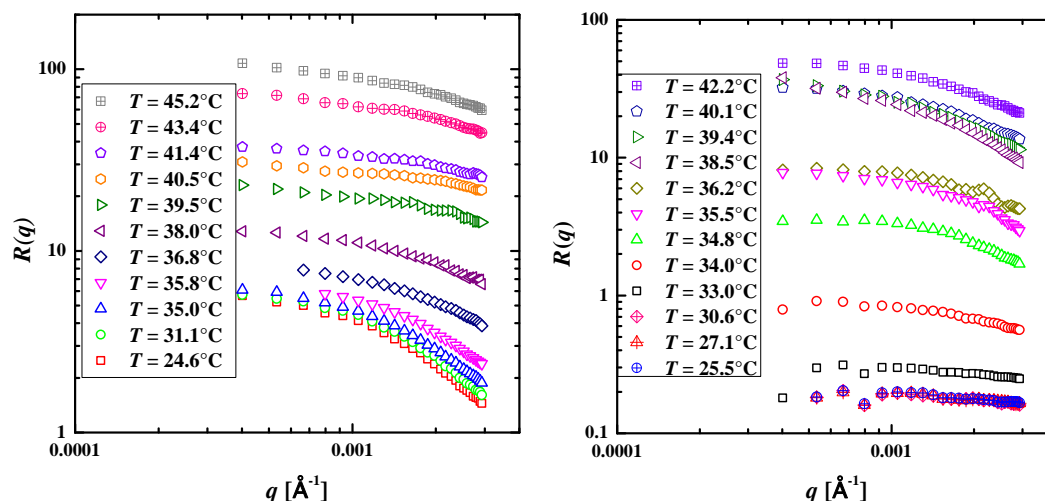


Figure 4.10: Selected SLS curves of PNIPAM particles C0 (left) and particles A (right), both at 0.1 wt% in H₂O and at different temperatures. The absolute scattering intensity increases with increasing T , and the slope at high q values decreases. The missing data points (left) plot are due to an instrumental error. The error bars are smaller than the symbols.

As can be seen in Figure 4.10 the most obvious trend among the data is the fact that the scattering intensity increases with increasing temperature, which can also be seen in the SANS curves in the low q -region. The reason for this is mainly the scattering contrast which increases due to a lower degree of hydration which results in a higher polymer concentration inside the particle and thus a higher scattering contrast

The second trend in Figure 4.10 is the fact that the slope in the high q -region gradually becomes less steep with increasing temperature. At first sight this seems obscure because the change from q^{-2} to q^{-4} dependence, which is expected for a change from gel-like scattering to the scattering from hard sphere, should lead to quite the opposite result. However, this change is not primarily connected to the structural changes but to the change of size of the particles. The shrinking of the particles with increasing temperature naturally leads to a shift of the scattering intensity to higher q -values which means that the q^{-4} dependences moves out of the SLS q -range. This is explained graphically in Figure 4.11 for the two particles with 5.6 wt% crosslinker.

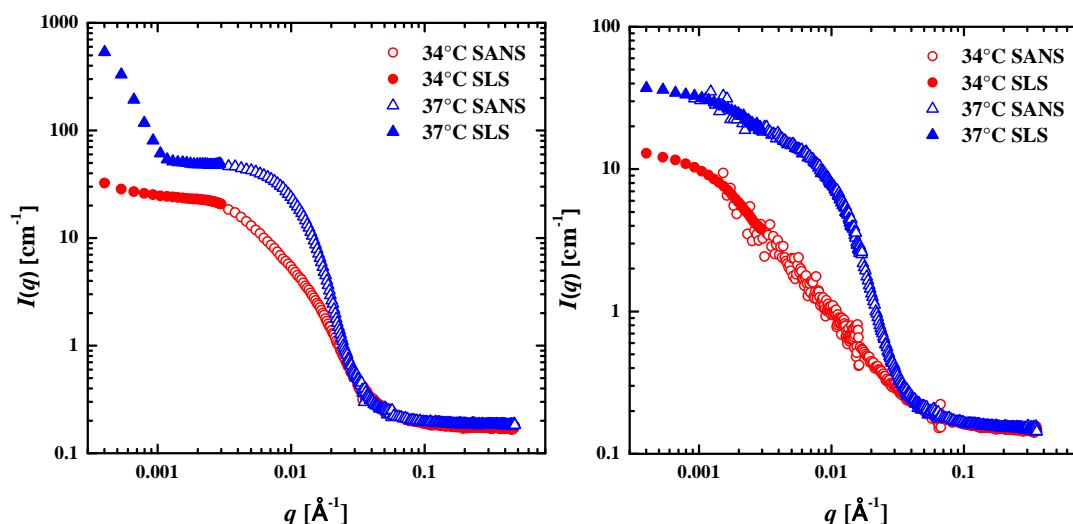


Figure 4.11: Plot of the static light scattering intensity together with SANS data at two different temperatures for particles C1 (left) and C0 (right). As can be seen the overlap of the SLS intensity and SANS data is reasonable. The enormous increase of scattering intensity of SLS data at 37°C in the left plot is due to dust scattering. Note that SANS data in the left plot were measured at the D33 instrument whereas the data in the right plot were gained from measurements at the D11 instrument which explains the different overlap of q -range.

Note that the q -range in which SLS and SANS data overlap in Figure 4.11 is different because the SANS data were collected at the D33 instrument in the left plot and at the D11 instrument in the right plot. The overlap is reasonable in both cases and shows very nicely that the slope in the high q -range of the SLS data is not connected to the power law dependence in the SANS data, especially at high temperatures.

In order to obtain structural information on the particles from the SLS measurements the data shown in Figure 4.10 were fitted with different models. Since all data represent the scattering of spherical particles the monodisperse sphere form factor according to Eq. 2-37 was used. For the large particles

synthesised without surfactant the Guinier approximation as shown in Eq. 2-87 was applied to estimate the radius of gyration. Although a description of the SLS data by means of the Lorentzian model according to Eq. 4-1 would be possible this is not reasonable. The Lorentzian model describes fluctuating polymer chains which can be observed only in the high q -range. The fitting functions are shown in Figure 4.12.

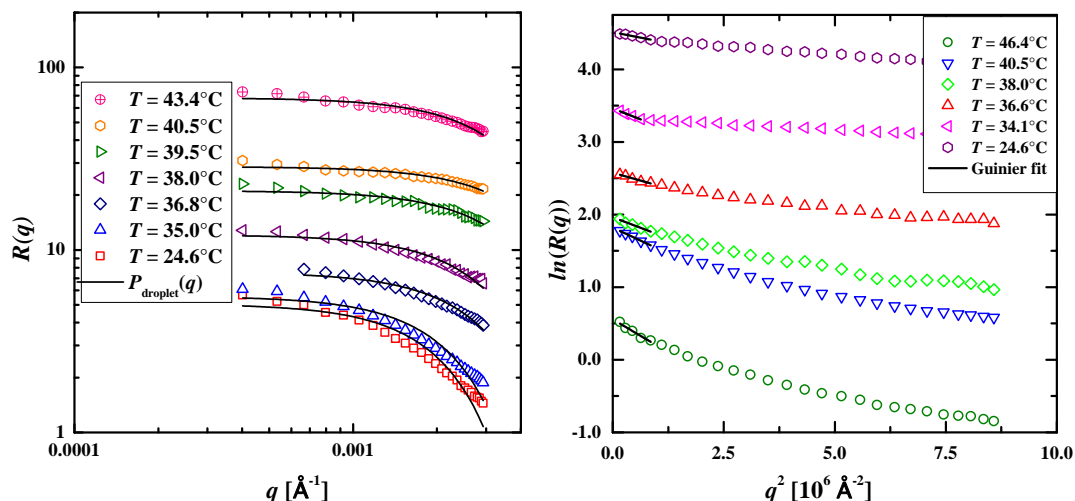


Figure 4.12: *Left:* Example scattering curves fitted with the sphere form factor $P_{\text{sphere}}(q)$. The deviations of $P_{\text{sphere}}(q)$ especially at low temperatures indicate that this model is not completely appropriate to describe microgel particles. Thus, these data should be treated carefully. *Right:* Plot of $R(q)$ on a \ln -scale against q^2 of selected scattering curves and the according Guinier fits to the scattering data at low q . Note that the q -range used for the Guinier fits fulfils the requirement that $qR_G < 1$ in all cases.

As can be seen in Figure 4.12 the sphere form factor $P_{\text{sphere}}(q)$ deviates considerably from the measured scattering intensity especially at low temperatures. This is very likely due to the rather inappropriate choice of model since the particles at these temperatures have a gel-like structure rather than a hard-sphere structure. The deviations as well as the awareness of the improper fitting model indicate that any data obtained with this model should be treated carefully. At high temperatures, however, $P_{\text{sphere}}(q)$ shows a reasonable description of the scattering data. The Guinier approximations shown in Figure 4.12 right are in all cases good fits to the scattering intensity.

The results of the different analysis methods are summarised in Figure 4.13. One finds a considerable difference between the hydrodynamic radius as determined via DLS measurements and the values obtained from SLS at low temperatures. This phenomenon is known in literature [64, 245, 323] and can be easily explained considering that DLS also measures the hydrate shell.

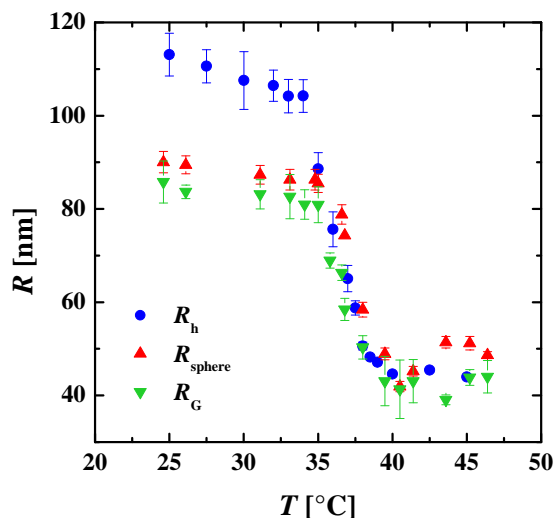


Figure 4.13: Plot of radii, obtained from different methods and fitting models, against temperature for particles C0. The hydrodynamic radius shows the highest values at low temperatures. The transition temperature and the radii at $T > \text{VPTT}$ are the same for all different methods (DLS, $P_{\text{droplet}}(q)$ and the Guinier approximation).

Additionally, SLS data at different concentrations were measured. Each concentration was measured at $T = 25^\circ\text{C}$, i.e. below the VPTT, as well as at $T = 40^\circ\text{C}$, i.e. above the VPTT. As can be expected higher concentrations display a higher scattering intensity (data not shown). These data were used for Zimm plots to obtain information on the molecular weight. The results are summarised in Table 4-5.

Comparing the molecular weight (MW) at different temperatures it becomes obvious that an increase of temperatures leads to an increase of MW. This effect is likely connected to the higher scattering contrast and is known in literature [64]. The comparison of MW of different particles at constant temperature reflects the DLS results in section 4.1.1. Thus, the particles with 1.9 wt% crosslinker are the largest ones at high temperature and thus have the highest molecular weight. The high swelling degree leads to a smaller molecular weight at low temperatures. The particles with 5.6 wt% crosslinker with a similar swelling ratio are almost of the same molecular weight whereas the particles with less crosslinker swell more and show a lower MW at low temperatures.

Table 4-5: Overview of the results of Zimm plots obtained from SLS data at four different concentrations. Each measurement was performed at 25°C which is well below the VPTT and at 40°C , i.e. above the VPTT. The analysis reveals a higher molecular weight (MW) for all particles at $T > \text{VPTT}$.

particles	crosslinker [wt%]	surfactant	MW @ 25°C [g mol ⁻¹]	MW @ 40°C [g mol ⁻¹]
C1	5.6	yes	$(6.2 \pm 0.9) \cdot 10^6$	$(1.2 \pm 0.8) \cdot 10^7$
C0	5.6	no	$(6.1 \pm 0.8) \cdot 10^6$	$(2.3 \pm 0.1) \cdot 10^7$
A	1.9	yes	$(4.5 \pm 0.8) \cdot 10^5$	$(7.9 \pm 0.9) \cdot 10^7$

4.2 Swelling and deswelling kinetics induced by sudden pressure jumps

Pressure jump experiments using the SHP-SANS cell as described in chapter 2.4.5 were performed in order to obtain information on the kinetics of structural changes as a response to a sudden pressure jump. Pressure and temperature induce exactly the same structural changes but at different transition temperatures. Thus, these experiments can be compared to temperature jump experiments. Thereby, both structural changes, i.e. from gel to sphere and from sphere to gel, can be followed. Using temperature jump methods the application of fast cooling steps remains a challenge and has not yet been solved satisfactorily. Therefore, the measurements presented in the following contribute to the investigation of the kinetics of structural changes of PNIPAM microgel particles.

The first kinetic experiments were performed at $T = 36.6^\circ\text{C}$ with the particles C1 with 5.6 wt% crosslinker. The pressure cycle was adjusted to last for 60 s with 30 s at each pressure (300 and 10 bar) with a time resolution of 2 s. The pressure-dependent scattering curves in Figure 4.6 indicate that this pressure jump traverses the change from sphere to swollen sphere, as can be seen by the Gaussian contribution at high pressure. The scattering curves as a function of time and pressure for are shown in Figure 4.14.

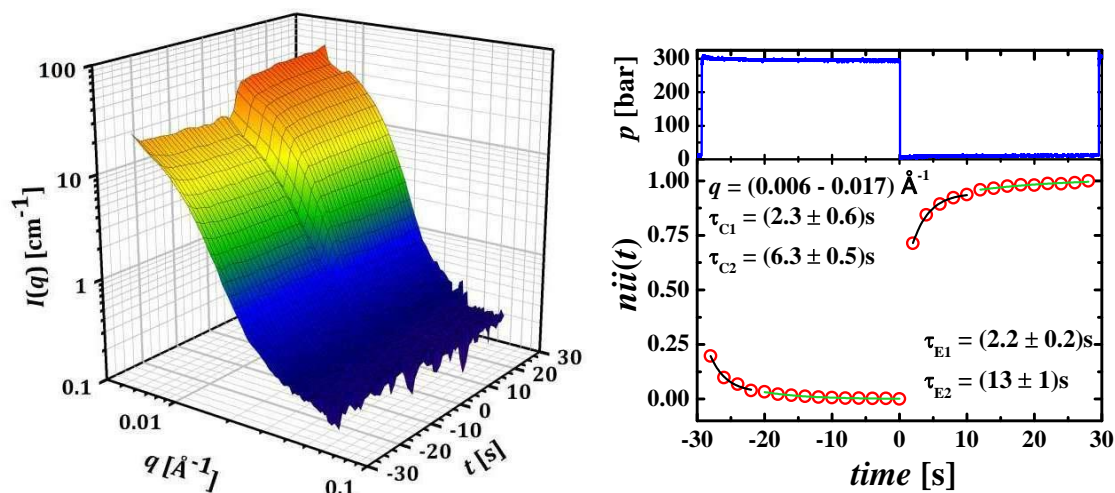


Figure 4.14: *Left:* Pressure-dependent scattering curves as a function of time of PNIPAM particles C1, recorded at $T = 36.6^\circ\text{C}$. The pressure jump takes places at $t = 0$ s from $p = 300$ bar (at $t < 0$ s) to $p = 5$ bar (at $t > 0$ s). Each pressure was kept constant for 30 s, scattering curves were recorded with a time resolution of 2 s. The change in forward scattering is very obvious after the pressure jump. *Right:* Normalised integrated intensity ($nii(t)$) as a function of time in the q -range from $0.006 - 0.017 \text{ \AA}^{-1}$ to the scattering curves shown left. The time resolution of $nii(t)$ is 2 s as well. After compression and expansion two exponential fitting functions (solid lines) were necessary to describe the data points sufficiently. The error is within the size of the symbols.

The scattering curves in Figure 4.14 left at times $t < 0$ s correspond to $p = 300$ bar and $t > 0$ to $p = 10$ bar. Especially the change of forward scattering is very obvious after the pressure jump at $t = 0$ s. Taking a closer look at the q -dependence in the medium q -range it becomes obvious that the slope of the scattering curves is much steeper at $p = 10$ bar than at 300 bar which is connected to the

higher sphere scattering contribution. At $p = 300$ bar the contribution of gel scattering is more pronounced.

In order to obtain detailed information on the kinetics of structural changes the normalised integrated intensities as a function of time ($nii(t)$) are shown in Figure 4.14 right. Thereby, the q -range for the integration was fixed to be between 0.006 \AA^{-1} and 0.017 \AA^{-1} since the scattering curves show an isosbestic point around $q \approx 0.017 \text{ \AA}^{-1}$. It was found that for both the processes after compression and expansion two exponential fitting functions were necessary to describe the data in a satisfactory way. Thereby, the first processes occurred on a time scale of about 2.2 s and 2.3 s, respectively, after compression and expansion. This process likely describes the primary structural changes between sphere to more hydrated sphere. The second, slower processes are likely to represent reordering processes and temperature relaxation since they happen on a rather long time scale of 6.3 and 13 s, respectively.

To gain more detailed information on the fast processes another pressure jump experiment was performed in which the pressure cycle was adjusted to last for 10 s with 5 s at each pressure and a time resolution of 0.2 s. The pressure-dependent scattering curves as a function of time are shown in Figure 4.15 left. Here, again the increase of forward scattering after expansion is very obvious.

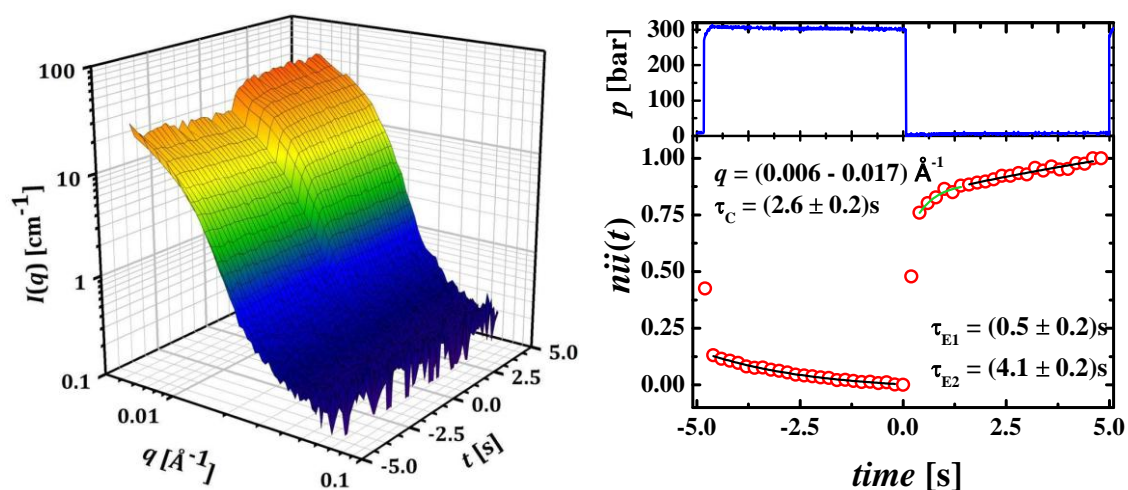


Figure 4.15: *Left:* Pressure-dependent scattering curves of PNIPAM particles C1 as a function of time. A concentration of 0.5 wt% particles in D_2O was used. The scattering curves were recorded at $T = 36.6^\circ C$. The pressure cycle starts at $p = 300$ bar which was held for 5 s, until at $t = 0.0$ s the pressure was changed to 5 bar for 5 s. A time resolution of 200 ms was applied. *Right:* Normalised integrated intensity ($nii(t)$) as a function of time for the scattering curves shown left in the q -range from $0.006 - 0.017 \text{ \AA}^{-1}$. While the data points after compression were described by one exponential fit two functions were necessary to describe the data points after expansion. The solid lines represent these exponential fitting functions and are proportional to $exp(-t/\tau)$. The pressure profile shown at the top also applies to the plot shown left. Note that the error is within the size of the symbols.

Analysing $nii(t)$ it was found that the process after compression can be described by means of one mono-exponential fitting function. The time constant found for this process $\tau_c = (2.6 \pm 0.2) \text{ s}$ resembles the one found for the faster process in the longer experiment (Figure 4.14). The data points

obtained after expansion, however, were described by two fitting functions. Thus, a first and fast process occurs on a time scale of 0.5 s and is followed by a slower process ($\tau_{E2} = (4.1 \pm 0.2)$ s). A single exponential fitting function would lead to $\tau = (2.2 \pm 1.2)$ s. Although this value is similar to the one obtained from the long experiment (Figure 4.14) the high error indicates that the description with two fitting functions is a better representation.

A similar experiment was performed using the particles C0, also with 5.6 wt% crosslinker but synthesised without surfactant. Thus, the pressure cycle was also adjusted to last for 10 s with 5 s at 300 bar and 5 bar, respectively. The resulting scattering curves as a function of time are shown in Figure 4.16 left. Although the absolute scattering intensity is slightly lower than in the previous experiment the increase of forward scattering intensity can clearly be observed after expansion, i.e. at $t > 0$ s. Furthermore, clearly the slope of scattering intensity changes from almost a straight line for $p = 300$ bar to more steep course with flattening intensity in the low q -range at $p = 10$ bar.

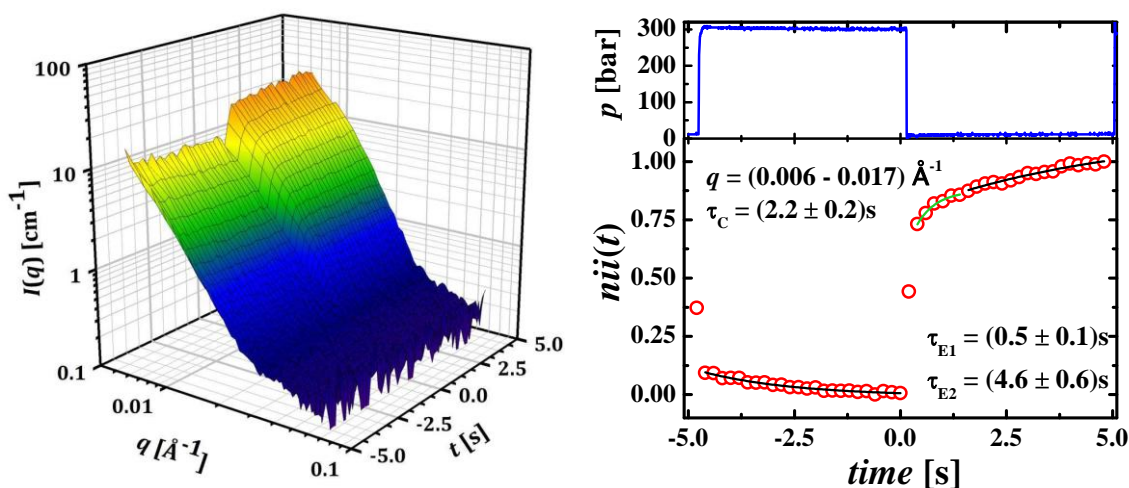


Figure 4.16: *Left:* 3D-plot of scattering curves as a function of time for the particles C0. The temperature was set to 37.0°C. The pressure cycle starts at $p = 300$ bar at $t = -5$ s. The pressure jump occurs after 5 s at $t = 0.0$ s to $p = 5$ bar. Scattering curves were recorded with a time resolution of 0.2 s. Again, especially the forward scattering intensity ($nii(t)$) and the slope of the scattering curves in the medium q -range change. *Right:* Normalised integrated intensity as a function of time for the q -range from $0.006 - 0.017 \text{ \AA}^{-1}$, also with a time resolution of 0.2 s. While the process after compression was described by one mono-exponential fitting function two of these were necessary for the process after expansion. Note that the error bars are smaller than the symbols.

The analysis of $nii(t)$ (Figure 4.16 right) revealed a trend comparable to the previous experiment. Considering the similarities of both particles this is not surprising. Thus, the process after compression was found to have a time constant of (2.2 ± 0.2) s which is slightly lower than the one found for particles C1 synthesised with surfactant. For the description of $nii(t)$ after expansion again two exponential fitting functions were necessary whereby the time constant describing the fast process is the same as the one found for the previous particles. The second time constant is (4.6 ± 0.6) s and thus higher than the one displayed in Figure 4.15 which might be caused by the higher polydispersity.

In order to investigate also the influence of the crosslinker contents pressure jumps between 300 bar and 5 bar were also conducted with the particles A containing 1.9 wt% crosslinker. Thereby, the same frequency of 0.1 Hz with 5 s at each pressure and a time resolution of 0.2 s were applied. The pressure-dependent scattering curves in a plot versus time (Figure 4.17 left) display the expected increase of forward scattering intensity after expansion.

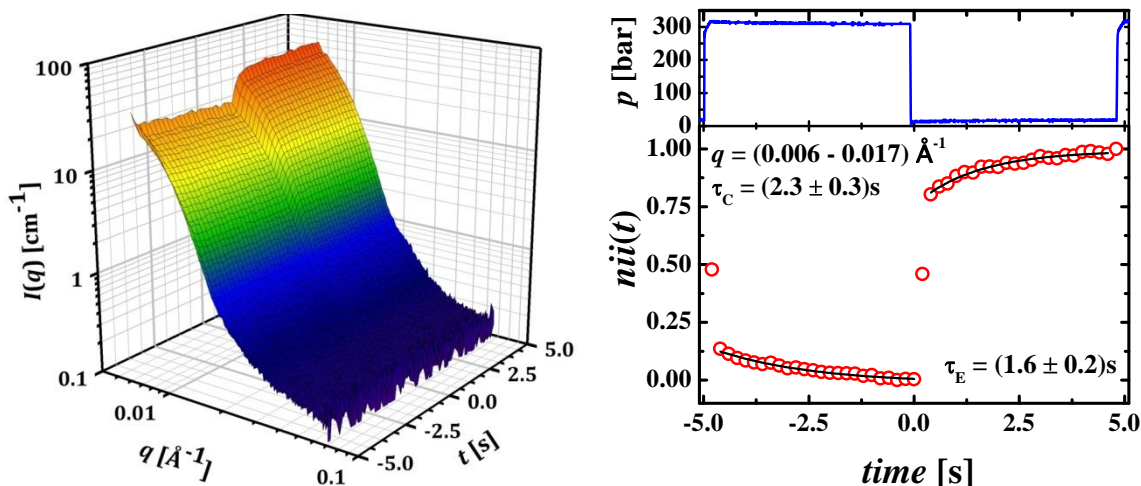


Figure 4.17: *Left:* Scattering curves as a function of time of PNIPAM particles A. The pressure cycle was adjusted to start at $p = 300$ bar at $t = -5$ s. The pressure jump occurs at $t = 0.0$ s to $p = 150$ bar which is also kept for 5 s. A time resolution of 0.2 s was applied. *Right:* Normalised integrated intensity ($nii(t)$) as a function of time, calculated for the scattering curves shown left in the q -range from $0.006 - 0.017 \text{ \AA}^{-1}$. Both the processes after compression and expansion were described with one mono-exponential fitting function. The error of $nii(t)$ is within the symbol size.

In contrast to previous experiments with particles with higher crosslinker contents both processes were described with only one exponential fitting function. Thereby, the process after compression was found to happen on a longer time scale than the one after expansion. Compared to previous experiments the time constant $\tau_C = (2.3 \pm 0.3)$ s is in the same order of magnitude than the other time constants describing the process after compression.

In order to elucidate the kinetics of structural changes in dependence of the crosslinker content the time constants presented here can be compared to previous results [29] of particles with 1.9 wt% and 3.8 wt% crosslinker. Thus, all time constants are summarised in Table 4-6.

Comparing the time constants describing the processes after compression one finds only the particles containing 3.8 wt% crosslinker showed two processes. Re-evaluation of these data revealed that a description with one exponential function is also possible, leading to $\tau_C = (1.7 \pm 0.1)$ s for this process. Now, one finds a trend of increasing τ with increasing crosslinker content if the particles with 1.9 wt% crosslinker presented here are not considered. The fact that for these particles a different time constant was found is probably due to the fact that the pressure jump experiment only reached the VPTT and did not traverse it (see static scattering curves in Figure 4.9). For the process after expansion, however, one finds exactly

the same time constants for both experiments with particles containing 1.9 wt% crosslinker. This indicates a change to dehydrated particles happens on the same time scale irrespective of the starting point. Considering the other particles, it shows that for all other crosslinker concentrations two exponential processes were found. Among these, the time constants also increase with increasing crosslinker content. Thus, it can be assumed that the first process is slowed down by the presence of crosslinker. The following, slower process shows a similar trend.

Table 4-6: Overview of time constants obtained from fitting functions to the normalised integrated intensities ($n_{ii}(t)$) of the pressure jumps shown in Figure 4.15, Figure 4.16 and Figure 4.17. Especially the processes after expansion indicate that structural changes occur on a longer time scale with increasing crosslinker content. The time constants of particles without name were taken from [29].

particles	crosslinker [wt%]	surfactant	τ after compression [s]	τ after expansion [s]
C1	5.6	yes	2.6 ± 0.2	0.5 ± 0.2
				4.1 ± 0.5
C0	5.6	no	2.2 ± 0.2	0.5 ± 0.2
				4.6 ± 0.6
A	3.8	yes	1.7 ± 0.1	0.4 ± 0.1
	1.9	yes	2.3 ± 0.3	1.6 ± 0.2
	1.9	yes	1.2 ± 0.1	1.6 ± 0.1

Having analysed the time constants for structural changes the question arises which processes are described. Therefore, a more detailed look at the scattering curves is reasonable. Selected scattering curves are shown in Figure 4.18. Regarding the process after compression, one finds that the major structural changes happen already during the pressure jump, i.e. with a time constant faster than 0.2 s. Considering the scattering curves this process can be attributed to a decrease of scattering contrast, i.e. to a diffusion of water molecules into the particles. The process which was described by time constants thus likely represents reordering processes. The processes after expansion, shown in Figure 4.18 right, indicate that the collapsing of polymer chains is slower and distinctly passes different mixed structures. The second process found for this conversion can be observed as an increase of forward scattering intensity and can thus be ascribed to an increase of scattering contrast, i.e. to diffusion of water molecules out of the particles scattering volume.

These results are very similar to the results found by Sun *et al.* in 2010 [324]. They investigated PNIPAM hydrogels by means of correlation infrared spectroscopy and proposed a mechanism of the volume phase transition. Their results indicate that during a heating process PNIPAM collapses along its backbone before water is expelled from the network, while in the cooling process, the water molecules diffuse into the network before the chain revival along the backbone occurs. Thereby, they found that in the heating process the chain collapse occurred with intermediate states while the chain

revival in the cooling process occurred with only conversion between two single states [324]. These results are in good accordance with the results obtained from pressure jump experiments.

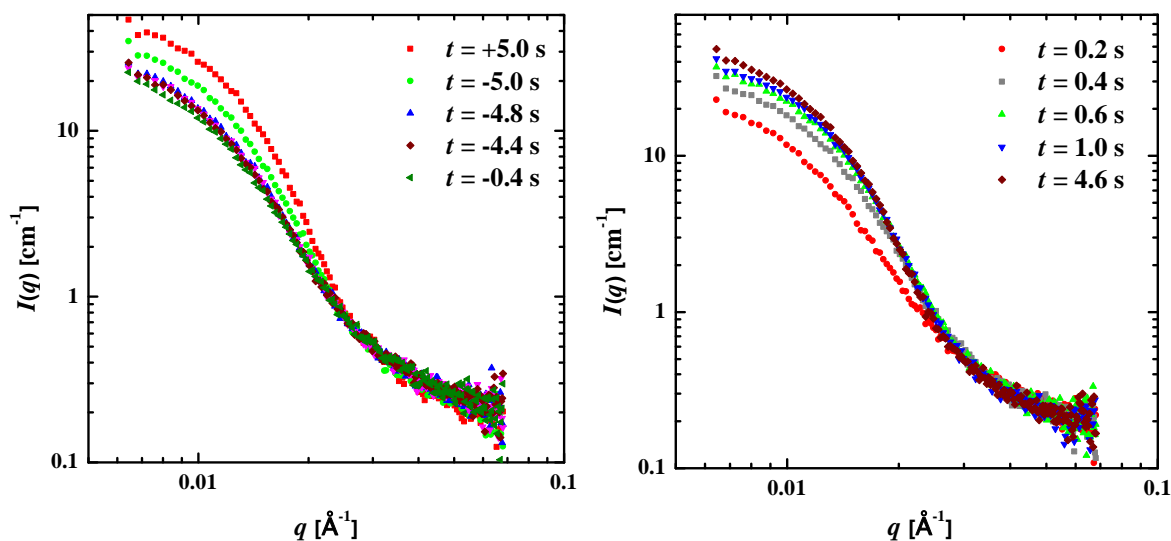


Figure 4.18: Selected scattering curves from the 3D plot shown in Figure 4.14 left of PNIPAM particles C1. *Left:* Scattering curves shortly before (red squares), during (green circles) and after compression. The major structural changes occur on a very fast time scale. *Right:* Scattering curves slightly after the pressure jump (0.2 s) and at subsequent times. While the first process can be observed until $t = 0.6$ s the process after that results only in a change of forward scattering intensity.

In order to obtain more detailed information on the structural changes selected scattering curves from Figure 4.15, i.e. of the pressure jump experiment with particles containing 5.6 wt% crosslinker, were described by fitting functions. Selected parameters are shown as a function of time in Figure 4.19. Here, the reason for the two different processes observed by analysing $nii(t)$ becomes obvious. First, the contribution of the Gaussian scattering intensity decreases after expansion until it does not contribute at all at $t > 1.4$ s. Furthermore, after the same time the decrease of Lorentzian contribution reaches constant values, indicating that the main part of gel-to-sphere transition is finished within this time frame. The main contribution to $nii(t)$ is, however, presumably to be found in the change of scattering length density difference $\Delta\rho$, which is shown in Figure 4.19 D. Here, it is especially interesting that the time constants strongly resemble the ones listed in Table 4-6. This is a good indication that $\Delta\rho$ is the main representative of the change of $nii(t)$. $\Delta\rho$ can be translated to diffusion of water molecules. It was shown by Philipp *et al.* that the diffusion coefficient of water in PNIPAM particles is very low [325] which explains the fast mayor changes in scattering intensity right after the pressure jump. However, they also mention the existence of more tightly-bound water molecules with higher diffusion coefficients. Thus, it is likely that the observed changes with time constants around 1 s are due to this class of water molecules.

The time constants obtained for $I_{\text{Gauss}}(0)$ and Λ_{G} after compression are somewhat higher, whereas the one for $\Delta\rho$ is slightly lower than the value obtained from $nii(t)$ analysis. Thus, it follows that $nii(t)$ represent a mixture of both contributions. These findings further support the processes suggested

earlier, i.e. that the processes after heating occur with intermediate states (i.e. with states which include Gaussian contributions). The process after cooling, i.e. compression, in contrast, only shows one process, indicating that the diffusion of water molecules occurs with the same time constant during the whole observation process.

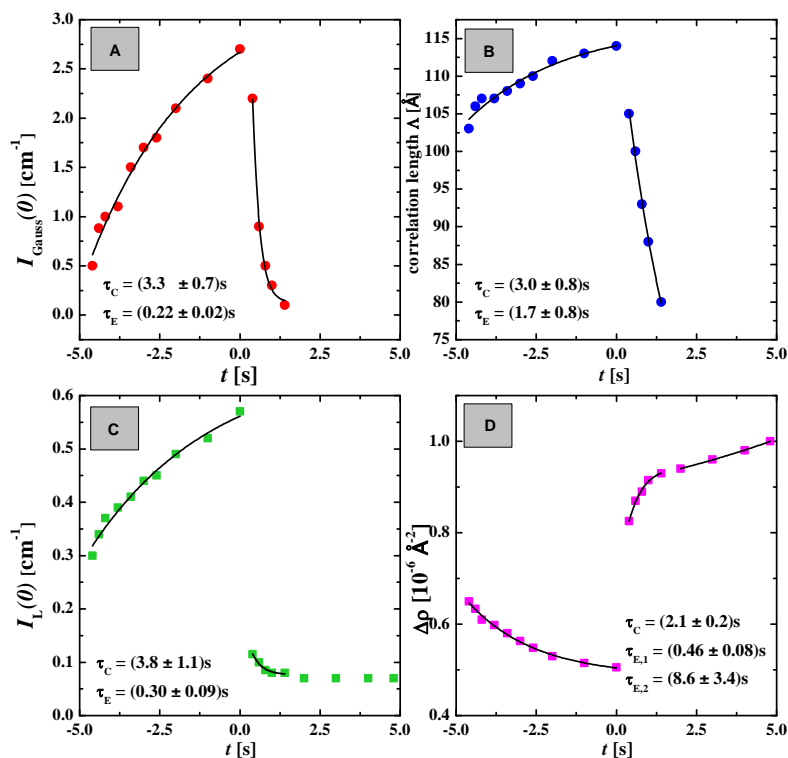


Figure 4.19: Selected fit parameters as a function of time, obtained from description of the scattering curves shown in Figure 4.15 (particles C1). The solid lines represent exponential fitting functions whereby the respective time constants are given in the plot. *A and B:* $I_{\text{Gauss}}(0)$ and Λ_G from the Gaussian contribution. Both values increase upon compression, clearly representing the hydration process, and rapidly decrease after expansion. Note that the Gaussian contribution was not found at $t > 1.4$ s after the expansion. *C:* $I_L(0)$ obtained from the Lorentzian description. Clearly, a fast change happens after expansion which is followed by a constant contribution. *D:* Scattering length density as a function of time. The decrease after compression is connected to hydration. Again, two processes are observed after expansion.

4.3 Microfluidics

Section 4.2 gives information on the kinetics of structural changes of PNIPAM particles as a response to a fast pressure jump. Since the state of the particles at elevated pressure is completely comparable to a state at atmospheric pressure and a slightly lower temperature it is reasonable to assume that the sequence of structural changes is the same for fast temperature jumps. In order to also investigate the kinetics of structural changes as a response to a fast temperature jump, both from low to high and from high to low temperatures, a new device was developed. This device is based on microfluidics.

Microfluidic setups consist of one or more narrow channels through which matter can be guided. It aims to investigate and develop miniature devices which can sense, pump, mix, monitor and control small volumes of fluids [326]. The applications include many different areas such as chemical synthesis, biological and chemical sensing, molecular separation or DNA sequencing [327-329].

The combination of microfluidics and PNIPAM is also described for various setups in literature, as for example the synthesis of polymer particles containing PNIPAM [330, 331]. Since it is possible to bring together different channels a microfluidic setup is especially well suited to investigate the features of co-nonsolvency [74, 332]. Temperature jumps have also been performed in a stopped-flow device by combining two channels with the polymer solution and hot solvent in the respective channels [71]. This experiment, however, does not study the pure response of the polymer particles to a change of temperature but the response of PNIPAM to a change of the solvent composition.

4.3.1 Newly developed microfluidic setup for temperature jumps

Since the information in literature is scarce on temperature jump kinetics of PNIPAM particles which are purely connected to a change of temperature a new approach was developed to study these kinetics. The newly designed setup utilises the high surface-to-volume ratio which is provided by very small channels and should allow to apply a different temperature in a very fast way. Thus, surrounding a channel with two different temperatures the response of liquid flowing through this channel can be followed by studying for example the transmission properties at different positions after the temperature jump. A schematic drawing of such a setup is shown in Figure 4.20.

The setup shown schematically in Figure 4.20 can be divided into three different parts or purposes. The first part is the syringe pump at the left which provides adjustable flow rates of the polymer dispersion through a flexible plastic tubing. This tubing then passes through a falcon tube which was modified in such a way that it can be connected to a water bath and can thus be used as a tempering device for the tubing. After the tubing exits the falcon tube it passes about 2 cm of non-controlled temperature before it is merged with a 1 mm X-ray capillary. This capillary is stuck through a casket made out of poly(dimethyl)siloxane (PDMS) which is glued onto a reflective silicon waver. The waver and thus the casket is placed on top of a metal block which can be connected to a water bath and thus

provides the second temperature for the temperature setup. In order to apply a constant temperature around the capillary the casket was filled with transparent silicon oil. The rear end of the capillary leads to a falcon tube which collects the liquid. The response of the polymer solution to the temperature jump can be followed by focussing the microscope onto the middle of the capillary and measuring the absolute intensity as a function of position. This method is enabled by the fact that the turbidity of a dispersion of PNIPAM particles increases with increasing temperature and has been applied before [72].

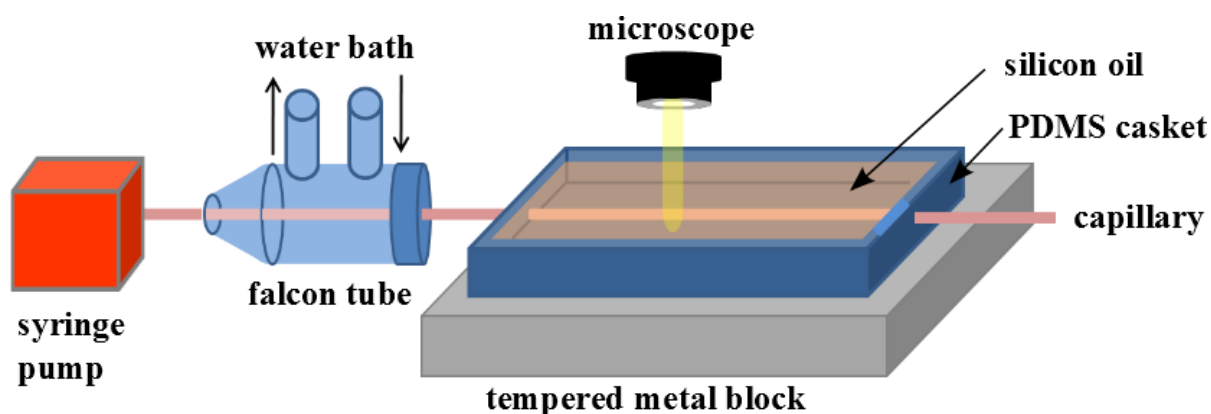


Figure 4.20: Schematic drawing of a newly designed microfluidic device for studying temperature-induced structural changes of PNIPAM particles. The polymer dispersion is pumped by a syringe pump with adjustable flow rate through a flexible plastic tubing. This tubing is temperature-controlled by guiding it through a modified Falcon tube which is connected to a water bath and thus functions as a tempering device. After leaving the Falcon tube the liquid enters the PDMS casket which is placed on a reflective surface and is temperature-controlled by a tempered metal block underneath it. Before entering the casket the tubing is connected to a 1 mm X-ray capillary to enable optical measurements. The whole setup is placed underneath a reflective microscope.

4.3.2 Results of temperature jump experiments

Using this setup eight positions and four different temperature jumps were studied. At each position five different flow rates were applied in order to be able to calculate different time intervals after the temperature jump. Before each measurement the applied temperatures were equilibrated for at least 15 minutes. A picture was taken of this equilibrated state. Integration of the total intensity of that picture provided the reference value for normalisation of the measurements taken under flow. This normalisation is necessary because the microscope was focussed after each change of position. After switching on the syringe pump the flow was kept constant for at least two minutes before a picture was taken. After switching off the pump the system was left for equilibration for at least 5 minutes and another picture of the equilibrated state was taken. In order to determine the total reflected intensity the integrated area of all pictures was integrated by 100 %. The difference of the absolute intensity of the two equilibrium pictures was less than 1 % in most cases. By measuring the absolute intensity this experiment can be regarded as a transmission experiment since the microscope used was a reflective microscope.

The particles under investigation were the particles containing 1.9 wt% crosslinker. The according DLS, SANS and kinetic data are shown in Figure 4.5 left, Figure 4.9 and Figure 4.17, respectively. The concentration of the particles was fixed at 2 wt% which is much higher than the concentration used for DLS and SANS experiments but was necessary in order to achieve as much difference of the signals at different temperatures as possible.

The results of the temperature jump experiment from 30°C to 40°C and from 40°C to 30°C are shown in Figure 4.21 by means of a plot of relative intensity versus time after the temperature jump.

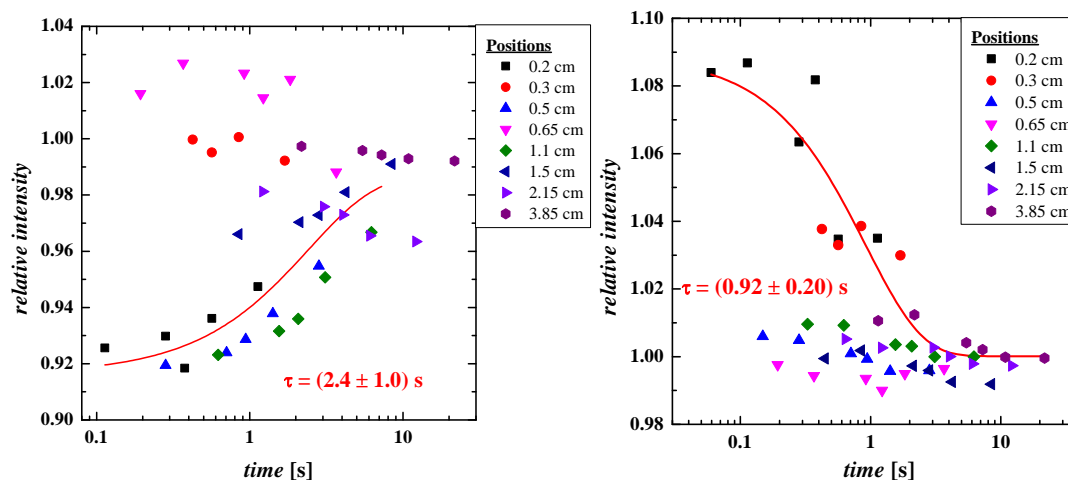


Figure 4.21: Plot of the relative intensity of a PNIPAM dispersion with 2 wt% particles with 1.9 wt% crosslinker, determined by means of a reflective microscope, versus time. The time was calculated from the flow rate and the position after the temperature jump from 30°C to 40°C (left) and from 40°C to 30°C (right). The temperature jump was performed by means of the setup shown in Figure 4.20. The relative intensity describes the intensity during a flow experiment normalised to the equilibrium intensity whereby the deviations are rather small if noticeable at all. Different symbols indicate the different positions at which the experiment was performed. Selected data were used to determine the time constants shown in red.

The time which is on the x-axis in Figure 4.21 was calculated from the flow rate and the position according to

$$time [s] = \frac{Position [m]}{Flow rate [m s^{-1}]} \quad \text{Eq. 4-1.}$$

The flow rate was adjusted at the syringe pump. The position describes the distance between the point at which the liquid enters the PDMS casket with the second temperature and the microscope.

Considering the scaling of the y-axis the deviation of the absolute intensity during flow experiments from the absolute intensity at the respective equilibrium state is in all cases less than 10%. Nevertheless, some data points seem to represent a systematic change in intensity. Fitting an exponential function to these data resulted in time constants of $\tau = (2.44 \pm 1.33) s$ for a temperature jump from 30°C to 45°C and $\tau = (0.92 \pm 0.20) s$ for the experiment from 40°C to 30°C. It seems that the temperature jump from 40°C to 30°C is faster than the other way round by a factor of about 2.5. This might, however, be caused by the part of tubing between the falcon tube and the PDMS casket which

is not temperature controlled. This part is about 2 cm long and will very likely lead to a cooling of the polymer dispersion before the polymer reaches the casket and thus the second temperature. On top of that this effect should be more pronounced for the temperature jump from high to low temperature as the temperature jump from low to high temperature should be less effected by a lower temperature at the non-tempered piece of tubing.

The same experiment was performed with the temperatures adjusted to 30°C and 45°C. The results in form of a plot of the relative intensity versus time are shown in Figure 4.22.

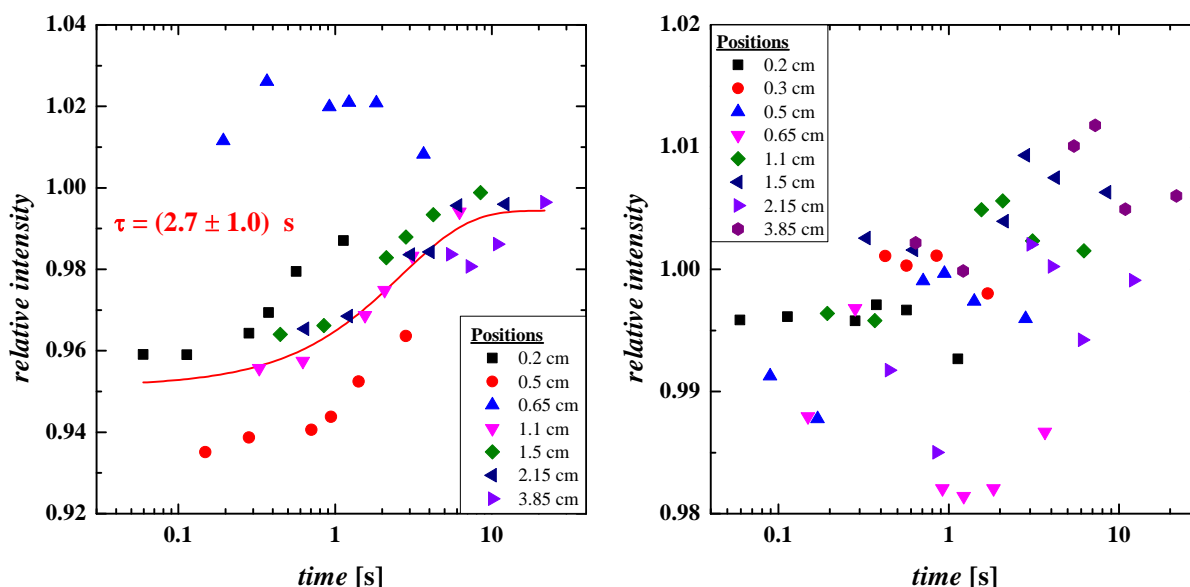


Figure 4.22: Plot of the relative intensity of a 2 wt% PNIPAM dispersion of particles with 1.9 % crosslinker versus time. The relative intensity was recorded by means of a reflective microscope. The time was calculated from the flow rate and the position after the temperature jump, which was from 30°C to 45°C (left) and from 45°C to 30°C (right) in this case. The relative intensity was calculated by normalising the intensity during the flow experiment to the intensity at the equilibrium temperature. The deviations from equilibrium intensity are, however, even smaller than in the previous experiment shown in Figure 4.21. The temperature jump from 45°C to 30°C does not allow determining a time constant since the normalised intensities are too close to equilibrium intensity.

Comparing the absolute values of relative intensity of the two temperature jump experiments it is striking that the deviations from equilibrium intensity are higher for the temperature jumps to and from 40°C. Since a higher temperature difference is expected to result in a larger difference of intensity this trend requires further investigation.

It was possible to determine a time constant for the temperature jump from 30°C to 45°C of $\tau = (2.65 \pm 1.04) \text{ s}$. This time constant is very close to the one determined for the temperature jump from 30°C to 40°C but slightly higher, indicating that a temperature jump to higher temperatures leads to a faster change of the structure of the polymer. For the temperature jump from 45°C to 30°C it was, however, not possible to determine a reasonable course of intensity with time since the difference of all measured relative intensities is less than 2 % (see scaling in Figure 4.22 right) which is too low to draw reliable conclusions. The reason for this result can very likely be found in the piece of tubing

between the falcon tube and the PDMS casket as discussed above. Compared to the temperature jump from 40°C this experiment with a starting temperature of 45°C should be even more effected, thus resulting in even lower differences of intensity.

4.3.3 Discussion

The experiments presented here are the first investigations of structural changes of PNIPAM particles which are purely induced by a fast change of temperature and can be performed in both directions. The novelty of these experiments naturally is accompanied by a few problems.

Thus, the small deviations in intensity between the flow experiment and equilibrium are problematic because this leads to low amplitudes and high errors. This can probably be improved by using polymer dispersions with higher concentration or a longer light path, i.e. a higher cell. The optimum setup would be a channel with a width of about 100 μm but a height of about 1 cm. A capillary with a higher diameter would deteriorate the surface-to-volume ratio so that temperature gradients become more likely. The necessarily thin walls of such a channel to allow a fast and homogeneous exchange of temperature is, however, experimentally challenging.

The piece of tubing between the Falcon tube and the PDMS casket provides another problem. It is about 2 cm long and not temperature-controlled which is probably the reason why the results of the temperature jumps from high to low temperature did not lead to a satisfactory result. This problem should be rather easy to fix with an improved setup.

One problem in both experiments is the fact that the intensity increases with increasing temperature. This is expected for scattering experiments (SANS, Figure 4.9 left) but not for reflective microscope which is a transmission setup. The light beam from the microscope passes the sample twice, i.e. on its way down through the sample to the reflective surface and on its way back to the microscope which should only improve the deviations from equilibrium intensity.

Comparing the obtained time constants to the results from pressure jump experiments (see Figure 4.17) one finds considerable differences. Thus, the trend found by means of SANS that the swelling occurs on a longer time scale than the chain collapse was not found here but seems to be the other way round. Admittedly, this trend was only found for these particles where all other experiments indicate that the dehydration and accumulation of polymer chains is slower than the swelling. Thus, the general trend seems reliable. Although the absolute values of time constants differ among different experiments they are at least in the same order of magnitude.

If one aims to publish data from this experimental setup one should, however, determine the time it takes the solvent to heat up after the pressure jump, for example by means of a temperature-sensitive dye such as *N*-acetyl-L-tryptophanamide (NATA) [71]. This should be done in order to be able to separate the time it takes to heat up the solvent from the response of the polymer particles to the change of temperature.

4.4 Conclusion

The interest in (PNIPAM) has grown rapidly because its characteristic volume phase transition temperature (VPTT) is located around 32°C and therefore very close to the temperature of the human body. Thereby, increasing molecular agitation with increasing temperature results in a breakdown of the local solvent structure around the particle which leads to a considerable decrease of the particle volume. Modifying these particles enables to use them for different purposes such as carrier materials for drugs or nano-actuators. In this work, the influence of hydrostatic pressure on the swelling behaviour of different PNIPAM particles was systematically investigated, whereby a cancellation effect of the VPTT for about 1 K per 100 bar was found. This can be explained by assuming that solvent molecules are pushed into polymer cavities which are solvent-inaccessible at atmospheric pressure. It turned out that an increase of crosslinker content leads to a higher cancellation effect, i.e. the VPTT was shifted to even higher temperatures, as was characterised by means of dynamic light scattering both at atmospheric and at elevated pressure. The analysis of temperature-dependent static light scattering measurements revealed a good agreement of the hydrodynamic radius and the radius of gyration obtained from a Guinier approximation to the scattering data. The cancellation effect of hydrostatic pressure was also found by means of SANS measurements which were also performed both at atmospheric and at high pressure. This allowed to systematically study the hydration and dehydration kinetics by means of periodic pressure jumps using the stroboscopic high-pressure SANS cell. Thereby, choosing an appropriate temperature allows accessing both states within the possible pressure range. The processes after compression, which represent diffusion of water molecules into the particle and thus swelling of the particle, happen on a time scale of 2.3 s regardless of the crosslinker content. In contrast to that, two processes were observed after expansion, i.e. after deswelling the particle, which were ascribed to be a fast (within less than 1 s) collapse of the polymer backbone followed by diffusion of water molecules out of the particle which happens on a time scale of 1.5 to 4 s depending on the crosslinker content. A newly developed microfluidic setup allowed studying the response of PNIPAM particles to a fast temperature jump whereby the obtained time constants are in the same range as the ones found in SANS experiments.

5 Microemulsions and PNIPAM under mutual confinement

Since the previous two chapters revolve around water-rich CO₂ microemulsions and PNIPAM particles it is obvious to also investigate the properties of both under mutual confinement. Such orthogonal self-assembled systems are especially relevant to biomedical applications since the complex mixture of structures which exist parallel to each other in living cells is the most prominent example for such systems. The combination of PNIPAM and microemulsions can provide the possibility of drug-releasing systems of both hydrophilic components (bound by PNIPAM) and hydrophobic substances (stored in oil-swollen microemulsion droplets). However, information on phase behaviour of microemulsions in presence of PNIPAM particles is scarce [87] because most available publications describe the synthesis of PNIPAM particles in microemulsion droplets [82, 83]. Therefore, the influence of PNIPAM on microemulsion systems was systematically investigated both for microemulsions at atmospheric and at high pressure. Although a combination of PNIPAM particles and CO₂ microemulsions does not provide an obvious application yet, it can be utilised to investigate the influence of microemulsion confinement on pressure-induced structural changes and the respective kinetics and vice versa.

5.1 Phase behaviour

Prior to measurements regarding the influence of PNIPAM on microemulsion phase behaviour it was necessary to make sure that all surfactant remaining from synthesis is removed from the polymer dispersion. This was done by means of dialysis for four days against distilled water. To verify that the surfactant (SDS) was removed an elementary analysis was performed for dialysed particles as well as for particles without any purification. Unfortunately, it turned out that the weight mass fraction of sulphur, which is a characteristic element for SDS, was lower than the detection limit in both cases. Thus, two PNIPAM samples were spiked with SDS (200 mg SDS added to 2 g of a 0.5 wt% dispersion of PNIPAM) but only one of them was dialysed. Elementary analysis revealed a sulphur mass fraction of about 10 wt% where 11 wt% are expected for pure SDS in the non-dialysed sample whereas no sulphur was detected in the dialysed sample. Therefore, it can be assumed that can be successfully removed by dialysis.

After verifying that surfactant from synthesis was successfully removed from the polymer dispersion the well-known microemulsion system H₂O – *n*-octane – C₁₂E₆ ($\gamma_a = 0.03$) was chosen as a starting system (Figure 5.1) [333]. The influence of PNIPAM (5.6 wt% crosslinker, compare Figure 4.2) on the phase behaviour was systematically investigated by increasing the amount of PNIPAM in the hydrophilic phase from $\xi = 0.0$ stepwise to $\xi = 0.021$ [334]. Note that the calculations of w_B and γ_a were performed disregarding the weight of the PNIPAM particles.

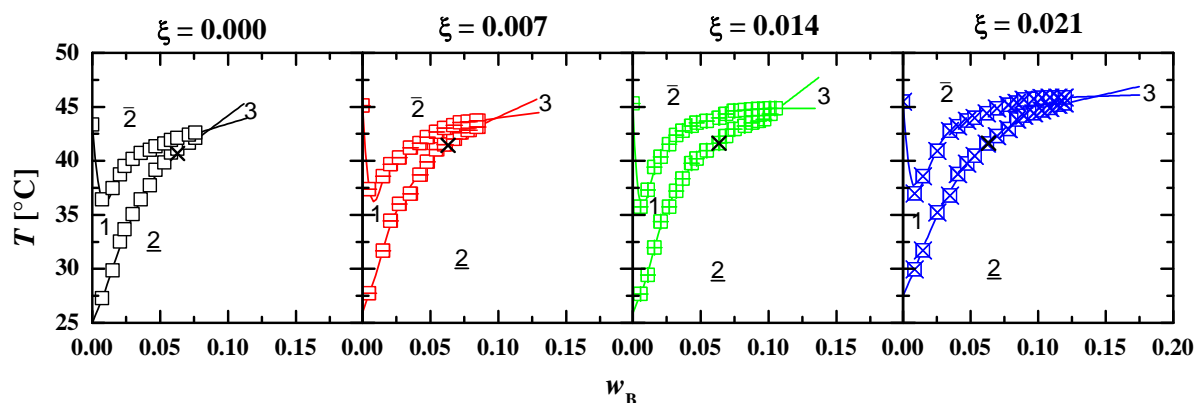


Figure 5.1: Temperature-dependent phase behaviour of the microemulsion $\text{H}_2\text{O}/\text{PNIPAM} - n\text{-octane} - \text{C}_{12}\text{E}_6$ ($\gamma_a = 0.03$) at different weight fractions ξ of PNIPAM in the hydrophilic phase. The efficiency increases from $w_{B,\max}(\xi = 0.0) = 0.089$ to $w_{B,\max}(\xi = 0.021) = 0.143$ by adding 2.1 wt% PNIPAM to the hydrophilic phase. The temperature of the point of maximum efficiency increases by 3°C . The crosses indicate the parameters of the DLS measurement presented in the following section. Taken from [334].

As can clearly be seen in Figure 5.1 the addition of PNIPAM particles to the hydrophilic phase increases the efficiency of the system. Thus, applying a PNIPAM weight fraction of 2.1% the point of maximum efficiency was shifted to $w_{B,\max} = 0.143$, which is an improvement of a factor of 1.6 compared to the system without PNIPAM ($w_{B,\max} = 0.089$). This trend is accompanied by an increase of temperature of the point of maximum efficiency of 3 K. This phase behaviour strongly reminds of the influence of hydrotropic salts on microemulsions. Here, T_u shifts to lower temperatures and T_1 to higher ones upon the addition of salts whereby the difference between both, i.e. the three-phase body, narrows. This trend goes along with a slight shift of the phase behaviour as well as an increase of efficiency [335].

After having characterised the influence of PNIPAM on the phase behaviour of microemulsions at atmospheric pressure the effect of PNIPAM on microemulsions with fluorinated surfactants and CO_2 was also investigated. Due to the higher complexity and time effort of measurements at elevated pressure only a concentration of 0.5 wt% PNIPAM in the hydrophilic phase was investigated in the model system $\text{H}_2\text{O} - \text{CO}_2 - \text{Zonyl FSO 100}/\text{Zonyl FSN 100}$ ($\gamma_a = 0.08$, $\delta_{\text{FSN}} = 0.75$). The PNIPAM particles used in these investigations were the ones characterised in Figure 4.2. The phase behaviour is shown in Figure 5.2 left.

Upon addition of PNIPAM to the microemulsions the efficiency increases significantly by a factor of 1.6 at $\beta_i = 0.0$ (compare Figure 3.1 left). This is similar to the increase at ambient pressure and 2.1 wt% PNIPAM which means that any effect is more pronounced here. Contrary to the results concerning the microemulsion system at atmospheric pressure a shift of the phase behaviour to lower temperature can be found for the microemulsion system with CO_2 . This might be due to the lower pH in this system which also influences the properties of PNIPAM [336]. It is known that the addition of sugar leads to a shift of the phase behaviour to lower temperatures due to hydration effects [337, 338].

The effect observed here is, however, much stronger. The increase of efficiency can partly be attributed to the higher CO₂ density at lower temperatures. Note that for the system at $\beta_i = 0.0$ no lower phase boundary was found.

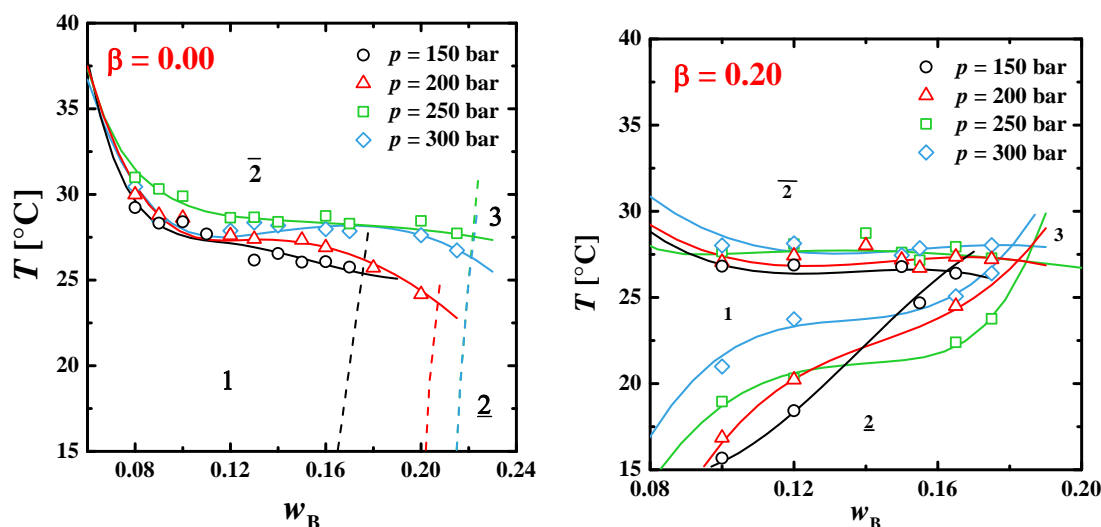


Figure 5.2: Temperature-dependent phase behaviour of the microemulsion system H₂O/ PNIPAM – CO₂/ cyclohexane – Zonyl FSO 100/ Zonyl FSN 100 at $\gamma_a = 0.08$, $\delta_{FSN} = 0.75$, 0.5 wt% PNIPAM in the hydrophilic phase and with cyclohexane contents $\beta_i = 0.0$ (left) and $\beta_i = 0.2$ (right). The efficiency increases considerably for both systems, especially for the one without cyclohexane. The one-phase region becomes more narrow upon the substitution of 20 wt% of CO₂ by cyclohexane (i.e. $\beta_i = 0.2$). A decrease of temperature of the upper phase boundary is observed in both cases.

Surprisingly, the efficiency increases only by a factor of about 1.2 upon substitution of 20 wt% of CO₂ by cyclohexane, as shown in Figure 5.2 right. Compared to the system without cyclohexane this equals a slight loss of efficiency which is, however, still higher than the system with cyclohexane without PNIPAM. The trend of a narrower one-phase region was also observed for the system without PNIPAM (Figure 3.1 right). Since cyclohexane interacts only repulsively with the fluorinated surfactant tails it can be assumed that the addition of cyclohexane leads to a stiffer membrane which is less tolerable to changes of temperature. Assuming that the increase of efficiency is caused by interactions of PNIPAM polymer chains and the surfactant head groups the addition of cyclohexane may lead to counteracting forces onto the amphiphilic film.

5.2 Light and neutron scattering

After having characterised the influence of PNIPAM particles on the phase behaviour at atmospheric and elevated pressure the microemulsion systems were studied by dynamic light scattering. While the structure size is not of primary importance here it was to be tested if both structures coexist. This could be confirmed for the microemulsion system H₂O – *n*-octane – C₁₂E₆ ($\gamma_a = 0.03$) at $w_B = 0.063$ as shown in Figure 5.3.

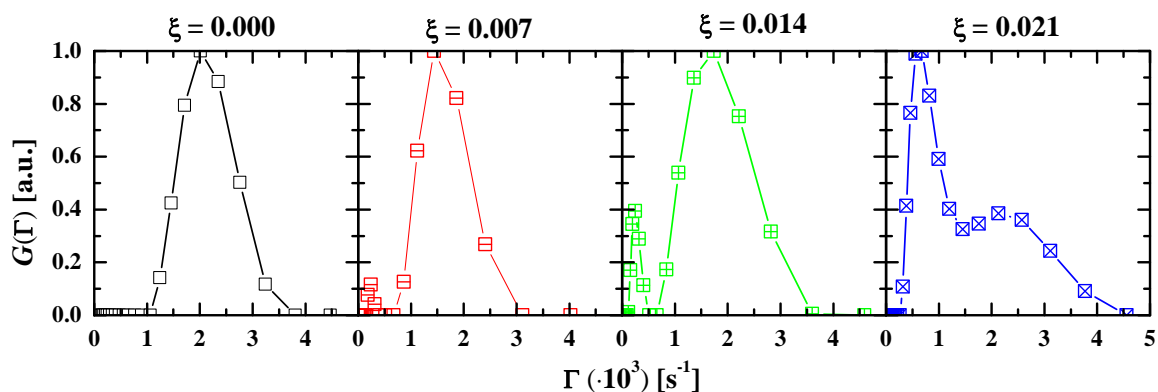


Figure 5.3: Plots of the distribution of relaxation rate Γ obtained from CONTIN analysis of DLS data of a measurement at $\theta = 40^\circ$. The microemulsion H₂O – *n*-octane – C₁₂E₆ at $\gamma_a = 0.03$, $w_B = 0.063$ at temperatures close to the *oefb* and four different weight mass fractions of PNIPAM in the hydrophilic phase, as indicated by the parameter ξ at the top, was investigated. The measurements were performed at compositions and temperatures as indicated in the respective phase diagrams in Figure 5.1. For the pure microemulsion system only one peak of relaxation rate can be obtained while a second peak becomes more and more pronounced with increasing PNIPAM concentration. Taken from [334].

In absence of PNIPAM the obtained monomodal distribution of relaxation rates corresponds to droplets of 5 nm (Figure 5.3 left). Upon the addition of 0.7 wt% PNIPAM to the microemulsion a small second peak appears which translates to a size of 67 nm and can thus be attributed to the polymer particles. This peak increases in height relative to the microemulsion peak with increasing concentration until it exceeds the microemulsion peak at a concentration of 2.1 wt% PNIPAM, clearly showing that two structures coexist.

The same result was also obtained for the high-pressure systems as can be observed in Figure 5.4.

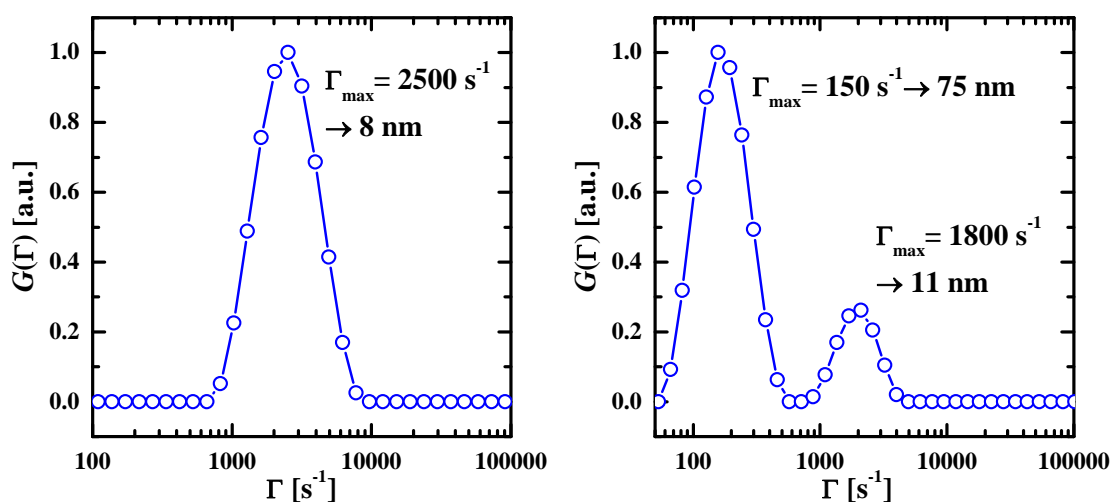


Figure 5.4: Plot of the distribution of relaxation rates for the microemulsion systems H₂O/ PNIPAM – CO₂/ cyclohexane – Zonyl FSO 100/ Zonyl FSN 100 at $\gamma_a = 0.08$, $\delta_{\text{FSN}} = 0.75$, $w_B = 0.1$, $T = 28^\circ\text{C}$ and $\beta_i = 0.2$ at $\xi = 0.0$ (left) and $\xi = 0.005$ (right), obtained from CONTIN analysis of DLS measurements at $\theta = 40^\circ$. There is only one structure peak for the system without PNIPAM but two for the microemulsion with PNIPAM in the hydrophilic phase. The relaxation rates correspond to structural sizes which are reasonable for microemulsion droplets and PNIPAM particles.

While the pure microemulsion exhibits a monomodal distribution, the microemulsion with 0.5 wt% PNIPAM in the hydrophilic phase is clearly bimodal. The relaxation rates of the peak maxima correspond to structural sizes which are well in the range of microemulsions and PNIPAM particles, respectively.

After verifying that PNIPAM particles and microemulsion droplets are present in two separate structures both at atmospheric as well as at elevated pressure the microemulsion system H₂O/D₂O/ PNIPAM – CO₂/ cyclohexane – Zonyl FSN 100 at $\gamma_a = 0.08$ and $\beta_i = 0.2$ was investigated by means of SANS. Note that for these investigations only Zonyl FSN 100 was used as a surfactant in order to shift the phase behaviour to higher temperature to ensure comparability to the phase behaviour of the microemulsion without cyclohexane (Figure 3.1). The scattering length density of water was adjusted to $1.84 \cdot 10^{-10} \text{ cm}^{-2}$ which equals the scattering length density of the surfactant mixture (not Zonyl FSN 100 but a mixture with 75% wt% of it, see Figure 3.2). It was expected that PNIPAM does not contribute much to the scattering intensity at these conditions so that the main scattering pattern should represent the microemulsion. The scattering curves of the microemulsion system at $w_B = 0.10$ and $T = 28^\circ\text{C}$ are shown in Figure 5.5.

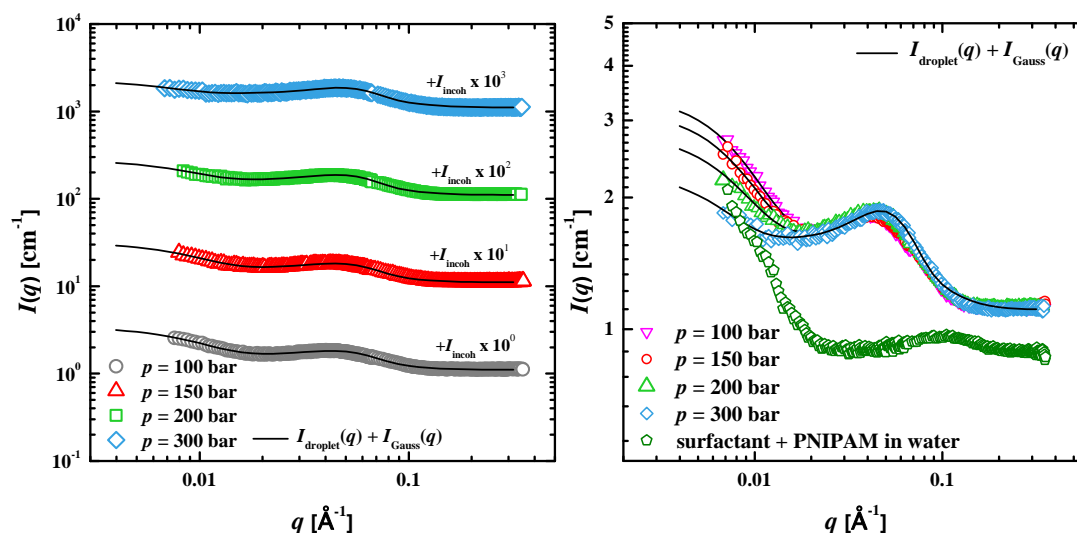


Figure 5.5: *Left:* Scattering curves of the system H₂O/D₂O/ PNIPAM – CO₂/ cyclohexane – Zonyl FSN 100 at $\gamma_a = 0.08$, $\beta_i = 0.2$, $\xi = 0.005$, $\phi_{D2O} = 0.35$, $w_B = 0.1$ and $T = 28^\circ\text{C}$. While the absolute scattering intensity is very low the scattering intensity shows a pronounced oscillation in the medium q -range caused by microemulsion droplets. *Right:* The increase of forward scattering in the low q -range is caused by PNIPAM particles, as can be clearly seen in the scattering curve obtained from the stock solution.

The scattering curves in Figure 5.5 strongly resemble the ones shown in Figure 3.4 D, which represent a non-optimum film contrast with considerable core scattering. Since the scattering length density of the H₂O/ D₂O mixture was adjusted to match the one of the surfactants the higher SLD of the hydrophilic phase must be due to the presence of PNIPAM particles. Although PNIPAM particles were already successfully matched at $\phi_{D2O} = 0.1$ [322] the present particles seem to have a higher SLD. This was also already indicated by the low scattering contrast observed for the temperature-dependent

measurements in section 4.1.2. The increase of scattering intensity in the low q -region can be attributed to the contribution of PNIPAM particles. This becomes especially obvious if the scattering curve of the stock solution of surfactant and PNIPAM (Figure 5.5 right) is compared to the scattering curves of surfactant stock solution as shown in Figure 3.2. Thus, the scattering curves shown in Figure 5.5 were described with a combination of the droplet form factor and the Gaussian contribution of the PNIPAM particles according to

$$I(q) = P_{\text{droplet}}(q) + I_{\text{Gauss}}(\mathbf{0}) \exp\left(\frac{-\Lambda^2 q^2}{3}\right) \quad \text{Eq. 5-1.}$$

Although PNIPAM particles likely also have a Lorentzian scattering contribution in the high q -region this is probably covered by the microemulsion scattering and was therefore neglected.

The parameters according to the fitting functions shown in Figure 5.5 are displayed in Table 5-1. The rather small radius found for the microemulsion droplets indicates that the surfactant film does not contribute to the scattering intensity, i.e. the SLD of the surfactants was successfully matched. The high values found for the thickness of the parameter d , however, combined with the low diffusivity parameter χ indicates that the radius represents the cyclohexane-rich core of the micelle with a high scattering length density rather than the whole micelle. The film scattering contribution was found to be in the range of the one applied for the film contrast experiment (Table 3-3). The core scattering, surprisingly, does not change as much as was observed for the system without cyclohexane. Considering the parameters of the Gaussian description it becomes obvious that the contribution decreases with increasing pressure while simultaneously the correlation length increases. This is reasonable considering that the particles become more hydrated with increasing pressure.

Table 5-1: Overview of fitting parameter to describe the scattering curves shown in Figure 5.5 for the system H₂O/D₂O/ PNIPAM – CO₂/ cyclohexane – Zonyl FSN 100 at $\gamma_a = 0.08$, $\beta_i = 0.2$, $\xi = 0.005$, $\phi_{\text{D}_2\text{O}} = 0.35$, $w_B = 0.1$ and $T = 28^\circ\text{C}$. The fitting functions were used according to Eq. 5-1.

p [bar]	R_0 [Å]	σ/R_0	χ [Å]	d [Å]	$\Delta\rho_{\text{core}}$ [10^{-6} Å^{-2}]	$\Delta\rho_{\text{film}}$ [10^{-6} Å^{-2}]	$I_{\text{Gauss}}(\mathbf{0})$ [cm^{-1}]	Λ [Å]
100	44	0.328	3.2	15.0	-1.42	1.15	1.85	180
150	44	0.325	3.0	15.3	-1.44	1.15	1.60	185
200	43	0.320	2.7	16.0	-1.46	1.15	1.20	200
300	43	0.320	2	16.3	-1.45	1.15	0.70	250

5.3 First kinetic experiment with microemulsions and PNIPAM

The combination of PNIPAM particles and a CO₂ microemulsion was chosen in order to obtain information on the influence of the respective structure on the kinetics of structural changes of the other system. Although the static scattering curves showed a very low scattering intensity a first pressure jump experiment was performed. Thereby, p_{high} was adjusted to 150 bar at which the microemulsion is in a thermodynamically stable state (see Figure 5.2). However, preliminary experiments and visual inspection thereof showed that a pressure jump to $p_{\text{low}} = 70$ bar did not induce a demixing process. Lowering p_{low} to 65 bar lead to the appearance of a few emulsion droplets. Thus, p_{low} was adjusted to 60 bar for the scattering experiment to ensure that demixing can be detected. The scattering curves to this experiment as a function of time are shown in Figure 5.6 left. The results of this experiment in form of the normalised integrated intensity, as can be seen in Figure 5.6 right, do not reflect a reliable increase of scattering intensity which is probably due to the low scattering intensity of the system.

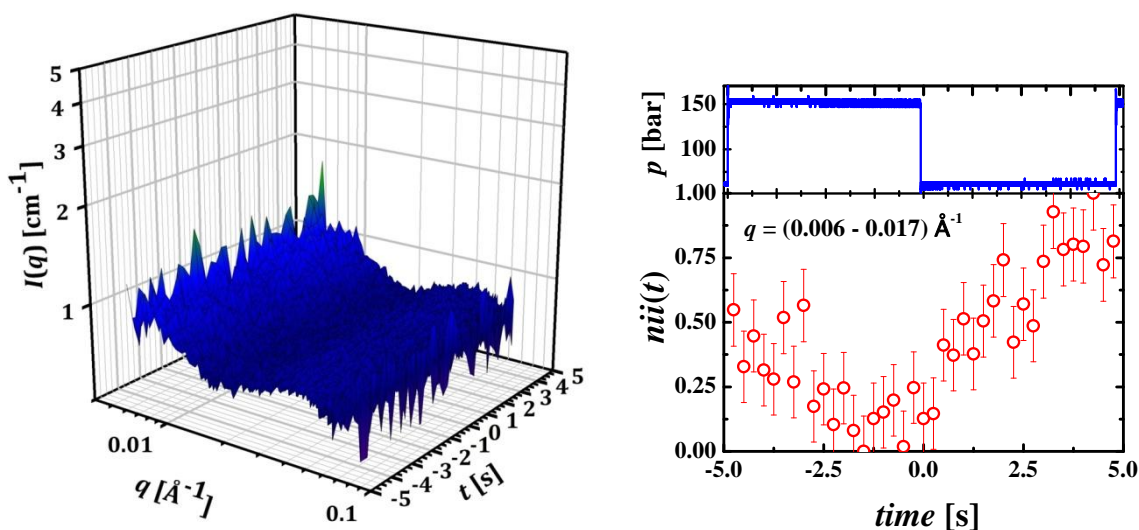


Figure 5.6: *Left:* Pressure-dependent scattering curves as a function of time for the system H₂O/D₂O/ PNIPAM – CO₂/ cyclohexane – Zonyl FSN 100 at $\gamma_a = 0.08$, $\beta_i = 0.2$, $\xi = 0.005$, $\phi_{\text{D}_2\text{O}} = 0.35$, $w_B = 0.1$ and $T = 28^\circ\text{C}$. The pressure cycle starts at $t = -5$ s at $p = 150$ bar until after 5 s ($t = 0$ s) the pressure is changed to 60 bar. The scattering curves are shown with a time resolution of 0.25 s. As can clearly be seen the overall scattering intensity is very low. *Right:* Normalised integrated intensity ($nii(t)$) as a function of time for the q -range from $0.006 \text{ \AA}^{-1} \leq q \leq 0.017 \text{ \AA}^{-1}$, also with a time resolution of 0.25 s. No reliable conclusion can be drawn due to the low scattering intensity.

5.4 Conclusion

Orthogonal self-assembled systems are a major issue in the field of science since the most important example for this topic is the living cell and the multiplicity of structures therein. Coexisting structures can also be expected for a combination of PNIPAM nanoparticles and diluted water-rich microemulsions. With PNIPAM being a promising substance for drug release purposes of hydrophilic

substances a combination of PNIPAM and microemulsions might allow to simultaneously release both hydrophilic and hydrophobic substances if the hydrophobic substance is kept inside an oil-swollen micelle. Thus, studying the microemulsion system $\text{H}_2\text{O}/\text{PNIPAM} - n\text{-octane} - \text{C}_{12}\text{E}_6$ with increasing PNIPAM concentrations ξ from 0 wt% to 2.1 wt% showed an increase of efficiency which is accompanied by an increase of temperature. This effect might be compared to the effect of hydrotropic salts on microemulsions which induces a raise in temperature and a narrowing of the three-phase body. A similar but more pronounced effect was found for the microemulsion system $\text{H}_2\text{O}/\text{PNIPAM} - \text{CO}_2 - \text{Zonyl FSO 100}/\text{Zonyl FSN 100}$ where an increase of efficiency by a factor of 1.6 was achieved already for 0.5 wt% PNIPAM in the hydrophilic phase. In contrast, this effect is accompanied by a shift of phase behaviour to lower temperatures. The addition of cyclohexane, however, slightly decreased the efficiency. More detailed analysis of the phase behaviour and microstructure is required to explain this effect and to test if polymer chains influence or even penetrate the interface. As expected, dynamic light scattering measurements revealed the presence of two separate structures for both microemulsions at atmospheric and at elevated pressure. SANS measurements of the system $\text{H}_2\text{O}/\text{D}_2\text{O}/\text{PNIPAM} - \text{CO}_2/\text{cyclohexane} - \text{Zonyl FSN 100}$ at $\beta_i = 0.2$, $\phi_{\text{D}_2\text{O}} = 0.35$, $w_B = 0.1$ and $T = 28^\circ\text{C}$ revealed a contrast situation which indicates that the PNIPAM particles have a higher scattering length density than expected. The overall scattering intensity, however, was very low so that no reliable results were obtained from pressure jump experiments. The visual inspection of these experiments, however, revealed that demixing processes were only induced if the pressure p_{low} was lowered to 65 bar. Considering this in combination with the improvement of efficiency it shows that PNIPAM can be used as a hydrophilic stabilising agent for fluorinated CO_2 -microemulsions.

6 Summary

The production of highly porous foams with nano-sized bubbles is currently investigated by science and industry. The effort is motivated by the prospect of a huge energy saving potential due to high-performance insulation capacities of nanoporous foams. On one hand, a simple and low-cost procedure is required and on the other hand current foaming procedures often suffer from coarsening of the foam pores during expansion. This also applies to the Principle of Supercritical Microemulsions (Figure 2.8) which utilises the high number density of CO₂-swollen microemulsion droplets with a size of about 10 nm as a template for nanoporous materials. To meet the challenges provided by coarsening a more detailed understanding of structure and dynamics of the underlying microemulsions is necessary.

The balanced microemulsion system brine – CO₂/ cyclohexane – Zonyl FSO 100/ Zonyl FSN 100 was systematically investigated at different cyclohexane mass fractions β_i in the hydrophobic phase prior to this thesis. It was found that replacing 20 wt% of CO₂ by cyclohexane allows to reduce the amount of surfactant by a factor of two to five, depending on the pressure (Figure 1.1 left) which is surprising due to repulsive interactions of cyclohexane and the fluorinated surfactant tails. A non-homogeneous distribution of cyclohexane with a depletion of cyclohexane close to the surfactants was proposed to explain this unexpected efficiency boosting. Thus, the first aim of this work was to perform a systematic small-angle neutron scattering contrast variation to elucidate the distribution of cyclohexane and CO₂ in a microemulsion droplet formed with fluorinated surfactants. The quantitative description of pressure-dependent scattering curves at four different contrast conditions by means of a spherical droplet form factor already indicated that the applied radial density distribution function is not able to describe the distribution of cyclohexane and CO₂ quantitatively over the whole q -range, since small but systematic deviations in the q -range slightly larger than the oscillation were observed (Figure 3.4). By means of a model-independent Fourier transformation the pair distance distribution functions in real space were obtained (Figure 3.6) and subsequently deconvoluted to radial scattering length density profiles (Figure 3.8). Thereby, a density profile that varies systematically over half of the droplet radius instead of a nearly constant scattering length density was found. These results confirm that a concentration gradient of cyclohexane is formed within the micelle with a high concentration of cyclohexane at the centre ($\beta_{\text{core}} \approx 0.5$ instead of 0.2 for a hypothetical homogeneous distribution) and a depletion of cyclohexane close to the amphiphilic film. Hence, the observed unexpected efficiency boosting of CO₂-microemulsions is caused by an improvement of the interactions of CO₂ and the fluorinated surfactant tails triggered by repulsive interactions between cyclohexane and the surfactants.

Having thoroughly examined the distribution of cyclohexane in a micelle swollen with CO₂ and cyclohexane the influence of cyclohexane in diluted microemulsions on phase behaviour and microstructure was systematically investigated for systems containing 10, 15 and 25 wt% cyclohexane in the hydrophobic phase (Figure 3.13, Figure 3.14 and Figure 3.16). It was found that the efficiency boosting described above for balanced microemulsion exists also for diluted microemulsions at $p \leq 250$ bar but in a less pronounced way. Thereby, spherical droplets were found at $p = 150$ bar which elongate at higher pressure and which grow in radius with increasing cyclohexane content. Using the improved stroboscopic high-pressure SANS cell (section 2.4.5), which allows to perform periodic pressure jumps, the kinetics of elongation within the thermodynamically stable state were investigated (section 3.2.2). It turned out that reordering processes from cylinder fragments to spherical droplets are slowed down. Thus, the time constant for this process was increased from smaller than 0.1 s to (0.80 ± 0.03) s at $\beta_i = 0.15$ (Figure 3.26). Studying the inverse process, i.e. the elongation and accumulation of spherical droplets with subsequent reordering to elongated structures, two processes were found whereby both were decelerated with increasing cyclohexane concentration. Thus, the structural changes were slowed down from (0.59 ± 0.05) s at $\beta_i = 0.0$ to (1.8 ± 0.3) s at $\beta_i = 0.15$.

In another set of experiments demixing was induced by performing pressure jumps to 70 bar at which a CO₂-in-water microemulsion coexists with a CO₂-excess phase (section 3.2.4). Thereby, a linear decrease of the scattering intensity in the medium q -range ($0.013 \text{ \AA}^{-1} \leq q \leq 0.034 \text{ \AA}^{-1}$) as well as a linear increase in the low q -region ($0.005 \text{ \AA}^{-1} \leq q \leq 0.013 \text{ \AA}^{-1}$) after expansion was found. Normalising the linear regions in the medium q -range to each other showed that cyclohexane systematically slows down demixing processes. This dependency can be described by an exponential function (Figure 3.31). Already 15 wt% of cyclohexane in the hydrophobic phase slow down the process by one order of magnitude. This is very likely due to the presence of a second dispersed phase component, i.e. cyclohexane, which is insoluble in the continuous phase and thus has a lower diffusion rate. Since the surface area must remain constant the growth of large emulsion droplets must be connected to a shrinking of microemulsion droplets and simultaneously to an increase of the particle number density. Lowering the monomeric solubility of the additive further by using higher oils (e.g. decane) may further decrease the demixing speed. Studying the influence of hydrophobicity of the additive is the subject of further experiments.

To enable measurements with a time resolution lower than 5 ms the TISANE option (section 2.4.7) was recently installed at the D22 instrument (Institute Laue-Langevin, Grenoble, France). By improving the maximum frequency of the stroboscopic high-pressure SANS cell from 4.3 Hz to 10 Hz it was for the first time possible to obtain a reasonable result from kinetic

measurements using the TISANE option (Figure 3.34). The remaining smearing of the signal was found to occur due to the high error of time resolution at experimental conditions which are too slow to satisfy the TISANE principle. Thus, the stroboscopic high-pressure SANS cell was constantly improved throughout this work so that pressure jumps with a maximum frequency of 22.7 Hz are possible (Figure 3.33). The combination of the further improved cell and TISANE experiments remains for future work.

Besides CO₂-microemulsions it was one goal to systematically examine the influence of hydrostatic pressure on poly-(*N*-isopropylacrylamid) (PNIPAM) microgel particles. The interest in PNIPAM has grown rapidly because its characteristic volume phase transition temperature (VPTT), which is connected to a considerable decrease of particle volume with increasing temperature, is located around 32°C and therefore very close to the temperature of the human body. Modifying these particles enables to use them for different purposes such as carrier materials for drugs or nano-actuators. A cancellation effect of the VPTT of about 1 K per 100 bar was found. Increasing the crosslinker content shifted the VPTT to even higher temperatures, as was characterised by means of dynamic light scattering both at atmospheric and at high pressure (Table 4-1). The analysis of temperature-dependent static light scattering measurements revealed a good agreement of the hydrodynamic radius and the radius of gyration obtained from a Guinier approximation (Figure 4.13). The shift of VPTT by hydrostatic pressure was also verified by SANS measurements at atmospheric and high pressure (section 4.1.2). Choosing an appropriate temperature at which both the swollen and the shrunken state are accessible at different pressures allowed to systematically study the hydration and dehydration kinetics by utilising the stroboscopic high-pressure SANS cell. The processes after compression, which represent diffusion of water molecules into the particle i.e. swelling, happen on a time scale of $\tau = (2.3 \pm 0.3)$ s regardless of the crosslinker content. In contrast to that, two processes were observed after expansion, i.e. after deswelling. While the first process is very fast ($\tau < 0.6$ s) it is followed by a slower one which happens on a time scale of 1.5 to 4 s (Table 4-6), depending on the crosslinker content, and is likely to represent diffusion of water molecules out of the polymer. A newly developed microfluidic setup allowed studying the response of PNIPAM particles to a fast temperature jump. The obtained time constants are in the same range as the ones found in SANS experiments (section 4.3).

Having examined both microemulsions and PNIPAM particles it is reasonable to also study mixtures of both as orthogonal self-assembled systems. Such systems represent a major issue in science since the most important example for this topic are living cells. With PNIPAM being a promising substance for drug release purposes of hydrophilic substance a combination of PNIPAM and microemulsions might allow to simultaneously release both hydrophilic and hydrophobic substances if the hydrophobic substance is kept inside an oil-swollen micelle.

Thus, by studying the phase behaviour of diluted microemulsions both at atmospheric and at elevated pressure an increase of efficiency was found in both cases (Figure 5.1 and Figure 5.2). The effect was more pronounced for the CO₂ microemulsion where the addition of 0.5 wt% PNIPAM particles improved the efficiency by a factor of 1.6. By analysing dynamic light scattering measurements close to the oil emulsification failure boundary the coexistence of PNIPAM particles and microemulsion droplets was verified for both types of microemulsions (Figure 5.3, Figure 5.4). SANS experiments performed at the mixture of CO₂ microemulsions and PNIPAM particles also revealed that two structures contribute to the scattering intensity (Figure 5.5). First kinetic experiments showed that demixing only occurs upon pressure jumps to 60 bar which is low compared to the PNIPAM-free system. Considering this and the higher efficiency PNIPAM seems to stabilise the microemulsion.

7 Appendix

7.1 Abbreviations and Symbols

1	index of the one phase state
2	index of a two phase state
$\underline{2}$	index of an oil-in-water microemulsion
$\overline{2}$	index of a water-in-oil microemulsion
3	index of the three phase state
α	weight fraction of oil in the binary mixture of water and oil
a	water excess phase
a_c	head group area of a single surfactant molecule
A	index of the hydrophilic microemulsion sub-phase
AAA	Anti-Ageing Agent
$A(q)$	scattering amplitude of a particle
AOT	Bis-(2-ethylhexyl) sulfosuccinate sodium salt
β	mass fraction of co-oil in a binary oil-mixture
β_i	effective mass fraction of co-oil in a binary mixture, monomeric solubilities considered
β_G	geometry factor in dynamic light scattering experiments
b_i	scattering length of an atom
B	index of the hydrophobic microemulsion sub-phase
B_1	value of autocorrelation function at infinite delay times τ
BIS	<i>N,N</i> -bis-methylenacrylamide
BMBF	German <i>Bundesministerium für Bildung und Forschung</i>
χ	parameter that describes the diffusivity of the droplet interface in the analytical density distribution function $f_{\text{droplet}}(r,R)$
c_a	oil-in-water microemulsion coexisting with an oil excess phase
c_b	water-in-oil microemulsion coexisting with a water excess phase
$c(\vec{r})$	direct correlation function
c_1, c_2	principle curvatures
C_iE_j	non-ionic surfactant of the general structure <i>n</i> -alkyl polyglycol ether
cep_α	upper critical end point
cep_β	lower critical end point
cmc	critical micelle concentration
cp_α	critical point of the binary oil-surfactant mixture
cp_β	critical point of the binary water-surfactant mixture
C	index of the amphiphilic microemulsion sub-phase
d_{Bragg}	spacing between planes of lattice
d_{sample}	thickness of the sample
D	diffusion coefficient
D_0	Diameter of a particle or micelle
DC	duty cycle of the chopper in a TISANE experiment
DECON	program package for deconvolution of scattering data into real space
DLS	dynamic light scattering

δ	weight fraction of the co-surfactant in the surfactant/co-surfactant mixture
d	effective thickness of the surfactant shell, used in $f_{\text{droplet}}(r,R)$
dn/dc	refractive index increment
$d\Sigma/d\Omega$	differential scattering cross-section
d_s	structural length according to <i>Bragg's law</i>
ε	salt weight fraction in the hydrophilic sub-phase of a microemulsion
ε_p	efficiency of a detector pixel
efb	<i>emulsification failure boundary</i>
$E(t)$	electric field amplitude in dynamic light scattering experiments
ϕ	volume fraction of oil in the binary mixture of water and oil
$\phi_{\text{D}_2\text{O}}$	volume fraction of D_2O in the $\text{H}_2\text{O}/\text{D}_2\text{O}$ mixture
$\phi_{\text{c,i}}$	volume fraction of the surfactant in the internal interface
ϕ_{disp}	volume fraction of the dispersed phase
ϕ_k	volume fraction of the component k
$f(\vec{r}), f(r,R)$	normalized radial density distribution function
f_a	amphiphilicity factor
f_C	chopper frequency
f_D	detector frequency
f_S	sample frequency
$f_{\text{core}}(r,R)$	radial density distribution function for the density profile of the droplet core
$f_{\text{droplet}}(r,R)$	analytical radial density distribution function for the density profile of droplets with core-shell architecture and diffuse interfaces
$f_{\text{film}}(r,R)$	<i>Gaussian</i> radial density distribution function for the density profile of the amphiphilic film
γ	overall surfactant weight fraction in a microemulsion
$\tilde{\gamma}$	surfactant weight fraction at the \tilde{X} -point
γ_{mon}	weight fraction of surfactant monomers in a water-oil mixture
γ_a	surfactant weight fraction in a binary water-surfactant mixture
$\gamma_{\text{c,mon,b}}$	weight fraction of surfactant monomers in oil
γ_m	surfactant weight fraction at the <i>optimum point</i>
$\gamma(r)$	one-dimensional spatial autocorrelation function
Γ	inverse relaxation time
$g_1(\tau)$	normalised field-time-autocorrelation function
$g_2(\tau)$	normalised intensity-field-autocorrelation function
ΔG_M	free mixing energy
$G(\vec{r})$	spatial autocorrelation function
GIFT	<i>generalised indirect Fourier transformation</i>
η	viscosity
h	<i>Planck's constant</i> = $6.626 \cdot 10^{-34}$ Js
\hbar	reduced <i>Planck constant</i> = $h/2\pi$
ΔH_M	mixing enthalpy
H	mean curvature of the amphiphilic film
H_0	spontaneous curvature of the amphiphilic film
HLB	hydrophilic lipophilic balance
Hz	Hertz

I	initiator molecule
$I(q)$	q -dependent scattering intensity
I_{BG}	background scattering intensity
I_{EC}	scattering intensity from the empty sample-cell
I_{EC,H_2O}	scattering intensity from the empty cell of the calibration standard H_2O
$I_{Gauss}(q)$	Gaussian spatial distribution
I_{H_2O}	scattering intensity from calibration standard H_2O
I_{incoh}	environmental background intensity
$I_L(q)$	Lorentzian scattering contribution
$I_{OZ}(0)$	Ornstein-Zernicke parameter
ILL	Institut Laue-Langevin
I_{sample}	scattering intensity from the sample
$I_{sphere}(q)$	description of scattering intensity of a sphere
J_0	incident neutron flux
$J_0(qr)$	zeroth order <i>Bessel</i> function of first kind
κ_i	cumulant parameter
k_B	<i>Boltzmann</i> constant
k_d	rate constant for dissociation of initiator
\vec{k}_i	wave vector of the incident neutron wave
k_i	rate constant of initiation
\vec{k}_s	wave vector of the scattered neutron wave
k_p	rate constant of propagation
k_t	rate constant of termination
K	contrast factor in static light scattering
λ	wavelength
λ_M	mean free path length
Λ	characteristic length scale of static heterogeneities of the Gaussian spatial distribution
l_c	length of a single surfactant molecule
L	cylinder length
L_3	L_3 -phase
L_α	lamellar phase
L_{CS}	chopper-to-sample distance
L_{SD}	sample-to-detector distance
LCST	lower critical solution temperature
m_i	mass of the component i
m_n	neutron mass = $1.675 \cdot 10^{-27}$ kg
M	molar mass
n	particle number density
n_s	number of segments in a kinetic SANS experiment or in DLS
N	total number of particles
ncb	near critical boundary
$nii(t)$	normalised integrated intensity as a function of time
NF-CID	<i>Nano-Foams by Continuity Inversion of Dispersions</i>
NIPAM	<i>N</i> -isopropylacrylamide
N_A	<i>Avogadro's</i> constant = $6.022 \cdot 10^{23}$ mol ⁻¹

$oefb$	<i>oil emulsification failure boundary</i>
o/w	oil-in-water
p	pressure
$p_{\text{high}}, p_{\text{low}}$	pressures adjusted for a pressure jump experiment
$\Delta p_{\text{Laplace}}$	Laplace pressure
$p(r)$	<i>pair distance distribution function</i>
p_c	critical pressure
p_R	polydispersity index
$P(q)$	monodisperse particle form factor
$\overline{P(q)}$	averaged particle form factor
$P_{\text{CS,M}}(q)$	monodisperse form factor for a spherical particle with core-shell architecture and a <i>Gaussian</i> density profile of the amphiphilic film
$P_{\text{CS}}(q)$	polydisperse form factor for a spherical particles with core-shell architecture and a <i>Gaussian</i> density profile of the amphiphilic film
$P_{\text{cross}}(q)$	scattering function for a cylinder cross-section with core-shell architecture and diffuse interfaces; based on the density distribution function $f_{\text{droplet}}(r,R)$
$P_{\text{cylinder}}(q)$	polydisperse form factor for a cylinder; only the polydispersity of the cylinder radius is taken into account
$P_{\text{droplet}}(q)$	polydisperse form factor for spherical droplets with core-architecture and diffuse interfaces; based on the density distribution function $f_{\text{droplet}}(r,R)$
$P_{\text{rod}}(q)$	monodisperse form factor of an infinitely thin rod
PDDF	<i>pair distance distribution function</i>
PIT	phase inversion temperature
PMMA	Poly-methylmethacrylate
PNIPAM	Poly-(<i>N</i> -isopropylacrylamide)
POSME	<i>Principle of Supercritical Microemulsion Expansion</i>
PS	Polystyrene
θ	scattering angle
q	absolute value of the scattering vector
\vec{q}	scattering vector; also called momentum transfer vector
ρ	scattering length density
ρ^0	macroscopic or mass density
ρ_{bulk}	scattering length density of the continuous bulk-phase of a droplet microemulsion
ρ_{core}	scattering length density of the droplet core
ρ_{film}	scattering length density of the amphiphilic film
ρ_k	scattering length density of the component k
ρ_{domain}	scattering length density of a domain or subphase
$\Delta\rho$	scattering length density difference
$\Delta\rho(\vec{r})$	scattering length density distribution function
$\Delta\rho_{\text{core}}$	difference in the scattering length densities of the droplet core and the surrounding bulk-medium
$\Delta\rho_{\text{droplet}}(r)$	scattering length density profile of droplets with core-shell architecture and diffuse interfaces, based on the density distribution function $f_{\text{droplet}}(r,R)$

$\Delta\rho_{\text{film}}$	difference in the scattering length densities of the amphiphilic film and the surrounding bulk-medium
\vec{r}	position vector in real space
R	droplet radius
$R\cdot$	radical molecule
R_0	mean droplet radius
R_1, R_2	principle curvature radii
R_G	radius of gyration
R_{HS}	interaction radius of hard spheres
R_i	rate of initiation
R_p	rate of propagation
R_t	rate of termination
$R(q)$	Raleigh ratio
rpm	rounds per minute
σ	standard variation of the distribution function $W(R, R_0, \sigma)$ of the radius
σ_{HS}	standard variation of the distribution function $W(R_{\text{HS}}, R_0, \sigma_{\text{HS}})$ of the hard-sphere radius
σ_L	standard variation of the distribution function $W_L(L, L_0, \sigma_L)$ of cylinder length
ΔS_M	mixing entropy
$S(q)$	monodisperse <i>interparticle</i> structure factor
$S_i(q)$	static light scattering intensity
$S_{\text{OZ}}(q)$	<i>Ornstein-Zernicke</i> structure factor for critical fluctuations
$S_{\text{PY}}(q)$	Percus-Yevick structure factor for interacting hard spheres
SANS	small angle neutron scattering
sc	supercritical
SDS	Sodium-dodecylsulfate
SHP-SANS cell	stroboscopic high pressure cell for small angle neutron scattering
SLD	scattering length density
SLS	static light scattering
τ	delay time
t	time
Δt_C	opening time of the chopper
t_{count}	counting time of kinetic SANS experiment
t_S	time of segment of a kinetic SANS experiment
T	temperature
\tilde{T}	temperature at the \tilde{X} -point
T_α	critical temperature of the binary oil-surfactant mixture
T_β	critical temperature of the binary water-surfactant mixture
T_c	critical temperature
T_C	chopper cycle in a TISANE experiment
T_D	detector cycle in a TISANE experiment
T_{EC}	Transmission of empty cell
T_g	glass transition temperature
T_l	lower critical end point temperature
t_M	measurement time of a DLS experiment
T_m	mean temperature, <i>i.e.</i> temperature at the <i>optimum point</i>

T_S	sample cycle in a TISANE experiment
T_u	upper critical end point temperature
$T(\gamma)$	phase diagram depending on temperature and surfactant mass fraction
$T(w_B)$	phase diagram depending on temperature and oil mass fraction
TISANE	<i>Time-Involved Small Angle Neutron scattering Experiments</i>
v	velocity of a neutron
v_c	volume of a single surfactant molecule
V	volume
V1, V2	valves of the stroboscopic high-pressure SANS cell
V_i	volume of component i
V_{part}	volume of a particle
VPTT	volume phase transition temperature
w_B	overall oil weight fraction
$w_{B,\text{max}}$	oil mass fraction at the point of maximum efficient in a $T(w_B)$ section
w/o	water in oil
wt	weight
$W_L(L, L_0, \sigma_L)$	distribution function of the radius R around the mean value R_0 (polydispersity σ)
$W_R(R, R, \sigma)$	distribution function of the radius R around the mean value R_0 (polydispersity σ)
$W_P(R_{\text{HS}}, R_{\text{HS},0}, \sigma_{\text{HS}})$	distribution function of the hard sphere radius R_{HS} around the mean value $R_{\text{HS},0}$ (polydispersity σ_{HS})
ξ	mass fraction of polymer particles in water
ξ_L	Lorentzian correlation length
ξ_{OZ}	correlation length of critical fluctuations
x	mole fraction
X_m	<i>optimum point, i.e.</i> fish tail point of a balanced microemulsion
\tilde{X}	fish tail point of a microemulsion with arbitrary α
z	constant describing the dependence of slope on cyclohexane content β_i

7.2 Experimental methods

7.2.1 Determination of the phase boundaries of microemulsions

All phase boundaries of microemulsions under high pressure were determined in a house-in high-pressure view cell which was designed by Schwan [339]. A technical drawing as well as a photograph of this cell is shown in Figure 7.1.

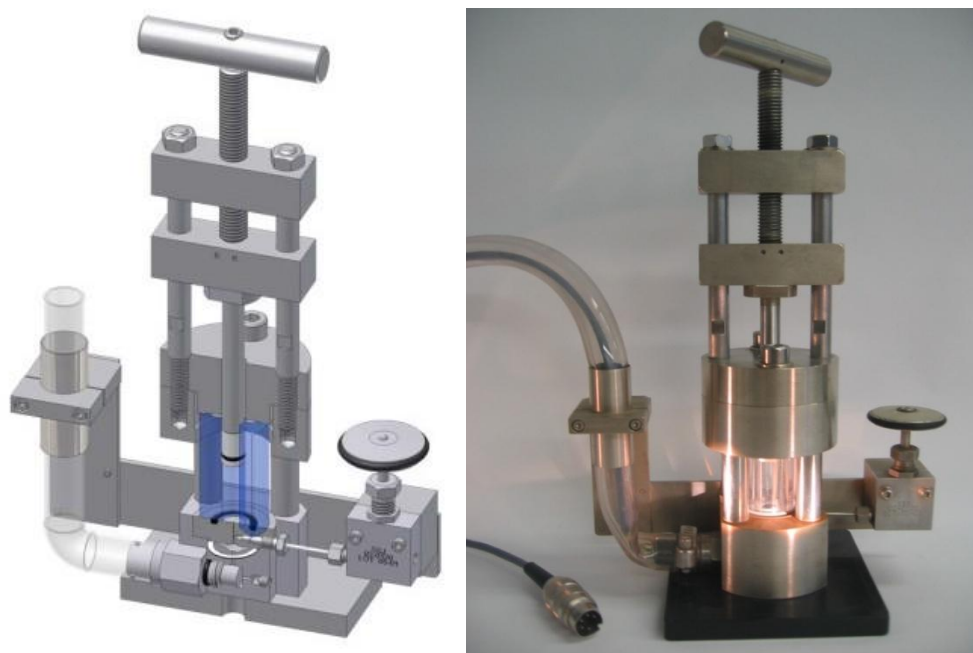


Figure 7.1: Technical sketch (left) and photograph (right) of the house-in built view cell for performing measurements under high pressure. The sapphire cylinder (blue in the technical drawing) allows visual inspection of the sample. The piston at the top is used to regulate the pressure. The valve at the right part of the cell connects to a capillary inlet at the bottom of the cell and is used for filling. The pressure gauge is also connected to the bottom of the cell. Taken from [32].

The most important part of the high-pressure view cell is the sapphire cylinder ($\varnothing_{\text{outside}} = 40 \text{ mm}$, $\varnothing_{\text{inside}} = 10 \text{ mm}$) which is marked in blue in the technical drawing in Figure 7.1 left. Due to its transparency it is possible to determine the number and type of coexisting microemulsion phases visually. The volume of this cell and therefore the pressure is variable and can be controlled by a movable piston. The pressure is measured by a pressure transducer (Type 81530, Burster, Germany) which is inserted into the bottom of the cell.

All samples were prepared directly inside the view cell. The amount of brine, surfactants and cyclohexane was controlled by weight with an accuracy of $\pm 0.001 \text{ g}$. A stir bar was added for homogenisation. After sealing the cell with the piston liquid CO_2 was added to the cell using a custom made filling apparatus equipped with a membrane reservoir. The amount of CO_2 was calculated from the volume of the cell and the density of CO_2 under the given conditions. The temperature variation was performed using a tempered water bath in which the view cell was placed (Figure 7.2).

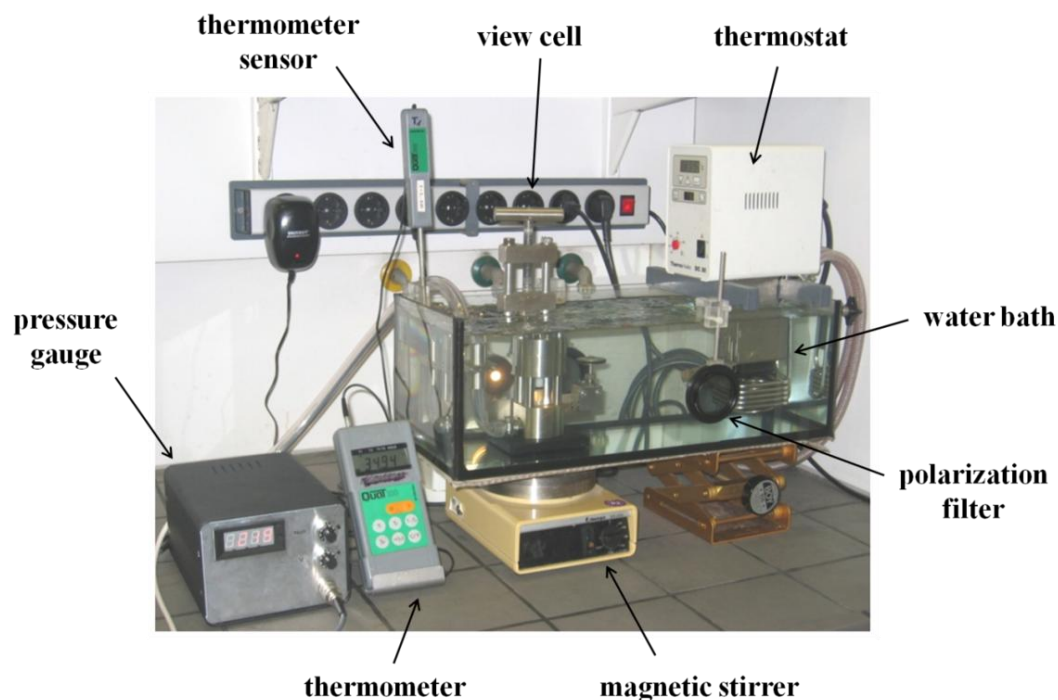


Figure 7.2: Experimental setup for the characterisation of the phase boundaries of a microemulsion system under high pressure. The view cell is placed into a temperature-controlled water bath which is also equipped with a magnetic stirrer. Taken from [39].

The water bath is equipped with a magnetic stirring device for homogenisation of the sample and a thermostat (DC 30, Thermo Haake) which allows to adjust the temperature with a precision of $\Delta T = \pm 0.1^\circ\text{C}$. After placing the sample in the water bath the pressure was adjusted under magnetic stirring. The evaluation of the type and number of the coexisting phases was performed by visual inspection of both the transmitted and the scattered light, whereby a microscope lamp (Belani, Gerhard Optik) was used to simplify the characterisation. To determine the existence of anisotropic phases two polarizer were placed in front of and behind the sample. The phase boundaries of multiple phases were determined by awaiting phase separation. After readjusting temperature and pressure this procedure was repeated until all phase boundaries were determined. The accuracy of the phase boundaries was $\pm 0.1^\circ\text{C}$.

Basically the same setup was used to temperature-control samples at atmospheric pressure. A sealable sample tube with a total volume of 10 mL and equipped with a magnetic stirrer was used as a sample holder. All amounts were controlled by weight.

7.2.2 Neutron Scattering

The neutron scattering data presented in this thesis were exclusively collected at the Institut Laue-Langevin in Grenoble, France. Since three different instruments, two different sample holders and a

number of different instrumental parameters were applied during different beam times these parameters are summarised in Table 7-1 and Table 7-2.

All measurements at normal pressure were performed in a 1 mm quartz cuvette of the type 404.000-QX designed by Hellma® made out of Suprasil® 300. The aperture in front of the sample holder always had a diameter of 13 mm.

The high-pressure sample holder and its developments are described in section 2.4.5. The different kinetic data recording modes are described in section 2.4.6 and section 2.4.7, respectively.

Note that the detector at the D22 instrument was used in an off-axis position to have access to a wider q -range. Thus, the beam centre was positioned about 400 mm left of the centre of the detector. The data treatment software GRASP accounts for that automatically.

The TISANE measurements described in section 3.3 also used the chopper system. The according parameters for the chopper are mentioned together with the respective experiments.

Table 7-1: Overview of instrumental parameters used for measurements at normal pressure at the Institut Laue-Langevin, Grenoble, France.

	D11, Hellma cuvette				D33, stopped flow cuvette			
Detector distance [m]	1.75	10	10	39	2	7.8	7.8	12.8
Collimation length [m]	10.5	8	10.5	40.5	7.8	7.8	7.8	12.8
Wavelength [Å]	6	6	6	6	6	6	6	6
Attenuator	--	3	--	--	--	2	--	--
Comments	TR				TR			

Table 7-2: Overview of instrumental parameters used for measurements at high pressure at the Institut Laue-Langevin, Grenoble, France, using the sample holder described in section 2.4.5.

Instrument	D22				D11			
Detector distance [m]	3	11.2	11.2	17.6	1.75	10	10	39
Collimation length [m]	11.2	11.2	11.2	17.6	10.5	8	10.5	40.5
Wavelength [Å]	6	6	6	6	6	6	6	6
Attenuator	--	2	--	--	--	3	--	--
Comments	TR				TR			
Kinetic counting mode	TISANE count/ KINETIC count/ LISTMODE count				KINETIC count			

7.2.3 Light Scattering

DYNAMIC LIGHT SCATTERING

All dynamic light scattering experiments were performed in a modified Brookhaven light scattering setup combined with a Helium-Neon Laser (GLG 5731, NEC co.) which produces a laser beam with a wavelength of $\lambda = 633$ nm. The goniometer setup, the photomultiplier and the detection system were used from the original setup, but the sample holder was completely exchanged as described in section 2.5.2. A cross section of this setup is shown in Figure 7.3. The preparation of microemulsion samples is very similar to the one described for the determination of phase boundaries in section 7.2.1. The volume of the device and thus the pressure can be controlled by a tunable piston (Figure 7.3 top middle). Knowing its exact position and thus also the exact volume of the cell CO_2 can be filled into the device. Prior to that the liquid stock solution is filled into the sample holder. The upper valve is used to fill in CO_2 while the lower valve is used for cleaning. In order to be able to homogenise the sample a magnetic stirrer was implemented below the sample volume. To control the temperature of the sample the outer ring of the sample holder is partly hollow and can be connected to an external water bath using the two connections at the top (gold in Figure 7.3).

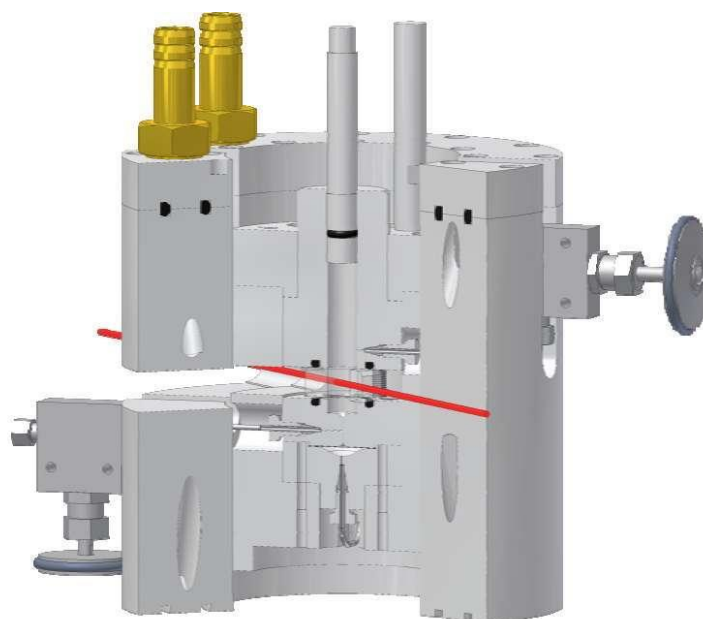


Figure 7.3: Cross section of the sample holding system of the modified Brookhaven Instruments Dynamic Light Scattering device. The laser beam (red) passes an optically cut sapphire disc and the scattered light can be detected continuously at angles between 30° and 150° .

A windows-based software provided by Brookhaven Instruments was used to control the goniometer setup and the measurements. Data analysis was performed using a house-in written iterative program package which applies the CONTIN method (Eq. 2-85) to all autocorrelation functions.

The deviations of absolute, volume-corrected scattering intensity are shown in Figure 7.4 left. As can be seen the scattering intensity deviates less than 2% from the intensity at 90° which is a very good result for a setup without index matching bath. The plot at the right shows that also the analysis of the data obtained from a dynamic light scattering experiment leads to reliable results.

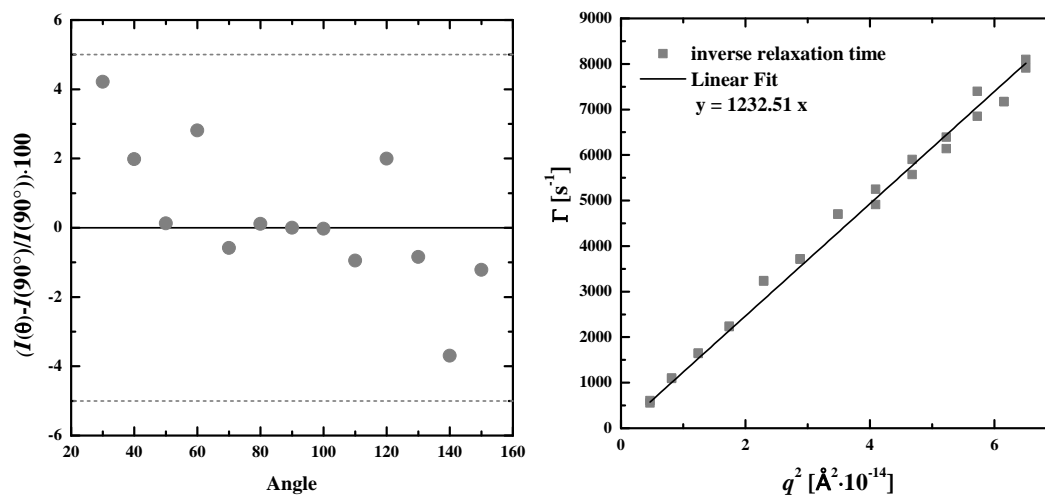


Figure 7.4: *Left:* Deviation of the volume-corrected scattering intensity at angle θ compared to $\theta = 90^\circ$ in percent. As can be seen, all values deviate less than 5% from the scattering intensity at 90° , most deviations are even below 2%. *Right:* Plot of the inverse relaxation time Γ against q^2 which results in a perfect linear trend.

STATIC LIGHT SCATTERING

The static light scattering setup used in this thesis is located at Imperial College, London, UK, in the Polymer and Microfluidics group in which Dr. João Cabral is group leader. The device is a SOFICA (Société Française d'Instrumentes de Contrôle et d'Analyses, Le Mesnil Saint-Denis, S. et O., France) photometer with a HeNe laser ($\lambda = 633$ nm), with modifications made by SLS Systemtechnik (G. Bauer, Denzlingen, Germany). It has a θ range of 15 to 105° , corresponding to a q range of 0.4 to $3 \cdot 10^{-3} \text{\AA}^{-1}$. A sealable cylindrical quartz cell manufactured by Hellma with a diameter of 3 cm was placed into a temperature-controlled toluene bath. The photomultiplier tube is calibrated to toluene (p.a. grade $\geq 99.7\%$, Sigma Aldrich) standard and is the reason for the high sensitivity of the SLS detection system when characterising low scattering or high absorbing samples.

7.2.4 Emulsion polymerisation

A three-necked 250 mL flask was equipped with a magnetic stir bar, a reflux condenser and a thermometer. 120 mL of distilled water was added to the flask and degassed for two hours. 0.510 g NIPAM monomer and the respective amounts of crosslinker *N,N'*-Methylenbisacrylamide (BIS) and sodiumdocylsulfate (SDS) were added. After reaching thermal equilibrium at 78°C in an oil bath 0.024 g potassium persulfate as radical initiator were added to start polymerisation. The reaction was carried out for 5 h at constant temperature. The resulting solution was filtered over a folded filter. The

size of the particles was controlled by DLS to ensure that the reaction had taken place completely. All particle dispersions were dialysed for four days against distilled water to remove surfactant and non-reacted monomer. For this purpose a dialysis hose for polymers and proteins with a size of 6-8 kDa was used which was purchased from scienova, Jena, Germany. The water was changed twice a day.

7.2.5 Microfluidics

A self-made setup was used to perform the temperature jump experiments. A schematic drawing of the setup is shown in Figure 4.20 and photographs of this setup are displayed in Figure 7.5. The microscope is a Olympus BX41M reflected light upright microscope. The syringe pump was produced by Braintree Scientific and is the type BS-800 2X.

The microscope was focussed onto the outer walls of the capillary. The distance between the two walls was determined using the movable stage of the microscope, which gives numerical information on the position of the stage, and the focus was placed at the exact middle between the two walls. A 50X long working distance objective was used for all experiments.

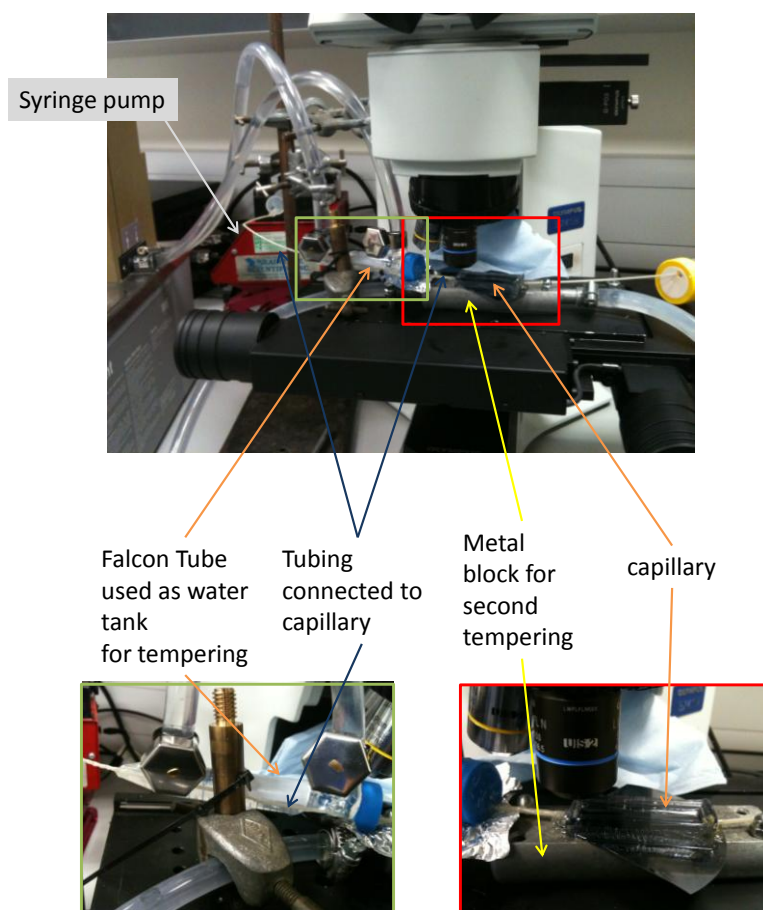


Figure 7.5: Photographs of the self-made device to perform fast temperature jumps. *Top:* Setup alignment with microscope and syringe pump (left). *Bottom:* Two different ways of applying temperatures. The Falcon tube (left, green frame) was modified so that it is connected to a water bath and tempers the tubing inside. After the Falcon tube the liquid enters a PDMS cassette on top of a metal block which can be temperature-controlled and provides the second temperature. The tubing crosses over to a 1 mm X-ray capillary.

7.3 Chemicals and Substances

Table 7-3: Overview of all chemicals used in this thesis.

Substance	Chemical formula	producer	molar mass [g mol ⁻¹]	purity
water	H ₂ O	--	18.02	double distilled
heavy water	D ₂ O	Eurisotop	20.03	99.1%
cyclohexane-h12	C ₆ H ₁₂	Sigma Aldrich	84.16	99.0%
cyclohexane-d12	C ₆ D ₁₂	Eurisotop	96.23	99.5%
Sodiumchloride	NaCl	Fluka	58.44	99.5%
sodium dodecyl sulphate (SDS)	CH ₃ (CH ₂) ₁₁ OSO ₃ Na	Sigma Aldrich	288.38	99.0%
Potassium peroxodisulfate	K ₂ S ₂ O ₈	Merck	270.32	99.0
Zonyl FSN 100	CF ₆₋₈ E ₈₋₁₂	Sigma Aldrich	≈ 950	tech. pure
Zonyl FSO 100	CF ₆₋₈ E ₆₋₁₀	Sigma Aldrich	≈ 725	tech. pure
<i>N</i> -isopropylacrylamide (NIPAM)	C ₆ H ₁₁ NO	Arcos Organics	113.13	99.0%

7.4 Tables

EFFICIENCY BOOSTING IN BALANCED MICROEMULSIONS

Table 7-4: Points of maximum efficiency for the balanced microemulsion systems H₂O/ NaCl – CO₂/ cyclohexane – Zonyl FSN 100/ Zonyl FSO 100 at $\alpha = 0.4$, $\delta_{\text{FSN}} = 0.75$, $\varepsilon = 0.01$, different $\beta_{\text{cyclohexane}}$ values and pressures. The phase diagrams are shown in [52]. The data points are shown graphically in Figure 1.1 left.

$\beta_{\text{cyclohexane}}$	surfactant mass fraction $\tilde{\gamma}$				temperature at efficiency point \tilde{T} [°C]			
	150 bar	200 bar	250 bar	300 bar	150 bar	200 bar	250 bar	300 bar
0	0.492	0.402	0.295	0.225	25.8	45.5	45.2	44.8
0.05	0.432	0.292	0.204	0.191	43.4	44.7	41.9	41.8
0.1	0.283	0.205	0.152	0.143	40.7	44.2	43.3	41.8
0.15	0.196	0.145	0.113	0.115	38.3	41.3	42.3	41.8
0.2	0.160	0.115	0.114	0.114	42.7	44.4	44.3	44.0
0.25	0.111	0.110	0.120	0.123	44.9	45.3	43.9	43.9
0.3	0.111	0.124	0.129	0.188	46.3	45.4	46.3	41.6
0.35	0.130	0.130	0.188	0.192	45.8	45.8	42.4	42.1
0.4	0.178	0.181	0.248	0.312	44.5	44.2	43.3	41.1

PHASE BEHAVIOUR OF WATER-RICH DILUTED MICROEMULSIONS

Table 7-5: Points of maximum efficiency for the diluted microemulsion systems H₂O/ NaCl – CO₂/ cyclohexane – Zonyl FSN 100/ Zonyl FSO 100 at $\gamma_a = 0.08$, $\delta_{FSN} = 0.75$, $\varepsilon = 0.01$ and different $\beta_{\text{cyclohexane}}$ values and pressures. The column at the right indicates the figures in which the respective phase behaviour is shown.

$\beta_{\text{cyclohexane}}$	$w_{B,\text{max}}$				T at $w_{B,\text{max}}$ [°C]				
	150 bar	200 bar	250 bar	300 bar	150 bar	200 bar	250 bar	300 bar	
0.00	0.100	0.118	0.132	0.147	28.6	33.0	35.5	36.9	Figure 3.1
0.10	0.103	0.107	0.122	0.147	32.4	34.5	36.0	39.1	Figure 3.13
0.15	0.108	0.125	0.134	0.140	32.5	37.0	36.9	37.0	Figure 3.14
0.20	0.148	0.141	0.137	0.137	38.6	36.3	35.4	36.0	Figure 3.1
0.25	0.112	0.130	0.131	0.137	34.3	38.4	37.7	37.6	Figure 3.16

DEMIXING KINETICS OF CO₂-MICROEMULSIONS

Time constants according to exponential fitting functions can easily be compared disregarding the amplitude of the change of scattering intensity. For linear dependencies, in contrast, the slope strongly depends on the amplitude of the described dependency. In order to enable a comparison of the slopes of the linear regions of $nii(t)$ the integrated intensities were normalised to 0 and 1 as described in the following. The highest integrated intensity of a system was divided by the highest intensity among all systems under consideration, and the data points of each system were multiplied with the respective quotient. Each series was normalised to zero by subtracting the lowest value of this series. The normalisation to 1 was conducted with respect to the highest value of all data points.

Table 7-6: Overview of slopes obtained from normalised $nii(t)$ (Figure 3.31) from pressure jumps to the thermodynamically unstable state for microemulsion systems with different cyclohexane contents.

β_i	0.00	0.10	0.15	0.20	0.25
slope [1/s]	-2.99 ± 0.15	-0.586 ± 0.033	-0.198 ± 0.008	0.152 ± 0.009	-0.068 ± 0.014

MICROEMULSIONS WITH PNIPAM PARTICLES AT ATMOSPHERIC PRESSURE

Table 7-7: Points of maximum efficiency of the microemulsion system H₂O/ PNIPAM – *n*-octane – C₁₂E₆ at $\gamma_a = 0.03$ and different weight mass fractions of PNIPAM particles (with 5.6 wt% crosslinker) in the hydrophilic phase. The phase behaviour is shown in Figure 5.1. Taken from [334].

wt% PNIPAM	0.000	0.007	0.014	0.021
$w_{B,\text{max}}$	0.089	0.097	0.104	0.143
T at $w_{B,\text{max}}$ [°C]	43.0	43.8	44.8	46.0

CO₂-MICROEMULSIONS WITH PNIPAM PARTICLES**Table 7-8:** Characteristics of the points of maximum efficiency

$\beta_{\text{cyclohexane}}$	$w_{B,\text{max}}$				T at $w_{B,\text{max}}$ [°C]			
	150 bar	200 bar	250 bar	300 bar	150 bar	200 bar	250 bar	300 bar
0.00	0.175	0.207	0.221	0.222	25.47	23.7	26.4	27.6
0.20	0.162	0.182	0.185	0.180	26.6	27.1	27.1	28.1

STATIC LIGHT SCATTERING RESULTS

Table 7-9: Overview of static light scattering results shown in Figure 4.13.

T [°C]	11.6	24.6	26.1	31.1	33.1	34.8	35.0	35.8	36.6
R_G [nm]	94.2 ± 3.8	85.8 ± 4.5	83.7 ± 1.5	83.2 ± 3.1	82.6 ± 4.7	81.0 ± 3.2	80.9 ± 3.9	69.0 ± 1.6	66.3 ± 1.6
R_{sphere} [nm]	92.3 ± 2.4	90.0 ± 2.3	89.5 ± 1.9	87.3 ± 2.0	86.3 ± 2.2	86.3 ± 2.2	85.5 ± 1.9		83.8 ± 2.1
T [°C]	36.8	38.0	39.5	40.5	41.4	43.6	45.2	46.4	
R_G [nm]	58.5 ± 2.4	50.3 ± 2.5	43.1 ± 5.3	41.3 ± 6.3	43.1 ± 4.6	39.1 ± 1.1	43.9 ± 1.7	44.0 ± 3.5	
R_{sphere} [nm]		74.6 ± 1.6	48.9 ± 1.3	41.9 ± 1.1	45.3 ± 1.0	51.4 ± 1.2	55.7 ± 1.4	48.6 ± 0.7	

PRESSURE-DEPENDENT SWELLING BEHAVIOUR OF PNIPAM PARTICLES

Table 7-10: Overview of hydrodynamic radii of particles with 5.6 wt% crosslinker, synthesised with (C1 in Figure 4.1, left) and without (C0, right) surfactant. The radii were measured at atmospheric pressure as well as at 300 bar. The temperature-dependent radii are shown in Figure 4.2 and Figure 4.3, respectively.

C1, 5.6 wt% crosslinker, with surfactant			C0, 5.6 wt% crosslinker, without surfactant		
T [°C]	R_h (1 bar) [nm]	R_h (300 bar) [nm]	T [°C]	R_h (1 bar) [nm]	R_h (300 bar) [nm]
25.0	86.2 ± 4.5	82.0 ± 3.7	25.0	113.1 ± 4.6	110.3 ± 5.0
27.5	84.2 ± 3.6	79.5 ± 3.2	27.5	110.6 ± 3.6	107.5 ± 3.8
30.0	82.4 ± 2.4	79.5 ± 3.2	30.0	107.6 ± 6.2	104.9 ± 5.2
32.0	75.3 ± 1.8	77.0 ± 2.3	32.0	106.5 ± 3.3	103.9 ± 6.6
33.0	70.7 ± 2.0	72.5 ± 2.1	33.0	104.2 ± 3.6	104.7 ± 3.9
33.5	67.3 ± 2.9	71.5 ± 3.0	34.0	104.2 ± 3.5	105.3 ± 3.1
34.0	60.0 ± 1.9	70.8 ± 2.6	35.0	88.6 ± 3.5	100.6 ± 4.0
34.5	52.4 ± 1.4	69.6 ± 3.6	36.0	75.6 ± 3.7	100.1 ± 5.7
35.0	39.7 ± 0.7	64.1 ± 2.0	37.0	65.1 ± 2.8	93.7 ± 5.7
35.5	38.3 ± 0.6	59.8 ± 1.5	37.5	58.8 ± 1.5	84.4 ± 3.8
36.0	40.6 ± 0.7	53.9 ± 2.5	38.0	50.6 ± 0.8	78.5 ± 3.1
36.5	40.4 ± 0.3	48.0 ± 1.1	38.5	48.3 ± 0.5	68.0 ± 2.6
37.0	38.3 ± 0.6	41.6 ± 1.0	39.0	47.1 ± 0.6	
37.5		40.8 ± 1.0	40.0	44.6 ± 0.6	51.0 ± 1.4
38.0	38.0 ± 0.4	41.8 ± 1.0	42.5	45.5 ± 0.5	42.5 ± 1.0
39.0	37.6 ± 0.5	42.3 ± 1.0	45.0	44.0 ± 0.6	42.5 ± 1.0
40.0		43.0 ± 1.0			
41.0	39.2 ± 0.4	43.4 ± 1.0			
42.5	36.2 ± 0.6	40.5 ± 1.0			

Table 7-11: Overview of temperature- and pressure-dependent hydrodynamic radii of PNIPAM particles containing 1.9 wt% crosslinker (particles A in Figure 4.1, left) and 3.8 wt% crosslinker (particles B in Figure 4.1). The graphical plots are shown in Figure 4.5.

A, 1.9 wt% crosslinker			B, 3.8 wt% crosslinker		
T [°C]	R_h (1 bar) [nm]	R_h (300 bar) [nm]	T [°C]	R_h (1 bar) [nm]	R_h (300 bar) [nm]
25.0	113.0 ± 4.5	114.9 ± 7.3	25.0	79.5 ± 7.3	78.0 ± 3.8
27.5	110.6 ± 3.6	104.0 ± 3.6	27.5	79.7 ± 5.6	76.4 ± 3.4
30.0	114.2 ± 9.8	106.1 ± 7.6	30.0	77.6 ± 7.3	73.1 ± 2.0
31.0	104.8 ± 7.7	103.6 ± 8.5	31.0	74.2 ± 3.4	71.7 ± 4.1
32.0	101.2 ± 2.9	105.8 ± 8.0	32.0	65.6 ± 4.3	72.5 ± 1.1
33.0	103.1 ± 2.6	102.3 ± 3.2	33.0	59.8 ± 5.3	69.6 ± 5.2
33.5	101.3 ± 2.3	105.1 ± 4.1	34.0	52.4 ± 1.5	65.9 ± 2.4
34.0	97.2 ± 2.6	102.3 ± 2.8	35.0	40.9 ± 1.3	64.0 ± 2.4
34.5	94.0 ± 1.1	101.3 ± 2.2	35.5	36.8 ± 1.0	59.9 ± 6.8
35.0	68.5 ± 3.9	94.6 ± 1.4	36.0	37.1 ± 1.0	51.7 ± 2.4
35.5		90.7 ± 1.4	36.5	35.4 ± 1.0	
36.0	64.4 ± 1.7	79.0 ± 3.1	37.0	34.9 ± 0.9	46.9 ± 1.2
36.5	58.0 ± 0.7	64.0 ± 1.0	37.5	35.5 ± 0.7	41.4 ± 1.8
37.0	65.5 ± 1.6	61.5 ± 1.8	38.0	33.1 ± 0.7	38.5 ± 1.2
37.5	68.5 ± 1.1	58.7 ± 1.0	39.0	33.0 ± 1.0	38.3 ± 1.1
38.0	63.1 ± 2.6	62.0 ± 1.8	40.0	35.5 ± 0.8	36.2 ± 1.0
39.0	57.7 ± 2.5	63.2 ± 1.8			
40.0	58.8 ± 2.7	58.2 ± 3.6			

8 Bibliography

- [1] N. J. Mills, *Polymer Foams Handbook*, Butterworth Heinemann, ISBN 978-0-7506-8069-1 **2007**.
- [2] W. Kaiser, *Kunststoffchemie für Ingenieure: Von der Synthese bis zur Anwendung*, Carl Hanser Verlag, ISBN 978-3446430471 **2011**.
- [3] B. P. Jelle, A. Gustavsen and R. Baetens, *The path to the high performance thermal building insulation materials and solutions of tomorrow*, Journal of Building Physics **2010**, 34, 2, 99-123.
- [4] N. Husing and U. Schubert, *Aerogels airy materials: Chemistry, structure, and properties*, Angewandte Chemie-International Edition **1998**, 37, 1-2, 23-45.
- [5] N. Haug, H. U. Pfensig, E. Schutt and U. Wiesmann, *Diffusion of Binary Gas Mixtures in Catalysts*, Chemie Ingenieur Technik **1970**, 42, 16, 1023-&.
- [6] M. Knudsen, *Annalen der Physik* **1909**,
- [7] K. Raed and U. Gross, *Modeling of Influence of Gas Atmosphere and Pore-Size Distribution on the Effective Thermal Conductivity of Knudsen and Non-Knudsen Porous Materials*, International Journal of Thermophysics **2009**, 30, 4, 1343-1356.
- [8] J. H. Seinfeld and S. N. Pandis, *Atmospheric Chemistry and Physics*, Wiley Interscience, **1998**.
- [9] S. G. Jennings, *The Mean Free-Path in Air*, Journal of Aerosol Science **1988**, 19, 2, 159-166.
- [10] P. Schmidt-Winkel, W. W. Lukens, D. Zhao, P. Yang, B. F. Chmelka and G. D. Stucky, *Siliceous mesostructured cellular foams with uniformly sized and shaped pores*, Organic/Inorganic Hybrid Materials Ii **1999**, 576, 241-246.
- [11] C. T. Alviso and R. W. Pekala, *Melamine-Formaldehyde Aerogels*, Abstracts of Papers of the American Chemical Society **1991**, 202, 51-Poly.
- [12] R. W. Pekala, L. W. Hrubesh, T. M. Tillotson, C. T. Alviso, J. F. Poco and J. D. Lemay, *A Comparison of Mechanical-Properties and Scaling Law Relationships for Silica Aerogels and Their Organic Counterparts*, Mechanical Properties of Porous and Cellular Materials **1991**, 207, 197-200.
- [13] R. W. Pekala, C. T. Alviso and J. D. Lemay, *Organic Aerogels - a New Type of Ultrastructured Polymer*, Chemical Processing of Advanced Materials **1992**, 671-683.
- [14] S. S. Kistler, *Coherent Expanded Aerogels and Jellies*, Nature **1931**, 127, 1, 741.
- [15] S. S. Kistler, *Coherent Expanded Aerogels*, The Journal of Physical Chemistry **1931**, 36, 52-64.
- [16] NASA, <http://stardust.jpl.nasa.gov/tech/aerogel.html>, **2005**.
- [17] Steiner, S., Walker, W., *About Aerogel*, www.aerogel.org, **2014**.
- [18] J. S. Colton and N. P. Suh, *The Nucleation of Microcellular Thermoplastic Foam with Additives .1. Theoretical Considerations*, Polymer Engineering and Science **1987**, 27, 7, 485-492.
- [19] J. S. Colton and N. P. Suh, *Nucleation of Microcellular Foam - Theory and Practice*, Polymer Engineering and Science **1987**, 27, 7, 500-503.
- [20] J. S. Colton and N. P. Suh, *The Nucleation of Microcellular Thermoplastic Foam with Additives .2. Experimental Results and Discussion*, Polymer Engineering and Science **1987**, 27, 7, 493-499.
- [21] D. F. Baldwin, C. B. Park and N. P. Suh, *Microcellular sheet extrusion system process design models for shaping and cell growth control*, Polymer Engineering and Science **1998**, 38, 4, 674-688.

- [22] D. F. Baldwin, C. B. Park and N. P. Suh, *An extrusion system for the processing of microcellular polymer sheets: Shaping and cell growth control*, Polymer Engineering and Science **1996**, 36, 10, 1425-1435.
- [23] B. Krause, K. Diekmann, N. F. A. van der Vegt and M. Wessling, *Open nanoporous morphologies from polymeric blends by carbon dioxide foaming*, Macromolecules **2002**, 35, 5, 1738-1745.
- [24] B. Krause, H. J. P. Sijbesma, P. Munuklu, N. F. A. van der Vegt and M. Wessling, *Bicontinuous nanoporous polymers by carbon dioxide foaming*, Macromolecules **2001**, 34, 25, 8792-8801.
- [25] B. Krause, N. F. A. van der Vegt and M. Wessling, *New way to produce porous polymeric membranes by carbon dioxide foaming.*, Abstracts of Papers of the American Chemical Society **2001**, 222, U326-U326.
- [26] B. Krause, R. Mettinkhof, N. F. A. van der Vegt and M. Wessling, *Microcellular foaming of amorphous high-T-g polymers using carbon dioxide*, Macromolecules **2001**, 34, 4, 874-884.
- [27] B. Krause, *Polymer Nanofoams*, PrintPartners Ipskamp B.V., ISBN 9036516471 **2001**.
- [28] R. Strey and A. Müller, *Erzeugung nanodisperser Einschlüsse in einer hochviskosen Matrix*, German Patent Application DE102010053064A1, No. WO02012072755A2, **2011**.
- [29] A. Müller, *Preparations of Polymer Nano-Foams: Templates, Challenges and Kinetics*, Cuvillier Verlag, ISBN 978-3954045662, **2013**.
- [30] S. A. E. Boyer and J. P. E. Grolier, *Modification of the glass transitions of polymers by high-pressure gas solubility*, Pure and Applied Chemistry **2005**, 77, 3, 593-603.
- [31] M. Schwan, T. Sottmann and R. Strey, *Aufgeschäumtes Material und Herstellungsverfahren für das aufgeschäumte Material*, European Patent Application No DE10260815B4, **2008**.
- [32] M. Schwan, L. G. A. Kramer, T. Sottmann and R. Strey, *Phase behaviour of propane- and scCO₂-microemulsions and their prominent role for the recently proposed foaming procedure POSME (Principle of Supercritical Microemulsion Expansion)*, Physical Chemistry Chemical Physics **2010**, 12, 23, 6247-6252.
- [33] O. Holderer, M. Klostermann, M. Monkenbusch, R. Schweins, P. Lindner, R. Strey, D. Richter and T. Sottmann, *Soft fluctuating surfactant membranes in supercritical CO₂-microemulsions*, Physical Chemistry Chemical Physics **2011**, 13, 8, 3022-3025.
- [34] M. Klostermann, T. Foster, R. Schweins, P. Lindner, O. Glatter, R. Strey and T. Sottmann, *Microstructure of supercritical CO₂-in-water microemulsions: a systematic contrast variation study*, Physical Chemistry Chemical Physics **2011**, 13, 45, 20289-20301.
- [35] M. Klostermann, R. Strey, T. Sottmann, R. Schweins, P. Lindner, O. Holderer, M. Monkenbusch and D. Richter, *Structure and dynamics of balanced supercritical CO₂-microemulsions*, Soft Matter **2012**, 8, 3, 797-807.
- [36] J. Eastoe, Z. Bayazit, S. Martel, D. C. Steytler and R. K. Heenan, *Droplet structure in a water-in-CO₂ microemulsion*, Langmuir **1996**, 12, 6, 1423-1424.
- [37] J. Eastoe, J. F. Dong, G. J. Hetherington, D. Steytler and R. K. Heenan, *Structure in microemulsions of di-chained surfactants*, Journal of the Chemical Society-Faraday Transactions **1996**, 92, 1, 65-72.
- [38] D. C. Steytler, T. R. Jenta, B. H. Robinson, J. Eastoe and R. K. Heenan, *Structure of reversed micelles formed by metal salts of bis(ethylhexyl) phosphoric acid*, Langmuir **1996**, 12, 6, 1483-1489.
- [39] L. Kramer, *Überkritische CO₂-Mikroemulsionen als Vorstufe für Nanoschäume*, Dissertation, **2008**.
- [40] M. Schwan, *Überkritische Mikroemulsionen zur Herstellung nanozellulärer Schäume - Principle of Supercritical Microemulsion Expansion*, PhD-Thesis, University of Cologne, ISBN 978-3865377302 **2005**.

- [41] J. O. Stoffer and T. Bone, *Polymerization in Water-in-Oil Micro-Emulsion Systems .1.*, Journal of Polymer Science Part a-Polymer Chemistry **1980**, 18, 8, 2641-2648.
- [42] J. O. Stoffer and T. Bone, *Polymerization in Water-in-Oil Micro-Emulsion Systems .2. Sem Investigation of Structure*, Journal of Dispersion Science and Technology **1980**, 1, 4, 393-412.
- [43] J. O. Stoffer and T. Bone, *Polymerization in Water in Oil Micro-Emulsion Systems Containing Methyl-Methacrylate*, Journal of Dispersion Science and Technology **1980**, 1, 1, 37-54.
- [44] J. O. Stoffer and T. Bone, *Pmma Microemulsion Polymerization*, Abstracts of Papers of the American Chemical Society **1987**, 194, 12-Macr.
- [45] W. Ostwald, *Ostwald Reifung*, Zeitschrift für Physikalische Chemie **1900**, 34, 495-503.
- [46] W. Koch and S. K. Friedlander, *Particle Growth by Coalescence and Agglomeration*, Particle & Particle Systems Characterization **1991**, 8, 1, 86-89.
- [47] E. Khazova, *Polymer-Nanoschäume aus Mikroemulsionen*, PhD Thesis, University of Cologne, **2009**.
- [48] M. Klostermann, *Quantitative Characterization of Supercritical Microemulsions and their Use for Preparing Highly Porous Sugar Foams*, Dissertation, **2011**.
- [49] A. Chalbi, D. Engelen, W. Friederichs, E. Khazova, S. Lindner, T. Sottmann and R. Strey, *Verfahren zur Herstellung eines geschäumten Materials, hierbei eingesetzte emulsionsförmige Zusammensetzung und hieraus erhältliches geschäumtes Material*, German Patent Application DE102010060386, **2012**.
- [50] P. Chiquet, J. L. Daridon, D. Broseta and S. Thibeau, *CO₂/water interfacial tensions under pressure and temperature conditions of CO₂ geological storage*, Energy Conversion and Management **2007**, 48, 3, 736-744.
- [51] H. Leitao, A. M. Somoza, M. M. T. daGama, T. Sottmann and R. Strey, *Scaling of the interfacial tension of microemulsions: A phenomenological description*, Journal of Chemical Physics **1996**, 105, 7, 2875-2883.
- [52] Y. Pütz, *Influence of hydrophobic additives on supercritical CO₂-microemulsions and their foaming properties*, Master Thesis, University of Cologne, **2012**.
- [53] Y. Pütz, L. Grassberger, P. Lindner, R. Schweins, R. Strey and T. Sottmann, *Unexpected efficiency boosting in CO(2)-microemulsions: A cyclohexane depletion zone near the fluorinated surfactants evidenced by a systematic SANS contrast variation study*, Physical Chemistry Chemical Physics **2015**, 17, 6122-6134.
- [54] V. H. Dalvi, V. Srinivasan and P. J. Rossky, *Understanding the Effectiveness of Fluorocarbon Ligands in Dispersing Nanoparticles in Supercritical Carbon Dioxide*, Journal of Physical Chemistry C **2010**, 114, 37, 15553-15561.
- [55] V. H. Dalvi and P. J. Rossky, *Molecular origins of fluorocarbon hydrophobicity*, Proceedings of the National Academy of Sciences of the United States of America **2010**, 107, 31, 13603-13607.
- [56] A. Muller, Y. Putz, R. Oberhoffer, N. Becker, R. Strey, A. Wiedenmann and T. Sottmann, *Kinetics of pressure induced structural changes in super- or near-critical CO₂-microemulsions*, Physical Chemistry Chemical Physics **2014**, 16, 34, 18092-18097.
- [57] D. Kipping, R. Gähler and K. Habicht, *Small angle neutron scattering at very high time resolution: Principle and simulations of `TISANE`*, Physics Letters A **2007**, 372, 1541-1546.
- [58] BMBF-project, *Time-Involved Small Angle Neutron Scattering (TISANE) 05K10PK3/05K10TS1*, **2010**.
- [59] A. Zintchenko, M. Ogris and E. Wagner, *Temperature dependent gene expression induced by PNIPAM-based copolymers: Potential of hyperthermia in gene transfer*, Bioconjugate Chemistry **2006**, 17, 3, 766-772.
- [60] Y. Z. You, K. K. Kalebaila, S. L. Brock and D. Oupicky, *Temperature-controlled uptake and release in PNIPAM-modified porous silica nanoparticles*, Chemistry of Materials **2008**, 20, 10, 3354-3359.

- [61] X. Feng, L. Chen, H. C. Zhao and Y. P. Zhao, *Temperature-sensitive Properties of PNIPAm/PVA Hydrogel Fibers Used for Artificial Muscles*, 2010 International Forum on Biomedical Textile Materials, Proceedings **2010**, 18-22.
- [62] K. Kratz, T. Hellweg and W. Eimer, *Structural changes in PNIPAM microgel particles as seen by SANS, DLS, and EM techniques*, Polymer **2001**, 42, 15, 6631-6639.
- [63] R. Pelton, *Temperature-sensitive aqueous microgels*, Advances in Colloid and Interface Science **2000**, 85, 1, 1-33.
- [64] L. Arleth, X. H. Xia, R. P. Hjelm, J. Z. Wu and Z. B. Hu, *Volume transition and internal structures of small poly(N-isopropylacrylamide) microgels*, Journal of Polymer Science Part B-Polymer Physics **2005**, 43, 7, 849-860.
- [65] I. Bischofberger, D. C. E. Calzolari and V. Trappe, *Co-nonsolvency of PNIPAM at the transition between solvation mechanisms*, Soft Matter **2014**, 10, 41, 8288-8295.
- [66] C. Scherzinger, A. Schwarz, A. Bardow, K. Leonhard and W. Richtering, *Cononsolvency of poly-N-isopropyl acrylamide (PNIPAM): Microgels versus linear chains and macrogels*, Current Opinion in Colloid & Interface Science **2014**, 19, 2, 84-94.
- [67] J. J. Lietor-Santos, B. Sierra-Martin, R. Vavrin, Z. B. Hu, U. Gasser and A. Fernandez-Nieves, *Deswelling Microgel Particles Using Hydrostatic Pressure*, Macromolecules **2009**, 42, 16, 6225-6230.
- [68] J. J. Lietor-Santos, B. Sierra-Martin, U. Gasser and A. Fernandez-Nieves, *The effect of hydrostatic pressure over the swelling of microgel particles*, Soft Matter **2011**, 7, 14, 6370-6374.
- [69] M. Karg, I. Pastoriza-Santos, B. Rodriguez-Gonzalez, R. von Klitzing, S. Wellert and T. Hellweg, *Temperature, pH, and ionic strength induced changes of the swelling behavior of PNIPAM-poly(allylactic acid) copolymer microgels*, Langmuir **2008**, 24, 12, 6300-6306.
- [70] T. D. Le, U. Olsson, H. Wennerstrom, P. Uhrmeister, B. Rathke and R. Strey, *Relaxation kinetics of an L-3 (sponge) phase*, Journal of Physical Chemistry B **2002**, 106, 36, 9410-9417.
- [71] J. Ye, J. Xu, J. M. Hu, X. F. Wang, G. Z. Zhang, S. Y. Liu and C. Wu, *Comparative study of temperature-induced association of cyclic and linear poly(N-isopropylacrylamide) chains in dilute solutions by laser light scattering and stopped-flow temperature jump*, Macromolecules **2008**, 41, 12, 4416-4422.
- [72] H. Inoue, K. Katayama, K. Iwai, A. Miura and H. Masuhara, *Conformational relaxation dynamics of a poly(N-isopropylacrylamide) aqueous solution measured using the laser temperature jump transient grating method*, Physical Chemistry Chemical Physics **2012**, 14, 16, 5620-5627.
- [73] L. Polo-Corrales and C. Rinaldi, *Monitoring iron oxide nanoparticle surface temperature in an alternating magnetic field using thermoresponsive fluorescent polymers*, Journal of Applied Physics **2012**, 111, 7, 07B334.
- [74] J. M. Hu, D. Wang, J. Xu, Z. Y. Zhu and S. Y. Liu, *Contraction and Collapsing Kinetics of Single Synthetic Polymer Chains at Small Quench Depths*, Macromolecular Chemistry and Physics **2010**, 211, 24, 2573-2584.
- [75] M. Reinhardt, J. Dzubiella, M. Trapp, P. Gutfreund, M. Kreuzer, A. H. Groschel, A. H. E. Muller, M. Ballauff and R. Steitz, *Fine-Tuning the Structure of Stimuli-Responsive Polymer Films by Hydrostatic Pressure and Temperature*, Macromolecules **2013**, 46, 16, 6541-6547.
- [76] P. E. Laibinis, J. J. Hickman, M. S. Wrighton and G. M. Whitesides, *Orthogonal Self-Assembled Monolayers - Alkanethiols on Gold and Alkane Carboxylic-Acids on Alumina*, Science **1989**, 245, 4920, 845-847.
- [77] H. Sato, Y. Miura, N. Saito, K. Kobayashi and O. Takai, *A micropatterned multifunctional carbohydrate display by an orthogonal self-assembling strategy*, Biomacromolecules **2007**, 8, 2, 753-756.

- [78] A. Heeres, C. van der Pol, M. C. A. Stuart, A. Friggeri, B. L. Feringa and J. van Esch, *Orthogonal self-assembly of low molecular weight hydrogelators and surfactants*, Journal of the American Chemical Society **2003**, 125, 47, 14252-14253.
- [79] A. Brizard, M. Stuart, K. van Bommel, A. Friggeri, M. de Jong and J. van Esch, *Preparation of nanostructures by orthogonal self-assembly of hydrogelators and surfactants*, Angewandte Chemie-International Edition **2008**, 47, 11, 2063-2066.
- [80] M. Laupheimer, T. Sottmann, R. Schweins and C. Stubenrauch, *Studying orthogonal self-assembled systems: microstructure of gelled bicontinuous microemulsions*, Soft Matter **2014**, 10, 43, 8744-8757.
- [81] M. Laupheimer, K. Jovic, F. E. Antunes, M. D. M. Miguel and C. Stubenrauch, *Studying orthogonal self-assembled systems: phase behaviour and rheology of gelled microemulsions*, Soft Matter **2013**, 9, 13, 3661-3670.
- [82] Y. Gong, Q. L. Liu, A. M. Zhu and Q. G. Zhang, *One-pot synthesis of poly(N-isopropylacrylamide)/chitosan composite microspheres via microemulsion*, Carbohydrate Polymers **2012**, 90, 1, 690-695.
- [83] L. F. Ding, T. Wang and L. G. Wu, *Synthesis of AgCl Nanoparticles in Ionic Liquid Microemulsion and Regulation of AgCl/poly(MMA-co-St) Hybrid Membranes*, Chinese Journal of Inorganic Chemistry **2014**, 30, 2, 323-330.
- [84] F. X. Bu, C. J. Du, Q. H. Zhang and J. S. Jiang, *One-pot synthesis of Prussian blue superparticles from reverse microemulsion*, Crystengcomm **2014**, 16, 15, 3113-3120.
- [85] S. Pascual, C. N. Urbani and M. J. Monteiro, *Functionalization of Polymer Nanoparticles Formed by Microemulsion RAFT-Mediated Polymerization*, Macromolecular Reaction Engineering **2010**, 4, 3-4, 257-263.
- [86] K. Sakata, S. Taguchi, S. Uemura, M. Kunitake, S. Kawano and T. Nishimi, *Continuous Porous Poly(N-isopropylacrylamide) Gels Prepared from a Bicontinuous Microemulsion*, Chemistry Letters **2014**, 43, 2, 240-242.
- [87] S. Q. Zhou and C. Wu, *Laser-Light Scattering Study of a Very Dilute Water/Sodium Bis(2-Ethylhexyl)Sulfosuccinate/N-Hexane Microemulsion Stabilized by Poly(N-Isopropylacrylamide)*, Macromolecules **1995**, 28, 15, 5225-5229.
- [88] J. H. Schulman and T. P. Hoar, *Transparent water-in-oil dispersions: the oleophobic hydro-micelle*, Nature **1943**, 152, 2.
- [89] J. H. Schulman, W. Stoeckenius and L. M. Prince, *Mechanism of Formation and Structure of Micro Emulsions by Electron Microscopy*, Journal of Physical Chemistry **1959**, 63, 10, 1677-1680.
- [90] P. A. Winsor, *Solvent properties of amphiphilic compounds*, Butterworths Scientific Publications **1954**,
- [91] P. A. Winsor, *Hydrotrophy, Solubilisation and Related Emulsification Processes .1. To .4.*, Transactions of the Faraday Society **1948**, 44, 6, 376-398.
- [92] H. Arai and K. Shinoda, *Effect of Mixing of Oils and of Nonionic Surfactants on Phase Inversion Temperatures of Emulsions*, Journal of Colloid and Interface Science **1967**, 25, 3, 396-&.
- [93] K. Shinoda and H. Arai, *Effect of Phase Volume on Phase Inversion Temperature of Emulsions Stabilized with Nonionic Surfactants*, Journal of Colloid and Interface Science **1967**, 25, 3, 429-&.
- [94] K. Shinoda and T. Ogawa, *Solubilization of Water in Nonaqueous Solutions of Nonionic Surfactants*, Journal of Colloid and Interface Science **1967**, 24, 1, 56-&.
- [95] K. Shinoda, *Correlation between Dissolution State of Nonionic Surfactant and Type of Dispersion Stabilized with Surfactant*, Journal of Colloid and Interface Science **1967**, 24, 1, 4-&.

- [96] M. Kahlweit, R. Strey, D. Haase, H. Kunieda, T. Schmeling, B. Faulhaber, M. Borkovec, H. F. Eicke, G. Busse, F. Eggers, T. Funck, H. Richmann, L. Magid, O. Soderman, P. Stilbs, J. Winkler, A. Dittrich and W. Jahn, *How to Study Microemulsions*, Journal of Colloid and Interface Science **1987**, 118, 2, 436-453.
- [97] M. Kahlweit and R. Strey, *Phase-Behavior of Ternary-Systems of the Type H₂O-Oil-Nonionic Amphiphile (Microemulsions)*, Angewandte Chemie-International Edition in English **1985**, 24, 8, 654-668.
- [98] R. Strey, *Microemulsion Microstructure and Interfacial Curvature*, Colloid and Polymer Science **1994**, 272, 8, 1005-1019.
- [99] J. Lyklema, *Microemulsions*, in *Fundamentals of Interface and Colloid Science*, Academic Press **2005**, ISBN-13: 000-0124605303, 1-96.
- [100] B. Z. Peng, G. J. Chen, C. Y. Sun, B. Liu, Y. Q. Zhang and Q. A. Zhang, *Dynamic Interfacial Tension between Water and n-Octane plus Sorbitan Monolaurate at (274.2 to 293.2) K*, Journal of Chemical and Engineering Data **2011**, 56, 4, 1617-1621.
- [101] T. Sottmann and R. Strey, *Ultralow interfacial tensions in water-n-alkane-surfactant systems*, Journal of Chemical Physics **1997**, 106, 20, 8606-8615.
- [102] M. Kahlweit, R. Strey, P. Firman and D. Haase, *Phase-Behavior of Ternary-Systems - H₂O-Oil-Nonionic Surfactant as a near-Tricritical Phenomenon*, Langmuir **1985**, 1, 3, 281-288.
- [103] R. Strey, *Water-nonionic surfactant systems, and the effect of additives*, Berichte Der Bunsen-Gesellschaft-Physical Chemistry Chemical Physics **1996**, 100, 3, 182-189.
- [104] G. J. T. Tiddy, *Surfactant-Water Liquid-Crystal Phases*, Physics Reports-Review Section of Physics Letters **1980**, 57, 1, 1-46.
- [105] D. J. Mitchell, G. J. T. Tiddy, L. Waring, T. Bostock and M. P. McDonald, *Phase-Behavior of Polyoxyethylene Surfactants with Water - Mesophase Structures and Partial Miscibility (Cloud Points)*, Journal of the Chemical Society-Faraday Transactions I **1983**, 79, 975-1000.
- [106] S. Burauer, T. Sachert, T. Sottmann and R. Strey, *On microemulsion phase behavior and the monomeric solubility of surfactant*, Physical Chemistry Chemical Physics **1999**, 1, 18, 4299-4306.
- [107] M. Kahlweit, R. Strey and G. Busse, *Microemulsions - a Qualitative Thermodynamic Approach*, Journal of Physical Chemistry **1990**, 94, 10, 3881-3894.
- [108] W. C. Griffin, *Classification of Surface-Active Agents by "HLB"*, Journal of the Society of Cosmetic Chemists, **1949**, 1, 5, 311-326.
- [109] W. C. Griffin, *Calculation of HLB-Value of Non-Ionic Surfactants*, Journal of the Society of Cosmetic Chemists **1954**, 5, 4, 249-256.
- [110] K. Shinoda and H. Saito, *Stability of O/W Type Emulsions as Functions of Temperature and Hlb of Emulsifiers - Emulsification by Pit-Method*, Journal of Colloid and Interface Science **1969**, 30, 2, 258-&.
- [111] H. Kunieda and K. Shinoda, *Phase-Behavior and Tricritical Phenomena in a Bile-Salt System*, Bulletin of the Chemical Society of Japan **1983**, 56, 4, 980-984.
- [112] M. Kahlweit, R. Strey, P. Firman, D. Haase, J. Jen and R. Schomacker, *General Patterns of the Phase-Behavior of Mixtures of H₂O, Nonpolar-Solvents, Amphiphiles, and Electrolytes .I.*, Langmuir **1988**, 4, 3, 499-511.
- [113] S. A. Safran and L. A. Turkevich, *Phase-Diagrams for Microemulsions*, Physical Review Letters **1983**, 50, 24, 1930-1933.
- [114] S. A. Safran, *Saddle-Splay Modulus and the Stability of Spherical Microemulsions*, Physical Review A **1991**, 43, 6, 2903-2904.

- [115] M. Kahlweit, R. Strey and G. Busse, *Weakly to Strongly Structured Mixtures*, Physical Review E **1993**, 47, 6, 4197-4209.
- [116] D. F. Evans and H. Wennerstrom, in *The colloid Domain: Where Physics, Chemistry and Technology meet (2nd Edition)*, Wiley-VCH **1999**, ISBN-13: 978-0471242475,
- [117] S. T. Milner, *Chain Architecture and Asymmetry in Copolymer Microphases*, Macromolecules **1994**, 27, 8, 2333-2335.
- [118] U. Olsson, K. Nagai and H. Wennerstrom, *Microemulsions with Nonionic Surfactants .I. Diffusion Process of Oil Molecules*, Journal of Physical Chemistry **1988**, 92, 23, 6675-6679.
- [119] B. Lindman, K. Shinoda, U. Olsson, D. Anderson, G. Karlstrom and H. Wennerstrom, *On the Demonstration of Bicontinuous Structures in Microemulsions*, Colloids and Surfaces **1989**, 38, 1-3, 205-224.
- [120] U. Olsson, U. Wurz and R. Strey, *Cylinders and Bilayers in a Ternary Nonionic Surfactant System*, Journal of Physical Chemistry **1993**, 97, 17, 4535-4539.
- [121] U. Olsson and P. Schurtenberger, *Structure, Interactions, and Diffusion in a Ternary Nonionic Microemulsion near Emulsification Failure*, Langmuir **1993**, 9, 12, 3389-3394.
- [122] U. Olsson, K. Nakamura, H. Kunieda and R. Strey, *Normal and reverse vesicles with nonionic surfactant: Solvent diffusion and permeability*, Langmuir **1996**, 12, 12, 3045-3054.
- [123] M. S. Leaver, U. Olsson, H. Wennerstrom, R. Strey and U. Wurz, *Phase-Behavior and Structure in a Nonionic Surfactant-Oil-Water Mixture*, Journal of the Chemical Society-Faraday Transactions **1995**, 91, 23, 4269-4274.
- [124] W. Jahn and R. Strey, *Microstructure of Microemulsions by Freeze-Fracture Electron-Microscopy*, Journal of Physical Chemistry **1988**, 92, 8, 2294-2301.
- [125] S. Burauer, L. Belkoura, C. Stubenrauch and R. Strey, *Bicontinuous microemulsions revisited: a new approach to freeze fracture electron microscopy (FFEM)*, Colloids and Surfaces a-Physicochemical and Engineering Aspects **2003**, 228, 1-3, 159-170.
- [126] L. Belkoura, C. Stubenrauch and R. Strey, *Freeze fracture direct imaging: A new freeze fracture method for specimen preparation in cryo-transmission electron microscopy*, Langmuir **2004**, 20, 11, 4391-4399.
- [127] S. H. Chen, S. L. Chang, R. Strey, J. Samseth and K. Mortensen, *Structural Evolution of Bicontinuous Microemulsions*, Journal of Physical Chemistry **1991**, 95, 19, 7427-7432.
- [128] O. Glatter, R. Strey, K. V. Schubert and E. W. Kaler, *Small angle scattering applied to microemulsions*, Berichte Der Bunsen-Gesellschaft-Physical Chemistry Chemical Physics **1996**, 100, 3, 323-335.
- [129] R. Strey, O. Glatter, K. V. Schubert and E. W. Kaler, *Small-angle neutron scattering of D₂O-C(12)E(5) mixtures and microemulsions with n-octane: Direct analysis by Fourier transformation*, Journal of Chemical Physics **1996**, 105, 3, 1175-1188.
- [130] J. Brunner-Popela, R. Mittelbach, R. Strey, K. V. Schubert, E. W. Kaler and O. Glatter, *Small-angle scattering of interacting particles. III. D₂O-C12E5 mixtures and microemulsions with n-octane*, Journal of Chemical Physics **1999**, 110, 21, 10623-10632.
- [131] H. Wennerstrom and U. Olsson, *On the Flexible Surface Model of Sponge Phases and Microemulsions*, Langmuir **1993**, 9, 2, 365-368.
- [132] T. Sottmann, R. Strey and S. H. Chen, *A small-angle neutron scattering study of nonionic surfactant molecules at the water-oil interface: Area per molecule, microemulsion domain size, and rigidity*, Journal of Chemical Physics **1997**, 106, 15, 6483-6491.

- [133] S. H. Chen, S. L. Chang and R. Strey, *On the Interpretation of Scattering Peaks from Bicontinuous Microemulsions*, Trends in Colloid and Interface Science Iv **1990**, 81, 30-35.
- [134] M. Teubner and R. Strey, *Origin of the Scattering Peak in Microemulsions*, Journal of Chemical Physics **1987**, 87, 5, 3195-3200.
- [135] M. Kotlarchyk, S. H. Chen and J. S. Huang, *Temperature-Dependence of Size and Polydispersity in a 3-Component Micro-Emulsion by Small-Angle Neutron-Scattering*, Journal of Physical Chemistry **1982**, 86, 17, 3273-3276.
- [136] M. Kotlarchyk and S. H. Chen, *Analysis of Small-Angle Neutron-Scattering Spectra from Polydisperse Interacting Colloids*, Journal of Chemical Physics **1983**, 79, 5, 2461-2469.
- [137] M. Kotlarchyk, S. H. Chen, J. S. Huang and M. W. Kim, *Structure of 3-Component Microemulsions in the Critical Region Determined by Small-Angle Neutron-Scattering*, Physical Review A **1984**, 29, 4, 2054-2069.
- [138] M. Gradzielski and D. Langevin, *Small-angle neutron scattering experiments on microemulsion droplets: Relation to the bending elasticity of the amphiphilic film*, Journal of Molecular Structure **1996**, 383, 1-3, 145-156.
- [139] M. Gradzielski, D. Langevin, T. Sottmann and R. Strey, *Droplet microemulsions at the emulsification boundary: The influence of the surfactant structure on the elastic constants of the amphiphilic film*, Journal of Chemical Physics **1997**, 106, 19, 8232-8238.
- [140] T. Foster, T. Sottmann, R. Schweins and R. Strey, *Small-angle-neutron-scattering from giant water-in-oil microemulsion droplets. II. Polymer-decorated droplets in a quaternary system*, Journal of Chemical Physics **2008**, 128, 6, 06492-1 - 06492-18.
- [141] T. Foster, T. Sottmann, R. Schweins and R. Strey, *Small-angle neutron scattering from giant water-in-oil microemulsion droplets. I. Ternary system*, Journal of Chemical Physics **2008**, 128, 5, 054502-1 - 054502-13.
- [142] T. Hellweg and R. von Klitzing, *Evidence for polymer-like structures in the single phase region of a dodecane/C12E5/water microemulsion: a dynamic light scattering study*, Physica A **2000**, 283, 3-4, 349-358.
- [143] C. A. Eckert, C. L. Liotta, D. Bush, J. S. Brown and J. P. Hallett, *Sustainable reactions in tunable solvents*, Journal of Physical Chemistry B **2004**, 108, 47, 18108-18118.
- [144] M. J. Dabney and F. V. Bright, *Interfacial Solvation within n-Alkane Monolayers in Contact with Supercritical CO₂*, Journal of Physical Chemistry C **2012**, 116, 34, 18340-18346.
- [145] J. D. Holmes, D. C. Steytler, G. D. Rees and B. H. Robinson, *Bioconversions in a water-in-CO₂ microemulsion*, Langmuir **1998**, 14, 22, 6371-6376.
- [146] M. Wang, B. Zhao, S. H. Xu, L. Lin, S. J. Liu and D. N. He, *Synthesis of hierarchically structured ZnO nanomaterials via a supercritical assisted solvothermal process*, Chemical Communications **2014**, 50, 8, 930-932.
- [147] M. C. McLeod, R. S. McHenry, E. J. Beckman and C. B. Roberts, *Synthesis and stabilization of silver metallic nanoparticles and premetallic intermediates in perfluoropolyether/CO₂ reverse micelle systems*, Journal of Physical Chemistry B **2003**, 107, 12, 2693-2700.
- [148] C. A. Eckert, B. L. Knutson and P. G. Debenedetti, *Supercritical fluids as solvents for chemical and materials processing*, Nature **1996**, 383, 6598, 313-318.
- [149] H. Peker, M. P. Srinivasan, J. M. Smith and B. J. McCoy, *Caffeine Extraction Rates from Coffee Beans with Supercritical Carbon-Dioxide*, Aiche Journal **1992**, 38, 5, 761-770.
- [150] E. Lack, H. Seidlitz and P. Toro, *Decaffeination of Coffee Samples by Co₂-Extraction*, 13th International Scientific Colloquium on Coffee **1989**, 236-245.

- [151] K. A. Consani and R. D. Smith, *Observations on the Solubility of Surfactants and Related Molecules in Carbon Dioxide at 50°C*, *The Journal of Supercritical Fluids* **1990**, 3, 51-65.
- [152] T. A. Hoefling, R. M. Enick and E. J. Beckman, *Microemulsions in near-Critical and Supercritical CO₂*, *Journal of Physical Chemistry* **1991**, 95, 19, 7127-7129.
- [153] A. Dardin, J. M. DeSimone and E. T. Samulski, *Fluorocarbons dissolved in supercritical carbon dioxide. NMR evidence for specific solute-solvent interactions*, *Journal of Physical Chemistry B* **1998**, 102, 10, 1775-1780.
- [154] G. G. Yee, J. L. Fulton and R. D. Smith, *Fourier-Transform Infrared-Spectroscopy of Molecular-Interactions of Heptafluoro-1-Butanol or 1-Butanol in Supercritical Carbon-Dioxide and Supercritical Ethane*, *Journal of Physical Chemistry* **1992**, 96, 15, 6172-6181.
- [155] P. Diep, K. D. Jordan, J. K. Johnson and E. J. Beekman, *CO₂-fluorocarbon and CO₂-hydrocarbon interactions from first-principles calculations*, *Journal of Physical Chemistry A* **1998**, 102, 12, 2231-2236.
- [156] C. R. Yonker and B. J. Palmer, *Investigation of CO₂/fluorine interactions through the intermolecular effects on the H-1 and F-19 shielding of CH₃F and CHF₃ at various temperatures and pressures*, *Journal of Physical Chemistry A* **2001**, 105, 2, 308-314.
- [157] M. Kanakubo, T. Umecky, C. C. Liew, T. Aizawa, K. Hatakeda and Y. Ikushima, *High-pressure NMR studies on solvation structure in supercritical carbon dioxide*, *Fluid Phase Equilibria* **2002**, 194, 859-868.
- [158] P. Raveendran and S. L. Wallen, *Exploring CO(2)-philicity: Effects of stepwise fluorination*, *Journal of Physical Chemistry B* **2003**, 107, 6, 1473-1477.
- [159] P. Raveendran, Y. Ikushima and S. L. Wallen, *Polar attributes of supercritical carbon dioxide*, *Accounts of Chemical Research* **2005**, 38, 6, 478-485.
- [160] V. H. Dalvi, V. Srinivasan and P. J. Rossky, *Understanding the Relative Effectiveness of Alkanethiol Ligands in Dispersing Nanoparticles in Supercritical Carbon Dioxide and Ethane*, *Journal of Physical Chemistry C* **2010**, 114, 37, 15562-15573.
- [161] K. Harrison, J. Goveas, K. P. Johnston and E. A. Orear, *Water-in-Carbon Dioxide Microemulsions with a Fluorocarbon-Hydrocarbon Hybrid Surfactant*, *Langmuir* **1994**, 10, 10, 3536-3541.
- [162] O. Holderer, M. Klostermann, M. Monkenbusch, R. Schweins, P. Lindner, R. Strey, D. Richter and T. Sottmann, *Soft fluctuating surfactant membranes in supercritical CO₂-microemulsions*, *Physical Chemistry Chemical Physics* **2011**, 13, 8, 3022-3025.
- [163] Y. Takebayashi, Y. Mashimo, D. Koike, S. Yoda, T. Furuya, M. Sagisaka, K. Otake, H. Sakai and M. Abe, *Fourier transform infrared spectroscopic study of water-in-supercritical CO₂ microemulsion as a function of water content*, *Journal of Physical Chemistry B* **2008**, 112, 30, 8943-8949.
- [164] Z. Shervani, Y. Ikushima, Y. Hakuta, H. Kunieda and K. Aramaki, *Effect of cosurfactant on water solubilization in supercritical carbon dioxide microemulsions*, *Colloids and Surfaces a-Physicochemical and Engineering Aspects* **2006**, 289, 1-3, 229-232.
- [165] K. J. Thurecht, D. J. T. Hill and A. K. Whittaker, *Investigation of spontaneous microemulsion formation in supercritical carbon dioxide using high-pressure NMR*, *Journal of Supercritical Fluids* **2006**, 38, 1, 111-118.
- [166] J. S. Keiper, J. A. Behles, T. L. Bucholz, R. Simhan, J. M. DeSimone, G. W. Lynn, G. D. Wignall, Y. B. Melnichenko and H. Frielinghaus, *Self-assembly of phosphate fluorosurfactants in carbon dioxide*, *Langmuir* **2004**, 20, 4, 1065-1072.
- [167] M. Sagisaka, S. Iwama, S. Hasegawa, A. Yoshizawa, A. Mohamed, S. Cummings, S. E. Rogers, R. K. Heenan and J. Eastoe, *Super-Efficient Surfactant for Stabilizing Water-in-Carbon Dioxide Microemulsionst*, *Langmuir* **2011**, 27, 10, 5772-5780.

- [168] R. Strey, T. Sottmann and M. Schwan, *Foamed material and method for the production of said foamed material*, Deutsches Patent No. 10260815.6, **2008**.
- [169] L. G. A. Kramer, *Überkritische CO₂-Mikroemulsionen als Vorstufen für Nanoschäume - Darstellung, Charakterisierung und Nanostruktur*, PhD Thesis, University of Cologne, **2008**.
- [170] J. Eastoe, A. Paul, A. Downer, D. C. Steytler and E. Rumsey, *Effects of fluorocarbon surfactant chain structure on stability of water-in-carbon dioxide microemulsions. Links between aqueous surface tension and microemulsion stability*, *Langmuir* **2002**, 18, 8, 3014-3017.
- [171] W. Ostwald, *Lehrbuch der Allgemeinen Chemie*, Leipzig, Germany, **1896**.
- [172] W. Ostwald, *Studien über die Bildung und Umwandlung fester Körper*, *Z. Phys. Chem.* **1897**, 22, 289.
- [173] G. R. Deen, C. L. P. Oliveira and J. S. Pedersen, *Phase Behavior and Kinetics of Phase Separation of a Nonionic Microemulsion of C12E5/Water/1-Chlorotetradecane upon a Temperature Quench*, *Journal of Physical Chemistry B* **2009**, 113, 20, 7138-7146.
- [174] S. Egelhaaf, U. Olsson, P. Schurtenberger, J. Morris and H. Wennerstrom, *Quantitative measurements of Ostwald ripening using time-resolved small-angle neutron scattering*, *Physical Review E* **1999**, 60, 5, 5681-5684.
- [175] A. Evilevitch, U. Olsson, B. Jonsson and H. Wennerstrom, *Kinetics of oil solubilization in microemulsion droplets. Mechanism of oil transport*, *Langmuir* **2000**, 16, 23, 8755-8762.
- [176] M. Kahlweit, *Ageing of Precipitates by Ostwald Ripening*, *Angewandte Chemie-International Edition* **1965**, 4, 5, 444-&.
- [177] M. Kahlweit, *Further Considerations on Theory of Aging (Ostwald Ripening)*, *Berichte Der Bunsen-Gesellschaft-Physical Chemistry Chemical Physics* **1974**, 78, 10, 997-1001.
- [178] T. Teramoto and F. Yonezawa, *Droplet growth dynamics in a water/oil/surfactant system*, *Journal of Colloid and Interface Science* **2001**, 235, 2, 329-333.
- [179] P. Meakin, *Steady-State Droplet Coalescence*, *Physica A* **1991**, 171, 1, 1-18.
- [180] W. Thompson, *On the equilibrium of vapour at a curved surface of liquid*, *Philosophical Magazine* **1871**, series 4, 42, 448-452.
- [181] R. Strey, T. Sottmann, W. Friederichs, S. Lindner, A. Chalbi, D. Engelen and E. Khazova, *Verfahren zur Herstellung eines geschäumten Materials, hierbei eingesetzte emulsionsförmige Zusammensetzung und hieraus erhältliches geschäumtes Material*, Bayer Material Science AG, No. DE102010060386A1, **2012**.
- [182] J. W. Cahn, *Phase Separation by Spinodal Decomposition in Isotropic Systems*, *Journal of Chemical Physics* **1965**, 42, 1, 93-&.
- [183] D. Engelen, Diploma Thesis (unpublished), University of Cologne, **2010**.
- [184] Tauer, K., *Polymerdispersionen*, http://mpikg.mpg.de/pdf/kolloidChemie/Skrpte/Klaus_Tauer_PolDisp-Skript_SS2007.pdf, **2007**.
- [185] R. G. Gilbert, *Emulsion Polymerization - A Mechanistic Approach*, Academic Press Inc. , ISBN 0122830601 **1995**.
- [186] W. V. Smith and R. H. Ewart, *Kinetics of Emulsion Polymerization*, *Journal of Chemical Physics* **1948**, 16, 6, 592-599.
- [187] Wikipedia, *Emulsionspolymerisation*, <http://de.wikipedia.org/wiki/Emulsionspolymerisation>, **2014**.

- [188] R. M. Fitch and C. H. Tsai, *Polymer Colloids - Particle Formation in Nonmicellar Systems*, Journal of Polymer Science Part B-Polymer Letters **1970**, 8, 10, 703-&.
- [189] F. K. Hansen and J. Ugelstad, *Emulsion Polymerization*, Academic Press New York **1982**, 383-412.
- [190] P. J. Feeney, E. Geissler, R. G. Gilbert and D. H. Napper, *Sans Study of Particle Nucleation in Emulsion Polymerization*, Journal of Colloid and Interface Science **1988**, 121, 2, 508-513.
- [191] F. K. Hansen, *Is There Life Beyond Micelles - Mechanisms of Latex Particle Nucleation*, Polymer Latexes **1992**, 492, 12-27.
- [192] F. M. Winnik, *Phase-Transition of Aqueous Poly-(N-Isopropylacrylamide) Solutions - a Study by Nonradiative Energy-Transfer*, Polymer **1990**, 31, 11, 2125-2134.
- [193] M. Stieger and W. Richtering, *Shear-induced phase separation in aqueous polymer solutions: Temperature-sensitive microgels and linear polymer chains*, Macromolecules **2003**, 36, 23, 8811-8818.
- [194] R. Kita and S. Wiegand, *Soret coefficient of poly(N-isopropylacrylamide)/water in the vicinity of coil-globule transition temperature*, Macromolecules **2005**, 38, 11, 4554-4556.
- [195] A. Loxley and B. Vincent, *Equilibrium and kinetic aspects of the pH-dependent swelling of poly(2-vinylpyridine-co-styrene) microgels*, Colloid and Polymer Science **1997**, 275, 12, 1108-1114.
- [196] I. J. Suarez, A. Fernandez-Nieves and M. Marquez, *Swelling kinetics of poly(N-isopropylacrylamide) minigels*, Journal of Physical Chemistry B **2006**, 110, 51, 25729-25733.
- [197] M. Heskins and J. E. Guillet, *Solution Properties of Poly(N-isopropylacrylamide)*, J.Macromol.Sci.-Chem. **1968**, A2, 8, 1441-1455.
- [198] H. G. Schild, *Poly (N-Isopropylacrylamide) - Experiment, Theory and Application*, Progress in Polymer Science **1992**, 17, 2, 163-249.
- [199] A. K. Lele, M. V. Badiger, M. M. Hirve and R. A. Mashelkar, *Thermodynamics of Hydrogen-Bonded Polymer Gel-Solvent Systems*, Chemical Engineering Science **1995**, 50, 22, 3535-3545.
- [200] A. K. Lele, M. M. Hirve, M. V. Badiger and R. A. Mashelkar, *Predictions of bound water content in poly(N-isopropylacrylamide) gel*, Macromolecules **1997**, 30, 1, 157-159.
- [201] F. Afroze, E. Nies and H. Berghmans, *Phase transitions in the system poly(N-isopropylacrylamide)/water and swelling behaviour of the corresponding networks*, Journal of Molecular Structure **2000**, 554, 1, 55-68.
- [202] F. M. Winnik, H. Ringsdorf and J. Venzmer, *Methanol Water as a Co-Nonsolvent System for Poly(N-Isopropylacrylamide)*, Macromolecules **1990**, 23, 8, 2415-2416.
- [203] H. G. Schild, M. Muthukumar and D. A. Tirrell, *Cononsolvency in Mixed Aqueous-Solutions of Poly(N-Isopropylacrylamide)*, Macromolecules **1991**, 24, 4, 948-952.
- [204] F. M. Winnik, M. F. Ottaviani, S. H. Bossmann, M. Garciagaribay and N. J. Turro, *Cononsolvency of Poly(N-Isopropylacrylamide) in Mixed Water-Methanol Solutions - a Look at Spin-Labeled Polymers*, Macromolecules **1992**, 25, 22, 6007-6017.
- [205] H. Kawaguchi, K. Fujimoto and Y. Mizuhara, *Hydrogel Microspheres .3. Temperature-Dependent Adsorption of Proteins on Poly-N-Isopropylacrylamide Hydrogel Microspheres*, Colloid and Polymer Science **1992**, 270, 1, 53-57.
- [206] K. Fujimoto, Y. Mizuhara, N. Tamura and H. Kawaguchi, *Interactions between Thermosensitive Hydrogel Microspheres and Proteins*, Journal of Intelligent Material Systems and Structures **1993**, 4, 2, 184-189.

- [207] S. Zakharchenko, N. Pureskiy, G. Stoychev, M. Stamm and L. Ionov, *Temperature controlled encapsulation and release using partially biodegradable thermo-magneto-sensitive self-rolling tubes*, *Soft Matter* **2010**, 6, 12, 2633-2636.
- [208] C. D. H. Alarcon, S. Pennadam and C. Alexander, *Stimuli responsive polymers for biomedical applications*, *Chemical Society Reviews* **2005**, 34, 3, 276-285.
- [209] P. M. Mendes, *Stimuli-responsive surfaces for bio-applications*, *Chemical Society Reviews* **2008**, 37, 11, 2512-2529.
- [210] M. J. Snowden, *The Use of Poly(N-Isopropylacrylamide) Lattices as Novel Release Systems*, *Journal of the Chemical Society-Chemical Communications* **1992**, 11, 803-804.
- [211] T. Shiroya, N. Tamura, M. Yasui, K. Fujimoto and H. Kawaguchi, *Enzyme Immobilization on Thermosensitive Hydrogel Microspheres*, *Colloids and Surfaces B-Biointerfaces* **1995**, 4, 5, 267-274.
- [212] G. Marcelo, M. Lopez-Gonzalez, F. Mendicuti, M. P. Tarazona and M. Valiente, *Poly(N-isopropylacrylamide)/Gold Hybrid Hydrogels Prepared by Catechol Redox Chemistry. Characterization and Smart Tunable Catalytic Activity*, *Macromolecules* **2014**, 47, 17, 6028-6036.
- [213] C. W. Chen and M. Akashi, *Synthesis, characterization, and catalytic properties of colloidal platinum nanoparticles protected by poly(N-isopropylacrylamide)*, *Langmuir* **1997**, 13, 24, 6465-6472.
- [214] M. R. Islam, A. Ahiabu, X. Li and M. J. Serpe, *Poly (N-isopropylacrylamide) Microgel-Based Optical Devices for Sensing and Biosensing*, *Sensors* **2014**, 14, 5, 8984-8995.
- [215] R. Contreras-Caceres, A. Sanchez-Iglesias, M. Karg, I. Pastoriza-Santos, J. Perez-Juste, J. Pacifico, T. Hellweg, A. Fernandez-Barbero and L. M. Liz-Marzan, *Encapsulation and growth of gold nanoparticles in thermoresponsive microgels*, *Advanced Materials* **2008**, 20, 9, 1666-1670.
- [216] N. Yamada, T. Okano, H. Sakai, F. Karikusa, Y. Sawasaki and Y. Sakurai, *Thermoresponsive Polymeric Surfaces - Control of Attachment and Detachment of Cultured-Cells*, *Makromolekulare Chemie-Rapid Communications* **1990**, 11, 11, 571-576.
- [217] L. Ionov, M. Stamm and S. Diez, *Reversible switching of microtubule motility using thermoresponsive polymer surfaces*, *Nano Letters* **2006**, 6, 9, 1982-1987.
- [218] L. Ionov, A. Synytska and S. Diez, *Temperature-induced size-control of bioactive surface patterns*, *Advanced Functional Materials* **2008**, 18, 10, 1501-1508.
- [219] I. Y. Galaev and B. Mattiasson, *'Smart' polymers and what they could do in biotechnology and medicine*, *Trends in Biotechnology* **1999**, 17, 8, 335-340.
- [220] L. Ionov and S. Diez, *Environment-Friendly Photolithography Using Poly(N-isopropylacrylamide)-Based Thermoresponsive Photoresists*, *Journal of the American Chemical Society* **2009**, 131, 37, 13315-13319.
- [221] Integrated Infrastructure Initiative for Neutron Scattering and Muon Spectroscopy (NMI3), *Neutron Research*, <http://nmi3.eu/neutron-research/techniques-for-.html>, **2014**.
- [222] J. Eastoe, *Scattering Techniques in Surfactant Chemistry*, **2002**, 96-130.
- [223] T. Brückel, G. Heger, D. Richter, G. Roth and R. Zorn, *Lectures*, in *Laboratory Course Neutron Scattering*, RWTH Aachen, University Münster, Forschungszentrum Jülich **2012**, ISBN 978-3-89336-789-4, all pages.
- [224] National Institute of Standards and Technology, *Neutron activation and scattering calculator*, <http://www.ncnr.nist.gov/resources/activation/>, **2012-2015**.
- [225] J. Oberdisse, *Adsorption and grafting on colloidal interfaces studied by scattering techniques*, *Current Opinion in Colloid & Interface Science* **2007**, 12, 1, 3-8.

- [226] F. Boue, F. Cousin, J. Gummel, J. Oberdisse, G. Carrot and A. El Harrak, *Small angle scattering from soft matter - application to complex mixed systems*, Comptes Rendus Physique **2007**, 8, 7-8, 821-844.
- [227] D. D. Lee, J. Barker and S. H. Chen, *Absolute Calibration of Small-Angle Neutron-Scattering Data Using Strong Coherent Scattering*, Journal De Physique Iv **1993**, 3, C8, 431-434.
- [228] I. Grillo, *Small-Angle Neutron Scattering and Applications in Soft Condensed Matter*, Springer Verlag Heidelberg, **2008**.
- [229] LAMP, <http://www.ill.eu/instruments-support/computing-for-science/cs-software/all-software/lamp/>, **2014**.
- [230] GRASP, <http://www.ill.eu/instruments-support/instruments-groups/groups/lss/grasp/>, **2014**.
- [231] M. Kotlarchyk, S. H. Chen and J. S. Huang, *Critical-Behavior of a Microemulsion Studied by Small-Angle Neutron-Scattering*, Physical Review A **1983**, 28, 1, 508-511.
- [232] M. Gradzielski, D. Langevin and B. Farago, *Experimental investigation of the structure of nonionic microemulsions and their relation to the bending elasticity of the amphiphilic film*, Physical Review E **1996**, 53, 4, 3900-3919.
- [233] M. Gradzielski, D. Langevin, L. Magid and R. Strey, *Small-Angle Neutron-Scattering from Diffuse Interfaces .2. Polydisperse Shells in Water-N-Alkane-C(10)E(4) Microemulsions*, Journal of Physical Chemistry **1995**, 99, 35, 13232-13238.
- [234] H. BaggerJorgensen, U. Olsson and K. Mortensen, *Microstructure in a ternary microemulsion studied by small angle neutron scattering*, Langmuir **1997**, 13, 6, 1413-1421.
- [235] T. Hellweg and D. Langevin, *Bending elasticity of the surfactant monolayer in droplet microemulsions: Determination by a combination of dynamic light scattering and neutron spin-echo spectroscopy*, Physical Review E **1998**, 57, 6, 6825-6834.
- [236] T. Hellweg, A. Brulet and T. Sottmann, *Dynamics in an oil-continuous droplet microemulsion as seen by quasielastic scattering techniques*, Physical Chemistry Chemical Physics **2000**, 2, 22, 5168-5174.
- [237] T. Neugebauer, *Berechnung der Lichtzerstreuung von Fadenkettenlösungen*, Annalen der Physik **1943**, 434, 509-533.
- [238] J. K. Percus and G. J. Yevick, *Analysis of Classical Statistical Mechanics by Means of Collective Coordinates*, Physical Review **1958**, 110, 1, 1-13.
- [239] D. J. Kinning and E. L. Thomas, *Hard-Sphere Interactions between Spherical Domains in Diblock Copolymers*, Macromolecules **1984**, 17, 9, 1712-1718.
- [240] J. S. Pedersen, *Determination of Size Distributions from Small-Angle Scattering Data for Systems with Effective Hard-Sphere Interactions*, Journal of Applied Crystallography **1994**, 27, 595-608.
- [241] B. Weyerich, J. Brunner-Popela and O. Glatter, *Small-angle scattering of interacting particles. II. Generalized indirect Fourier transformation under consideration of the effective structure factor for polydisperse systems*, Journal of Applied Crystallography **1999**, 32, 197-209.
- [242] L. S. Ornstein and F. Zernicke, *Accidental deviations of density and opalescence at the critical point of a single substance*, Proc. Acad. Sci. **1914**, 17, 793-806.
- [243] P.-G. De Gennes, *Scaling concepts in polymer physics*, Ithaca and London: University Press, **1979**.
- [244] M. Gradzielski, D. Langevin, T. Sottmann and R. Strey, *Small angle neutron scattering near the wetting transition: Discrimination of microemulsions from weakly structured mixtures*, Journal of Chemical Physics **1996**, 104, 10, 3782-3787.

- [245] M. Stieger, W. Richtering, J. S. Pedersen and P. Lindner, *Small-angle neutron scattering study of structural changes in temperature sensitive microgel colloids*, Journal of Chemical Physics **2004**, 120, 13, 6197-6206.
- [246] M. Shibayama, T. Tanaka and C. C. Han, *Small-Angle Neutron-Scattering Study on Poly(N-Isopropyl Acrylamide) Gels near Their Volume-Phase Transition-Temperature*, Journal of Chemical Physics **1992**, 97, 9, 6829-6841.
- [247] M. Shibayama, T. Tanaka and C. C. Han, *Small-Angle Neutron-Scattering Study on Weakly Charged Temperature Sensitive Polymer Gels*, Journal of Chemical Physics **1992**, 97, 9, 6842-6854.
- [248] R. Bracewell, *Fourier Transformation and its Applications*, McGraw Hill, New York, **1986**.
- [249] *Fourier Transformation and Deconvolution*, in *Neutrons, X-rays and light: Scattering methods applied to soft condensed matter*, Elsevier North Holland Delta Series **2002**, 103-126.
- [250] O. Glatter, *Interpretation of Real-Space Information from Small-Angle Scattering Experiments*, Journal of Applied Crystallography **1979**, 12, Apr, 166-175.
- [251] O. Glatter, *Evaluation of Small-Angle Scattering Data from Lamellar and Cylindrical Particles by the Indirect Transformation Method*, Journal of Applied Crystallography **1980**, 13, Dec, 577-584.
- [252] O. Glatter, *New Method for Evaluation of Small-Angle Scattering Data*, Journal of Applied Crystallography **1977**, 10, Oct1, 415-421.
- [253] J. BrunnerPopela and O. Glatter, *Small-angle scattering of interacting particles .1. Basic principles of a global evaluation technique*, Journal of Applied Crystallography **1997**, 30, 431-442.
- [254] A. Bergmann, G. Fritz and O. Glatter, *Solving the generalized indirect Fourier transformation (GIFT) by Boltzmann simplex simulated annealing (BSSA)*, Journal of Applied Crystallography **2000**, 33, 1212-1216.
- [255] O. Glatter, *Convolution Square Root of Band-Limited Symmetrical Functions and Its Application to Small-Angle Scattering Data*, Journal of Applied Crystallography **1981**, 14, Apr, 101-108.
- [256] R. Mittelbach and O. Glatter, *Direct structure analysis of small-angle scattering data from polydisperse colloidal particles*, Journal of Applied Crystallography **1998**, 31, 600-608.
- [257] E. W. Kaler, J. F. Billman, J. L. Fulton and R. D. Smith, *A Small-Angle Neutron-Scattering Study of Intermicellar Interactions in Microemulsions of Aot, Water, and near-Critical Propane*, Journal of Physical Chemistry **1991**, 95, 1, 458-462.
- [258] T. Koga, S. Q. Zhou and B. Chu, *Dynamic light-scattering study of self-assembly of diblock copolymers in supercritical carbon dioxide*, Applied Optics **2001**, 40, 24, 4170-4178.
- [259] K. Pressl, M. Kriechbaum, M. Steinhart and P. Lagner, *High pressure cell for small-and wide-angle x-ray scattering*, Review of Scientific Instruments **1997**, 68, 12, 4588-4592.
- [260] L. Z. Liu, Z. G. Cheng, K. Inomata, S. Q. Zhou and B. Chu, *Synchrotron SAXS and laser light scattering studies of aggregation behavior of poly(1,1-dihydroperfluorooctyl acrylate-b-vinyl acetate) diblock copolymer in supercritical carbon dioxide*, Macromolecules **1999**, 32, 18, 5836-5845.
- [261] J. Kohlbrecher, A. Bollhalder, R. Vavrin and G. Meier, *A high pressure cell for small angle neutron scattering up to 500 MPa in combination with light scattering to investigate liquid samples*, Review of Scientific Instruments **2007**, 78, 12, 607520-1 - 607520-5.
- [262] M. D. Lechner, D. G. Steinmeier and N. Vennemann, *Small Angle Neutron Scattering under high pressure*, Makromolekulare Chemie, Rapid Communication **1985**, 6, 281-284.

- [263] T. Koga, S. Q. Zhou, B. Chu, J. L. Fulton, S. Yang, C. K. Ober and B. Erman, *High-pressure cell for simultaneous small-angle x-ray scattering and laser light scattering measurements*, Review of Scientific Instruments **2001**, 72, 6, 2679-2685.
- [264] M. Steinhart, M. Kriechbaum, K. Pressl, H. Amenitsch, P. Laggner and S. Bernstorff, *High-pressure instrument for small- and wide-angle x-ray scattering. II. Time-resolved experiments*, Review of Scientific Instruments **1999**, 70, 2, 1540-1545.
- [265] J. Woenckhaus, R. Kohling, R. Winter, P. Thiagarajan and S. Finet, *High pressure-jump apparatus for kinetic studies of protein folding reactions using the small-angle synchrotron x-ray scattering technique*, Review of Scientific Instruments **2000**, 71, 10, 3895-3899.
- [266] C. Jeworrek, S. Uelner and R. Winter, *Phase behavior and kinetics of pressure-jump induced phase transitions of bicellar lipid mixtures*, Soft Matter **2011**, 7, 6, 2709-2719.
- [267] Institut Laue-Langevin, GRASP, <http://www.ill.eu/instruments-support/instruments-groups/groups/lss/grasp/home/>, **2014**.
- [268] Institut Laue-Langevin, LAMP, <http://www.ill.eu/instruments-support/computing-for-science/cs-software/all-software/lamp/the-lamp-book/>, **2014**.
- [269] Helmholtz Zentrum Berlin, BerSANS, http://www.helmholtz-berlin.de/forschung/oe/em/supraleitung/instrumente/v4/data-analysis_en.html, **2014**.
- [270] U. Keiderling, *The new 'BerSANS-PC' software for reduction and treatment of small angle neutron scattering data*, Applied Physics a-Materials Science & Processing **2002**, 74, S1455-S1457.
- [271] B. Spiegelhalder, *Final Design Report: Neutron Chopper System NCS034*, **2011**.
- [272] R. Gähler and R. Golub, ILL SC 99 **1999**, 73.
- [273] A. Wiedenmann, U. Keiderling, K. Habicht, M. Russina and R. Gähler, *Dynamics of field-induced ordering in magnetic colloids studied by new time-resolved small-angle neutron-scattering techniques*, Physical Review Letters **2006**, 97, 5, 057202-1 - 054202-4.
- [274] D. Kipping, R. Gähler and K. Habicht, *Small angle neutron scattering at very high time resolution: Principle and simulations of 'TISANE'*, Physics Letters A **2008**, 372, 10, 1541-1546.
- [275] P. Lindner, *Scattering Experiments*, in *Neutrons, X-rays and Light: Scattering Methods Applied to Soft Condensed Matter*, Elsevier Science and Technology **2002**, ISBN 9780444511225, 23-48.
- [276] MalvernInstruments, *Dynamic Light Scattering: An Introduction in 30 Minutes*, Malvern Instruments, **2014**.
- [277] Müller, A., *Lichtstreuung an Nanomaterialien*, http://www.meerholz.uni-koeln.de/fileadmin/user_upload/Docs/Praktikum/Versuchsanleitungen/Skript-Lichtstreuung_A._Mueller.pdf, **2011**.
- [278] S. Y. Wei and K. Saitow, *In situ multipurpose time-resolved spectrometer for monitoring nanoparticle generation in a high-pressure fluid*, Review of Scientific Instruments **2012**, 83, 7, 073110-1 - 073110-8.
- [279] R. G. Alargova, S. Deguchi and K. Tsujii, *Dynamic light scattering study of polystyrene latex suspended in water at high temperatures and high pressures*, Colloids and Surfaces a-Physicochemical and Engineering Aspects **2001**, 183, 303-312.
- [280] G. Meier and H. Kriegs, *A high pressure cell for dynamic light scattering up to 2 kbars with conservation of plane of polarization*, Review of Scientific Instruments **2008**, 79, 1, 13102-1 - 13102-5.

- [281] T. W. Kermis, D. Li, O. Guney-Altay, I. H. Park, J. H. van Zanten and M. A. McHugh, *High-pressure dynamic light scattering of poly(ethylene-co-1-butene) in ethane, propane, butane, and pentane at 130 degrees C and kilobar pressures*, *Macromolecules* **2004**, 37, 24, 9123-9131.
- [282] B. H. Zimm, *Apparatus and Methods for Measurement and Interpretation of the Angular Variation of Light Scattering - Preliminary Results on Polystyrene Solutions*, *Journal of Chemical Physics* **1948**, 16, 12, 1099-1116.
- [283] A. Guinier and G. Fournet, *Small-angle Scattering of X-rays*, in *Structure of matter series*, Wiley **1955**,
- [284] J. Eastoe, A. Downer, A. Paul, D. C. Steytler, E. Rumsey, J. Penfold and R. K. Heenan, *Fluoro-surfactants at air/water and water/CO₂ interfaces*, *Physical Chemistry Chemical Physics* **2000**, 2, 22, 5235-5242.
- [285] A. Favrelle, C. Boyere, K. M. Tran, D. Alaimo, B. Calvignac, M. Paquot, F. Boury, C. Jerome and A. Debuigne, *Surface activity of a fluorinated carbohydrate ester in water/carbon dioxide emulsions*, *Journal of Colloid and Interface Science* **2013**, 398, 273-275.
- [286] J. Eastoe, A. Paul, S. Nave, D. C. Steytler, B. H. Robinson, E. Rumsey, M. Thorpe and R. K. Heenan, *Micellization of hydrocarbon surfactants in supercritical carbon dioxide*, *Journal of the American Chemical Society* **2001**, 123, 5, 988-989.
- [287] S. Cummings, R. Enick, S. Rogers, R. Heenan and J. Eastoe, *Amphiphiles for supercritical CO₂*, *Biochimie* **2012**, 94, 1, 94-100.
- [288] A. Mohamed, M. Sagisaka, M. Hollamby, S. E. Rogers, R. K. Heenan, R. Dyer and J. Eastoe, *Hybrid CO₂-philic Surfactants with Low Fluorine Content*, *Langmuir* **2012**, 28, 15, 6299-6306.
- [289] M. Sagisaka, D. Koike, S. Yoda, Y. Takebayashi, T. Furuya, A. Yoshizawa, H. Sakai, M. Abe and K. Otake, *Optimum tail length of fluorinated double-tail anionic surfactant for water/supercritical CO₂ microemulsion formation*, *Langmuir* **2007**, 23, 17, 8784-8788.
- [290] A. Mohamed, M. Sagisaka, F. Guittard, S. Cummings, A. Paul, S. E. Rogers, R. K. Heenan, R. Dyer and J. Eastoe, *Low Fluorine Content CO₂-philic Surfactants*, *Langmuir* **2011**, 27, 17, 10562-10569.
- [291] S. A. Safran, *Bicontinuous to Lamellar Transitions in L₃-Phases and Microemulsions*, *Langmuir* **1991**, 7, 9, 1864-1866.
- [292] K. V. Schubert, G. Busse, R. Strey and M. Kahlweit, *Microemulsions with Formamide as Polar-Solvent*, *Journal of Physical Chemistry* **1993**, 97, 1, 248-254.
- [293] P. K. Kilpatrick, C. A. Gorman, H. T. Davis, L. E. Scriven and W. G. Miller, *Patterns of Phase-Behavior in Ternary Ethoxylated Alcohol Normal-Alkane - Water Mixtures*, *Journal of Physical Chemistry* **1986**, 90, 21, 5292-5299.
- [294] S. T. Cui, H. D. Cochran and P. T. Cummings, *Vapor-liquid phase coexistence of alkane carbon dioxide and perfluoroalkane carbon dioxide mixtures*, *Journal of Physical Chemistry B* **1999**, 103, 21, 4485-4491.
- [295] A. Iezzi, P. Bendale, R. M. Enick, M. Turberg and J. Brady, *Gel Formation in Carbon-Dioxide Semifluorinated Alkane Mixtures and Phase-Equilibria of a Carbon-Dioxide Perfluorinated Alkane Mixture*, *Fluid Phase Equilibria* **1989**, 52, 307-317.
- [296] G. Porod, *Small Angle X-ray scattering*, ed. O. Glatter and O. Kratky, Academic Press London, , pp 18-50, **1982**.
- [297] J. A. Silas and E. W. Kaler, *Effect of multiple scattering on SANS spectra from bicontinuous microemulsions*, *Journal of Colloid and Interface Science* **2003**, 257, 2, 291-298.
- [298] O. Glatter and O. Kratky, *Small Angle X-Ray Scattering*, Academic Press, p 179, **1982**.

- [299] S. H. Chen, S. M. Choi and P. LoNostro, *Measurement of interfacial curvatures in micro-phase-separated bicontinuous structures using small-angle neutron scattering*, Nuovo Cimento Della Societa Italiana Di Fisica D-Condensed Matter Atomic Molecular and Chemical Physics Fluids Plasmas Biophysics **1998**, 20, 12bis, 1971-1988.
- [300] A. K. Thakre, W. K. den Otter and W. J. Briels, *Domain formation and growth in spinodal decomposition of a binary fluid by molecular dynamics simulations*, Physical Review E **2008**, 77, 1, 011503-1 - 011503-6.
- [301] A. S. Kabalnov and E. D. Shchukin, *Ostwald Ripening Theory - Applications to Fluorocarbon Emulsion Stability*, Advances in Colloid and Interface Science **1992**, 38, 69-97.
- [302] C. Wagner, *Theorie Der Alterung Von Niederschlagen Durch Umlösen (Ostwald-Reifung)*, Zeitschrift für Elektrochemie **1961**, 65, 7-8, 581-591.
- [303] M. Kahlweit, F. Lichterfeld, R. Strey and J. Jen, *Decomposition of Alloys: the Early Stages*, 2nd Acta-Scripta Metall. Conference, 61, **1984**.
- [304] U. Olsson, H. Bagger-Jørgensen, M. Leaver, J. Morris, K. Mortensen, R. Strey, P. Schurtenberger and H. Wennerström, *Stable, metastable and unstable oil-in-water droplets*, Progresses in Colloid and Polymer Science **1997**, 106, 6-13.
- [305] H. Wennerstrom, J. Morris and U. Olsson, *Homogeneous nucleation in an emulsion/droplet microemulsion system*, Langmuir **1997**, 13, 26, 6972-6979.
- [306] G. R. Deen and J. S. Pedersen, *Late-stage coarsening of oil droplets of excess oil in microemulsions following a temperature quench*, Zeitschrift Fur Metallkunde **2006**, 97, 3, 285-289.
- [307] J. Vollmer, D. Vollmer and R. Strey, *Oscillating phase separation in microemulsions .2. Description by a bending free energy*, Journal of Chemical Physics **1997**, 107, 9, 3627-3633.
- [308] W. I. Higuchi and J. Misra, *Physical Degradation of Emulsions Via Molecular Diffusion Route and Possible Prevention Thereof*, Journal of Pharmaceutical Sciences **1962**, 51, 5, 459-&.
- [309] P. Bender, A. Günther, D. Honecker, A. Wiedenmann, A. Tschöpe, A. Michels and R. Birringer, *Relaxation dynamics of Ni nanorod colloid studied by Time-resolved Small Angle Neutron Scattering (TISANE)*, manuscript in preparation **2015**,
- [310] A. Wiedenmann, U. Keiderling, R. P. May and C. Dewhurst, *Dynamics of field-induced ordering processes in ferrofluids studied by polarised small-angle neutron scattering*, Physica B-Condensed Matter **2006**, 385, 453-456.
- [311] U. Olsson, H. Bagger-Jørgensen, M. S. Leaver, J. V. Morris, K. Mortensen, R. Strey, P. Schurtenberger and H. Wennerstrom, *Stable, metastable and unstable oil-in-water droplets*, Progr Colloid Polym Sci **1997**, 106, 6-13.
- [312] Y. Q. Zhang, T. Tanaka and M. Shibayama, *Super-Absorbency and Phase-Transition of Gels in Physiological Salt-Solutions*, Nature **1992**, 360, 6400, 142-144.
- [313] J. Eliassaf, *Aqueous-Solutions of Poly(N-Isopropylacrylamide)*, Journal of Applied Polymer Science **1978**, 22, 3, 873-874.
- [314] M. Shibayama, K. Kawakubo, F. Ikkai and M. Imai, *Small-angle neutron scattering study on charged gels in deformed state*, Macromolecules **1998**, 31, 8, 2586-2592.
- [315] J. J. Lietor-Santos, U. Gasser, R. Vavrin, Z. B. Hu and A. Fernandez-Nieves, *Structural changes of poly(N-isopropylacrylamide)-based microgels induced by hydrostatic pressure and temperature studied by small angle neutron scattering*, Journal of Chemical Physics **2010**, 133, 3, 034901.
- [316] H. Hirose and M. Shibayama, *Kinetics of volume phase transition in poly(N-isopropylacrylamide-co-acrylic acid) gels*, Macromolecules **1998**, 31, 16, 5336-5342.

- [317] M. Philipp, U. Muller, R. J. J. Rioboo, R. Sanctuary, P. Muller-Buschbaum and J. K. Kruger, *Kinetic processes at the demixing transition of PNIPAM solutions*, *Soft Matter* **2013**, 9, 41, 9887-9896.
- [318] A. Meier-Koll, V. Pipich, P. Busch, C. M. Papadakis and P. Muller-Buschbaum, *Phase Separation in Semidilute Aqueous Poly(N-isopropylacrylamide) Solutions*, *Langmuir* **2012**, 28, 23, 8791-8798.
- [319] R. H. Pelton, H. M. Pelton, A. Morphesis and R. L. Rowell, *Particle Sizes and Electrophoretic Mobilities of Poly(N-Isopropylacrylamide) Latex*, *Langmuir* **1989**, 5, 3, 816-818.
- [320] X. Wu, R. H. Pelton, A. E. Hamielec, D. R. Woods and W. Mcphee, *The Kinetics of Poly(N-Isopropylacrylamide) Microgel Latex Formation*, *Colloid and Polymer Science* **1994**, 272, 4, 467-477.
- [321] A. Guillermo, J. P. C. Addad, J. P. Bazile, D. Duracher, A. Elaissari and C. Pichot, *NMR investigations into heterogeneous structures of thermosensitive microgel particles*, *Journal of Polymer Science Part B-Polymer Physics* **2000**, 38, 6, 889-898.
- [322] T. Hellweg, C. D. Dewhurst, W. Eimer and K. Kratz, *PNIPAM-co-polystyrene core-shell microgels: Structure, swelling behavior, and crystallization*, *Langmuir* **2004**, 20, 11, 4330-4335.
- [323] S. Seelenmeyer, I. Deike, S. Rosenfeldt, C. Norhausen, N. Dingenouts, M. Ballauff, T. Narayanan and P. Lindner, *Small-angle x-ray and neutron scattering studies of the volume phase transition in thermosensitive core-shell colloids*, *Journal of Chemical Physics* **2001**, 114, 23, 10471-10478.
- [324] S. T. Sun, J. Hu, H. Tang and P. Y. Wu, *Chain Collapse and Revival Thermodynamics of Poly(N-isopropylacrylamide) Hydrogel*, *Journal of Physical Chemistry B* **2010**, 114, 30, 9761-9770.
- [325] M. Philipp, K. Kyriakos, L. Silvi, W. Lohstroh, W. Petry, J. K. Kruger, C. M. Papadakis and P. Muller-Buschbaum, *From Molecular Dehydration to Excess Volumes of Phase-Separating PNIPAM Solutions*, *Journal of Physical Chemistry B* **2014**, 118, 15, 4253-4260.
- [326] F. Habbal, *Basic Principles in Microfluidics*, in *Fundamentals of Microfabrication with Applications to BioMEMS*, Harvard University **2008**,
- [327] P. A. Auroux, Y. Koc, A. deMello, A. Manz and P. J. R. Day, *Miniaturised nucleic acid analysis*, *Lab on a Chip* **2004**, 4, 6, 534-546.
- [328] D. Auslander, S. Auslander, G. Charpin-El Hamri, F. Sedlmayer, M. Muller, O. Frey, A. Hierlemann, J. Stelling and M. Fussenegger, *A Synthetic Multifunctional Mammalian pH Sensor and CO₂ Transgene-Control Device*, *Molecular Cell* **2014**, 55, 3, 397-408.
- [329] P. R. Miller, X. Y. Xiao, I. Brener, D. B. Burckel, R. Narayan and R. Polsky, *Microneedle-Based Transdermal Sensor for On-Chip Potentiometric Determination of K⁺*, *Advanced Healthcare Materials* **2014**, 3, 6, 876-881.
- [330] S. Q. Huang, B. C. Lin and J. H. Qin, *Microfluidic synthesis of tunable poly-(N-isopropylacrylamide) microparticles via PEG adjustment*, *Electrophoresis* **2011**, 32, 23, 3364-3370.
- [331] W. Wang, T. Luo, X. J. Ju, R. Xie, L. Liu and L. Y. Chu, *Microfluidic Preparation of Multicompartment Microcapsules for Isolated Co-encapsulation and Controlled Release of Diverse Components*, *International Journal of Nonlinear Sciences and Numerical Simulation* **2012**, 13, 5, 325-332.
- [332] X. C. Zhou, J. F. Li, C. Wu and B. Zheng, *Constructing the phase diagram of an aqueous solution of poly(N-isopropyl acrylamide) by controlled microevaporation in a nanoliter microchamber*, *Macromolecular Rapid Communications* **2008**, 29, 16, 1363-1367.
- [333] P. Naumann, S. Datta, T. Sottmann, B. Arlt, H. Frielinghaus and S. Wiegand, *Isothermal Behavior of the Soret Effect in Nonionic Microemulsions: Size Variation by Using Different n-Alkanes*, *Journal of Physical Chemistry B* **2014**, 118, 12, 3451-3460.

- [334] V. Rauch, *Einfluss von PNIPAM auf Phasenverhalten und Mikrostruktur von Mikroemulsionen*, Bachelor Thesis, unpublished work, **2014**.
- [335] M. Kahlweit, R. Strey and P. Firman, *Search for Tricritical Points in Ternary-Systems - Water Oil Nonionic Amphiphile*, Journal of Physical Chemistry **1986**, 90, 4, 671-677.
- [336] L. Q. Cao, L. P. Chen, X. J. Chen, L. H. Zuo and Z. W. Li, *Synthesis of smart core-shell polymer in supercritical carbon dioxide*, Polymer **2006**, 47, 13, 4588-4595.
- [337] R. Schwering, *Polymerization of highly viscous bicontinuous and droplet microemulsions*, PhD Thesis, University of Cologne, **2008**.
- [338] H. Dave, F. Gao, M. Schultz and C. C. Co, *Phase behavior and SANS investigations of edible sugar-limonene microemulsions*, Colloids and Surfaces a-Physicochemical and Engineering Aspects **2007**, 296, 1-3, 45-50.
- [339] M. Schwan, *Überkritische Mikroemulsionen zur Herstellung nanozellulärer Schäume - Principle of Supercritical Microemulsion Expansion*, in Cuvillier **2005**, ISBN: 978-3865377302, .

ERKLÄRUNG

Ich versichere, dass ich die von mir vorgelegte Dissertation selbständig angefertigt, die benutzten Quellen und Hilfsmittel vollständig angegeben und die Stellen der Arbeit - einschließlich Tabellen, Karten und Abbildungen -, die anderen Werken im Wortlaut oder dem Sinn nach entnommen sind, in jedem Einzelfall als Entlehnung kenntlich gemacht habe; dass diese Dissertation noch keiner anderen Fakultät oder Universität zur Prüfung vorgelegen hat; dass sie - abgesehen von unten angegebenen Teilpublikationen - noch nicht veröffentlicht worden ist sowie, dass ich eine solche Veröffentlichung vor Abschluss des Promotionsverfahrens nicht vornehmen werde. Die Bestimmungen der Promotionsordnung sind mir bekannt. Die von mir vorgelegte Dissertation ist von Prof. Dr. R. Strey betreut worden.

Köln, den 09. Februar 2015

TEILPUBLIKATIONEN

- [1] Müller, A., Pütz, Y., Oberhoffer, R., Becker, N., Strey, R., Wiedenmann, R., Sottmann, T., *Kinetics of pressure-induced structural changes in super- or near-critical CO₂-microemulsions*, Physical Chemistry Chemical Physics **2014**, 16, 34, 18092-18097.
- [2] Pütz, Y., Grassberger, L., Lindner, P., Schweins, R., Strey, R. and Sottmann, T., *Unexpected efficiency boosting in CO(2)-microemulsions: A cyclohexane depletion zone near the fluorinated surfactants evidenced by a systematic SANS contrast variation study*, Physical Chemistry Chemical Physics **2015**, DOI: 10.1039/C4CP05435K , accepted manuscript.

Öffentliche Vorträge:

- [3] Pütz, Y., Müller, A., Oberhoffer, R., Becker, N., Strey, R., Wiedenmann, A., Sottmann, T., *Kinetics of pressur-induced structural changes in super- or near-critical CO₂-microemulsions*, Studying Kinetics with Neutrons, Grenoble, France, **2014**.
- [4] Pütz, Y., Grassberger, L., Lindner, P., Schweins, R., Strey, R. and Sottmann, T., *Cyclohexane as efficiency booster for fluorinated CO₂-microemulsions: A systematic SANS contrast variation study*, 20th Internations Symposium on Surfactants in Solution, Coimbra, Portugal, **2014**.
- [5] Pütz, Y., Grassberger, L., Lindner, P., Schweins, R., Strey, R. and Sottmann, T., *Cyclohexane as efficiency booster for fluorinated CO₂-microemulsions: A systematic SANS contrast variation study*, Deutsche Tagung für Forschung mit Synchrotronstrahlung, Neutronen und Ionenstrahlen an Großgeräten, Bonn, Germany, **2014**.

Curriculum Vitae

Name Yvonne Pütz
Born 13.12.1987, Bad Soden, Germany



Education

1994-1998 Elementary School: Grundschule Oberbrechen, Germany.
1998-2007 High School: St. Mary's Convent School, Limburg, Germany.
Final secondary-school examinations (Grade 1.6)

Academic Education

2007-2010 Studies of Food Chemistry, Justus-Liebig University Giessen, Germany (Grade 1.9, Bachelor of Science).
04-09/2010 Bachelor Thesis at the University of Aberdeen, Great Britain, on "*Uptake and Translocation of antimony in Thunbergia alata*", advisors: Prof. Dr. J. Feldmann, University of Aberdeen, and Prof. Dr. H. Zorn, University of Giessen.
2010-2012 Studies of Chemistry, University of Cologne, Germany (Grade: 1.2, Master of Science).
10/2011-04/2012 Master Thesis at the University of Cologne, Germany, on "*Influence of hydrophobic additives on supercritical CO₂-microemulsions and their foaming properties*", advisor Prof. Dr. R. Strey.

Scientific Career

Since 01/2011 Research assistant and PhD-thesis at the Institute of Physical Chemistry, University of Cologne, Prof. Dr. R. Strey's group.
07/2012-12/2014 Frequent research trips to the Institut Laue-Langevin, Grenoble, France.
07-08/2014 Research visit at Imperial College London, Great Britain, Dr. J. T. Cabral's group.

Scholarships and Awards

07/2012 "Fachgruppen Förderpreis, Department of Chemistry, University of Cologne, Germany.
11/2012-10/2014 "Chemiefonds-Stipendium", PhD scholarship
Fonds der Chemischen Industrie (FCI), Germany.